Durham University

# Durham E-Theses

## *Calculations of the electronic structure and optical properties of strained II-VI superlattices.*

Hall, David Oakley

**How to cite:**

Hall, David Oakley (1991) *Calculations of the electronic structure and optical properties of strained II-VI superlattices.*, Durham theses, Durham University. Available at Durham E-Theses Online: http://etheses.dur.ac.uk/1549/

**Use policy**

The full-text may be used and/or reproduced, and given to third parties in any format or medium, without prior permission or charge, for personal research or study, educational, or not-for-profit purposes provided that:

- a full bibliographic reference is made to the original source
- a link is made to the metadata record in Durham E-Theses
- the full-text is not changed in any way

The full-text must not be sold in any format or medium without the formal permission of the copyright holders.

Please consult the full Durham E-Theses policy for further details.

Academic Support Office, The Palatine Centre, Durham University, Stockton Road, Durham, DH1 3LE
e-mail: e-theses.admin@durham.ac.uk Tel: +44 0191 334 6107
http://etheses.dur.ac.uk

# CALCULATIONS OF THE ELECTRONIC STRUCTURE AND OPTICAL PROPERTIES OF STRAINED II-VI SUPERLATTICES.

by

D. O. Hall, BA (Oxon)

A thesis
submitted in candidature for
the degree of Doctor of Philosophy
at the University of Durham
May 1991

The copyright of this thesis rests with the author.
No quotation from it should be published without
his prior written consent and information derived
from it should be acknowledged.

- 9 JUL 1992

# DECLARATION

I hereby declare that the work reported in this thesis has not previously been submitted for any degree and is not being currently submitted in candidature for any other degree.

__________________

The work reported in this thesis was carried out by the candidate.

__________________

PhD Supervisor.

__________________

PhD Candidate.

D. O. Hall

# CALCULATIONS OF THE ELECTRONIC STRUCTURE AND OPTICAL PROPERTIES OF STRAINED II-VI SUPERLATTICES.

Ph.D., 1991

## ABSTRACT

This thesis consists of calculations of the electronic bandstructure, wavefunctions and interband momentum matrix elements of the strained-layer II-VI telluride superlattices CdTe-ZnTe and HgTe-ZnTe. The calculations have been performed using the empirical pseudopotential method. The complex bandstructures of the bulk materials of the sublayers are calculated, and test solutions are formed at each energy. The test solutions are checked for continuity of wavefunction and derivative of wavefunction at the interfaces, to find the energies of states in the heterostructure. The method includes spin, and interband mixing. The effects of mixing on the interband momentum matrix elements is investigated. The polarisation dependence of the momentum matrix elements is calculated, and compared with the results of tight-binding calculations.

The results of calculations are compared with other theoretical calculations from the literature, and with experiment. It is shown that the experimental information on CdTe-ZnTe superlattices can be explained on the basis of the pseudopotential calculations, although there are differences on details. There are fewer results of experiments on HgTe-ZnTe superlattices, and so the calculations have been compared with results on other Hg-based II-VI superlattices. It is found that, while most results can be explained, there are important questions about the interpretation of some results, particularly for narrow gap and long period systems.

# ACKNOWLEDGEMENTS

I would like to thank my supervisor Dr. Stuart Brand for introducing me to this project, and for his rigorous criticism of my work. I also am grateful to Dr. R. A. Abram for offering ideas, and encouraging me to attend conferences and meetings, through which I have gained a wider sense of the physics community. Particular thanks go to Dr. D. T. Hughes, who has given me a great deal of help and advice throughout the time I have spent at Durham. For advice on II-VI semiconductors I have often turned to Dr. P. Clifton. I have also had useful discussions with other members, too numerous to mention, of the theory and II-VI groups in the Applied Physics department at Durham.

I acknowledge financial support from the Science and Engineering Research Council for the period of this research.

To Kathryn

*This losing oneself completely in the banalities of daily life is something that I generally cannot understand or endure. See, for example, how Goethe rose above material things with a calm superiority. Just think of what he had to live through: the great French Revolution, which at near range must have seemed a bloody and aimless farce, and then from 1793 to 1815 a continuous sequence of wars. I do not demand that you write poetry as Goethe did, but his view of life, the universality of his interests, the inner harmony of the man, everyone can create for himself or at least strive for.*

Rosa Luxembourg

CONTENTS

Chapter One : Introduction. 1

1.1 Background. 1

1.2 II-VI Superlattices. 3

1.3 Theory of electrons in heterostructures. 5

1.4 Thesis plan. 7

Chapter Two : Theory. 10

2.1 Bulk complex bandstructure. 10

2.2 The matching technique. 13

2.3 Superlattice energy levels. 20

2.4 Quantum well energy levels. 22

2.5 Interface matching plane. 25

2.6 Wavefunctions and charge density plots. 26

2.7 Momentum matrix element calculations. 28

2.8 Valence and conduction band offsets. 32

2.9 Calculations of energy levels and wavefunctions. 34

2.9.1 Quantum well. 35

2.9.2 Superlattice. 37

2.10 Interband momentum matrix elements. 39

2.10.1 Quantum well. 39

2.10.2 Superlattice. 40

2.11 Summary. 42

Chapter Three : Strained layer heterostructures. 44

3.1 Introduction and background. 44

3.1.1 Introduction. 44

3.1.2 Elasticity theory. 45

3.1.3 Critical thickness. 49

3.2 Pseudopotential theory of pressure effects. 51

3.2.1 Pressure effects. 51

3.2.2 Empirical pseudopotential method. 51

3.2.3 Strain effects. 53

3.2.4 Method used in calculations. 55

3.3 Semiconductors under hydrostatic pressure. 57

3.3.1 Basics. 57

3.3.2 Bandgaps of wide gap II-VI semiconductors. 58

3.3.3 HgTe hydrostatic pressure effects. 58

3.4 Semiconductor bandstructure under biaxial strain. 59

3.4.1 Introduction. 59

3.4.2 CdTe and ZnTe. 59

3.4.3 HgTe. 60

3.5 Summary. 62

**Chapter Four : The $(CdTe)_N - (ZnTe)_N$ superlattice.** 63

4.1 Introduction and background. 63

4.1.1 Introduction. 63

4.1.2 Strain effects. 65

4.1.3 Valence-band offsets. 67

4.1.4 Calculations. 68

4.2 Results. 69

4.2.1 Energy levels. 69

4.2.1.1 Monolayer superlattices, N=1. 69

4.2.1.2 N=2 and N=3. 70

4.2.1.3 N=3-15. 71

4.2.1.4 N=16-30. 72

4.2.2 Band mixing and wavefunctions. 72

4.2.3 Matrix elements and comparison with experiment. 75

4.3 Summary. 78

Chapter Five : Interface matching planes. 80

5.1 Introduction. 80

5.2 Interfaces and matching planes. 82

5.3 Symmetry of superlattice electronic states. 87

5.4 Results with bond-centre matching. 89

5.4.1 Introduction. 89

5.4.2 Energy levels. 89

5.4.3 Wavefunctions. 91

5.4.4 Matrix element calculations. 92

5.5 Discussion. 94

Chapter Six : The $(HgTe)_{3N} - (ZnTe)_N$ superlattice. 95

6.1 Introduction and background. 95

6.1.1 Introduction. 95

6.1.2 Strain effects. 96

6.1.3 Valence-band offset. 98

6.2 Superlattice electronic structure. 101

6.2.1 Energy levels. 101

6.2.2 Interface states. 101

6.2.3 Bandstructure. 104

6.3 Optical properties. 108

6.3.1 Introduction. 108

6.3.2 $N \leq 5$. 108

6.3.3 $N \geq 8$. 110

6.4 The $(HgTe)_{15}$-$(ZnTe)_5$ superlattice. 114

6.4.1 Introduction. 114

6.4.2 Bandstructure and wavefunctions. 114

6.4.3 Momentum matrix elements. 117

6.4.4 Effective masses. 118

6.5 Summary. 119

Chapter Seven : Summary and conclusion. 120

7.1 Summary. 120

7.2 Suggestions for further work. 125

7.3 Conclusion. 126

Appendices.

A: Limits. 127

B: Formfactors for GaAs, AlAs, and $Ga_{0.7}Al_{0.3}As$. 129

C: Formfactors for CdTe, ZnTe, and HgTe. 132

References 136

## Figures

| Figure number. | After page |
|---|---|
| 2.1 | 11 |
| 2.2 | 14 |
| 2.3 | 35 |
| 2.4, 2.5 and 2.6 | 37 |
| 2.7 and 2.8 | 38 |
| 3.1, 3.2 and 3.3 | 58 |
| 3.4 and 3.5 | 59 |
| 3.6, 3.7 and 3.8 | 60 |
| 4.1 | 68 |
| 4.2, 4.3 and 4.4 | 69 |
| 4.5 | 72 |
| 4.6 | 73 |
| 4.7 | 74 |
| 4.8 and 4.9 | 75 |
| 5.1, 5.2, 5.3 and 5.4 | 89 |
| 5.5 | 91 |
| 5.6 and 5.7 | 92 |

6.1 and 6.2 100
6.3 101
6.4 104
6.5 105
6.6 106
6.7 107
6.8 108
6.9 110
6.10 and 6.11 114
6.12 and 6.13 115
6.14 117

# CHAPTER ONE

# INTRODUCTION

## 1.1 : Background.

The superlattice concept was developed in 1969 by Esaki and Tsu, in the course of a feasibility study of resonant electron tunnelling through thin barriers and wells (see Esaki, 1986, for a historical survey). Two types of superlattices were considered, doping and compositional, and of these, compositional superlattices have excited the most interest. Compositional superlattices may be made, in principle at least, from any pair or combination of semiconductors. Early work on heterostructures mainly concentrated upon semiconductors which were nearly lattice matched, due to the difficulties of growing two semiconductors of different lattice parameters epitaxially. Strain was seen as a problem to avoid. However, in 1982 Osbourn pointed out that the mismatch could be used to change the electronic structure of semiconductors (Osbourn, 1983), and so was another parameter which could be varied to engineer the properties of superlattices. The field of strained layer superlattices has grown considerably in the past few years (e.g. Pearsall, 1990 B; O'Reilly, 1989; Dunstan and Adams, 1990), with the widening of the range of combinations of materials which may be considered for heterostructures.

For a given pair of semiconductors which make up a superlattice, the most important properties for device design are the valence and conduction band offsets, $\Delta E_V$ and $\Delta E_C$. There are four types of heterointerfaces between two semiconductors: type I, in which the electron and hole states are both confined in the same sublayers; type II staggered, where the electrons and holes are confined in different sublayers of the superlattice, and the conduction and valence bands do not overlap; type II misaligned, for which the electrons and holes are confined in different sublayers, and the valence band edge of one semiconductor is above the conduction band edge of the other; and type III, when the well region is a zero gap semiconductor (Esaki, 1986). The offsets $\Delta E_V$ and $\Delta E_C$ are still hard both to predict reliability and to measure, but many advances have been made in this respect (Van de Walle, 1989; Lambrecht and Segall, 1990).

The field of semiconductor heterostructures has matured considerably in recent years, and the basic principles are now widely understood (Jaros, 1989). However, there still remain considerable areas where more fundamental research is needed. Most work on heterostructures has concentrated on nearly lattice matched III-V semiconductors, particularly those based on GaAs, AlAs, and their alloys, and there are many strained layer systems which remain to be fully explored. One area with potential is the study and use of II-VI superlattices.

## 1.2 : II – VI superlattices.

The II-VI semiconductors have a wide range of bandgaps, from ZnS with a bandgap of 3.8 eV at low temperatures to the Hg-based compounds which are semimetallic. There are two groups of II-VI zincblende semiconductors which are important for superlattices, the Zn compounds ZnS, ZnSe and ZnTe, and the tellurides HgTe, CdTe and ZnTe. The cadmium compounds CdS and CdSe, form in hexagonal structures, and so are not considered here. HgS (cinnabar) undergoes a phase transition from $\alpha$-HgS (trigonal) to $\beta$-HgS (zincblende) at around 610 K, as temperature is raised at atmospheric pressure. HgSe is stable in zincblende form at room temperature, but has not been used in a superlattice.

Wide gap superlattices of ZnTe, ZnSe, and ZnS, and their alloys, have been studied extensively in recent years (McGill *et al.*, 1989 B; Quiroga *et al.*, 1990; Rajakarunanayake *et al.*, 1988; Wu *et al.*, 1990; Fujiyasu and Mochizuki, 1985) mainly to make lasers that emit in the blue to improve storage density on laser discs, and blue LEDs for information displays (Glass, 1987). Most II-VI semiconductors can be doped either p-type or n-type, but not both, so it is difficult to form pn junctions, but this problem may be overcome through the use of heterojunctions (McCaldin, 1989).

The telluride semiconductors HgTe, CdTe, and ZnTe have been made into superlattices HgTe-CdTe (Faurie *et al.*, 1982), HgTe-ZnTe (Faurie *et al.*, 1986) and CdTe-ZnTe (Monfroy *et al.*, 1986). One area of interest is in the low bandgaps. At present the main commercial semiconductor material used for infrared detection is the alloy mercury cadmium telluride (Dornhaus and Nimtz, 1983). This has the worst physical properties of any semiconductor in mass production (Triboulet, 1990), so it is possible that the next generation of infrared detectors will use some other material or structure, and one possibility is to use superlattices based on HgTe. The HgTe-based superlattices have also been found to have very high hole mobilities (Chu *et al.*, 1988). The wider gap CdTe-ZnTe superlattices have also been extensively studied in recent years

(Mathieu *et al.*, 1988, 1990; Gil *et al.*, 1989). Interest has been expressed in their potential non-linear optical properties (Feldman, 1990) because CdTe has the highest electro-optic coefficient of the zinc-blende semiconductors (Glass, 1987). The combination of high lattice mismatch with small band offset brings the possibility of studying unusual states in the valence band due to the crossover of the heavy and light-hole states.

In parallel with these technological developments, there have been advances in the theory needed to understand them. The role of the theorist in the development of semiconductor heterostructures has been very active. The possibilities opened up by modern growth techniques are almost limitless, so it is necessary to first use theoretical and mathematical modelling techniques to design heterostructures for the properties required.

## 1.3 : Theory of electrons in heterostructures.

The various methods used to calculate the electronic structure of heterostructures start from two distinct points of view. The heterostructure potential may be thought of as a series of electrostatic wells and barriers, similar to the early model of the potential acting upon an electron in a solid (Kronig and Penney, 1930), or the heterostructure may be thought of as a new material with an enlarged unit cell in the growth direction. The first of these, the envelope function approximation (EFA) is based upon the model of shallow impurities in a semiconductor (Kohn, 1957). The heterostructure electronic states are built up from band edge bulk states multiplied by envelope functions. This model may be modified, with the use of different effective masses in each region, and new matching conditions at the interfaces, and in various forms remains the most usual method for modelling the properties of semiconductor heterostructures (Bastard, 1988 A, pp63-118; Smith and Mailhiot, 1990). In the second approach, any method which has been used for bulk bandstructure calculations may be used to calculate the superlattice bandstructure, with the use of an enlarged unit cell (Giannozzi *et al.*, 1990). These *ab-initio* supercell methods are in principle the most accurate approach, since they entail few approximations. However, they have the major disadvantage for studies of practical systems in that they involve solving a matrix which increases rapidly in size as the superlattice period increases, so are not suitable for periods longer than about 20 Å. Methods have been developed which approach the accuracy of *ab-initio* methods, but use a more reasonable amount of computer time, by taking advantage of the symmetry of the superlattice. A bulk bandstructure is calculated for some semiconductor, either one of the constituents of the superlattice or an alloy intermediate to the constituents, then the superlattice wavefunctions are found as a sum of the bulk Bloch states. The set of states over which the sum is performed is determined by symmetry (Gilbert and Gurman, 1989). The bulk bandstructure is said to be folded, or translated, into the small superlattice

Brillouin zone. This approach has been used with the empirical pseudopotential method (Gell *et al.*, 1986 A; Jaros, 1990; Xia, 1989) and with the tight-binding method (Brey and Tejedor, 1987). Doing the calculations this way still entails an increase in computer time with increasing period, but at a much slower rate, because the superlattice states near the bulk band edges may be built up from bulk states coming from only a few bulk bands.

The two basic approaches can be seen as complementary. It has been argued that in some superlattices the envelope function approximation breaks down completely (Jaros, 1988), but this view has been contested (Bastard, 1988 B). The various envelope function approaches are best for wide layers, and for calculations of energy levels, while the calculations based on bulk methods are best for short period superlattices, for detailed calculations. An approach which has some of the advantages of both methods is the complex bandstructure matching method, in which the bulk complex bandstructure of each constituent material is calculated, test solutions are formed in each sublayer as a sum of bulk states, and are tested to see whether interface matching conditions are fulfilled. This approach has been taken using the empirical tight-binding method (Schulman and Chang, 1985) and the empirical pseudopotential method (Brand *et al.*, 1987). The main advantage of this method is that, once the initial calculations of bulk bandstructure have been carried out, the superlattice electronic structure calculation is fast and entails no increase in computer time with superlattice period. Calculations can also be performed for quantum wells (Brand and Hughes, 1987) and barriers (Monaghan and Brand, 1987), without the need to assume periodicity.

## 1.4. Thesis plan.

The aim of this thesis is to study the electronic bandstructure and interband momentum matrix elements of the highly strained II-VI telluride semiconductor superlattices CdTe-ZnTe and HgTe-ZnTe. Comparison is made between the calculations presented here and previous studies. The CdTe-ZnTe superlattice has been previously studied by the Kronig-Penney method (Mathieu *et al.*, 1988, 1990; Shtrikman *et al.*, 1989; Shtrikman and Finkman, 1989), the Bastard envelope function approximation (Gil *et al.*, 1989) and the tight-binding method (Quiroga *et al.*, 1989). The HgTe-ZnTe superlattice has been studied using the Kronig-Penney method (Mullins *et al.*, 1990). There have been calculations of the properties of lower strain HgTe-based superlattices by the tight-binding complex bandstructure method (Meyer *et al.*, 1988 A, B) and the empirical pseudopotential method (Beavis *et al.*, 1990 A; Zoryk and Jaros, 1987; Xia, 1989), which are useful for comparison.

In chapter two the method used for the study of electronic states in semiconductor superlattices and quantum wells, the complex bandstructure matching technique, is presented. The extraction of wavefunction coefficients is described, with the method for plotting the spatial charge density of any particular state and for calculating intersubband momentum matrix elements. An example of the use of this method on the $Ga_{0.7}Al_{0.3}As$-GaAs-$Ga_{0.7}Al_{0.3}As$ quantum well and the $Ga_{0.7}Al_{0.3}As$-GaAs superlattice is shown, and calculated electronic bandstructure and interband squared momentum matrix elements are presented.

Chapter three contains the extensions to the theory which are needed to calculate the properties of strained-layer heterostructures. Some results from macroscopic elasticity theory which are needed for the calculation of the strain in the sublayers of an epitaxially grown pseudomorphic heterostructure are quoted or derived. The application of the empirical pseudopotential method to the calculation of the bulk bandstructures of strained semiconductors is described, and calculations of the variation of direct bandgaps with hydrostatic pressure,

and of the bulk bandstructure under biaxial strain, are presented. The complex bandstructure matching technique is unchanged, apart from the prior calculation of bulk bandstructure, and once this has been done takes full account of the effects of strain upon the superlattice and quantum well bandstructures.

Chapter four consists of a study of $(CdTe)_N$-$(ZnTe)_N$ strained-layer superlattices. The calculations are compared quantitatively with calculations using the Kronig-Penney method, and qualitatively with experiment. It is shown that the energy levels found by the pseudopotential calculation are close to those from the Kronig-Penney calculation for long-period superlattices, with wide sublayers for both well and barrier, when the states due to different bulk maxima (i.e. light-hole, heavy-hole) are not close in energy. However, for short period superlattices, and when mixing occurs, there are differences. The results for very short period superlattices are compared with calculations from the literature, and are found to show the main features from other calculations, particularly the narrowing of the bandgap of the monolayer ($N = 1$) superlattice. The crossing of the HH1 and LH1 subbands, and the anticrossing of the HH1 and LH2 subbands, are considered in some detail. The results are compared with the limited experimental information available. There are differences between calculation and experiment, but these could probably be removed by the reassessment of various bulk parameters and the value of the valence band offset.

In the complex bandstructure matching technique it is necessary to choose a matching plane between the sublayers, and it is found that moving the matching plane affects the calculated energy levels and wavefunctions. However, the effect is different in each case, and it is found that the results of calculations of a $Ga_{0.7}Al_{0.3}As$-GaAs-$Ga_{0.7}Al_{0.3}As$ quantum well electronic states do not change much for different interface matching planes, but that some of the energy levels of the $(CdTe)_N$-$(ZnTe)_N$ superlattice are changed noticeably. These effects are considered in chapter five. Those systems which are most likely to be affected by the choice of matching plane are identified, and the physical basis for the changes is considered. The electronic states of the $(CdTe)_N$-$(ZnTe)_N$ superlattice are

calculated with a new matching plane between the sublayers, and compared with the results in chapter four, and with experiment.

In chapter six, calculations of the electronic bandstructure and intersubband momentum matrix elements of $(HgTe)_{3N}$-$(ZnTe)_N$ superlattices are presented. The resulting optical and electronic properties are discussed, and are compared with experimental and theoretical results from the literature on HgTe-based heterostructures. It is shown that HgTe-ZnTe superlattices have all the features of HgTe-CdTe superlattices, with the additional use of the strain between the sublayers as an extra parameter to tailor their properties.

# CHAPTER TWO

# THEORY

In this chapter the method for the calculation of the bandstructure and optical properties of semiconductor heterostructures is described.

## 2.1 : Bulk complex bandstructure.

The solution to the Schrödinger equation in periodic systems was shown by Bloch to be of the form,

$$\phi_{\underline{k}}(\underline{r}) = e^{i\underline{k}\cdot\underline{r}}u_{\underline{k}}(\underline{r})$$

where $u_{\underline{k}}(\underline{r})$ is a term with the periodicity of the lattice and $\underline{k}$ is the wavevector. In bulk crystals, $\underline{k}$ is real and hence $\phi_{\underline{k}}(\underline{r})$ extends throughout the whole system. However, there are also solutions to the Schrödinger equation with $\underline{k}$ imaginary or complex, describing wavefunctions with a magnitude which decays in one direction and grows in the opposite direction. The wavefunction near an interface can be built up from a sum of functions which decay away from the interface. This wavefunction can be normalised since it is bounded in one direction. Since this complex bandstructure was first described (Tamm, 1932) it has been analysed in great detail (Heine, 1963), the full complex bandstruc-

ture of many bulk semiconductors has been calculated (Chang, 1982), and the observation of "Tamm states" in superlattices has been reported (Ohno *et al.*, 1990). For the calculations presented here, the bulk complex bandstructure is calculated according to the approach of Chang and Schulman (1982) including spin (Brand and Hughes, 1987; Hughes, 1989) using the empirical pseudopotential method (Cohen and Bergstresser, 1966; Chelikowsky and Cohen, 1976; Cohen and Heine, 1970). All calculations have been performed for heterostructures grown in the [100]-direction. If there is an interface across the crystal in the (011)-plane, the wavefunction in the crystal at a given energy can be found as a sum of bulk states with real k-vectors in-plane, but with real, imaginary, or complex k's in the [100]-direction. However, only those evanescent or complex states which decay away from the interface are included in the sum. If there are two parallel interfaces close together, the restriction upon which evanescent and complex states can be included in the sum is removed because the states are bounded in both directions, and states which decay in both directions may be included. This is the basis of the complex bandstructure matching technique used in this thesis. In principle all the bandstructure at a given energy can be calculated accurately, but in practice the Hamiltonian is solved using a finite number of plane waves, and does not have translation symmetry in $\underline{k}$, so some of the states produced by the computer calculation with large real $k_x$ vectors are not valid (Smith and Mailhiot, 1990). In addition the bulk calculation produces states with large imaginary $k_x$ vectors which have a decay length shorter than the width of one atom, and so are not appropriate for the calculation of electronic states. This means that the set of bulk states used in the calculation must be chosen with care.

The complex bandstructure of GaAs in the [100]-direction is shown in figure 2.1 (taken from Brand *et al.*, 1987). As the energy changes the number of bands stays the same. For example, at the top of the valence band the real light and heavy hole bands become imaginary bands, one of which (from the light

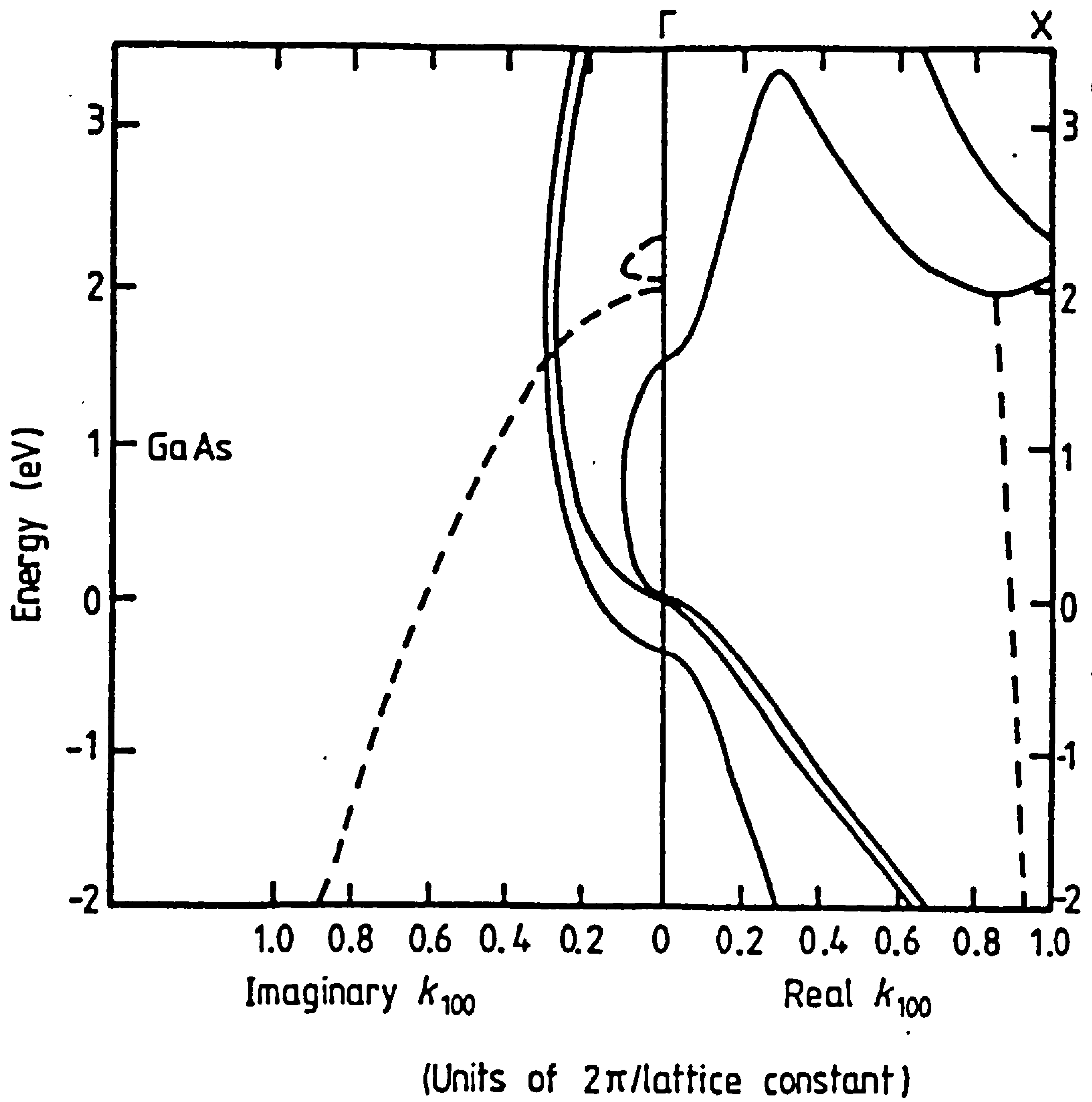


Figure 2.1. Part of the bulk complex bandstructure of GaAs in the [100]-direction, with spin included. Solid lines indicate real and imaginary solutions, dotted lines represent complex solutions.

hole) joins the bottom of the conduction band, the other going up to join a higher conduction band. The shape of the bands is simple, so the complex bandstructure can be calculated using methods which were originally developed for calculating ordinary bandstructure. The shape of the complex bandstructure was first investigated in the 1960s by measuring the tunnelling current through a thin sample of semiconductor with varying voltage such that the electrons had an energy in the bandgap of the semiconductor. The wavevector in the bandgap of InAs was shown (Parker and Mead, 1968) to be described by a symmetrical two band expression of the form

$$E = \left(\frac{E_g^2}{4} + \frac{\hbar^2 k^2 E_g}{2m^*}\right)^{\frac{1}{2}} - \frac{E_g}{2}$$

with $E_g$ the bandgap of the semiconductor, and the zero of energy at the conduction band edge. It was inferred that the evanescent bands in the forbidden gap of other small gap semiconductors could be described by a similar expression.

## 2.2 : The Matching Technique

The bandstructure is calculated using a pseudopotential method, with a plane wave basis. Each bulk wavefunction with complex wavevector $\underline{q}$ can be expressed in the form, summing over a set of plane waves $\underline{G}$,

$$\phi_{\underline{q}}(\underline{r}) = \sum_{\underline{G}} a_{\underline{G}}(\underline{q}) e^{i(\underline{G}+\underline{q})\cdot\underline{r}}. \qquad 2.1$$

The nth sublayer in a heterostructure is shown schematically in figure 2.2. In the growth direction the original periodicity of the crystal has been removed, so the electronic states within the layer may be formed as sums of the original bulk states at that energy and in-plane $\underline{q}$-vector,

$$\psi(\underline{r}) = \sum_{i} C_i \phi_i(\underline{r}). \qquad 2.2$$

The $C_i$ are constants, and $\psi(\underline{r})$ the heterostructure wavefunction at that particular energy and in-plane $\underline{q}$-vector. In principle the sum is infinite, but in practice will be over a finite set of bulk states. To calculate the energy levels in the heterostructure, test solutions of the form 2.2 at a particular energy and in-plane $\underline{q}$ in each sublayer are checked for continuity of wavefunction and of derivative of wavefunction at the interfaces. If these conditions are fulfilled, there will be an allowed state in the heterostructure at that energy and in-plane $\underline{q}$, which may be either discrete, if the heterostructure is aperiodic in the [100]-direction, or part of a band of states if the heterostructure is periodic in the [100]-direction. All heterostructures for which calculations have been performed are periodic in the plane of the well, and so there is an in-plane bandstructure. The method is similar to that used by Inkson and co. workers to study electron tunnelling in heterostructures (e.g. Marsh and Inkson, 1984; Ko *et al.*, 1990).

The mathematical approach will first be described in general terms, in a form which will allow the calculation of electronic states in any two-dimensional (or quasi two-dimensional) heterostructure, followed by the formulation which

has been used for the systems considered in this thesis. Consider the nth sublayer in a heterostructure (figure 2.2), of arbitrary composition, with interfaces at $x_{n-1}$ and at $x_n$, where $x_n > x_{n-1}$. The superlattice wavefunction at an energy E in the nth sublayer may be expressed as,

$$\psi_n(\underline{r}) = \sum_{j=1}^{2N} b_j^n \sum_{\underline{G}} a_{\underline{G},j}^n e^{i(\underline{q}_j^n+\underline{G})\cdot\underline{r}}. \qquad x_{n-1} \leq x \leq x_n \quad 2.3$$

$a_{\underline{G},j}^n$ is the coefficient of $\underline{G}$ for the jth state, with wavevector $\underline{q}_j^n$ in the nth sublayer of the heterostructure. It is convenient to reduce the 3D wavevector to the form $\underline{q}_j = (k_j, \underline{q}_{2,j})$ where $k_j$ is the component perpendicular to the interfaces and $\underline{q}_{2,j}$ is the 2D in-plane wavevector. The summation here is over 2N bulk states, including spin. Suitable values of N will be considered later. Two continuity conditions at the interfaces are used:

$$\psi_n(x_n) = \psi_{n+1}(x_n)$$

$$\text{and} \quad \frac{d\psi_n}{dx}(x_n) = \frac{d\psi_{n+1}}{dx}(x_n) \qquad 2.4$$

at the nth interface. From continuity of wavefunction,

$$\sum_{j=1}^{2N} b_j^n \sum_{\underline{G}} a_{\underline{G},j}^n e^{i(k_j^n+G_x)x_n} e^{i(\underline{q}_{2,j}^n+\underline{G}_2)\cdot\underline{r}_2}$$

$$= \sum_{j'=1}^{2N} b_{j'}^{n+1} \sum_{\underline{G}'} a_{\underline{G}',j'}^{n+1} e^{i(k_{j'}^{n+1}+G'_x)x_n} e^{i(\underline{q}_{2,j'}^{n+1}+\underline{G}'_2)\cdot\underline{r}_2} \qquad 2.5$$

and from continuity of derivative of wavefunction,

$$\sum_{j=1}^{2N} b_j^n \sum_{\underline{G}} a_{\underline{G},j}^n i(k_j^n + G_x) e^{i(k_j^n+G_x)x_n} e^{i(\underline{q}_{2,j}^n+\underline{G}_2)\cdot\underline{r}_2}$$

$$= \sum_{j'=1}^{2N} b_{j'}^{n+1} \sum_{\underline{G}'} a_{\underline{G}',j'}^{n+1} i(k_{j'}^{n+1} + G'_x) e^{i(k_{j'}^{n+1}+G'_x)x_n} e^{i(\underline{q}_{2,j'}^{n+1}+\underline{G}'_2)\cdot\underline{r}_2} \qquad 2.6$$

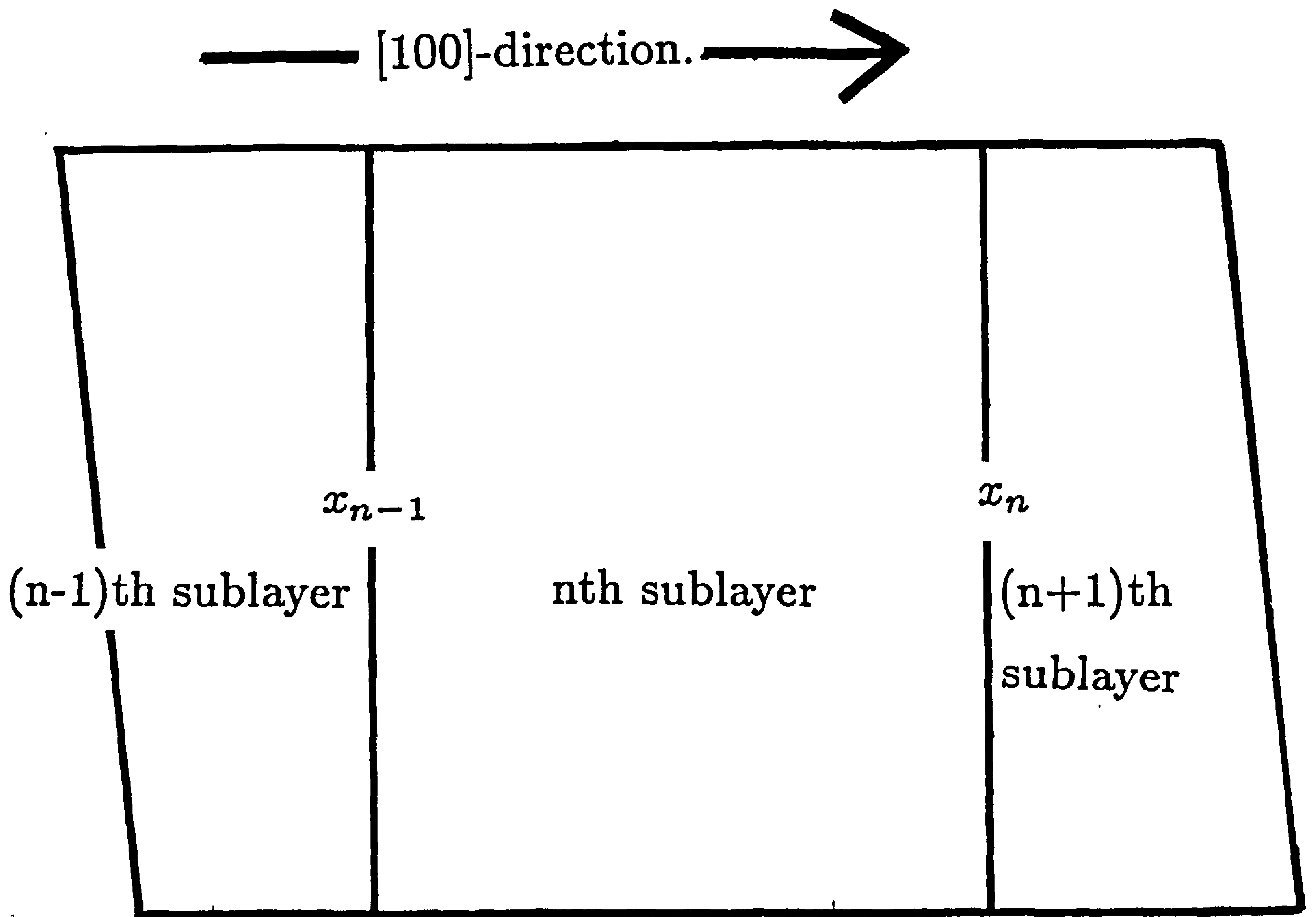


Figure 2.2. A schematic diagram showing the nth sublayer in a heterostructure, and part of the (n-1)th and (n+1)th sublayers. The interfaces are at $x_{n-1}$ and at $x_n$.

$\underline{G}_2$, $\underline{G}_2'$ and $\underline{r}_2$ are respectively the 2D projections of $\underline{G}$, $\underline{G}'$ and $\underline{r}$ on the interface plane. Because of the retention of bulk periodicity within the interface plane $\underline{q}^n_{2,j} = \underline{q}^{n+1}_{2,j'}$ for all $j, j'$ in the nth, (n+1)th layers, and by extension in all the layers in the system. Thus 2.5 reduces to

$$\sum_{j=1}^{2N} b_j^n \sum_{\underline{G}} a^n_{\underline{G},j} e^{i\underline{G}_2\cdot\underline{r}_2} e^{i(k_j^n+G_x)x_n}$$

$$= \sum_{j'=1}^{2N} b_{j'}^{n+1} \sum_{\underline{G}'} a^{n+1}_{\underline{G}',j'} e^{i\underline{G}_2'\cdot\underline{r}_2} e^{i(k_{j'}^{n+1}+G_x')x_n} \qquad 2.7$$

Multiplying both sides by $e^{i\underline{G}_2''\cdot\underline{r}_2}$ and integrating over the interface,

$$\sum_{j=1}^{2N} b_j^n \sum_{\underline{G}} a^n_{\underline{G},j} e^{i(k_j^n+G_x)x_n} \delta_{\underline{G}_2,\underline{G}_2''}$$

$$= \sum_{j'=1}^{2N} b_{j'}^{n+1} \sum_{\underline{G}'} a^{n+1}_{\underline{G}',j'} e^{i(k_{j'}^{n+1}+G_x')x_n} \delta_{\underline{G}_2',\underline{G}_2''} \qquad 2.8$$

But $\underline{G}_2''$ is an arbitrary 2D lattice vector, and since $\underline{G}_2$ and $\underline{G}_2'$ are summed over the same sets, we may write for all $\underline{G}_2$,

$$\sum_{j=1}^{2N} b_j^n P^n_{\underline{G}_2,j}(x_n) = \sum_{j'=1}^{2N} b_{j'}^{n+1} P^{n+1}_{\underline{G}_2,j'}(x_n) \qquad at\ x = x_n \quad 2.9$$

$$\text{with } P^n_{\underline{G}_2,j}(x_n) = \sum_{\underline{G}'} a^n_{\underline{G}',j} \delta_{\underline{G}_2,\underline{G}_2'} \delta_{G_S,G_S'} exp(i(k_j^n + G_x')x_n) \qquad 2.10$$

and similarly for $P^{n+1}_{\underline{G}_2,j}(x_n)$. The notation

$G_S$ = spin orientation of $\underline{G}_2$,

$G_S'$ = spin orientation of $\underline{G}'$,

$\underline{G}_2'$ = $(y, z)$ components of $\underline{G}'$,

$G_x'$ = $x$ component of $\underline{G}'$,

has been used.

As an example, the coefficient of the spin-up orientation of the (0,0) 2D projection of $P^n_{\underline{G}_2,j}(x_n)$ is given by

$$P^n_{(0,0)\uparrow,j}(x_n) = a^n_{(0,0,0)\uparrow,j} e^{ik^n_j x_n} + a^n_{(2,0,0)\uparrow,j} e^{i(k^n_j + 2\frac{2\pi}{\Lambda_x})x_n} + a^n_{(\bar{2},0,0)\uparrow,j} e^{i(k^n_j - 2\frac{2\pi}{\Lambda_x})x_n} + \dots \qquad 2.11$$

A similar set of equations to 2.9 is obtained from 2.6,

$$\sum_{j=1}^{2N} b^n_j Q^n_{\underline{G}_2,j}(x_n) = \sum_{j'=1}^{2N} b^{n+1}_{j'} Q^{n+1}_{\underline{G}_2,j'}(x_n) \qquad 2.12$$

$$\text{where } Q^n_{\underline{G}_2,j}(x_n) = \sum_{\underline{G}'} a^n_{\underline{G}',j} i(k^n_j + G'_x)\delta_{\underline{G}_2,\underline{G}'_2}\delta_{G_S,G'_S} exp(i(k^n_j + G'_x)x_n) \qquad 2.13$$

with the same notation as 2.10.

Equations 2.9 and 2.12 may be expressed in matrix form as

$$\underline{\mathbf{B}}''_n \underline{\mathbf{b}}_n = \underline{\mathbf{B}}'_{n+1} \underline{\mathbf{b}}_{n+1} \qquad 2.14$$

expressing the matching equations at $x = x_n$, where $\underline{\mathbf{b}}_n$, $\underline{\mathbf{b}}_{n+1}$ are column vectors containing the expansion coefficients $b^n_1, b^n_2, b^n_3, \dots$ and $b^{n+1}_1, \dots$ respectively. $\underline{\mathbf{B}}''_n$ and $\underline{\mathbf{B}}'_{n+1}$ are square matrices. The superscripts $'$, $''$ show whether the matrix contains the coefficients from the side of lower $x$ ($'$) or higher $x$ ($''$). So, for example, $\underline{\mathbf{B}}'_n$ represents matching equations at $x_{n-1}$, $\underline{\mathbf{B}}''_n$ represents matching equations at $x_n$, but both contain sums of coefficients from the nth sublayer of the heterostructure. Similarly there will be a series of equations at $x = x_{n-1}$, $x_{n-2}$ etc,

$$\underline{\mathbf{B}}''_{n-1} \underline{\mathbf{b}}_{n-1} = \underline{\mathbf{B}}'_n \underline{\mathbf{b}}_n \qquad \text{at } x = x_{n-1} \quad 2.15$$

$$\underline{\mathbf{B}}''_{n-2} \underline{\mathbf{b}}_{n-2} = \underline{\mathbf{B}}'_{n-1} \underline{\mathbf{b}}_{n-1} \qquad \text{at } x = x_{n-2} \quad 2.16$$

The matrices are arranged in the following way,

$$\underline{\mathbf{B}}'_n = \begin{bmatrix} P^{j=1}_{(0,0),\uparrow}(x_{n-1}) & P^{j=2}_{(0,0),\uparrow}(x_{n-1}) & .. & .. \\ P^{j=1}_{(1,1),\uparrow}(x_{n-1}) & P^{j=2}_{(1,1),\uparrow}(x_{n-1}) & .. & .. \\ ...... & ...... & .. & .. \\ ...... & ...... & .. & .. \\ Q^{j=1}_{(0,0),\uparrow}(x_{n-1}) & Q^{j=2}_{(0,0),\uparrow}(x_{n-1}) & .. & .. \\ Q^{j=1}_{(1,1),\uparrow}(x_{n-1}) & Q^{j=2}_{(1,1),\uparrow}(x_{n-1}) & .. & .. \\ ...... & ...... & .. & .. \\ ...... & ...... & .. & .. \end{bmatrix} \qquad 2.17$$

From (2.15-2.16)

$$\underline{\mathbf{b}}_n = (\underline{\mathbf{B}}'_n)^{-1}[\underline{\mathbf{B}}''_{n-1}(\underline{\mathbf{B}}'_{n-1})^{-1}]\underline{\mathbf{B}}''_{n-2}\underline{\mathbf{b}}_{n-2}$$

$$\text{put} \quad [\underline{\mathbf{B}}''_{n-1}(\underline{\mathbf{B}}'_{n-1})^{-1}] = \underline{\mathbf{T}}_{n-1}$$

and

$$\underline{\mathbf{b}}_n = (\underline{\mathbf{B}}'_n)^{-1}\underline{\mathbf{T}}_{n-1}\underline{\mathbf{T}}_{n-2}......\underline{\mathbf{T}}_2\underline{\mathbf{B}}''_1\underline{\mathbf{b}}_1 \equiv \underline{\mathbf{S}}_n\underline{\mathbf{b}}_1 \qquad 2.18$$

$\underline{\mathbf{S}}_n$ is defined by equation 2.18, and will be used later.

These equations may be solved to find the electronic states of the heterostructure. The approach differs slightly depending upon whether the system is periodic or aperiodic in the growth direction.

Although 2.18 may be used to solve for any superlattice or quantum well, there are simplifications which may be made by considering the physics underlying the calculations, in many cases. Consider again the nth sublayer in a heterostructure. The equation which follows from continuity of wavefunction at $x_n$ is

$$\sum_{j=1}^{2N} b_j^n \sum_{\underline{G}} a^n_{\underline{G},j} e^{ik_j^n x_n} \delta_{\underline{G}_\parallel,\underline{G}''_\parallel} e^{iG_s x_n}$$

$$= \sum_{j'=1}^{2N} b_{j'}^{n+1} \sum_{\underline{G}'} a^{n+1}_{\underline{G}',j'} e^{ik_{j'}^{n+1} x_n} \delta_{\underline{G}'_\parallel,\underline{G}''_\parallel} e^{iG'_s x_n}$$

We are considering zinc-blende or diamond structure semiconductors, so it is known that for any $\underline{G}$, $G_x$, $G_y$ and $G_z$ must be either all even or all odd, in units of $2\pi/A$. Terms of the same $\underline{G}_2$ are equated at the interfaces, so it follows that $G_x$ and $G'_x$ are both even or both odd. Thus the terms $\exp(iG_x x_n)$ and $\exp(iG'_x x_n)$ are both +1 or both −1, so long as $x_n$ is a whole number of monolayers, and will cancel out. The equation due to matching wavefunctions at $x_n$, 2.9, is still

$$\sum_{j=1}^{2N} b_j^n P_{\underline{G}_2,j}^n(x_n) = \sum_{j'=1}^{2N} b_{j'}^{n+1} P_{\underline{G}_2,j'}^{n+1}(x_n) \text{ at } x = x_n$$

$$\text{but now } P_{\underline{G}_2,j}^n(x_n) = \sum_{\underline{G}'} a_{\underline{G}',j}^n \delta_{\underline{G}_2,\underline{G}'_2} \delta_{G_s,G'_s} exp(ik_j^n x_n), \qquad 2.19$$

c.f. equation 2.10.

There are a similar set of equations for $Q$, leading to

$$Q_{\underline{G}_2,j}^n(x_n) = \sum_{\underline{G}'} a_{\underline{G}',j}^n i(k_j^n + G'_x) \delta_{\underline{G}_2,\underline{G}'_2} \delta_{G_s,G'_s} exp(ik_j^n x_n), \qquad 2.20$$

c.f. equation 2.13.

i.e. the matrix coefficients $P_{\underline{G}_2,j}^n(x_n)$, $Q_{\underline{G}_2,j}^n(x_n)$, etc., only depend upon $\exp(ik_j^n x_n)$ and not on $\exp(iG_x x_n)$, a great simplification. For example the coefficient of the spin-up orientation of the (0,0) 2D projection is given by

$$P_{(0,0)\uparrow,j}^n(x_n) = (a_{(0,0,0)\uparrow,j}^n + a_{(2,0,0)\uparrow,j}^n + a_{(\bar{2},0,0)\uparrow,j}^n + ...) exp(ik_j^n x_n) \qquad 2.21$$

It follows that

$$\underline{\mathbf{B}}''_n = \underline{\mathbf{B}}'_n \underline{\mathbf{D}}_n, \qquad 2.22$$

where $\underline{\mathbf{D}}_n$ is a diagonal matrix with elements of the form $\exp(ik_j^n(x_n - x_{n-1}))$. See appendix A for a discussion of the interpretation of equations 2.21 and 2.22 if $k_j^n$ is imaginary or complex. If all layers in a heterostructure are of whole monolayer width, we can replace eqns 2.14, 2.15 and 2.16 with

$$\underline{\mathbf{B}}_n\underline{\mathbf{D}}_n\underline{\mathbf{b}}_n = \underline{\mathbf{B}}_{n+1}\underline{\mathbf{b}}_{n+1} \qquad \text{at } x = x_n \quad 2.23$$

$$\underline{\mathbf{B}}_{n-1}\underline{\mathbf{D}}_{n-1}\underline{\mathbf{b}}_{n-1} = \underline{\mathbf{B}}_n\underline{\mathbf{b}}_n \qquad \text{at } x = x_{n-1} \quad 2.24$$

$$\underline{\mathbf{B}}_{n-2}\underline{\mathbf{D}}_{n-2}\underline{\mathbf{b}}_{n-2} = \underline{\mathbf{B}}_{n-1}\underline{\mathbf{b}}_{n-1} \qquad \text{at } x = x_{n-2} \quad 2.25$$

where the $\underline{\mathbf{B}}'_n$, *etc.*, in 2.14-2.16 have been replaced by the $\underline{\mathbf{B}}_n$, *etc.*, which are matrices arranged as shown in 2.17, but with the $\underline{\mathbf{P}}$'s and $\underline{\mathbf{Q}}$'s defined by equations 2.19 and 2.20. Hence

$$\underline{\mathbf{b}}_n = (\underline{\mathbf{B}}_n)^{-1}[\underline{\mathbf{B}}_{n-1}\underline{\mathbf{D}}_{n-1}(\underline{\mathbf{B}}_{n-1})^{-1}]\underline{\mathbf{B}}_{n-2}\underline{\mathbf{D}}_{n-2}\underline{\mathbf{b}}_{n-2}.$$

$$\text{put } \underline{\mathbf{B}}_{n-1}\underline{\mathbf{D}}_{n-1}(\underline{\mathbf{B}}_{n-1})^{-1} = \underline{\mathbf{T}}_{n-1},\ etc.$$

$$\text{so } \underline{\mathbf{b}}_n = (\underline{\mathbf{B}}_n)^{-1}\underline{\mathbf{T}}_{n-1}\cdots\cdots\underline{\mathbf{T}}_2\underline{\mathbf{B}}_1\underline{\mathbf{D}}_1\underline{\mathbf{b}}_1 \equiv \underline{\mathbf{S}}_n\underline{\mathbf{b}}_1 \qquad 2.26$$

If the sublayers in a heterostructure are all of whole monolayer width, all that needs to be stored for each sublayer is one set of 2D-Fourier component sums to make up the matrices $\underline{\mathbf{B}}_n$, and the $\underline{\mathbf{k}}^n$'s, rather than all the wavefunction information, for each sublayer, which requires a far greater amount of memory.

## 2.3 : Superlattice Energy Levels.

If the heterostructure is periodic, with a period of n sublayers between $x = x_0$ and $x = x_n$, then by Bloch's theorem

$$\psi(x_n) = e^{ik_{SL}L}\psi(x_0) \qquad 2.27$$

where $L = x_n - x_0$ and $k_{SL}$ is the superlattice growth direction k-vector, between 0 and $\pi/L$. Hence

$$\underline{\mathbf{B}}'_{n+1}\underline{\mathbf{b}}_{n+1} = e^{ik_{SL}L}\underline{\mathbf{B}}'_1\underline{\mathbf{b}}_1 \qquad 2.28$$

In general, from 2.14 and 2.28

$$\underline{\mathbf{B}}''_n\underline{\mathbf{b}}_n = \underline{\mathbf{B}}'_{n+1}\underline{\mathbf{b}}_{n+1} \equiv \underline{\mathbf{B}}'_1 e^{ik_{SL}L}\underline{\mathbf{b}}_1$$

$$\underline{\mathbf{b}}_1 = e^{-ik_{SL}L}(\underline{\mathbf{B}}'_1)^{-1}\underline{\mathbf{B}}''_n\underline{\mathbf{S}}_n\underline{\mathbf{b}}_1 \qquad 2.29$$

However, if all layers are of integer monolayer thickness, from 2.26 and 2.28,

$$\underline{\mathbf{b}}_1 = e^{-ik_{SL}L}(\underline{\mathbf{B}}_1)^{-1}\underline{\mathbf{B}}_n\underline{\mathbf{D}}_n\underline{\mathbf{S}}_n\underline{\mathbf{b}}_1 \qquad 2.30$$

Finally, 2.29 or 2.30 is solved to find the superlattice bandstructure. Note that there will be solutions at all energies, but the solutions of interest have $k_{SL}$ between $-1$ and 1 (in units of $\pi/L$).

Most superlattices considered in the literature have two sublayers in each period, $(AB)_M(CD)_N$ where M+N is even and M and N are both whole numbers. For historical reasons (Kronig and Penney, 1930) this is usually described as having a well region between $x = 0$ and $x = a$ and a barrier region between $x = 0$ and $x = -b$, with a period $L = a + b$.

Then at $x = 0$

$$\underline{\mathbf{M}}_B \underline{\mathbf{b}} = \underline{\mathbf{M}}_W \underline{\mathbf{w}} \qquad 2.31$$

and at $x = +a$,

$$\underline{\mathbf{M}}_W \underline{\mathbf{D}}_W \underline{\mathbf{w}} = e^{ik_{SL}L} \underline{\mathbf{M}}_B \underline{\mathbf{D}}_B \underline{\mathbf{b}} \qquad 2.32$$

where $\underline{\mathbf{D}}_W$ is a diagonal matrix containing terms of the form $\exp(ik_i^W a)$ and $\underline{\mathbf{D}}_B$ is a diagonal matrix containing terms of the form $\exp(-ik_j^B b)$, where $k_i^W$ and $k_j^B$ are the bulk x-direction k-vectors in the well and barrier regions respectively, which may be real, imaginary, or complex, in the well and barrier regions respectively. $\underline{\mathbf{M}}_B$ and $\underline{\mathbf{M}}_W$ are square matrices arranged according to 2.17 for the well and barrier regions, with $\underline{\mathbf{P}}$'s and $\underline{\mathbf{Q}}$'s defined by 2.19 and 2.20. These equations simplify to give

$$\underline{\mathbf{w}} = e^{ik_{SL}L} (\underline{\mathbf{D}}_W)^{-1} (\underline{\mathbf{M}}_W)^{-1} \underline{\mathbf{M}}_B \underline{\mathbf{D}}_B (\underline{\mathbf{M}}_B)^{-1} \underline{\mathbf{M}}_W \underline{\mathbf{w}}. \qquad 2.33$$

which can be solved for $k_{SL}$ between $-1$ and 1, in units of $\pi/L$.

A superlattice $(AB)_M(CD)_N$, with M+N odd, has four sublayers in each period, $(AB)_M(CD)_N(AB)_M(CD)_N$ , and the electronic states are found as solutions of 2.29/2.30.

## 2.4 : Quantum well energy levels.

For a quantum well, which has n sublayers between two barriers at $x = x_0$ and $x = x_n$, the matching equations at $x = x_0$ and $x = x_n$ are different from those shown in equation 2.9. In the left-hand barrier, at $x \leq x_0$, only evanescent states which decay towards $x = -\infty$ are allowed, and in the right-hand barrier, at $x \geq x_n$, only evanescent states which decay towards $x = +\infty$ are allowed. Thus at $x = x_0$,

$$\sum_{j=1}^{N} b_j^0 P^0_{\underline{G}_2,j}(x_0) = \sum_{j'=1}^{2N} b_{j'}^1 P^1_{\underline{G}'_2,j'}(x_0), \qquad 2.34$$

and at $x = x_n$,

$$\sum_{j''=1}^{2N} b_{j''}^n P^n_{\underline{G}''_2,j''}(x_n) = \sum_{j'''=1}^{N} b_{j'''}^{n+1} P^{n+1}_{\underline{G}'''_2,j'''}(x_n), \qquad 2.35$$

with $b^0$, $P^0$ and $b^{n+1}$, $P^{n+1}$, representing the left and right barriers respectively, and $b^1$, $P^1$, $b^n$, $P^n$ representing the 1st and nth sublayers respectively.

Now the lhs of 2.35 can be expressed as

$$\underline{\mathbf{P}}_n \underline{\mathbf{b}}_n \qquad 2.36$$

where $\underline{\mathbf{P}}_n$ is a square matrix, 2N× 2N, of which the elements in the top half are all zeroes, and the bottom half contains the $P$'s.

$$\underline{\mathbf{P}}_n = \begin{bmatrix} \cdots\cdots & \cdots\cdots & \cdots\cdots \\ \cdots\cdots & \ldots 0 \ldots & \cdots\cdots \\ \cdots\cdots & \cdots\cdots & \cdots\cdots \\ P^{j''=1}_{(0,0),\uparrow}(x_n) & P^{j''=2}_{(0,0),\uparrow}(x_n) & \cdots\cdots \\ \cdots\cdots & \cdots\cdots & \cdots\cdots \\ \cdots\cdots & \cdots\cdots & \cdots\cdots \end{bmatrix} \qquad 2.37$$

Using 2.18 or 2.26 it is possible to write

$$\underline{\mathbf{b}}_n = \underline{\mathbf{S}}_n \underline{\mathbf{b}}_1$$

and so 2.36 can be rewritten as

$$\underline{\mathbf{P}}_n \underline{\mathbf{S}}_n \underline{\mathbf{b}}_1 \tag{2.38}$$

Then 2.34, 2.35 and 2.38 can be combined to give a matrix equation

$$\begin{bmatrix} \underline{\mathbf{P}}_0 & \underline{\mathbf{0}} \\ \underline{\mathbf{0}} & \underline{\mathbf{P}}_{n+1} \end{bmatrix} \begin{bmatrix} \underline{\mathbf{b}}_0 \\ \underline{\mathbf{b}}_{n+1} \end{bmatrix} = \begin{bmatrix} \underline{\mathbf{P}}_1 \\ \underline{\mathbf{P}}_n \underline{\mathbf{S}}_n \end{bmatrix} \underline{\mathbf{b}}_1 \tag{2.39}$$

$$\text{i.e. } \underline{\mathbf{P}}_B \underline{\mathbf{b}} = \underline{\mathbf{P}}_W \underline{\mathbf{b}}_1, \tag{2.40}$$

where the upper $N \times 2N$ section of $\underline{\mathbf{P}}_W$ corresponds to 2.34 and the lower $N \times 2N$ section of $\underline{\mathbf{P}}_W$ corresponds to 2.35/2.38.

A similar set of equations can be written by matching coeficients of derivatives of wavefunctions at $x = x_0$ and $x = x_n$ to give

$$\underline{\mathbf{Q}}_B \underline{\mathbf{b}} = \underline{\mathbf{Q}}_W \underline{\mathbf{b}}_1 \tag{2.41}$$

and hence

$$\underline{\mathbf{Q}}_W^{-1} \underline{\mathbf{Q}}_B \underline{\mathbf{P}}_B^{-1} \underline{\mathbf{P}}_W \underline{\mathbf{b}}_1 = \underline{\mathbf{b}}_1. \tag{2.42}$$

Equation 2.42 may then be solved by scanning through energies to find the bound states, and their wavefunctions.

The standard quantum well consists of a single well layer between two barrier layers, which may be both of the same material, or of different materials. The well region stretches from $x = 0$ to $x = a$, and is of integer monolayer thickness. The matching equations at the interfaces are, at $x = 0$,

$$\sum_{j=1}^{N} b_j^I P_{\underline{\mathbf{G}}_2, j}^I(0) = \sum_{j'=1}^{2N} w_{j'} P_{\underline{\mathbf{G}}'_2, j'}^W(0) \tag{2.43}$$

and at $x = a$,

$$\sum_{j'=1}^{2N} w_{j'} P_{\underline{\mathbf{G}}'_2, j'}^W(a) = \sum_{j''=1}^{N} b_{j''}^{III} P_{\underline{\mathbf{G}}''_2, j''}^{III}(a) \tag{2.44}$$

where $b^I_j$, $P^I_{\underline{G}_2,j}$, $b^{III}_{j''}$, $P^{III}_{\underline{G}''_2,j''}$, and $w_{j'}$, $P^W_{\underline{G}'_2,j'}$, contain coefficients and bulk Bloch function information for the left (I) and right (III) barrier regions, and the well region, respectively, and are defined according to equation 2.19. Equations 2.43 and 2.44 are combined to obtain a matrix equation of the form

$$\begin{bmatrix} \underline{\mathbf{P}}^I & \underline{\mathbf{0}} \\ \underline{\mathbf{0}} & \underline{\mathbf{P}}^{III} \end{bmatrix} \begin{bmatrix} \underline{\mathbf{b}}^I \\ \underline{\mathbf{b}}^{III} \end{bmatrix} = \underline{\mathbf{P}}_W \underline{\mathbf{w}} \qquad 2.45$$

$$\text{i.e. } \underline{\mathbf{P}}_B \underline{\mathbf{b}} = \underline{\mathbf{P}}_W \underline{\mathbf{w}} \qquad 2.46$$

where the upper N $\times$ 2N section of $\underline{\mathbf{P}}_W$ corresponds to 2.43 and the lower section of $\underline{\mathbf{P}}_W$ corresponds to 2.44. Similar equations for continuity of derivative of wavefunction at interfaces lead to a second matrix equation of the form

$$\begin{bmatrix} \underline{\mathbf{Q}}^I & \underline{\mathbf{0}} \\ \underline{\mathbf{0}} & \underline{\mathbf{Q}}^{III} \end{bmatrix} \begin{bmatrix} \underline{\mathbf{b}}^I \\ \underline{\mathbf{b}}^{III} \end{bmatrix} = \underline{\mathbf{Q}}_W \underline{\mathbf{w}} \qquad 2.47$$

$$\text{i.e. } \underline{\mathbf{Q}}_B \underline{\mathbf{b}} = \underline{\mathbf{Q}}_W \underline{\mathbf{w}} \qquad 2.48$$

and hence

$$\underline{\mathbf{w}} = \underline{\mathbf{Q}}_W^{-1} \underline{\mathbf{Q}}_B \underline{\mathbf{P}}_B^{-1} \underline{\mathbf{P}}_W \underline{\mathbf{w}} \qquad 2.49$$

The energies and wavefunction coefficients of bound states in the quantum well may be found by setting up equation 2.49 as a matrix equation and solving it, looking for eigenvalues equal to 1.0. The eigenvalue is a continuous function of the energy close to the solution, so it is straightforward to zero in on the energy of a solution.

## 2.5 : Interface matching plane.

The complex bandstructure matching technique assumes abrupt interfaces between the sublayers of a heterostructure. The pseudopotentials of individual atoms are explicitly included in the calculation, so the position of the interface on an atomic scale must be specified. The change of matching plane is performed mathematically as follows. The bulk complex bandstructure is found in the usual way, in the form

$$\phi_{\underline{q}}(\underline{r}) = \sum_{\underline{G}} a_{\underline{G}}(\underline{q}) e^{i(\underline{G}+\underline{q})\cdot\underline{r}}$$

The origin for $\underline{r}$ is conventionally at mid-bond. To change the matching plane, the wavefunction needs to be known relative to a new origin, $\underline{t}$, and is written, with $\underline{r} = \underline{r}' + \underline{t}$,

$$\phi_{\underline{q}}(\underline{r}) = \sum_{\underline{G}} a_{\underline{G}}(\underline{q}) e^{i(\underline{G}+\underline{q})\cdot(\underline{r}'+\underline{t})}$$

$$= \sum_{\underline{G}} a'_{\underline{G}}(\underline{q}) e^{i(\underline{G}+\underline{q})\cdot\underline{r}'}$$

$$\text{where } a'_{\underline{G}}(\underline{q}) = a_{\underline{G}}(\underline{q}) e^{i(\underline{G}+\underline{q})\cdot\underline{t}}$$

Then the $a'_{\underline{G}}(\underline{q})$'s can be substituted for the $a_{\underline{G}}(\underline{q})$'s in any of the equations above. The physical meaning and effect of different matching planes will be considered in chapter five.

## 2.6 : Wavefunctions and charge density plots.

The wavefunctions of a superlattice with two sublayers in each period will be discussed in this section; the extension to other structures is straightforward. The wavefunction in the well is found by solving equation 2.33 for $k_{SL}$ between $-1$ and 1 $(\pi/L)$. The wavefunction in the barrier is obtained from that in the well by using $\underline{b} = (\mathbf{M}_B)^{-1}\mathbf{M}_W\underline{w}$. The wavefunction in the well, $\psi_W(\underline{r})$, at an energy E and in-plane wavevector $\underline{q}_2$ is

$$\psi_W(\underline{r}) = \sum_{j=1}^{2N} w_i \sum_{\underline{G}} a^W_{\underline{G},j} e^{i(\underline{q}^W_j + \underline{G})\cdot\underline{r}} \qquad 0 < x < a \quad 2.50$$

where the $a^W_{\underline{G},j}$ are the Fourier coefficients for the bulk material of which the well is composed at energy E, the $\underline{q}^W_j$ are the bulk $\underline{k}$-vectors, with in-plane wavevector $\underline{q}^W_2$ (i.e. $\underline{q}^W_j = (k^W_j, \underline{q}^W_2)$), and the $w_i$ are the coefficients of the bulk states.

Throughout this thesis plots will be presented of the spatial distribution of charge density of states in superlattices and quantum wells. The charge density at $\underline{r}$, $\psi^*_W(\underline{r})\psi_W(\underline{r})$, is given by

$$\psi^*_W(\underline{r})\psi_W(\underline{r})$$

$$= \sum_{j=1}^{2N}\sum_{j'=1}^{2N} w_j w^*_{j'} \sum_{\underline{G}}\sum_{\underline{G}'} a^W_{\underline{G},j}(a^W_{\underline{G}',j'})^* e^{i(\underline{q}^W_j + \underline{G} - (\underline{q}^W_{j'})^* - \underline{G}')\cdot\underline{r}} \qquad 0 \leq x \leq a \quad 2.51$$

In many cases it is clearer to present the charge density averaged over the plane of the layers, since this may be compared easily with the results of calculations using the envelope function approximation (EFA). Some simple algebra leads to

$$\int_{-\infty}^{\infty}\int_{-\infty}^{\infty} \psi^*_W(\underline{r})\psi_W(\underline{r})dydz$$

$$\propto \sum_{j=1}^{2N}\sum_{j'=1}^{2N}\sum_{\underline{G}}\sum_{\underline{G}'} w_j w_{j'}^* a_{\underline{G},j}^W (a_{\underline{G}',j'}^W)^* e^{i(k_j^W + G_z - (k_{j'}^W)^* - G_z')x} \delta_{\underline{G}_2,\underline{G}_2'}$$

$$0 \leq x \leq a \quad 2.52$$

and a similar form for the barrier region, $0 \geq x \geq -b$.

For a quantum well, exactly the same equations are used except that in the barriers the summation is only over $j, j' = 1 \rightarrow N$.

## 2.7 : Momentum matrix element calculations.

The momentum matrix element $\underline{\mathbf{M}}_{if}$ is given by (Greenaway and Harbeke, 1968, p.35),

$$\underline{\mathbf{M}}_{if} = \int_V d\underline{\mathbf{r}}\; e^{-i(\underline{\mathbf{k}}_i - \underline{\kappa})\cdot\underline{\mathbf{r}}}\; \psi_i^*(\underline{\mathbf{k}}_i,\underline{\mathbf{r}})\; \underline{\mathbf{e}}.\underline{\nabla}\; e^{i\underline{\mathbf{k}}_f\cdot\underline{\mathbf{r}}}\; \psi_f(\underline{\mathbf{k}}_f,\underline{\mathbf{r}}) \qquad 2.53$$

where $\underline{\kappa}$ is the wavevector of the incident light, $\underline{\mathbf{k}}_i$, $\underline{\mathbf{k}}_f$ the wavevectors and $\psi_i$, $\psi_f$ the wavefunctions of the initial and final states.

From 2.53

$$\underline{\mathbf{M}}_{if} = \int_V d\underline{\mathbf{r}}\psi_i^*(\underline{\mathbf{k}}_i,\underline{\mathbf{r}})\; \underline{\mathbf{e}}.\underline{\nabla}\;\; \psi_f(\underline{\mathbf{k}}_f,\underline{\mathbf{r}})\; \delta_{\underline{\mathbf{k}}_i-\underline{\kappa},\underline{\mathbf{k}}_f},$$

so since $|\underline{\kappa}| \ll |\underline{\mathbf{k}}_i|, |\underline{\mathbf{k}}_f|$,

$$\underline{\mathbf{M}}_{if} \approx \int_V d\underline{\mathbf{r}}\; \psi_i^*(\underline{\mathbf{k}}_i,\underline{\mathbf{r}})\; \underline{\mathbf{e}}.\underline{\nabla}\; \psi_f(\underline{\mathbf{k}}_f,\underline{\mathbf{r}})\delta_{\underline{\mathbf{k}}_i,\underline{\mathbf{k}}_f} \qquad 2.54$$

At a given energy E and in-plane wavevector $\underline{\mathbf{q}}_2$ at which there is a solution with wavevector $(k_{SL},\underline{\mathbf{q}}_2)$, there will also be a solution with wavevector $(-k_{SL},\underline{\mathbf{q}}_2)$, where $k_{SL}$ is real (we are not concerned with solutions with $k_{SL}$ imaginary or complex). At each of these wavevectors there are two states, due to spin. The solutions produced by the computer calculation are random combinations of the two spin states. If the two states at $(k_{SL},\underline{\mathbf{q}}_2)$ produced by the computer calculation are $A\psi_1'$, $B\psi_2'$, where A and B are constants, these are normalised so that $|\psi_1'|^2 = |\psi_2'|^2 = 1$ and are used to form two states $\psi_1$ and $\psi_2$ where

$$\psi_1 = \frac{1}{\sqrt{2}} \frac{\psi_1' - (\psi_2'^*\psi_1')\psi_2'}{|\psi_1' - (\psi_2'^*\psi_1')\psi_2'|}$$

$$\psi_2 = \frac{1}{\sqrt{2}}\psi_2'$$

so

$$|\psi_1|^2 + |\psi_2|^2 = 1 \text{ and } \psi_1^* \psi_2 = 0 \qquad 2.55$$

and similarly for the states at $(-k_{SL},\ \underline{q}_2)$.

In principle, valence and conduction band states of the same $\underline{k}_{SL}$ are generated, and the matrix elements worked out between them. In practice, the heterostructure bandstructure calculation involves finding the growth direction superlattice wavevector $k_{SL}$ at a given energy and in-plane wavevector, with $\underline{k}_{SL} = (k_{SL}, \underline{q}_2)$, so the $k_{SL}$'s in the calculated valence and conduction subband states are never exactly the same. More importantly, in some cases it may be difficult to get values which are particularly close, either to each other or to any required value of $k_{SL}$. For subbands of high $m^*_{SL}$ a very small change in energy produces a large change in $k_{SL}$, so it is at best time consuming and at worst difficult to obtain a state of a particular required $k_{SL}$. However, for such subbands, the superlattice is almost a multiple quantum well, so the state shows little variation with $k_{SL}$. Often, the interband matrix element of most interest is at superlattice zone centre $\overline{\Gamma}$ or zone edge $\overline{X}$, but at these critical points the subband goes through a maximum or minimum, and it is difficult to find a solution. The precise values of $k_{SL}$ of the two states is of different importance depending upon what is being compared. For example a graph of zone-centre matrix elements against superlattice period will need states which are very close to zone centre to show a smooth variation, but the difference between an allowed or forbidden transition within one particular heterostructure will often be obvious without any fine-tuning of wavevector.

At $\underline{k}_{SL} = (k_{SL}, \underline{q}_2)$, the valence and conduction subband wavefunctions in the well region are given by

$$\psi_V(\underline{r}) = \sum_{j=1}^{2N} \sum_{\underline{G}} V_j a_{\underline{G},j} e^{i(\underline{q}_j^V + \underline{G})\cdot \underline{r}}$$

$$\psi_C(\underline{r}) = \sum_{j'=1}^{2N} \sum_{\underline{G}'} C_{j'} a_{\underline{G}',j'} e^{i(\underline{q}_{j'}^C + \underline{G}')\cdot \underline{r}}$$

The derivation here is for a superlattice with well region between 0 and $a$, and barrier region from 0 to $-b$, with states found from solutions of equation 2.33. The intersubband matrix element is given by

$$\underline{\mathbf{M}}_{CV}$$

$$= \int_0^a \int_{-\infty}^{\infty} \int_{-\infty}^{\infty} dxdydz \sum_{j=1}^{2N} \sum_{j'=1}^{2N} \sum_{\underline{G}} \sum_{\underline{G}'} C^*_{j'} V_j a^*_{\underline{G}',j'} a_{\underline{G},j} i[(\underline{q}^V_j + \underline{G}).\underline{e}] e^{i(\underline{q}^V_j - (\underline{q}^C_{j'})^* + \underline{G} - \underline{G}').\underline{r}}$$

$$\propto \sum_{j=1}^{2N} \sum_{j'=1}^{2N} \sum_{\underline{G}} \sum_{\underline{G}'} C^*_{j'} V_j a^*_{\underline{G}',j'} a_{\underline{G},j} i[(\underline{q}^V_j + \underline{G}).\underline{e}] \delta_{\underline{q}^V_{2,j}, \underline{q}^C_{2,j'}} \delta_{\underline{G}_2, \underline{G}'_2}$$

$$\times \; L \qquad \text{if } (k^V_j - (k^C_{j'})^* + G_x - G'_x) = 0$$

$$\times \; \frac{e^{i(k^V_j - (k^C_{j'})^* + G_x - G'_x)L} - 1}{i(k^V_j - (k^C_{j'})^* + G_x - G'_x)} \qquad \text{if } (k^V_j - (k^C_{j'})^* + G_x - G'_x) \neq 0 \quad 2.56$$

Care must be taken with units. $k^V_j$, $G_x$, $k^C_{j'}$, $G'_x$ are in units $\frac{2\pi}{a_x}$; $q^{V,C}_y$, $q^{V,C}_z$, $G_y$, $G_z$, $G'_y$, $G'_z$ are in units $\frac{2\pi}{a_y}$, while $L$ is in $\frac{a_x}{2} \times$ well width in monolayers. $\underline{e}$ is the polarisation of the electric vector of the incoming light.

The contribution to the intersubband matrix element from the well region is added to a contribution from the barrier region to determine the total matrix element.

In the superlattice the barrier region is treated exactly the same as the well region, save that the x-direction integration is from 0 to $b$.

The solution for a quantum well is exactly as for the superlattice in the well region. The barrier regions involve integration in the $x$-direction from 0 to $-\infty$ in the left hand barrier, and to $+\infty$ in the right hand barrier. The $x$-dependent part of equations 2.56 gives

$$\frac{-1}{i(k^V_j - (k^C_{j'})^* + G_x - G'_x)} \qquad \text{in the left hand barrier,}$$

and $\dfrac{1}{i(k_j^V - (k_{j'}^C)^* + G_x - G'_x)}$ in the right hand barrier.

## 2.8 : Valence and conduction band offsets.

The origin of the valence and conduction band offsets between different materials has been a matter of debate for as long as heterostructures have been studied. There are two different conceptions of the offset, that it is controlled by bulk properties, and is therefore independent of the orientation and condition of the interfaces, or that it is controlled by the formation of interface bonds and charge transfer at interfaces, or some combination of the two. The physical bases of these approaches have been reviewed (Flores and Tejedor, 1987). The sophistication of model prediction of offsets has improved greatly over the past decade (see e.g. Harrison, 1980, pp. 252-255). One major change has been the rejection of the common-anion rule (McCaldin *et al.*, 1976), which stated that the valence-band offset between semiconductors with a common anion would be small, i.e. $\approx$ 100 meV, based on the assumption that the zone-centre valence-band maximum is made entirely of anion p-states. This has been shown to be not entirely true, since there is a significant admixture of cation d-orbitals into the valence band maximum, which may be as large as 12% in the II-VI's (Wei and Zunger, 1987). This explains for example the HgTe-CdTe valence-band offset, which would be predicted from the common-anion rule to be small, but is in fact around 350 – 500 meV (Meyer *et al.*, 1990; Tersoff, 1989).

Two recent model calculations are the model solid approach (Van de Walle, 1989), which considers offsets as being explained solely on the basis of bulk properties, with no need to consider charge transfer, and the interface bond polarity model (Lambrecht and Segall, 1990), which considers a combination of bulk and interface properties. Reviews of other models, first principles calculations and experimental results are contained within these two references. Since both the interface bonding and the bulk properties depend upon the atomic constituents and structure of the two semiconductors, both approaches are valid and should be expected to come up with similar results. The main difference is that models which take account of interface effects can in principle take account of orienta-

tion of interfaces, but this effect is expected to be small for interfaces between semiconductors which are both group-IV, both III-V or both II-VI.

For the calculational method used in this thesis the bandstructures are matched as shown earlier, shifted relative to one another by some amount, and this can easily be varied, if necessary, to take account of different conditions. The offset is considered to be due to bulk properties of each material, since the whole calculation only uses bulk parameters. The top of the valence bands in each material is defined relative to some fixed reference energy, and from the difference of these values the valence band offsets may be calculated.

## 2.9 : Calculations of energy levels and wavefunctions.

In the remainder of this chapter some examples of calculations of energy levels and wavefunctions will be presented. To perform the calculations it is necessary to decide how many bulk states to use in the summation. The matrices for the calculations are arranged as shown in equation 2.17, and are square. The size of the matrices is four times the number of 2D wavevectors which are matched at the interfaces. The 2D $\underline{G}$'s must be matched in whole groups, i.e. if (1,1) is used, (-1,1) must also be used, and so on. The groups of lowest $|\underline{G}_2|$ are $< 00 >$, $< 11 >$, $< 20 >$, and $< 22 >$, the first of which contains one $\underline{G}_2$, and the others contain four each. Thus it is possible to match with 1, 5, 9, 13 or more $\underline{G}_2$'s, and thus with four, 20, 36 or 52 bulk states, including spin. It is found that increasing from four to 20 states makes a large difference to energy levels, but that increasing beyond 20 states in most cases makes no difference to the calculated energy levels and causes an increase in numerical problems.

For GaAs, using the bandstructure shown in figure 2.1, if the matching energy was for example just below the valence band top, at about $-0.2$ eV, the 20 bulk states used in matching would generally be the real heavy and light holes, and the imaginary spin-split-off band, with four states each at $+k$ spin-up and spin-down and $-k$ spin-up and spin-down, and the complex band emanating from the conduction-band $\Delta$-minimum, which has eight states, including complex conjugates and spin.

Calculations have been performed of the energy levels of $Ga_{0.7}Al_{0.3}As$-$GaAs$-$Ga_{0.7}Al_{0.3}As$ quantum well, with a well width of 20 monolayers, and of $(Ga_{0.7}Al_{0.3}As)_M$-$(GaAs)_{20}$ superlattices, with $M = 40$, 20, 10, and 4, matching at bond centre, using the pseudopotential formfactors given in appendix B. $Ga_{1-x}Al_xAs$-$GaAs$-$Ga_{1-x}Al_xAs$ heterostructures were the first for which the characteristic 2D optical absorption spectrum — the step function — was observed (Dingle *et al.*, 1974). The absorption edge seen in experiments on 2D-heterostructures is due to the form of the density of states for a 2D-system

being a step function (Bassani and Pastori Parravicini, 1975, pp 158-159). The quantum well energy levels have been compared with calculations performed using a matching plane at the centre of the As plane, and good agreement in energy is found, with a $\leq 1$ meV energy difference. However, the calculations performed using a matching plane at the centre of the As plane were numerically less well behaved than the other calculations, so bond centre matching has been used for all the calculations presented in the rest of this chapter. At this well thickness there is little interaction between valence band states at quantum well Brillouin-zone centre (Brand and Hughes, 1987), which is an advantage for a basic exposition of results.

### 2.9.1 : Quantum well.

The zone-centre energy levels of a quantum well composed of 20 monolayers of GaAs, surrounded by $Al_{0.3}Ga_{0.7}As$ barriers, are shown in table 2.1, column 2. Probability density plots of the quantum well zone-centre bound state wavefunctions are shown in figure 2.3, averaged over the quantum well layer. The wavefunctions of the two conduction band and first three valence band quantum well Brillouin-zone centre states are much as expected from a Bastard envelope-function description (Bastard, 1981),

$$\psi_{i,j}(\underline{r}) = F_i(x)u_j(\underline{r}) \qquad 2.57$$

where $F_i(x)$ is an envelope function and $u_j(\underline{r})$ is a bulk Brillouin zone-centre Bloch function. The spatial distribution of probability densities in the confined electronic states has been measured using an isoelectronic planar substitution within the well region of GaAs/GaAlAs QWs (Gerard and Marzin, 1990), which perturbs the transition energies, and the wavefunctions are found to be very similar to those of figure 2.3. The different types of state, heavy-hole, light-hole and electron are easily identified by their characteristic cell-periodic Bloch-

| Main Constituent of QW State | Energy of QW State | Critical Point | Energy of SL states-same well width as QW. Barrier width (monolayers). 40 | 20 | 10 | 4 |
|---|---|---|---|---|---|---|
| E2 | 1.735 | $\bar{\Gamma}$ | 1.736 | 1.749 | — | — |
| | | $\bar{X}$ | 1.734 | 1.727 | 1.713 | 1.691 |
| E1 | 1.583 | $\bar{X}$ | 1.583 | 1.585 | 1.593 | 1.617 |
| | | $\bar{\Gamma}$ | 1.582 | 1.581 | 1.575 | 1.554 |
| HH1 | -0.017 | $\bar{\Gamma}$ | -0.017 | -0.017 | -0.016 | -0.014 |
| | | $\bar{X}$ | -0.017 | -0.017 | -0.017 | -0.019 |
| LH1 | -0.042 | $\bar{\Gamma}$ | -0.042 | -0.041 | -0.034 | -0.022 |
| | | $\bar{X}$ | -0.042 | -0.042 | -0.050 | -0.053 |
| HH2 | -0.064 | $\bar{X}$ | -0.063 | -0.063 | -0.062 | -0.068 |
| | | $\bar{\Gamma}$ | -0.064 | -0.064 | -0.065 | -0.075 |
| HH3 | -0.131 | $\bar{\Gamma}$ | -0.131 | -0.131 | -0.126 | -0.117 |
| | | $\bar{X}$ | -0.131 | -0.130 | -0.123 | -0.112 |
| LH2 | -0.136 | $\bar{X}$ | -0.135 | -0.130 | -0.140 | — |
| | | $\bar{\Gamma}$ | -0.138 | -0.146 | — | — |

Table 2.1. Critical point energies of $Ga_{0.7}Al_{0.3}As$-$(GaAs)_{20}$-$Ga_{0.7}Al_{0.3}As$ quantum well and $(Ga_{0.7}Al_{0.3}As)_M$-$(GaAs)_{20}$ superlattices. The zero of energy is at the top of the GaAs valence band. The GaAs bandgap is 1.519 eV.

| Polarisation | 100 | 011 |
|---|---|---|
| E-HH | 0.000 | 0.750 |
| E-LH | 1.000 | 0.250 |

Table 2.2. Ratio of $|M|^2$ in an infinite quantum well.

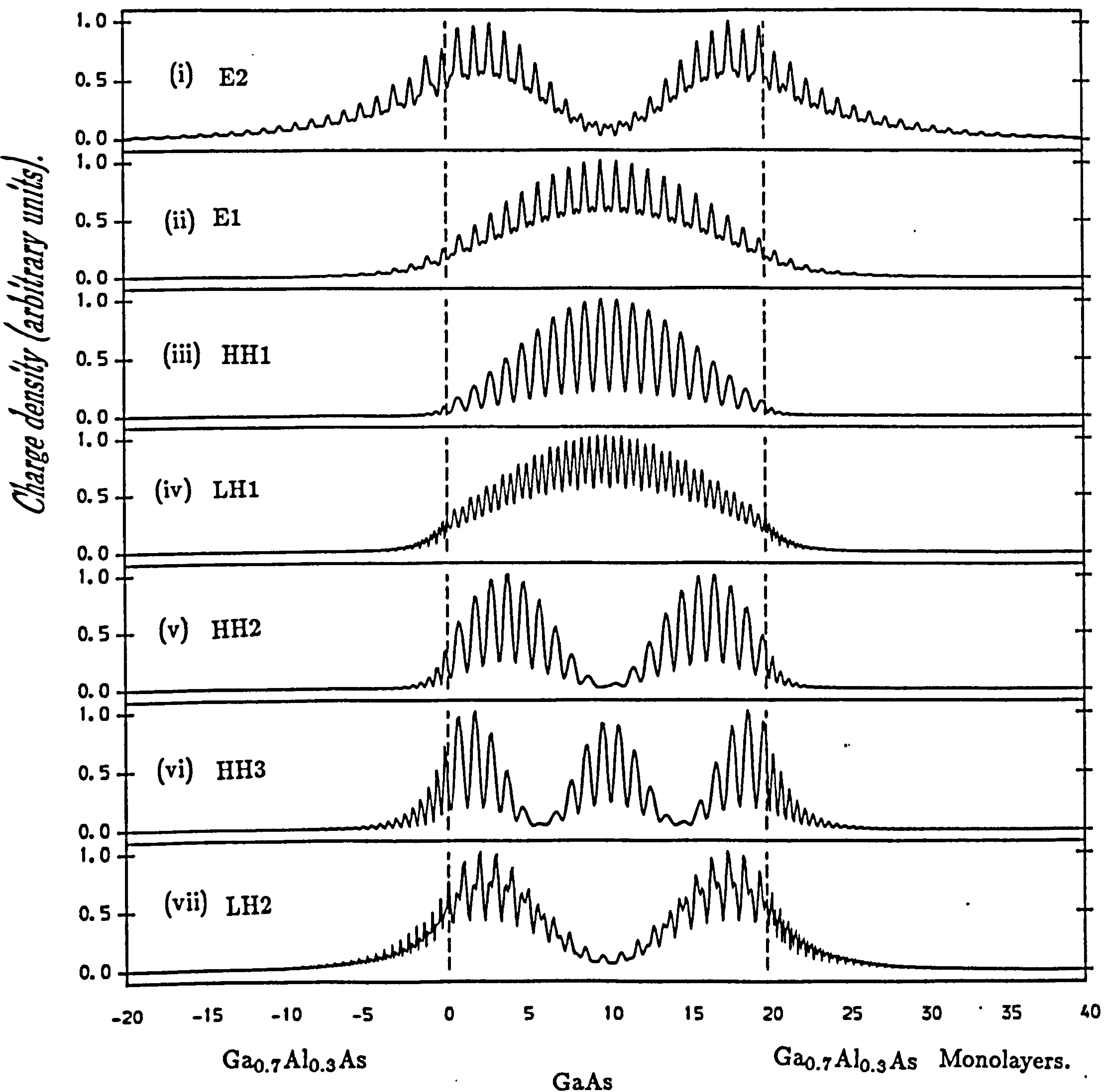


Figure 2.3. Quantum well bound state charge density plots along the x-axis, averaged over the plane of the well. (i) E2, (ii) E1, (iii) HH1, (iv) LH1, (v) HH2, (vi) HH3, (vii) LH2.

functions, which are due to the different combinations of bulk $p_x$, $p_y$, $p_z$ and $s$-states making up the quantum well states. The fourth and fifth valence band states show some deviation from this simple description due to a small mixing. This mixing can be described by an extension to the Bastard envelope-function description to allow for band mixing at zone-centre. It has been shown (Bastard, 1988 A, p 113) that this mixing is due to the inversion asymmetry of the zinc-blende lattice. Assuming that the only relevant interaction is between the second light-hole state (LH2) and the third heavy-hole state (HH3), the wavefunction of the fourth valence state can be written as

$$\psi_{V4}(\underline{r}) = C_{LH2}\psi_{LH2}(\underline{r}) + C_{HH3}\psi_{HH3}(\underline{r}) \qquad 2.58$$

where $\psi_{LH2}(\underline{r})$ and $\psi_{HH3}(\underline{r})$ are unmixed envelope-function quantum-well Brillouin-zone centre states of the form 2.57. The secular determinant

$$\det \begin{vmatrix} E_{LH2} - E & V_{LH2,HH3} \\ V_{LH2,HH3} & E_{HH3} - E \end{vmatrix} = 0. \qquad 2.59$$

may then be solved to find the energies $E_{4,5}$ of the mixed states in terms of $E_{LH2}$ and $E_{HH3}$, which are the LH2 and HH3 energy levels, without mixing, with

$$V_{LH2,HH3} \approx \int \psi^*_{LH2}(\underline{r}) V_{QW}(\underline{r}) \psi_{HH3}(\underline{r}) d\underline{r} \qquad 2.60$$

where $V_{QW}(\underline{r})$ is the quantum well perturbing potential. The eigenvalues of 2.59 are

$$E = \frac{1}{2}(E_{LH2} + E_{HH3} \pm \delta) \qquad 2.61$$

$$\text{with } \delta = [(E_{LH2} - E_{HH3})^2 + 4|V_{LH2,HH3}|^2]^{\frac{1}{2}} \qquad 2.62$$

If $E_{LH2} = E_{HH3}$, the energy separation of the mixed states is $\Delta E = 2|V_{LH2,HH3}|$, or a few meV (Bastard, 1988A, p 115), and the wavefunctions are $\psi(\underline{r}) =$

$\frac{1}{\sqrt{2}}[\psi_{LH2}(\underline{r}) \pm \psi_{HH3}(\underline{r})]$. In the present calculation, the mixing between the fourth and fifth quantum well states is small.

The mixing can be seen most clearly in state V4 (fig.2.4), in which the LH2 admixture can be seen to be enough to reduce the central peak in the charge density relative to the outer two.

### 2.9.2 : Superlattice.

In table 2.1, in addition to the QW bound state energies, the energies of the $(GaAs)_{20}$-$(Ga_{0.7}Al_{0.3}As)_M$ superlattices, at superlattice zone centre ($\overline{\Gamma}$) and growth direction zone edge ($\overline{X}$), with $M = 40, 20, 10$, and 4, are listed. The $M = 40$ superlattice is practically a multiple quantum well as far as low energy is concerned: of the bound states only the E2 and LH2 have dispersion greater than 1 meV, and all the superlattice zone-centre ($\overline{\Gamma}$) energies are displaced from those of the quantum well by less than this. There is a conceptual difference, the quantum well $\underline{q}_2 = \underline{0}$ energy levels are discrete, whereas the superlattice has a finite x-direction dispersion, however thick the barrier layers, but it is generally assumed that a periodic heterostructure with sufficiently thick barriers may be considered as a multiple quantum well.

The bandstructure of the four superlattices under consideration along the growth axis is plotted in figs. 2.5 and 2.6. Fig 2.5(a-d) shows the conduction band, the subbands broadening as the barrier width is decreased. This broadening can be roughly fitted in the form (Christen *et al.*, 1990)

$$E^{SL} = E^{SQW} - \Delta_1 - \Delta_2 cos(k_{SL}\ L), \qquad 2.63$$

where $E^{SQW}$ is the discrete energy state of a single QW, $k_{SL}$ is the $x$-component of $\underline{k}_{SL}$, and L is the superlattice period. $\Delta_1$ is the shift from the quantum well zone centre energy to the centre of the superlattice subband, while $\Delta_2$ is half the superlattice subband width, $2\Delta_2 = E(\overline{X}) - E(\overline{\Gamma})$. The conduction

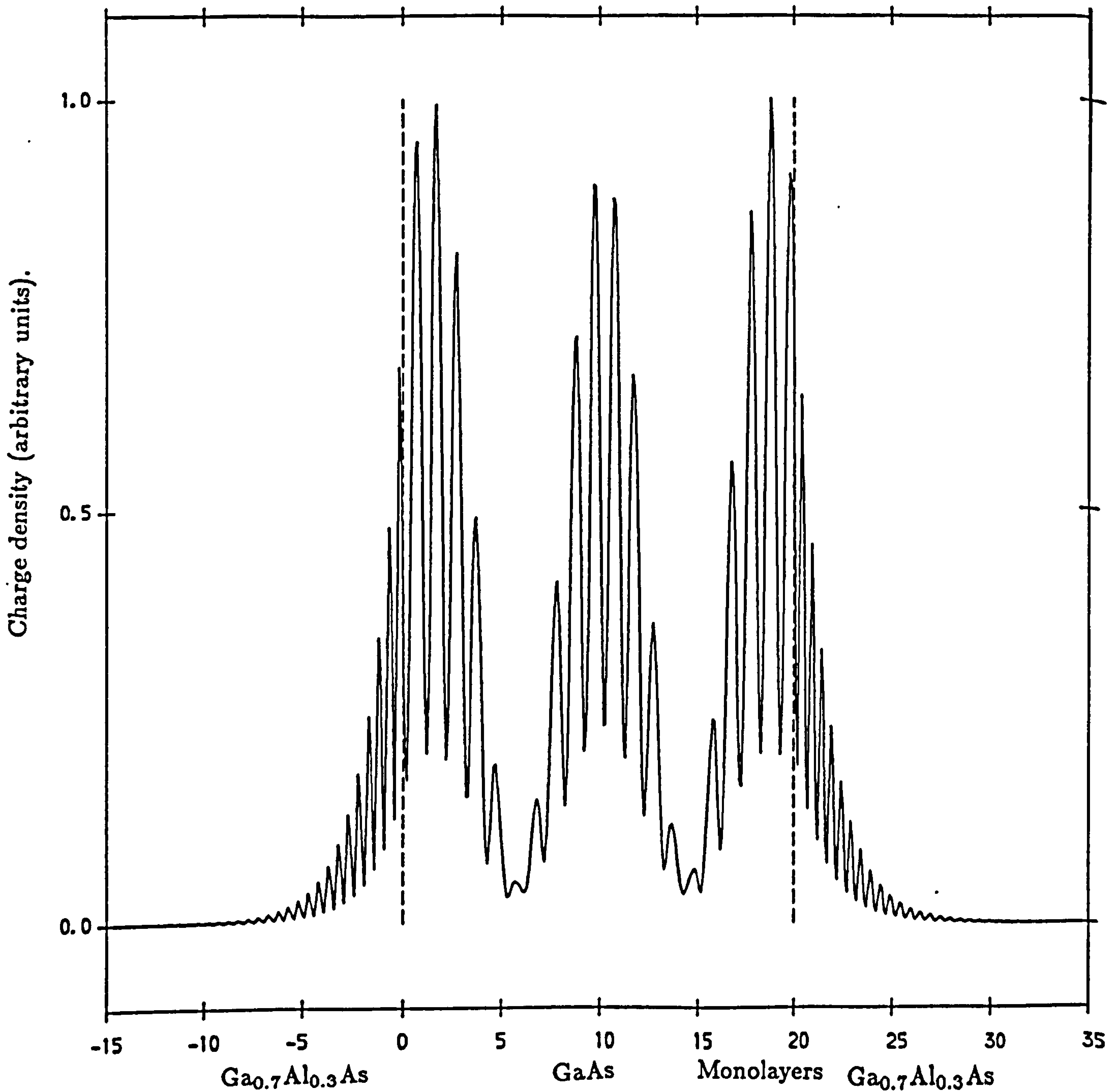


Figure 2.4. Quantum well fourth valence-band state charge-density plot along x-axis, averaged over the plane of the well.

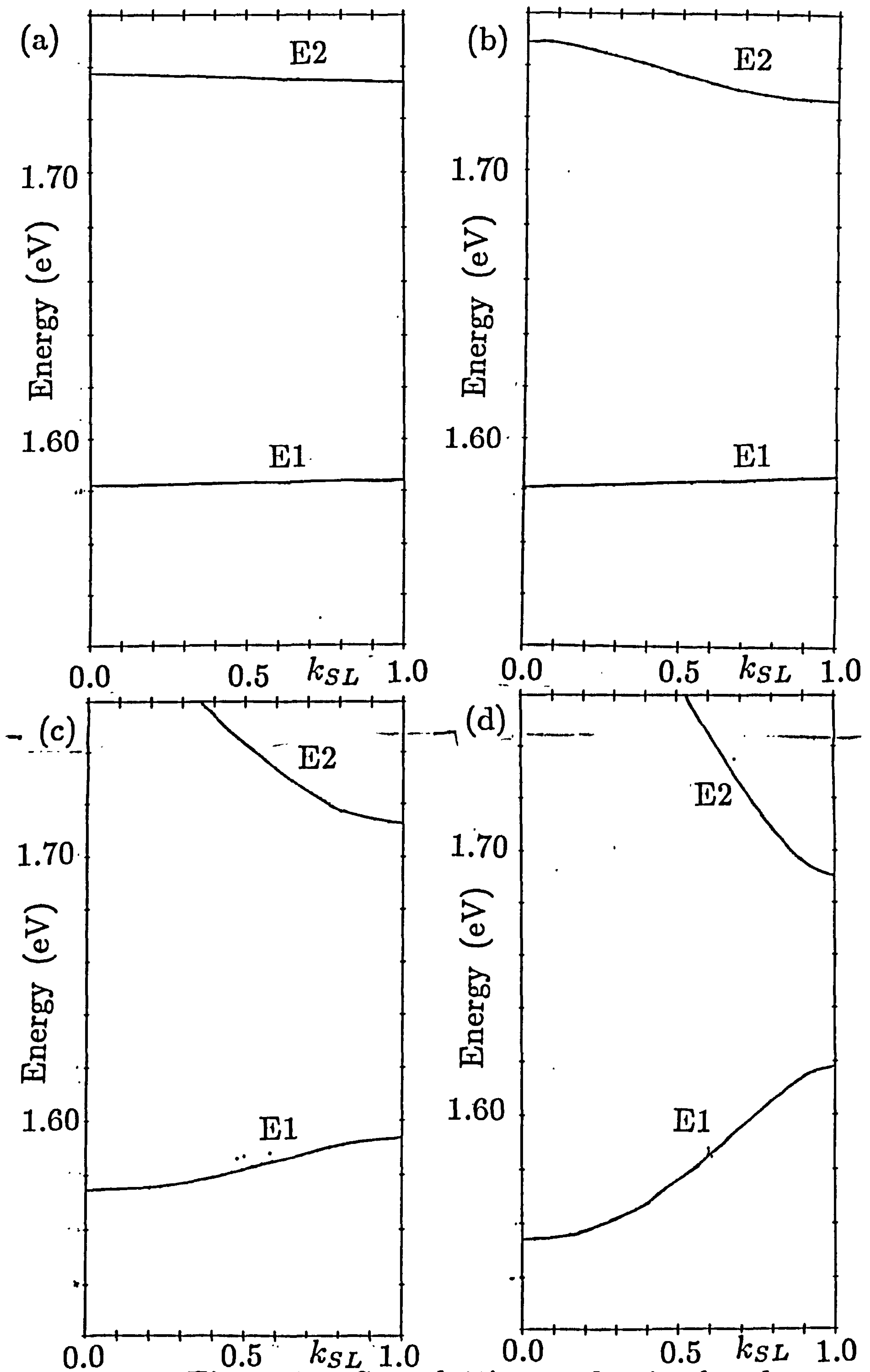


Figure 2.5. Superlattice conduction band subbandstructure, $(GaAs)_{20}$-$(Ga_{0.7}Al_{0.3}As)_M$ superlattice with (a) M=40, (b) M=20, (c) M=10, (d) M=4.

bands, fig 2.5(a-d) can be roughly described by the relationship 2.63, as can the valence bands for the superlattices with weakly coupled wells, fig 2.6 (a-b). The valence bands of the $(GaAs)_{20}$-$(Ga_{0.7}Al_{0.3}As)_M$ superlattices, with M=10 or 4, show strong interactions between the fourth and fifth bands (fig.2.6 (c) and (d)), while for $M = 4$ the second and third bands also interact (fig.2.6 (d)). The bands anticross along the superlattice $k_{SL}$ direction, and so cannot be described by 2.63. In figures 2.7 and 2.8 the charge density of the $(GaAs)_{20}$-$(Ga_{0.7}Al_{0.3}As)_4$ superlattice states along the x-direction, the superlattice growth direction, and averaged over the plane of the layers, are plotted out. Fig 2.7 shows the wavefunctions at superlattice $\overline{\Gamma}$, and fig 2.8 shows the wavefunctions at superlattice $\overline{X}$. While the superlattice bands anticross, the character crosses, e.g. the second valence band is mainly LH1 at $\overline{\Gamma}$, but mainly HH2 at $\overline{X}$.

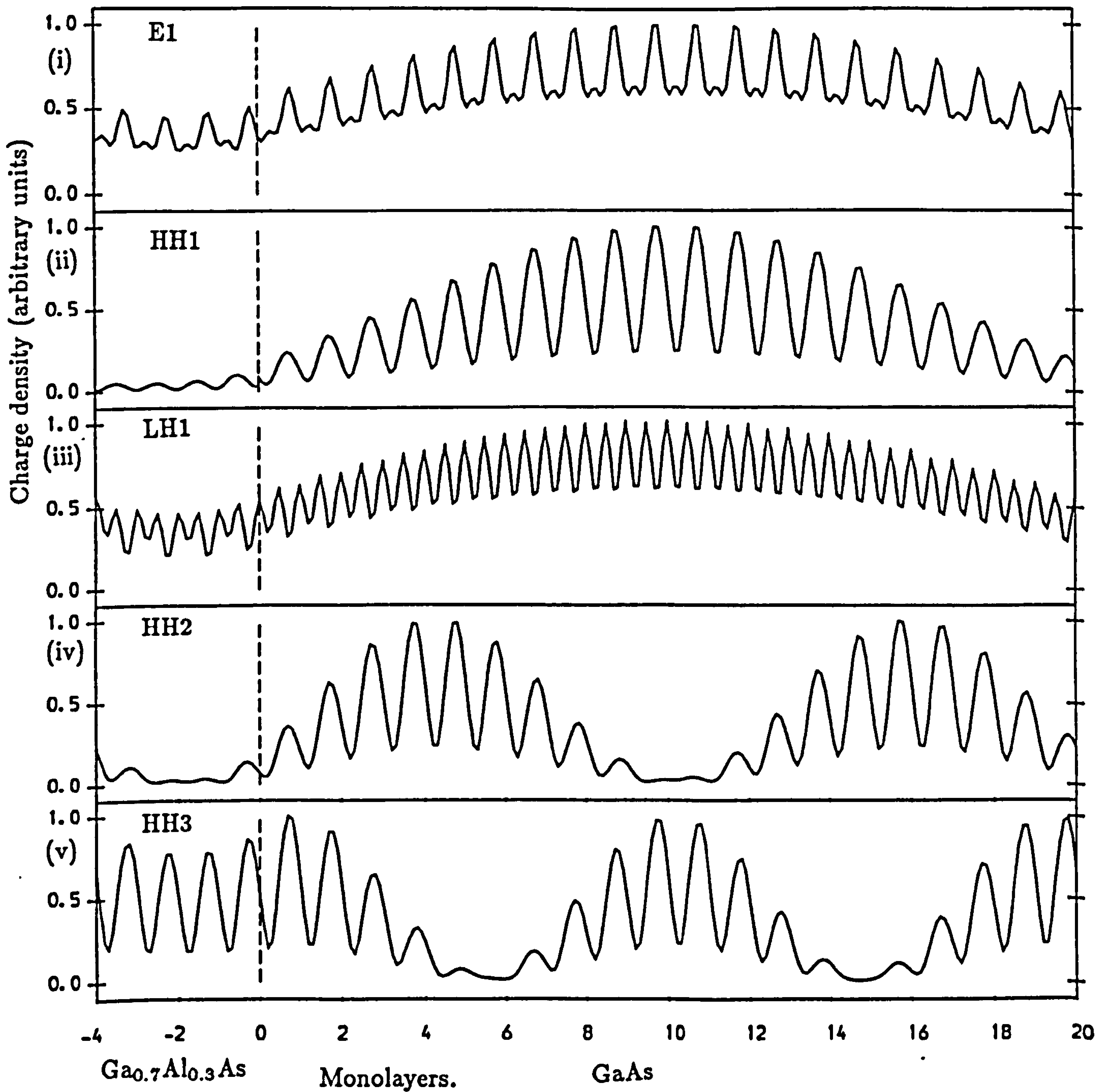


Figure 2.7. Superlattice wavefunction charge density plots at $\overline{\Gamma}$, (i) E1, (ii) HH1, (iii) LH1, (iv) HH2, (v) HH3, averaged over the plane of the layer.

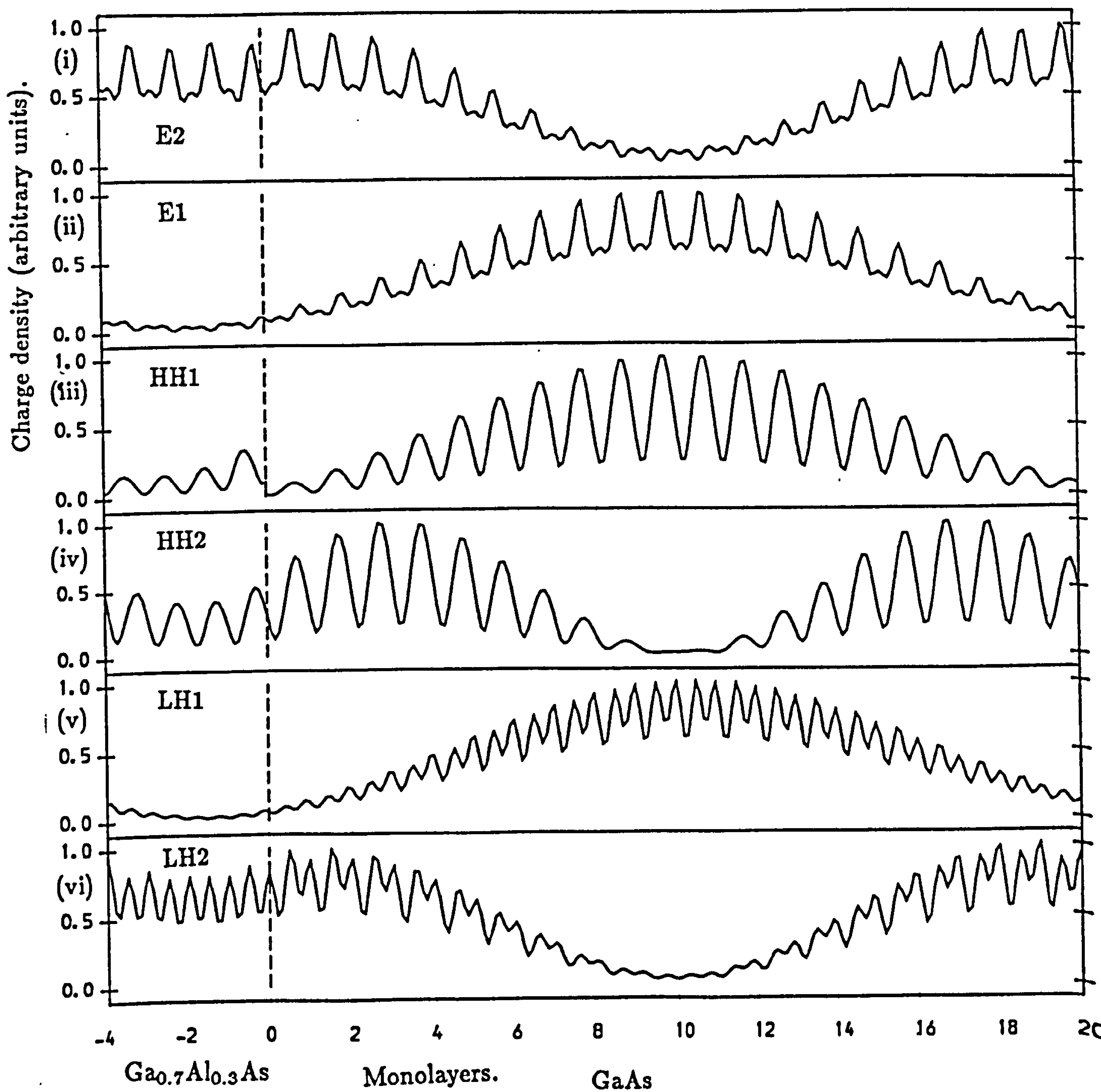


Figure 2.8. Superlattice wavefunction charge density plots at $\overline{X}$, (i) E2, (ii) E1, (iii) HH1, (iv) HH2, (v) LH1, (vi) LH2, averaged over the plane of the layer.

## 2.10 : Interband momentum matrix elements.

### 2.10.1 : Quantum well.

The interband momentum matrix elements of the GaAlAs-GaAs-GaAlAs quantum wells have been previously calculated from envelope-function models, (Bastard, 1988 A, p248). The relative size of squared matrix elements for E(n)-HH(n) and E(n)-LH(n) transitions in a heterostructure with infinite quantum wells in both valence and conduction bands is shown in table 2.2, with polarisation dependence as predicted by the tight-binding model (Chang and Schulman, 1985). The polarisation dependence of matrix elements has also been calculated using $\underline{k}.\underline{p}$ perturbation theory, with qualitatively similar results (Yamanishi and Suemune, 1984). Polarisation dependent photoluminescence has been observed experimentally from quantum wells and superlattices (Fujiwara *et al*, 1987, 1989; Weiner *et al.*, 1985; Kobayashi *et al.*, 1983) and has been used to study the subband structure of quantum wells (Sooryakumar, 1988).

For real systems, with finite valence and conduction bands, the ratio

$|M^{(011)}_{E(n),HH(n)}|^2/|M^{(011)}_{E(n),LH(n)}|^2$

will change due to the different penetration into the barriers of the three types of state considered here, because of the different well depths and effective masses of the conduction and valence bands. However this will not in itself change the ratio of matrix elements for the different polarisations

$|M^{(100)}_{E(n),H(n)}|^2/|M^{(011)}_{E(n),H(n)}|^2$.

For finite wells, pairs of valence and conduction subbands may have finite $|M|^2$ if they are both of even parity or both of odd parity. If one is even and one odd then $|M|^2$ is zero.

The pseudopotential intersubband matrix elements are shown in table 2.3, with the squared matrix element $|M^{100}_{E1-LH1}|^2$ set to equal 1.0. From table 2.3, $|M^{(011)}_{E1-HH1}|^2/|M^{(011)}_{E1-LH1}|^2 = 2.6$ rather than 3.0. The E1 and LH1 wavefunctions have spread more into the barrier than the HH1 wavefunction (figure 2.3)

| C,V | $E_{gap}$,QW. | (100) | (011) | | $E_{gap}$,SL | (100) | (011) |
|---|---|---|---|---|---|---|---|
| E1-V1 | 1.600 | 0.000 | 0.800 | $\overline{\Gamma}$<br>$\overline{X}$ | 1.568<br>1.636 | 0.000<br>0.011 | 0.560<br>1.402 |
| E1-V2 | 1.625 | 1.000 | 0.304 | $\overline{\Gamma}$<br>$\overline{X}$ | 1.576<br>1.670 | 1.000<br>0.001 | 0.217<br>0.003 |
| E1-V3 | 1.647 | 0.000 | 0.000 | $\overline{\Gamma}$<br>$\overline{X}$ | 1.629<br>1.685 | 0.000<br>0.860 | 0.000<br>0.339 |
| E1-V4 | 1.714 | 0.000 | 0.019 | $\overline{\Gamma}$<br>$\overline{X}$ | 1.671<br>1.729 | 0.000<br>0.005 | 0.015<br>0.002 |
| E1-V5 | 1.719 | 0.000 | 0.001 | | | | |
| E2-V1 | 1.753 | 0.000 | 0.000 | $\overline{X}$ | 1.710 | 0.001 | 0.002 |
| E2-V2 | 1.778 | 0.000 | 0.000 | $\overline{X}$ | 1.744 | 0.000 | 0.506 |
| E2-V3 | 1.800 | 0.000 | 0.546 | $\overline{X}$ | 1.759 | 0.006 | 0.002 |
| E2-V4 | 1.867 | 0.040 | 0.017 | $\overline{X}$ | 1.803 | 0.636 | 0.281 |
| E2-V5 | 1.872 | 0.701 | 0.286 | | | | |

Table 2.3. $|M'_{CV}|^2 (= |M_{CV}|^2/|M^{100}_{E1-LH1}|^2)$ vs energy gaps for the $Ga_{0.7}Al_{0.3}As$-$(GaAs)_{20}$-$Ga_{0.7}Al_{0.3}As$ quantum well and the $(GaAs)_{20}$-$(Ga_{0.7}Al_{0.3}As)_4$ superlattice.

and so their overlap is increased relative to the situation in the infinite well. This would be expected from the envelope function model. $|M^{(011)}_{E1-HH3}|^2/|M^{(011)}_{E1-HH1}|^2 =$ 0.02. This again is a consequence of the finite well depths and differing effective masses, and would be found in an envelope-function calculation which took account of these factors (Fang *et al.*, 1988).

$|M^{(100)}_{E1-LH1}|^2/|M^{(011)}_{E1-LH1}|^2 = 3.3$, $|M^{(100)}_{E2-LH2}|^2/|M^{(011)}_{E2-LH2}|^2 = 2.5$, rather than 4.0, as predicted from the tight-binding method (Chang and Schulman, 1985; table 2.2). This shows that the proportions of $p_x$, $p_y$ and $p_z$ bulk states in the quantum well light-hole states change with energy, reflecting the bulk light-hole band effective mass non-parabolicity.

The effect of mixing upon the matrix elements can be seen in the E1-V5 and E2-V4 squared matrix elements, which would be found to be zero in a method which did not include mixing at zone centre. This mixing could produce observable effects in the optical spectra from this quantum well.

### 2.10.2 : Superlattice.

The $(GaAs)_{20}$-$(Ga_{0.7}Al_{0.3}As)_4$ superlattice intersubband momentum matrix elements have been calculated at superlattice $\overline{\Gamma}$ and $\overline{X}$ symmetry points (table 2.3), to show the effects of interwell coupling. The polarisation dependence of the states is predicted by the tight-binding model to be the same as for the quantum well, but there are changes due to the bulk light-hole nonparabolicity, because the states are at different energies to those in the quantum well. The crossing of band character has a clear effect upon the matrix elements. For example the anticrossing of the V2 and V3 subbands referred to in section 2.9 is reflected in the matrix elements. The E1-LH1 (100) matrix element is still the largest $\overline{\Gamma}$ matrix element, but the E1-HH1 $\overline{X}$ (011) matrix element is larger. This is due to the very close match of the HH1 and E1 envelopes at $\overline{X}$ (fig.2.8). The change in intersubband matrix elements between $\overline{\Gamma}$ and $\overline{X}$ is significant in some cases, by a factor of two for the E1-HH1 (E1-V1) transition. This would

affect the intersubband absorption lineshape.

There have been a number of calculations performed of the electronic structure and optical properties of GaAs-$Ga_{1-x}Al_xAs$ superlattices (e.g. Schulman and Chang, 1985; Chang and Schulman, 1985; Gell *et al.*, 1986A, 1987; Brey and Tejedor, 1987) The polarisation dependence of optical matrix elements has been described before (Chang and Schulman, 1985), although the relative size of matrix elements found here differs somewhat from that paper due to the differential spread of different states into the barriers, at different points in the superlattice Brillouin zone. In addition the E1-HH3 zone-centre matrix element is here shown to be non-zero even when there is no band mixing.

## 2.11 : Summary.

In this chapter a method has been described for calculating the bound states of semiconductor quantum wells and both bound and unbound states of semiconductor superlattices. The bulk complex bandstructure of all materials in the heterostructure is calculated at a given energy and in-plane k-vector. Test solutions are formed from these, and are tested for continuity of wavefunction and derivative of wavefunction at each interface. The initial calculation of the bulk bandstructure takes the majority of the computer time needed by the method, and once this has been done the remainder of the calculation is fairly quick, which makes the method very flexible. Most importantly, unlike supercell methods, the calculation takes no longer for long-period superlattices than for short period superlattices, and can also be used to calculate the bound states of quantum wells. The method also takes account of the bulk bandstructure nonparabolicity.

The superlattice states are described as sums of bulk states, so the results can be related to envelope function calculations. However, the method goes beyond the envelope function approximation in that it takes account of the difference in the Bloch functions of the separate constituents of a heterostructure, and allows for mixing at the Brillouin-zone centre, which is important since the optical properties of quantum wells and superlattices are dominated by zone-centre transitions.

Using this method the probability densities of wavefunctions may be plotted out, both along a line in the growth direction and averaged over the layer plane. The averaged plots are similar to the results of envelope function calculations, but also include an atomic scale variation. The effects of mixing at zone centre can be seen in the plots, even if the mixing is small.

The model also allows for the calculation of intersubband momentum matrix elements. These show a polarisation dependence similar to that found by tight-binding calculations. The matrix elements involving light-hole states have a

polarisation dependence which varies with energy, due to the change in the proportion of $p_x$, $p_y$, and $p_z$ states in the bulk Bloch functions which make up the superlattice wavefunctions.

In the next chapter the modifications which are needed to the calculations to account for strain are described. The changes are in the calculation of the bulk bandstructure, and there are no changes to the calculation of the superlattice bandstructure once this has been done.

# CHAPTER THREE

# STRAINED LAYER HETEROSTRUCTURES

## 3.1 : Introduction and background.

### 3.1.1 : Introduction.

The method presented in chapter two for calculating heterostructure bandstructures can be used for strained layer superlattices and quantum wells. However, the initial calculation of bulk bandstructure is slightly more complicated, due to the effects of strain. The strain in each layer in a heterostructure can be determined from elasticity theory, and the relevant parts of this will be reviewed in the first part of the chapter. The method used to calculate bulk strained electronic structure by the semi-empirical pseudopotential method is described, and some examples of bulk bandstructure under the strain found in epitaxial layers are presented. The method described can be applied to any zincblende or diamond structure semiconductor.

### 3.1.2 : Elasticity theory for strained layers.

For heterostructures grown in the high symmetry directions [100] the relationship between stress and strain is straightforward. If a stress $\sigma_{xx}$ is applied alone (Todd, 1981, p78),

$$\epsilon_{xx} = \frac{\sigma_{xx}}{E_{100}}, \; \epsilon_{yy} = \epsilon_{zz} = \frac{-\nu\sigma_{xx}}{E_{100}} \qquad 3.1$$

where $E_{100}$ is Young's Modulus and $\nu$ is Poisson's ratio, which is defined by

$$\nu = -\frac{\text{transverse strain}}{\text{longitudinal strain}}.$$

For ease of notation in the following discussion $E_{100}$ is written as $E$.

If three stresses $\sigma_{xx}$, $\sigma_{yy}$, and $\sigma_{zz}$ are applied simultaneously,

$$\epsilon_{xx} = \frac{1}{E}[\sigma_{xx} - \nu(\sigma_{yy} + \sigma_{zz})],$$

by superposition. Now put $\sigma_{yy} = \sigma_{zz}$,

$$\text{then } \epsilon_{xx} = \frac{1}{E}[\sigma_{xx} - 2\nu\sigma_{yy}],$$

$$\text{and } \epsilon_{yy} = \frac{1}{E}[\sigma_{yy} - \nu(\sigma_{xx} + \sigma_{yy})],$$

$$= \frac{1}{E}[\sigma_{yy}(1-\nu) - \nu\sigma_{xx}].$$

For a biaxial stress, as is found in a strained layer of a heterostructure,

$$\sigma_{yy} = \sigma_{zz}, \; \sigma_{xx} = 0 \qquad 3.2$$

and so

$$\epsilon_{xx} = \frac{-2\nu}{1-\nu}\epsilon_{yy}, \; \epsilon_{zz} = \epsilon_{yy}. \qquad 3.3$$

The strain described by equation 3.3 is generally referred to as a biaxial strain. It has been pointed out (Anastassakis, 1990) that while equation 3.2 describes a biaxial stress, i.e. one component of $\sigma$ is zero, equation 3.3 does not describe a biaxial strain, because $\epsilon_{ii} \neq 0$ for $i = x,\ y,$ or $z$, and the term bisotropic strain is suggested. However, in this thesis the term biaxial strain is used, in keeping with most of the literature.

The energy density in a layer under the strain 3.3 is found from (Todd, 1981, p100)

$$\frac{dU}{dV} = \sum_i \int \sigma_{ii} d\epsilon_{ii},$$

neglecting shear strains, and with $i = x,\ y,\ z.$ Using equation 3.2 and

$$\epsilon_{yy} = \frac{1}{E}[(1-\nu)\sigma_{yy}],$$

it follows that

$$\frac{dU}{dV} = 2\int \sigma_{yy} d\epsilon_{yy}$$

$$= \frac{1}{2} 2\sigma_{yy}^2 \frac{1-\nu}{E}$$

$$= \frac{\epsilon_{yy}^2 E}{1-\nu},$$

and so

$$\frac{dU}{dV} = \frac{E\epsilon^2}{1-\nu} \qquad 3.4$$

E is Young's modulus and $\epsilon$ the in-plane strain ($= \epsilon_{yy}, \epsilon_{zz}$). This energy density can be used to work out the in-plane lattice constant of a freestanding superlattice and the expected critical thickness.

Consider a freestanding superlattice with a period composed of two sublayers of different semiconductors of thicknesses $L_1$ and $L_2$ monolayers respectively.

These bulk materials have initial lattice constants $a_1$ and $a_2$, Young's moduli $E_1$ and $E_2$, and Poisson's ratios $\nu_1$ and $\nu_2$. If the superlattice has an in-plane lattice constant $a$, the in-plane strains in layers 1 and 2 are

$$\epsilon_1 = \frac{a - a_1}{a_1}, \quad \epsilon_2 = \frac{a - a_2}{a_2} \tag{3.5}$$

In the growth direction,

$$\epsilon_\perp = \frac{-2\nu}{1-\nu}\epsilon_\parallel = \frac{a_\perp - a_i}{a_i}$$

and so the lattice constant of the 1st sublayer in the growth direction is given by

$$a_{1\perp} = a_1 - \frac{2\nu_1}{1-\nu_1}(a - a_1)$$

which may be written as

$$a_{1\perp} = a_1(1 - \rho_1\epsilon_1)$$

where $\rho_1 = 2\nu_1/(1-\nu_1)$.

The x-direction layer thickness of the strained sublayer 1 is $L_1 a_{1\perp}$, so the energy stored in layer 1 per unit area is

$$U_1 = \frac{E_1 L_1 a_1}{1-\nu_1}\epsilon_1^2(1 - \rho_1\epsilon_1),$$

assuming the energy density is uniform. Similarly the energy stored in sublayer 2 per unit area is

$$U_2 = \frac{E_2 L_2 a_2}{1-\nu_2}\epsilon_2^2(1 - \rho_2\epsilon_2).$$

The total energy per unit area is

$$U = U_1 + U_2.$$

To calculate the in-plane lattice constant $a$, $U$ is minimised with respect to $a$, i.e.

$$\frac{dU}{da} = \frac{dU_1}{da} + \frac{dU_2}{da}$$

$$= \frac{E_1 L_1}{1-\nu_1}(2\epsilon_1 - 3\rho_1\epsilon_1^2) + \frac{E_2 L_2}{1-\nu_2}(2\epsilon_2 - 3\rho_2\epsilon_2^2) = 0$$

using $d\epsilon_1/da_1 = 1/a_1$, *etc.*

For a minimum, we also need $d^2U/da^2 > 0$. However,

$$\frac{d^2U}{da^2} = \frac{E_1 L_1}{a_1(1-\nu_1)}(2 - 6\rho_1\epsilon_1) + \frac{E_2 L_2}{a_2(1-\nu_2)}(2 - 6\rho_2\epsilon_2)$$

which is positive for all strains considered.

The equation for $dU/da$ is quite difficult to solve analytically, although it may be solved numerically. It may be simplified by assuming that $\frac{3}{2}\rho_1\epsilon_1 = \frac{3}{2}\rho_2\epsilon_2 = 0$, which introduces an error of approximately the lattice mismatch (as a percentage). This is the equivalent of assuming that the thickness of the sublayer stays at the unstrained value. Then

$$\frac{dU}{da} = \frac{2E_1 L_1 \epsilon_1}{1-\nu_1} + \frac{2E_2 L_2 \epsilon_2}{1-\nu_2} = 0$$

i.e.

$$a = \frac{E_1L_1/(1-\nu_1) \ + \ E_2L_2/(1-\nu_2)}{E_1L_1/(1-\nu_1)a_1 \ + \ E_2L_2/(1-\nu_2)a_2} \qquad 3.6$$

where $L_1$ and $L_2$ are in monolayers. The extension to superlattices with more than two sublayers in each period is straightforward.

### 3.1.3 : Critical thickness.

Layers may be grown pseudomorphically, i.e. lattice matched and without formation of misfit defects, if the energy density per unit area of surface is below some threshold energy necessary for the formation of defects (Frank and Van der Merwe, 1949B). The energy stored per unit area, $E_{st}$, increases linearly with layer thickness t,

$$E_{st} = \frac{E\epsilon^2 t}{1 - \nu} \qquad 3.7$$

while the energy required to form misfit dislocations, $E_{dis}$, increases as $ln(t)$ (O'Reilly, 1989; Matthews and Blakeslee, 1974), but has a finite positive value at small $t$, which is why $E_{st} < E_{dis}$ at small $t$. The expressions for $E_{dis}$ in the literature vary, and will depend upon the type of defects which are important in a particular material. It is possible to get some feeling for the numbers from simple considerations, within a particular family of materials. Taking the II-VI Tellurides as an example, it has been found that calculated critical thickness curves for ZnTe and CdTe are within 7 % of each other (Miles *et al*, 1987), while the stiffness parameters of HgTe and CdTe are within 10 % of each other, about the error on these values (Dornhaus and Nimtz, 1983, p122), so it is reasonable to assume that CdTe, HgTe and ZnTe will have similar critical thicknesses for the same strain. In fact, it has been shown that the critical thicknesses for ZnTe grown on CdTe and for CdTe grown on ZnTe are the same (Cibert *et al*, 1991), supporting the assumption that critical thicknesses are the same for both biaxial tension and compression (Frank and Van der Merwe, 1949A). From experiment, thin CdTe layers grown between thicker layers of ZnTe, under 6 % biaxial compressive strain, have a critical thickness of 5 monolayers (Cibert *et al.*, 1990). $E_{dis}$ varies slowly, so as a first approximation may be assumed to be constant. With 6 % strain,

$$E_{dis}(6\%) = \frac{E}{1-\nu}(0.06)^2[5(a_\perp/2)]$$

where $a_\perp$ is the lattice constant in the growth direction. At a lower strain, the critical thickness $t_c$ may be found from

$$E_{st} = \frac{E}{1-\nu}\epsilon^2 t_c \approx E_{dis}(6\%)$$

$$\text{i.e. } t_c \approx 5(\frac{0.06}{\epsilon})^2 \text{ Monolayers.}$$

For the freestanding superlattices considered in chapters four and six, the predictions from this calculation are:

Chapter four : $(CdTe)_N$-$(ZnTe)_N$ superlattice,

CdTe $t_c \approx 14$ monolayers, under 3.6 % biaxial compressive strain, and

ZnTe $t_c \approx 31$ monolayers, under 2.4 % biaxial tensile strain, suggesting that the superlattices with $N$ up to 13 may be grown defect free.

Chapter six : $(ZnTe)_N$-$(HgTe)_{3N}$ superlattice,

ZnTe $t_c \approx 13$ monolayers, under 3.8 % biaxial tensile strain, and

HgTe $t_c \approx 45$ monolayers, under 2 % biaxial compressive strain, suggesting that superlattices with $N$ up to 12 may be grown defect free.

The predictions of theory and results of experiments will be considered in more detail in chapters four and six, but are in general agreement with the above simple calculations.

There is in addition a critical thickness for the whole heterostructure (Matthews and Blakeslee, 1975). This is approximately that for an alloy of the average composition on the substrate. If the whole heterostructure is below this critical thickness it will have the in-plane lattice constant of the substrate; above this critical thickness, it relaxes to the freestanding lattice constant by the formation of misfit defects.

## 3.2 : Pseudopotential theory of pressure effects.

### 3.2.1 : Introduction.

In this section the theory which is needed to calculate the bulk bandstructure of semiconductors under pressure and strain using the empirical pseudopotential method will be presented. The pseudopotential method is ideal for these calculations, since no extra terms need to be introduced into the calculations to account for the effects of strain and the reduction in symmetry of the crystal. However, although there is no change to the method, the pseudopotential formfactors which enter the calculations do change under strain, so some way to derive a new set of formfactors must be used.

### 3.2.2 : The empirical pseudopotential method.

The wavefunctions in a solid are rapidly varying near the atomic cores, but smoothly varying away from the cores. In a plane wave basis, the core region requires a large number of plane waves, while the region away from the cores requires only a few plane waves. The pseudopotential method takes account of this. In the pseudopotential method the one electron pseudopotential Hamiltonian is rewritten (Chelikowsky and Cohen, 1976)

$$H = -\frac{\hbar^2}{2m}\nabla^2 + V_p(\underline{r}) \qquad 3.8$$

where $V_p(\underline{r})$ is a weak pseudopotential which has the same eigenvalues as the true crystal potential, but eigenfunctions which vary smoothly in the ionic core region. Away from the ion core, the eigenfunctions are very similar to the true eigenfunctions.

In the local empirical pseudopotential method the ionic pseudopotentials are assumed to be spherical, so the formfactors depend only on the magnitude

of $\underline{G}$. In this case we may write

$$V_p(\underline{r}) = \frac{1}{N}\sum_{j=1}^{N}\sum_{|\underline{G}|\leq G_0} V_j(\underline{G})e^{-i\underline{G}.(\underline{r}-\underline{R}_j)}$$

where j is summed over the two atoms in the zincblende unit cell, $V_j(G)$ is the formfactor at $\underline{G}$ for the jth atom, which is summed over $\underline{G}$ vectors where $|\underline{G}| \leq G_0$, and $G_0$ is some cut-off, and $\underline{R}_j$ is the position of the jth atom.

In the case of the zincblende unit cell, taking the origin of coordinates to be halfway between the two atoms in the unit cell,

$$\underline{R}_1 = a(1/8, 1/8, 1/8) = \underline{\tau},$$

$$\underline{R}_2 = -\underline{\tau}$$

where $a$ is the lattice parameter. $V_p(\underline{r})$ may be written as (Cohen and Bergstresser, 1966)

$$V_p(\underline{r}) = \sum_{|\underline{G}|\leq G_0} (S^S(\underline{G})V^S(\underline{G}) + iS^A(\underline{G})V^A(\underline{G}))e^{-i\underline{G}.\underline{r}} \qquad 3.9$$

where $S^S(\underline{G})$ and $S^A(\underline{G})$ are the symmetric and antisymmetric structure factors, and $V^S(\underline{G})$ and $V^A(\underline{G})$ are the symmetric and antisymmetric pseudopotential formfactors. These are defined by

$$S^S(\underline{G}) = cos\underline{G}.\underline{\tau}$$

$$S^A(\underline{G}) = sin\underline{G}.\underline{\tau}$$

$$V^S(\underline{G}) = \frac{1}{2}[V_1(\underline{G}) + V_2(\underline{G})]$$

$$V^A(\underline{G}) = \frac{1}{2}[V_1(\underline{G}) - V_2(\underline{G})] \qquad 3.10$$

$$\text{with } V_1(\underline{G}) = \frac{2}{\Omega}\int V_1(r)e^{-i\underline{G}.\underline{r}}d\underline{r}$$

and similarly for $V_2$, where $V_1$ and $V_2$ are the atomic pseudopotentials, and $\Omega$ is the volume of the unit cell. For the diamond structure $V^A = 0$ and the structure factor is just $cos\underline{G}.\underline{r}$.

The five reciprocal lattice vectors of lowest magnitude are $|\underline{G}|^2 = 3, 4, 8,$ and 11. The symmetric structure factor is zero for $|\underline{G}|^2 = 4$, and the antisymmetric structure factor is zero for $|\underline{G}|^2 = 8$. The formfactors for higher values of $|\underline{G}|$ would make a difference to energy levels comparable with the errors due to the use of a local pseudopotential, so are not included. To calculate the bandstructure of an unstrained bulk zincblende structure semiconductor it is only necessary to know the values of six pseudopotential formfactors, three symmetric and three antisymmetric.

### 3.2.3 : Strain effects.

If the crystal is under strain, either hydrostatic or uniaxial, some modification must be made to the calculation. The pseudopotential of an atom in a solid, in $q$ space at $q = |\underline{G}|$, is related to that in real space by

$$V_p(\underline{G}) = \frac{2}{\Omega}\int V_p(\underline{r})e^{-i\underline{G}.\underline{r}}d^3r \qquad 3.11$$

so the change in volume of the unit cell alters the formfactor at a given $\underline{G}$, and in addition the pseudopotential in real space will change under strain. The $\underline{G}$ vectors change inversely with the change of lattice parameter with pressure, and new values of the symmetric and antisymmetric formfactors have to be found. A fit is found for the $V_p(\underline{G})$, to take account of the way various bands in the bulk bandstructure move under applied hydrostatic pressure and biaxial strain. This fit will take account of the changes in $V_p(\underline{r})$ with strain. The simplest approach is to estimate gradients to the curves at the required values of $q$ (Cardona, 1972; Hughes, 1989), which has the advantage of simplicity, and

of using either formfactors from the literature or ones fitted to bulk properties only, but the disadvantages that it doubles the number of input numbers, and that a gradient is just an approximation which may be good for a small change $\Delta|\underline{G}|$, but will work less well for a large change, e.g. caused by a high pressure. Alternatively, curves may be fitted through the symmetric and antisymmetric formfactors (Melz, 1971; Bassani and Brust, 1963). This curve, and hence the formfactors, may need to be adjusted to fit the bandgaps and pressure and strain dependencies from experiment. If curves are just fitted through existing formfactors, some pressure dependencies may be correctly accounted for, but others may not be (Melz, 1971). Producing a new curve which models the unstrained bandstructure and pressure and strain dependencies involves a greater amount of preparatory work, since a whole new set of formfactors needs to be determined for each material, but once a fit has been found it should work for a wide range of deformations.

For uniaxial strain, the number of formfactors which are needed increases due to the reduction in symmetry of the crystal. For example, under uniaxial strain along the (100)-axis, the formfactors for $\underline{G} = \frac{2\pi}{a_x}(2,0,0)$ are different to those for $\underline{G} = \frac{2\pi}{a_y}(0,2,0)$ or $\frac{2\pi}{a_z}(0,0,2)$. The formfactors may be calculated from gradients or curves, in the same way as for hydrostatic strain. The structure factors do not change. For example, under (100) uniaxial strain the reciprocal lattice vector $\underline{G} = (l,m,n)2\pi/a_0$ changes to

$$\underline{G}' = 2\pi(\frac{a_y^2}{a_x.a_y^2}l, \frac{a_y a_x}{a_x.a_y^2}m, \frac{a_y a_x}{a_x a_y^2}n)$$

assuming $a_y = a_z$; $\underline{\tau} = (1/8,\ 1/8,\ 1/8)a_0$ changes to

$$\underline{\tau}' = (a_x/8,\ a_y/8,\ a_y/8)$$

so $\underline{G}'.\underline{\tau}' = \underline{G}.\underline{\tau}$ and the structure factors are unchanged (Hughes, 1989).

3.2.4 : Method used in calculations.

A fit is needed for the symmetric and antisymmetric formfactors for a small region around the q-values at which formfactors are taken. For example, a hydrostatic pressure of 10 GPa produces a change in lattice constant of about 5 % in ZnTe, and the largest change in q which this produces, at $q = \sqrt{11}$, is 0.17, in units $\frac{2\pi}{a_0}$. All the in-plane strains considered in this thesis are less than 4 %. The approach taken is to choose a numerical form, then to fit the constants to experimental results. It is probable that slightly different forms will be needed to model different materials; however, the same form should work for materials with broadly similar bandstructures. It is found that one form of curves gives good agreement with experiment for the wide gap II-VI semiconductors, but a slightly different form of the antisymmetric potential is needed to fit the HgTe inverted gap bandstructure.

In the empirical pseudopotential method, a variety of different sets of formfactors may be chosen for any material, which will all be of the same form, but will not be exactly the same. For any particular strained bandstructure, it is possible to fit directly to the bandgaps which are predicted by a deformation potential calculation, but it is better to use as general a fit as possible. The fits which are chosen for each material will depend in detail upon which properties are important in a given calculation. As always in empirical pseudopotential calculations, only a limited number of properties may be fitted to with a given accuracy, but it is then possible to check that other properties show the right behaviour, at least qualitatively.

To make fits to the formfactors, curves were chosen which have a fairly simple algebraic form. The curves used are of the form, with $q$ in units of $2\pi/a_0$,

$$V_S(q) = Aq^3 + Bq^2 + C, \; q \leq 3.0 \qquad 3.13$$

$$V_S(q) = (Aq^3 + Bq^2 + C)e^{-D(q^2-9.0)}, \; q \geq 3.0 \qquad 3.14$$

$$V_A(q) = Ee^{-Fq^2} + G. \qquad 3.15$$

In one case, HgTe, a better fit was found using 3.13 and 3.14 for $V_S$, but a slightly different equation for $V_A$,

$$V_A(q) = Ee^{-Fq^4} + G. \qquad 3.16$$

The value of $V_S$ at $q = 0$ is $C = -\frac{2}{3}E_F$ (Cohen and Heine, 1970, p87), which leaves six constants to determine, the same as in the original formulation of the empirical pseudopotential method. The remaining six constants are fitted to various sets of experimental information. Details of fits are given in appendix C.

Use of curves rather than gradients allows for some non-linearity in the change of formfactors with strain. These curves are not the same as the actual symmetric and antisymmetric formfactor curves in q-space, which would be used for example in a supercell calculation of superlattice bandstructure, because they take account of the variation of the real space pseudopotential with pressure and strain. The curves are only valid near the initial q values at which formfactors are taken, i.e. $V_S(q)$ at $q = \sqrt{3}$, $\sqrt{8}$, and $\sqrt{11}$, and $V_A(q)$ at $q = \sqrt{3}$, 2, and $\sqrt{11}$. For larger values of $q$, $V_S$ and $V_A$ tend to zero.

## 3.3 : Semiconductors under hydrostatic pressure.

### 3.3.1 : Introduction.

The change in lattice constant of a semiconductor under hydrostatic pressure may be calculated from (Murnaghan, 1944),

$$\frac{V_0}{V} = (1 + \frac{B_0'}{B_0}P)^{1/B_0'} \qquad 3.17$$

which may be reorganised to give the lattice constant under a pressure P,

$$a = \frac{a_0}{(\frac{B_0'}{B_0}P + 1)^{1/3B_0'}} \qquad 3.18$$

In many cases the derivative of bulk modulus, $B_0'$, is not known to any great accuracy. However, at low pressures any innacuracy in $B_0'$ will only affect the change in lattice constant by a small amount, and so where values are not known definitely they have been estimated.

From equations 3.17-3.18 the change in lattice parameter with pressure may be found, and hence the change in bandgap may be calculated as a function of pressure using the theory described in 3.2. Results are shown in the following section.

Because the bulk modulus increases with pressure, a slight sublinearity of bandgap with pressure is often found, as in experiments using very high pressures on II-VI semiconductors (Ves *et al.*, 1985; Strössner *et al.*, 1987).

### 3.3.2 : Bandgaps of wide gap II − VI semiconductors.

The pressure dependencies of the direct bandgaps of the wide band gap II-VI telluride semiconductors ZnTe and CdTe have been calculated, using fits given in appendix C. Figures 3.1 and 3.2 show the calculated change in bandgaps with pressure, compared with some recent experimental results.

The calculated variation of the bandgap of ZnTe under hydrostatic pressure is shown in figure 3.1, compared with a fit to the experimental results (Strössner *et al.*, 1987). For the effective pressures that the sublayers are under in strained layer heterostructures, $\approx 1 \rightarrow 2$ GPa, the difference between the two curves will not be important.

For CdTe (fig 3.2) there are good recent experimental results for bandgaps under hydrostatic pressure, with pressure up to 3.5 GPa (Dunstan *et al.*, 1988). The best fit to the experimental pressure dependence of the direct gap was found to be linear (Dunstan *et al.*, 1988, 1989), although the relatively small range of pressures covered leaves the possibility open that there is a slight sub- or even supra-linearity in the pressure dependence. The calculated pressure dependence of bandgap shown here has a slightly larger linear pressure dependence than the experiment, together with a small sublinearity.

### 3.3.3 : HgTe hydrostatic pressure effects.

HgTe has an inverted bandgap, with the $\Gamma_6$ band which forms the conduction band in other zinc-blende structure semiconductors below the $\Gamma_8$ bands. The effect of small hydrostatic pressures is to move the $\Gamma_6$ band upwards relative to the $\Gamma_8$ bands; this does not open up a bandgap. However, for large hydrostatic pressures the $\Gamma_6$ band edge will move above the $\Gamma_8$ bands, and become the lowest conduction band. The calculated variation of the $\Gamma_6 - \Gamma_8$ gap is shown in figure 3.3; this is compared with the experimental result (Madelung *et al.*, 1982B, p239).

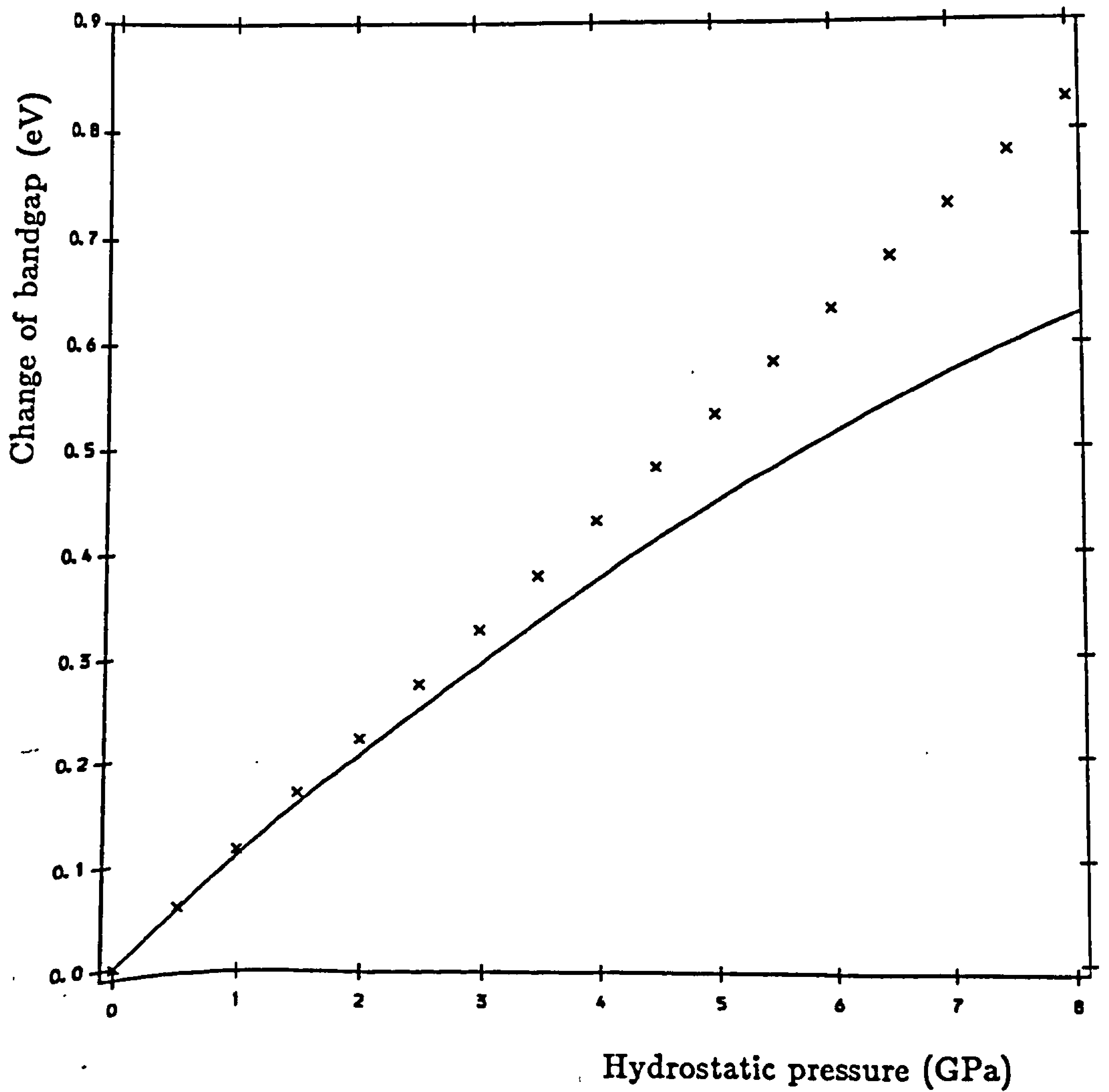


Figure 3.1. Change of direct bandgap of ZnTe under hydrostatic pressure. Crosses: pseudopotential calculation. Full line: fit to experiment (Strössner *et al.*, 1987).

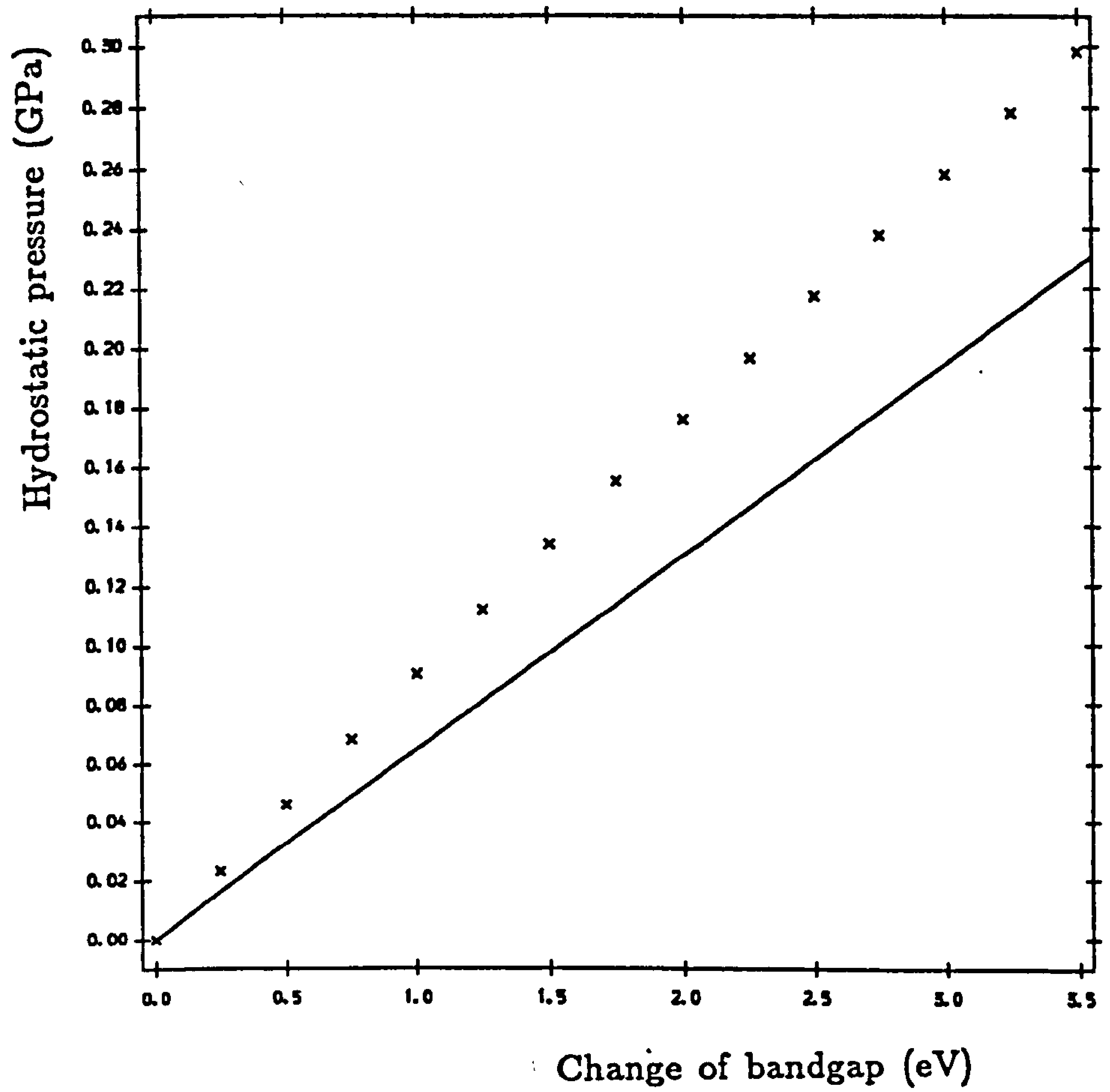


Figure 3.2. Change of direct bandgap of CdTe under hydrostatic pressure. Crosses: pseudopotential calculation. Full line: fit to experiment (Dunstan *et al.*, 1988).

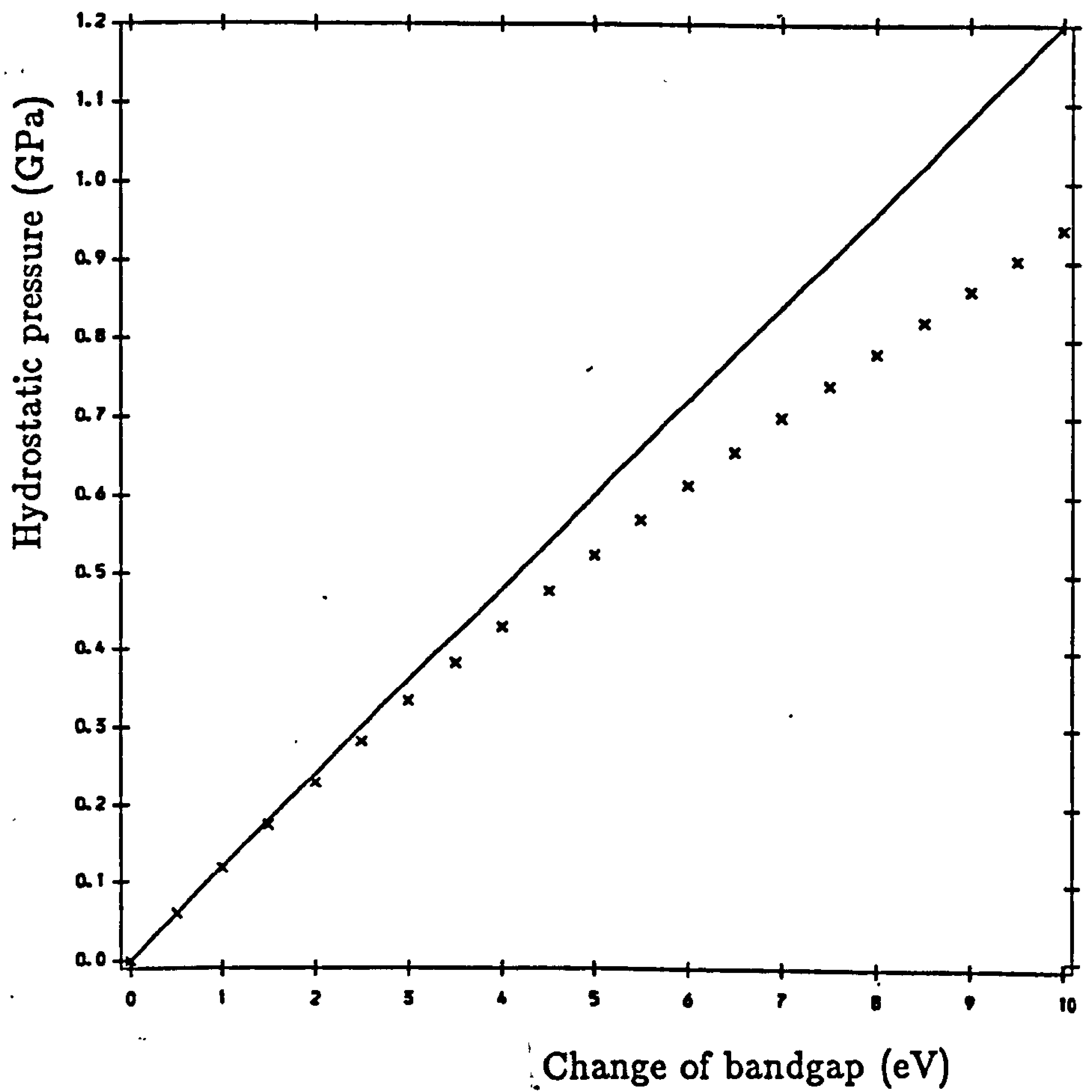


Figure 3.3. Change of direct bandgap ($E(\Gamma_6)$-$E(\Gamma_8)$) of HgTe under hydrostatic pressure. Crosses: pseudopotential calculation. Full line: fit to experiment (Madelung *et al.*, 1982 A).

## 3.4 : Semiconductor bandstructure under biaxial strain.

### 3.4.1 Introduction.

The bandstructure of the three semiconductors ZnTe, CdTe and HgTe has been calculated under the biaxial strain found in sublayers of superlattices. The bandstructure of semiconductors with a positive bandgap under biaxial strain has been extensively treated in the literature, so CdTe and ZnTe are just shown with the strain found in the superlattices considered in chapter four, the $(CdTe)_N$-$(ZnTe)_N$ superlattices. The bandstructure of zero gap semiconductors under biaxial strain is less familiar (Averous, 1979), so the bandstructure of HgTe is shown with varying in-plane strain.

### 3.4.2 CdTe and ZnTe.

The bandstructure of these two semiconductors was determined using the method set out in 3.2. Two different approaches were taken. For CdTe, the initial curves were chosen so as to give agreement with a deformation potential calculation for the strain found in the $(CdTe)_N$-$(ZnTe)_N$ superlattice of chapter four. The ZnTe fit is that for which the hydrostatic pressure dependence was shown earlier, and gives good agreement with the deformation potential calculation for the uniaxial strain splitting. Thus this fit may be used in a variety of cases, and has been used in chapters four, five, and six for different strains.

The bandstructure of CdTe is shown under 3.6 % biaxial compression in figure 3.4, along the [100] and [010]-directions, with [100] the growth direction. This strain is that of the CdTe sublayers in the $(CdTe)_N$-$(ZnTe)_N$ superlattice. The strain splits the bands at the top of the valence band by 150 meV, the top band with a heavy effective mass along [100] and a light mass along [010], the second a light mass along [100] and a heavy mass along [010].

The ZnTe is strained in the opposite sense to the CdTe in the $(CdTe)_N$-$(ZnTe)_N$ superlattice. The bandstructure is shown in figure 3.5. Due to the

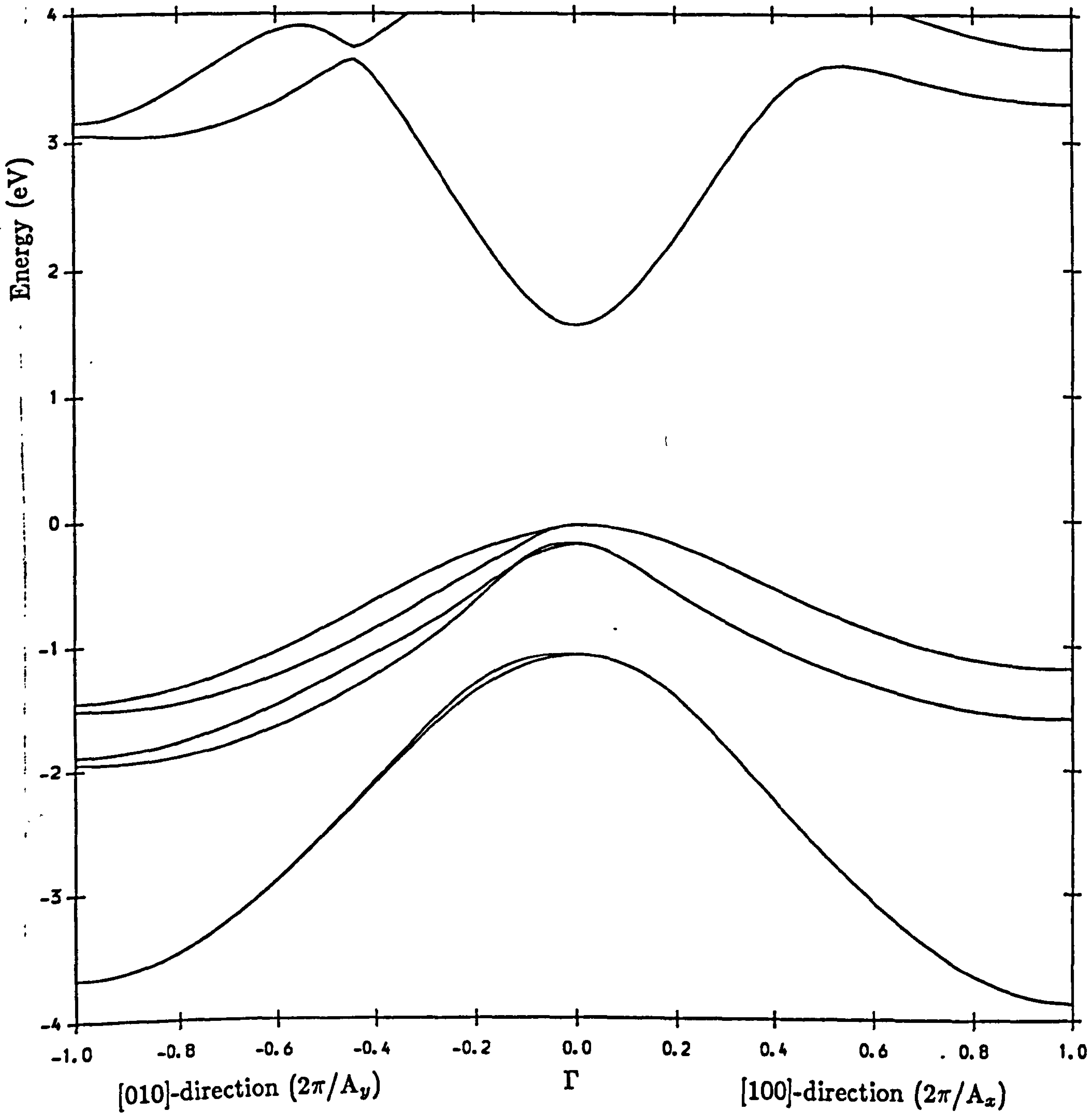


Figure 3.4. Bulk bandstructure of CdTe under 3.6 % biaxial compression, as in $(CdTe)_N$-$(ZnTe)_N$ superlattices, in [100] and [010] directions.

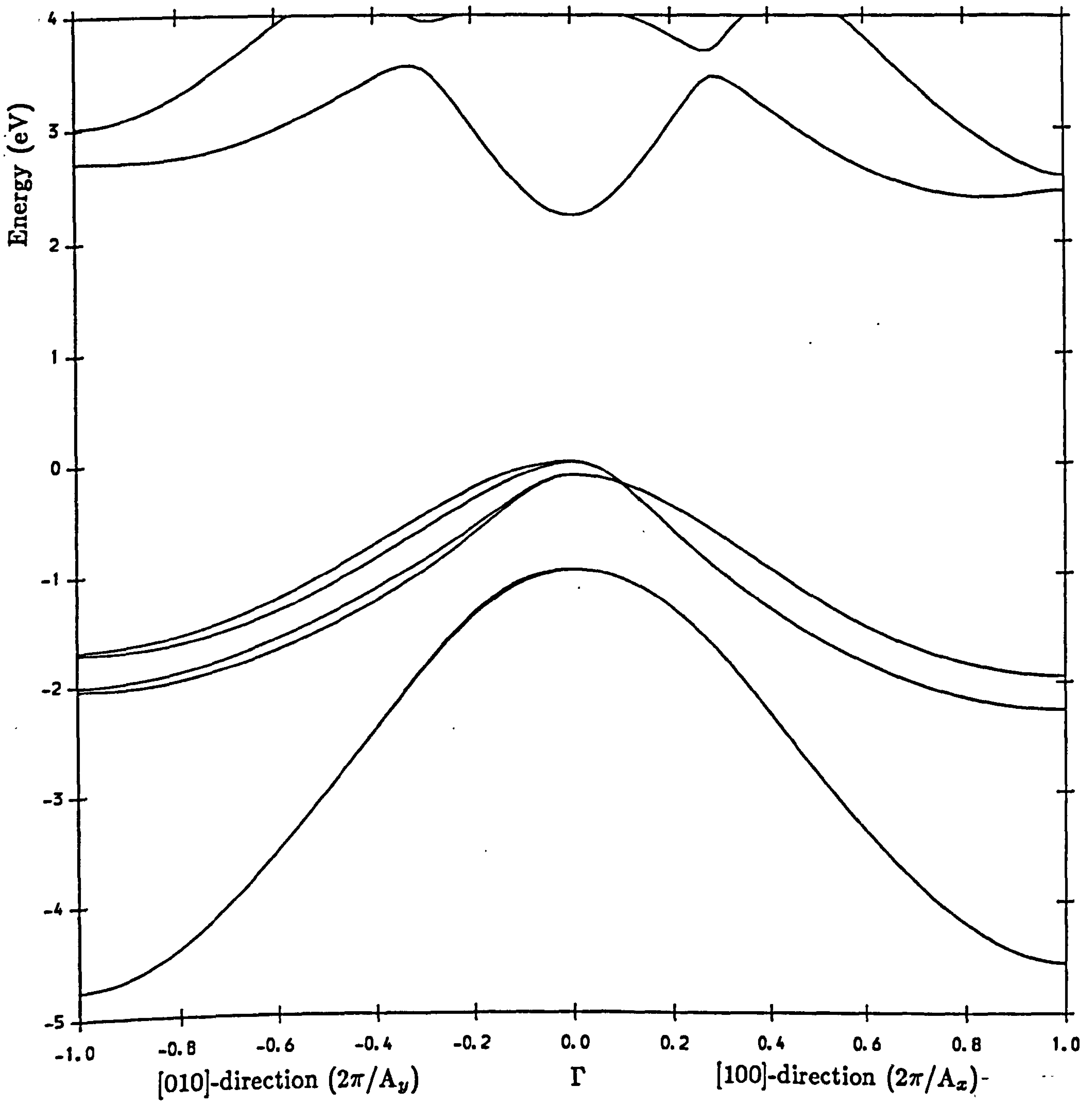


Figure 3.5. Bulk bandstructure of ZnTe under 2.4 % biaxial tension, as in $(CdTe)_N$-$(ZnTe)_N$ superlattices, in [100] and [010] directions.

biaxial tension, the upper band has a light mass in [100] and a heavy mass in [010], and vice-versa for the second band, with a splitting of 120 meV.

### 3.4.3 HgTe.

The bandstructure of the zero gap semiconductor HgTe (figure 3.6) differs from those of CdTe or ZnTe in that the $\Gamma_6$ band, which is the conduction band in CdTe or ZnTe, is below the degenerate $\Gamma_8$ bands in the valence band, while the upper and lower $\Gamma_8$ bands are respectively the lowest conduction band and the heavy-hole band. The lowest conduction band is like a light-hole band in CdTe or ZnTe, save for the inverted effective mass. The zero gap at $\Gamma$ is symmetry induced, and so remains under hydrostatic pressure, which does not change the symmetry of the crystal. The conventional gap, $\Gamma_6 - \Gamma_8$, is negative and decreases in magnitude under hydrostatic pressure.

With a reduction in symmetry the bands separate at $\Gamma$, the conduction band behaving as a light-hole in a wide-gap semiconductor, the upper valence band as a heavy-hole band (Averous, 1979). Under biaxial tension, as found in the CdTe-HgTe-CdTe quantum well, the bandstructure near $\Gamma$ is as shown in figure 3.7. The bands have separated at $\Gamma$, due to the reduction in symmetry. In the [100]-direction, the growth direction, the upper band is electron-like and the lower band is heavy-hole-like, but in-plane the bands are inverted, as usual in semiconductors under a biaxial strain. Close to zone-centre, in the in-plane [011]-direction, the hole band has an inverted electron-like effective mass, while the electron band has a heavy-hole-like effective mass. These anticross, giving an indirect bandgap of about 5 meV and a direct bandgap of about 10 meV. The hole band splits away from zone-centre, due to the reduction in symmetry.

In figure 3.8, the bulk bandstructure of HgTe under 2 % biaxial compression, as in the $(HgTe)_{3N} - (ZnTe)_N$ superlattice, is shown. The $\Gamma_8$ degeneracy has been removed, and the lowest electron band has a heavy-hole-like mass in the

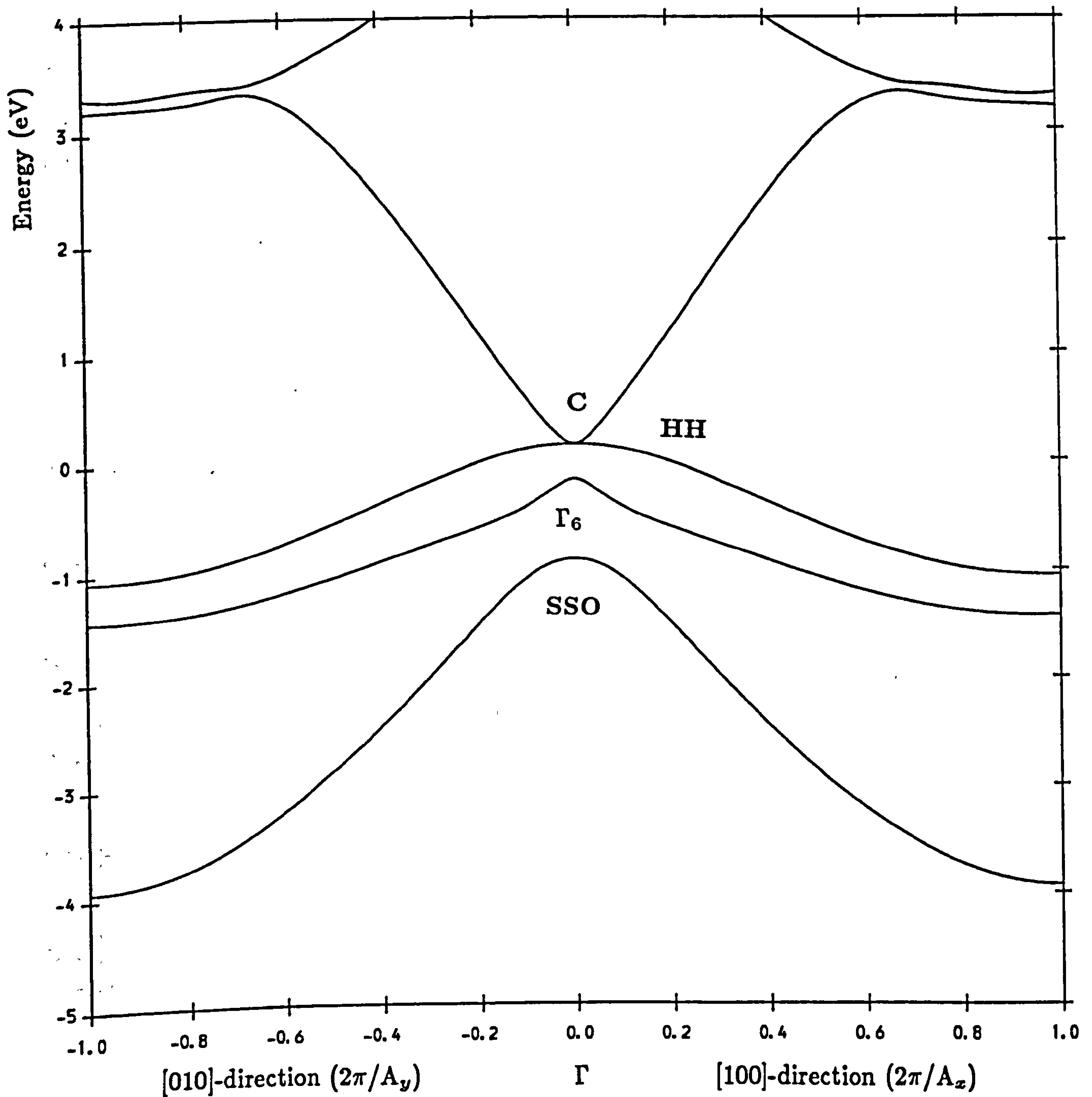


Figure 3.6. Bulk bandstructure of unstrained HgTe. The two identical directions [100] and [010] are shown for comparison with figure 3.8.

The states are marked near zone centre as HH, C, $\Gamma_6$, SSO, for the heavy-hole band, conduction band, inverted $\Gamma_6$ band and spin-split-off band respectively.

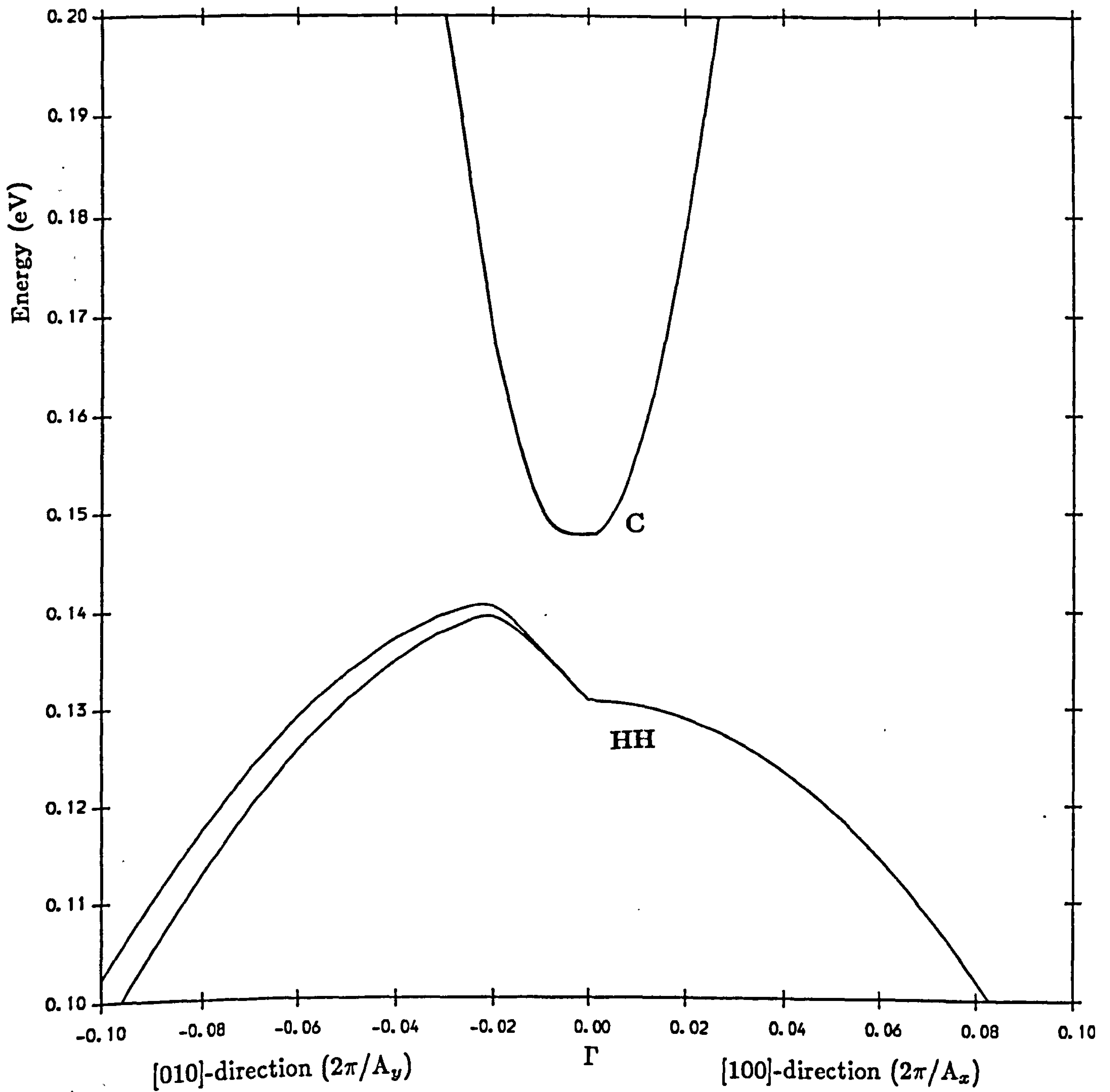


Figure 3.7. Bulk bandstructure of HgTe under 0.3 % bi-axial tension, near zone-centre, as in CdTe-HgTe-CdTe quantum well, along [100] and [010].

The states are marked near zone centre as HH, C, for the heavy-hole band, and conduction band.

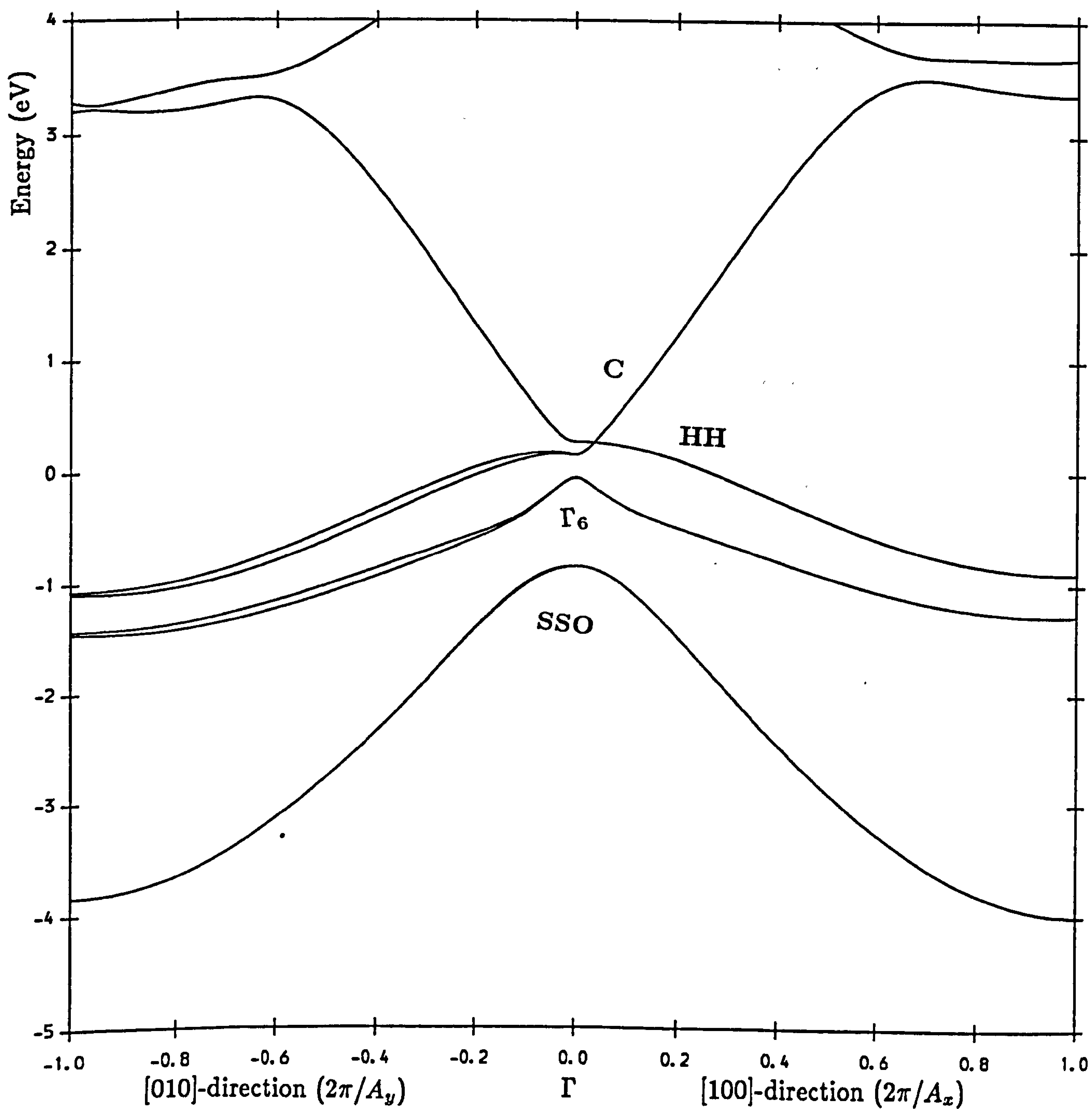


Figure 3.8. Bulk bandstructure of HgTe under 2 % biaxial compression, as in $(HgTe)_{3N}$-$(ZnTe)_N$ superlattice, in [100] and [010] directions.

The states are marked near zone centre as HH, C, $\Gamma_6$, SSO, for the heavy-hole band, conduction band, inverted $\Gamma_6$ band and spin-split-off band respectively.

[100] direction, while the highest hole band has an electron-like mass in the [100]-direction. In semiconductors with a positive bandgap, e.g. CdTe, under biaxial compression the $\Gamma_8$ band splits, with the upper band having a heavy mass in the growth direction, the lower band having a light mass in the growth direction, as shown for CdTe in figure 3.4. The zone-centre splitting is qualitatively the same in the biaxially compressed HgTe, except that due to the inverted bandstructure is more complicated. In figure 3.8 the highest hole band and the lowest electron band anticross in the growth direction at $k \approx (0.05, 0, 0)$, with a bandgap of $\approx 1$ meV. As with the strained CdTe, the masses are reversed in the in-plane directions, with the upper band having a light electron-like mass and the lower band having a heavier mass. However, due to the proximity of the $\Gamma_6$ band, the lower band also has an electron-like effective mass at zone centre. The valence-bands split in-plane, again due to the lowering of the symmetry of the crystal.

## 3.5 : Summary.

In this chapter the method used for the initial calculation of bulk strained bandstructure has been described. The theory which is needed to calculate the deformation of the sublayers in any superlattice, given their elastic parameters, the thickness of each sublayer in monolayers, and the unstrained lattice parameter of each material, has been derived. The elements of pseudopotential theory which are needed to calculate the bandstructure of the semiconductor under strain were reviewed, and then the method which has been used in this thesis for the calculations was described. It was shown that the approach can be used to model the behaviour of the bandgaps under hydrostatic pressure, and some calculated bandgap variations are shown for the II-VI tellurides. Finally the bulk bandstructure under biaxial strain was shown for the superlattices which are considered in chapters four, five, and six.

# CHAPTER FOUR

# THE CDTE-ZNTE SUPERLATTICE

## 4.1 : Introduction and background.

### 4.1.1 : Introduction.

The CdTe-ZnTe strained-layer superlattice has aroused much interest as a potential material for optical devices, with a bandgap in the range 1.6-2.4 eV. The superlattice was first grown in 1986 (Monfroy *et al.*, 1986), and its photoluminescence (Miles *et al.*, 1986) and structure (Miles *et al.*, 1987) were described soon afterwards. The low temperature photoluminescence was found to be several orders of magnitude brighter than that of an alloy of equivalent composition, with a lower energy bandgap, but the intensity decreased with increasing temperature, and had almost vanished at 65K, due to the low exciton binding energy. A comparison of experimental bandgaps with second-order $\underline{k}.\underline{p}$ calculations indicated that the superlattices were freestanding rather than lattice-matched to the substrates, while reflection high-energy electron diffraction (RHEED) measurements, performed during growth, showed that the lattice constants of the sublayers of a 25 Å CdTe / 25 Å ZnTe superlattice changed sharply through the first micron of growth, but beyond that settled down to a

freestanding value. The residual strain in superlattices was measured by X-ray diffraction and compared with critical thickness calculations, and there was evidence of defect formation in several of the superlattices, although the extent of strain relaxation could not be measured using this method.

The luminescence of several CdTe-ZnTe superlattices was found to have an anomalous character, suggesting that the excitons were strongly localised at low temperatures (Hefetz *et al.*, 1986), which was interpreted as the result of layer width variation within the superlattices, and consequent strain inhomogeneity, but has also been said to be due to the localisation of the heavy-hole states at interfaces, as found in tight-binding calculations (Quiroga *et al.*, 1989). However, this anomaly in the luminescence is not found for ZnTe-CdTe-ZnTe quantum wells (Collet *et al.*, 1991), backing up the earlier explanation. A second distinct absorption line has been found for superlattices with CdTe layer widths greater than 25 Å (Shtrikman *et al.*, 1989; Shtrikman and Finkman, 1989).

The first full theoretical and experimental analysis of the properties of CdTe-ZnTe superlattices was carried out by Mathieu *et al.* (1988). They showed that the superlattices could be, depending upon offset and strain, type I heavy-hole and type II light-hole, type I both light and heavy-hole, or type II both light and heavy-hole. This unusual situation comes about because the uniaxial strain splitting of the top of the valence bands, due to the 6.2 % lattice mismatch between the constituent bulk semiconductors, is of the same order as the valence band offset. If the valence band offset were zero, i.e. if the bulk valence-band edges were aligned in the absence of strain, the addition of mismatch strain would cause the CdTe heavy-hole to move up, and the ZnTe heavy-hole to move down in energy, but the CdTe light-hole to move down and the ZnTe light-hole to move up. Thus there would be heavy-hole wells in the CdTe sublayers and light-hole wells in the ZnTe sublayers. The CdTe bandgap is much smaller than that of the ZnTe, by about 0.8 eV at low temperatures, so there is a large electron well in the CdTe sublayers for all suggested offsets. There are a variety of ways in which the strain may be distributed between the layers, depending upon

the ratio of layer thicknesses, as described in chapter three. A multiple quantum well of these materials has been grown matched to a substrate, and away from the freestanding configuration, but this heterostructure only contained 21 periods (Menéndez *et al.*, 1987), of 1 $\mu$m total length. Other heterostructures which have been reported in the literature are of 150-400 periods (Monfroy *et al.*, 1986) and 105-250 periods (Shtrikman *et al.*, 1989), and are longer than the critical thickness for the whole superlattice, so have freestanding lattice parameters.

### 4.1.2 : Strain effects.

The calculations presented in this chapter are for freestanding $(CdTe)_N$-$(ZnTe)_N$ superlattices, with N=1-30. The in-plane lattice constant is calculated from elasticity theory to be 6.24 Å, and the growth direction lattice constants are calculated to be 6.79 Å for CdTe and 5.94 Å for ZnTe. The CdTe sublayers are under 3.6 % biaxial compressive strain, while the ZnTe sublayers are under 2.4 % biaxial tensile strain. The best model to calculate the critical thickness of strained layers is still a matter of debate, although a number have been proposed. Calculations by three different models of critical thickness against misfit for CdTe are available in the literature (Miles *et al.*, 1987). The critical thicknesses using ZnTe stiffness parameters were found to be within 7 % of those for CdTe, so the same graph may be used for both materials, considering the low accuracy of such calculations. The three models suggest critical thicknesses of 13 to 38 monolayers for the ZnTe and 4 to 29 monolayers for the CdTe, for the strain in this superlattice. In a recent experiment, CdTe quantum wells grown by MBE on CdZnTe were found to have critical thicknesses of about 12 monolayers for 3.6 % strain, and about 20 monolayers for 2.4 % strain (Cibert et al., 1991). It has been suggested (Houghton *et al.*, 1990; Miles and McGill, 1989) that critical thicknesses for superlattice sublayers will be two or more times those for the single overlayers assumed in the models (Miles *et al.*, 1987), or for buried strained layers (Cibert *et al.*, 1990, 1991), due to the greater difficulty of forming

dislocations in the superlattice geometry, and this is supported by experimental evidence from SiGe/Si superlattices. A consideration of the literature suggests that superlattices with N up to about 20-30 may be free from dislocations, given careful growth.

The strain affects the relative alignment of bulk valence and conduction bands. The hydrostatic component of the strain shifts the valence and conduction bands relative to one another, and to those of other layers. The shifts of valence and conduction bands are taken to occur in the ratio 33:67 for both materials. Camphausen *et al.* (1971) find $\Delta E_v^P = 0.33 \Delta E_g^P$ for ZnTe and $0.35 \Delta E_g^P$ for CdTe, while Dunstan *et al.* (1989) find $\Delta E_v^P = 0.34 \Delta E_g^P$ for CdTe ($\Delta E_g^P$ is the change of bandgap under a hydrostatic pressure $P$, and $\Delta E_v^P$ is the shift of valence band edge relative to another semiconductor in a heterostructure). However, other calculations have found $\Delta E_v^P = 0.12 \Delta E_g^P$ for both CdTe and ZnTe, using a model solid theory (Van de Walle, 1989). For the strain in this superlattice, the effect is to introduce a relative shift of valence band edges, moving the ZnTe average valence band top up, and that of CdTe down. The separation produced, for the $(\mathrm{CdTe})_N$-$(\mathrm{ZnTe})_N$ superlattice, is 55 meV for the ratios used in this chapter, but only 20 meV for the lower ratios, introducing a 35 meV uncertainty. Thus, the calculations presented in this chapter for the $(\mathrm{CdTe})_N$-$(\mathrm{ZnTe})_N$ superlattice with a valence-band offset $\Delta E_v$ (ZnTe/CdTe)= +0.060 eV using the 33:67 ratio for $\Delta E_V : \Delta E_C$, are the same as with a valence band offset of +0.095 eV with the 12 : 88 ratio. So long as there is no agreement in the literature about these ratios for the two materials, it is necessary to state what values have been used in the interpretation of experiment or in performing a calculation. The wide range of values found for valence-band offset when experimental and theoretical bandgaps are compared (Mathieu *et al.*, 1988, 1990) may be due to the use of the wrong ratios, but may also be due to uncertainties in other parameters, particularly uniaxial deformation potentials.

The uniaxial part of the strain is assumed to split the bulk heavy and light hole bands at $\Gamma$ symmetrically about the shifted average edges. The ZnTe

strained light-hole edge is set as the zero of energy relative to which, with zero valence band offset, the ZnTe heavy-hole edge is at −0.124 eV, the CdTe heavy-hole edge is at −0.040 eV, and the CdTe light-hole edge is at −0.193 eV.

### 4.1.3 : Valence – band offset.

The valence band offset at the ZnTe/CdTe heterojunction has been measured and calculated by a number of workers. Values have been proposed between −0.130 eV and +0.130 eV, with positive values indicating that the ZnTe valence band edge moves up relative to the CdTe valence band edge. Katnani and Margaritondo (1983) found $\Delta E_v = -0.100$ eV from indirect measurements of heterojunction photoemission relative to Ge. Duc *et al.* (1987) found $\Delta E_v = +0.100 \pm 0.060$ eV in the (111)-direction, and Hsu and Faurie (1988) found $\Delta E_v = +0.067 \pm 0.085$ eV in the (100) direction, both measurements made by core-level X-ray photoemission spectroscopy. Wei and Zunger (1987) proposed the first-principles calculated value $\Delta E_v = +0.130$ eV, while Van de Walle *et al.* (1988) found $\Delta E_v = -0.100$ eV using a model solid theory, and Bertho *et al.* (1990) predicted $-0.128 \pm 0.005$ eV based on a self-consistent tight-binding calculation. By comparison of experiment and theory, using Kronig-Penney calculations, Mathieu *et al.* have proposed (1988) $\Delta E_v = +0.060 \pm 0.020$ eV and (1990) $\Delta E_v = +0.055 \pm 0.040$ eV, using two different sets of deformation potentials to fit one set of experimental results. By comparison of photoluminescence at high pressure with Bastard envelope function calculations, Gil *et al.* (1989) found $\Delta E_v = +0.075$ eV. This last experimental result is very useful, since it showed that at ambient pressure there is a small heavy-hole well in the CdTe for both a $(CdTe)_7$-$(ZnTe)_6$ and a $(CdTe)_8$-$(ZnTe)_{11}$ superlattice, and that the lowest energy PL peak is type-II light-hole for both superlattices. This allows some of the uncertainty in parameter sets to be overcome. For the set used here, taken from the literature, and detailed in appendix C, there is a heavy-hole well in CdTe for $\Delta E_v \leq +0.083$ eV, and a heavy-hole well in ZnTe for $\Delta E_v \geq +0.085$

eV, while the heavy-hole bulk bands at $\Gamma$ are aligned if $\Delta E_v = +0.084$ eV, so the closest fit with experiment is expected to be with $\Delta E_v$ between $\approx +0.060$ and $+0.080$ eV. In addition, to examine the interesting physics of the heavy-hole type-I-type-II crossover, a larger offset has also been considered.

### 4.1.4 : Calculations.

Calculations have been carried out for N=1 to 30, with a basis set of 130 plane waves for the bulk calculation, and using 20 bulk states in each region, with spin. The II-VI semiconductors have a $\Delta$-minimum only a few meV below the X-point. For the CdTe bulk bandstructure in the $(CdTe)_N$-$(ZnTe)_N$ superlattice (fig 3.4), the axial strain has shifted the conduction band secondary minimum of CdTe from $\Delta$ to $X$, removing the camel's back. In unstrained CdTe there are a set of eight complex bands (including spin) which emanate from the $\Delta$-minimum, and would be included in the matching set. For strained CdTe there is no $\Delta$-minimum, and so in the basis set two sets of four complex X-point related states are used instead of the $\Delta$-minimum complex states.

In the following presentation of results, electron states are denoted as E1, E2..., etc., in order of increasing energy, hole states as H1, H2,.., etc., in order of decreasing energy; if hole states can be (or need be) identified as being heavy-hole or light-hole dominated then they are also denoted HH1, HH2,.., etc., or LH1, LH2,.., etc., respectively. The ZnTe strained light-hole edge is used as the zero of energy in all calculations. The energies of the bulk heavy-hole, light-hole and conduction band edges are shown in figure 4.1 with the offsets $\Delta E_v = +0.0$ eV, $+0.060$ eV and $+0.140$ eV.

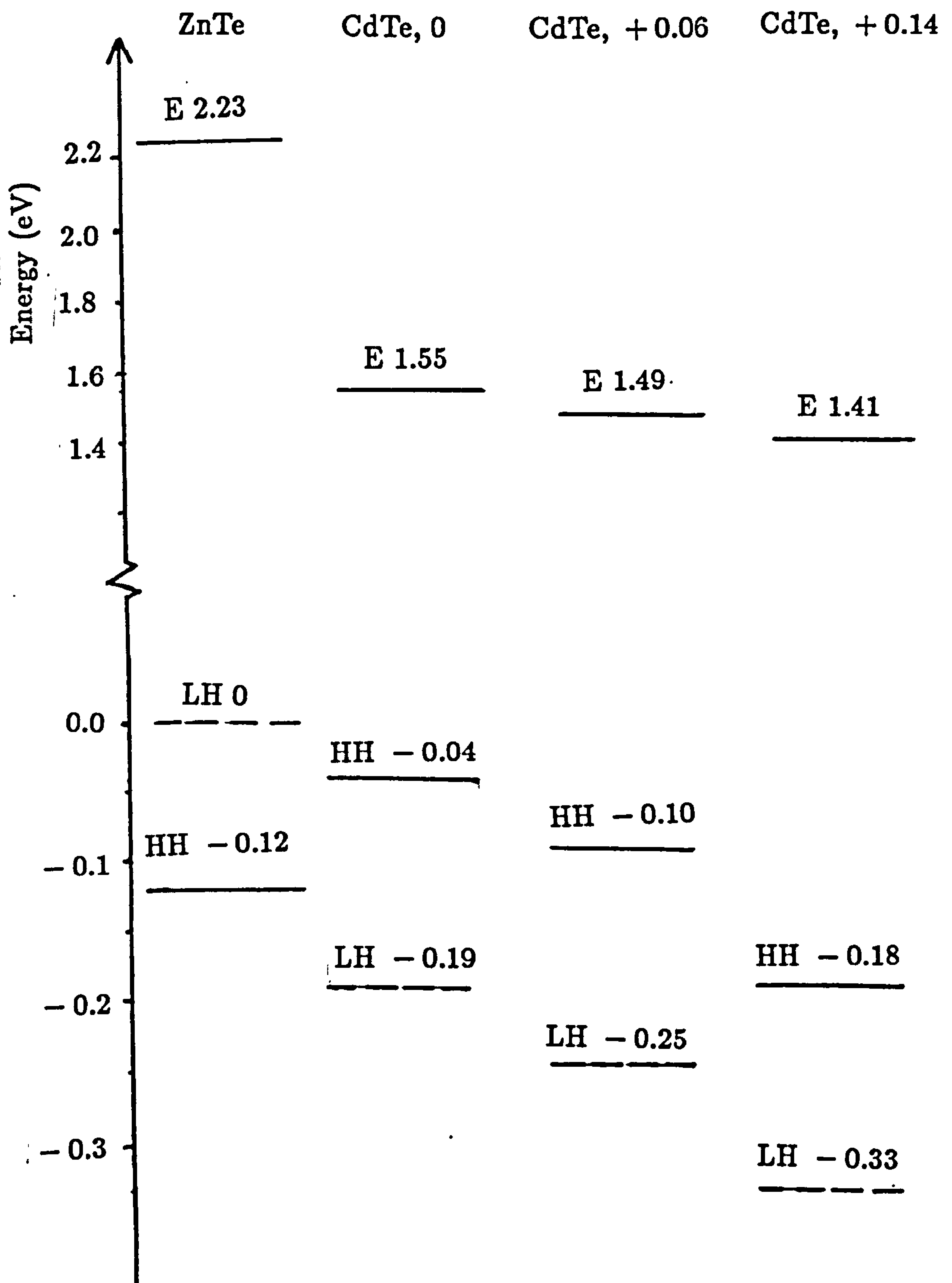


Figure 4.1. Bulk electron and hole edges of strained ZnTe and CdTe with the valence band offsets $\Delta E_V$ (ZnTe/CdTe) = 0, +0.06 eV and +0.14 eV. Different energy scales are used in the valence and conduction bands.

## 4.2 : Results.

### 4.2.1 : Energy Levels.

The calculations have been carried out with the centre of the common Te-plane between the sublayers as the interface matching plane. In figures 4.2 and 4.3 the superlattice pseudopotential valence subband energy of $(CdTe)_N$-$(ZnTe)_N$ superlattices with N=1-30 are presented with $\Delta E_v = +0.060$ eV and $\Delta E_v = +0.140$ eV, respectively. In fig 4.4 are presented the lowest conduction subband $\overline{\Gamma}$ energy levels with N=1-15 and $\Delta E_v = +0.060$ eV. The pseudopotential calculations are compared with Kronig-Penney calculations with effective masses and energy levels from the pseudopotential bulk strained bandstructure.

#### 4.2.1.1 : Monolayer Superlattices, N = 1.

The physics of monolayer superlattices, with each period comprising one monolayer of each material, has been extensively studied for the nearly lattice matched $(GaAs)_1$-$(AlAs)_1$ superlattice (Gilbert and Gurman, 1987, 1989; Gell *et al.*, 1986A; Hughes, 1989; Ishibashi *et al.*, 1985). The II-VI superlattices $(HgTe)_1$-$(CdTe)_1$, $(CdTe)_1$-$(ZnTe)_1$ and $(HgTe)_1$-$(ZnTe)_1$ have been less often described, but it has been predicted that they will have very similar electronic structure to the $(GaAs)_1$-$(AlAs)_1$ superlattice (Wei and Zunger, 1988).

Layers within at least one monolayer of an isolated interface are affected by charge transfer, so if superlattice sublayers are less than three monolayers thick they cannot be considered as separate bulk layers. Any non self-consistent calculation must be compared with self-consistent calculations and with experiment to see whether it reflects the essential physics of the situation. This comparison has previously been made with the method used here for $(GaAs)_1$-$(AlAs)_1$ superlattices (Hughes, 1989) and qualitative agreement was found.

The conduction band edge of the $(CdTe)_1$-$(ZnTe)_1$ superlattice has been

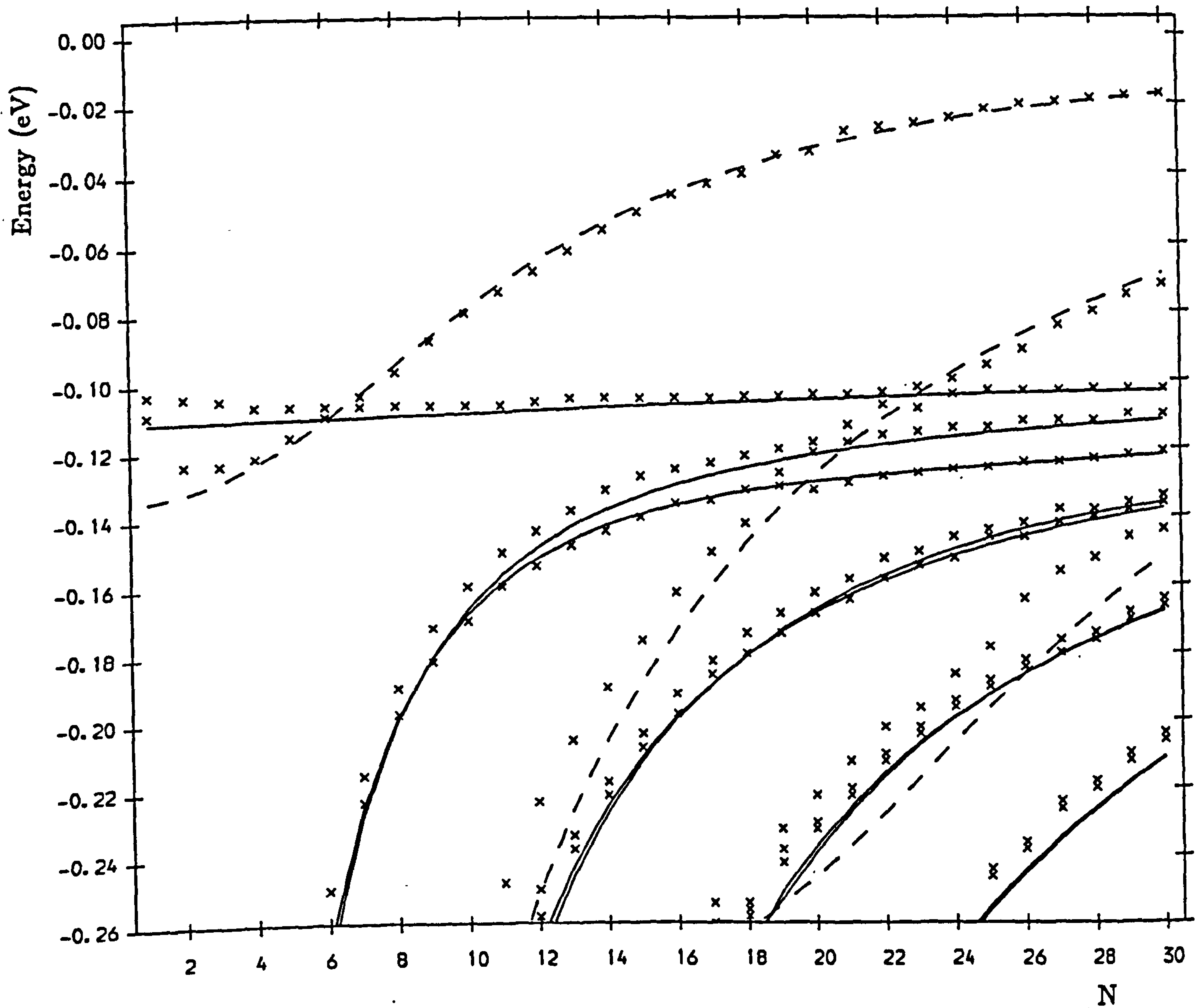


Figure 4.2. Valence band energy levels at $\overline{\Gamma}$ of the $(CdTe)_N$-$(ZnTe)_N$ superlattice with $\Delta E_V = +0.060$ eV, matching at a plane through the centre of the Te interface layer; N varies from 1 to 30. Kronig-Penney results are marked by a full line for heavy holes and a broken line for light holes; pseudopotential results are marked by crosses.

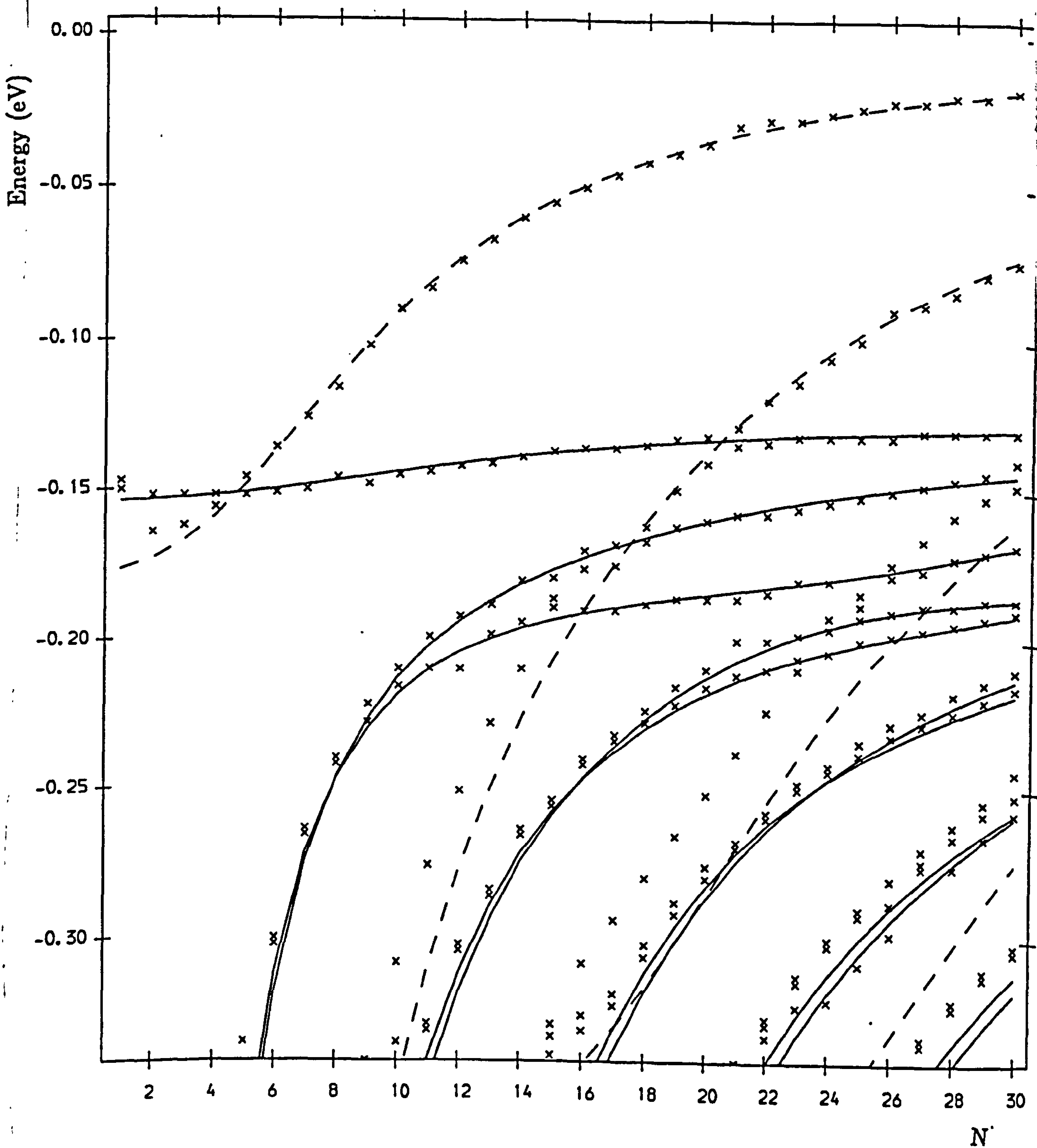


Figure 4.3. Valence band energy levels at $\overline{\Gamma}$ of the $(CdTe)_N$-$(ZnTe)_N$ superlattice with $\Delta E_V = +0.140$ eV, matching at a plane through the centre of the Te interface layer; N varies from 1 to 30. Kronig-Penney results are marked by a full line for heavy holes and a broken line for light holes; pseudopotential results are marked by crosses.

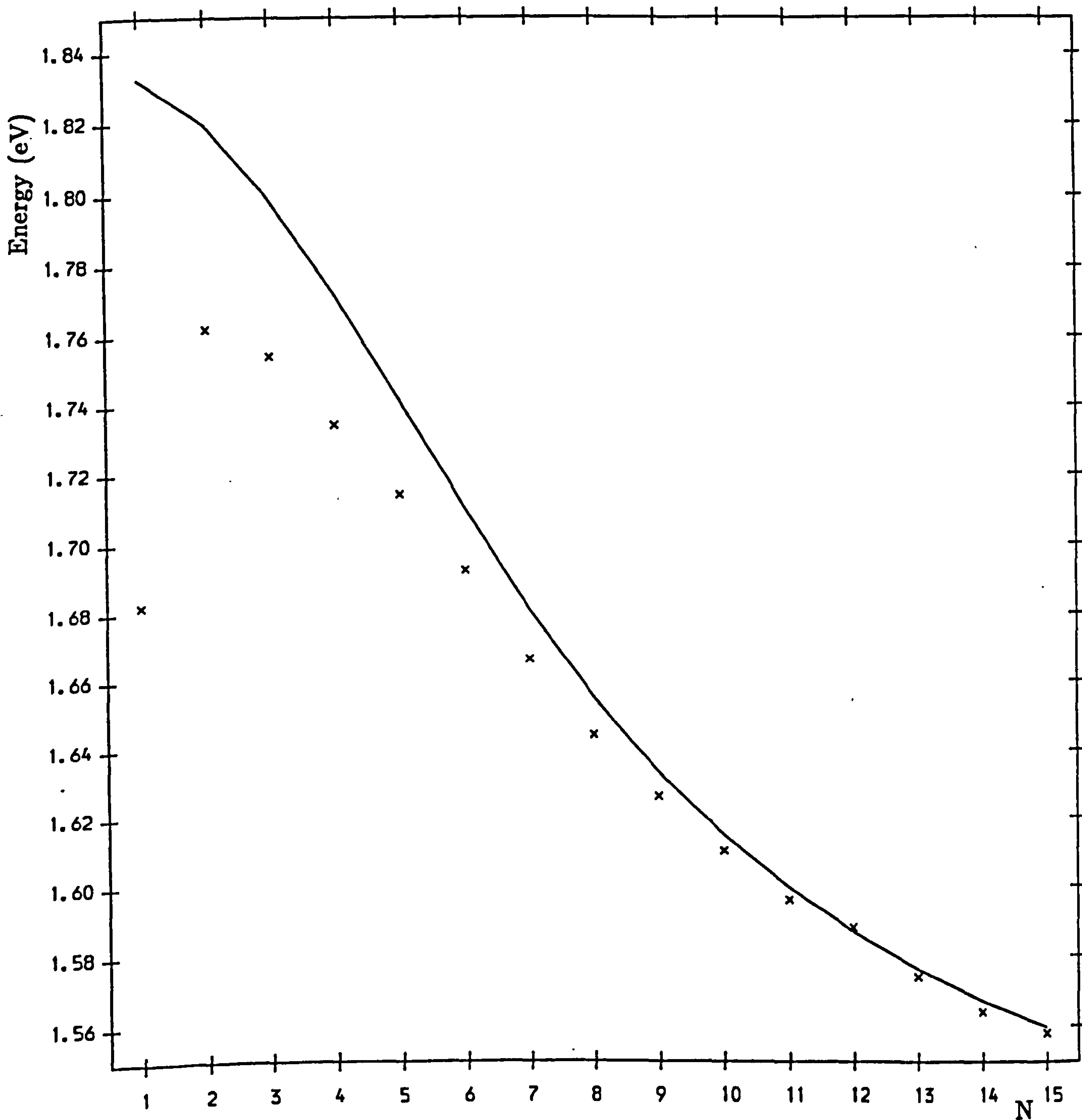


Figure 4.4. Energy levels of the lowest conduction band subband at $\overline{\Gamma}$ of the $(CdTe)_N$-$(ZnTe)_N$ superlattice with $\Delta E_V = +0.060$ eV, matching at a plane through the centre of the Te interface layer; $N$ varies from 1 to 15. Kronig-Penney results are marked by a full line; pseudopotential results are marked by crosses.

found by a self-consistent LDA calculation to be derived from bulk zone-centre states, and about 0.11 eV below the well centre (i.e. the average of CdTe and ZnTe Γ-edges), at the relaxed geometry (Wei and Zunger, 1988). The empirical pseudopotential calculations with $\Delta E_v$ = +0.060 eV finds the edge about 0.17 eV below the well centre, and 0.15 eV below the Kronig-Penney calculated energy level (figure 4.4).

The HH1 and LH1 states of the monolayer superlattice are very close together ($\approx$ 5 meV) at $\overline{\Gamma}$ for both offsets (figures 4.2 and 4.3). This is in contrast to the Kronig-Penney calculation, which predicts a HH1-LH1 splitting of 21 meV with $\Delta E_v$ = +0.060 eV, and of 27 meV with $\Delta E_v$ = +0.140 eV. In unstrained $(GaAs)_1$-$(Ga_{0.7}Al_{0.3}As)_1$ superlattices (Brand *et al.*, 1987) agreement was found in the valence band between pseudopotential and effective mass calculations. The Kronig-Penney model treats all states separately, and finds the zone-centre energies of ground states in a monolayer superlattice at the average of the bulk band edges (weighted by the layer thicknesses of a strained layer superlattice), which is the same for both heavy and light-hole states of an unstrained superlattice, but different for a strained superlattice. In the pseudopotential calculation the HH1 and LH1 at $\overline{\Gamma}$ of the $(CdTe)_1$-$(ZnTe)_1$ superlattice are closer together.

4.2.1.2 : N = 2 and N = 3.

The lowest $\overline{\Gamma}$ bandgap increases by 80 meV from $N$ = 1 to $N$ = 2. This increase parallels that found for the $(GaAs)_N$-$(AlAs)_N$ superlattices by self-consistent LDA calculations of 50 meV (Wei and Zunger, 1988) from N=1 to N=2. A self-consistent pseudopotential calculation finds a similar increase in $(GaAs)_N$-$(AlAs)_N$ superlattices, but the lowest states are strongly mixed bulk Γ and $X$-state (Gilbert and Gurman, 1987; 1989). Tight-binding methods show a monotonic decrease in bandgap with increasing N (Wu *et al.*, 1990) for II-VI strained layer superlattices. There is no previous calculation of the electronic states of the $(CdTe)_2$-$(ZnTe)_2$ superlattice in the literature, so no direct com-

parison can be made. The valence subband HH1 and LH1 energies at $\overline{\Gamma}$ are further apart for N=2 than for N=1, and both are lower in energy for N=2 than for N=1, contradicting the Kronig-Penney calculation. This brings the energy levels closer to that predicted by the Kronig-Penney calculation with increasing N.

#### 4.2.1.3 : N = 3 − 15.

For $(CdTe)_N$-$(ZnTe)_N$ superlattices with N=3-15, there is a monotonic decrease of bandgap with N. The difference between the energies found for the lowest conduction subband at $\overline{\Gamma}$ using the Kronig-Penney and pseudopotential calculations decreases with increasing N, to within the numerical error of the calculation for $N \geq 10$ (figure 4.4; see appendix A). The valence band energies of HH1 and LH1 are very close to the Kronig-Penney calculations for $N \geq 3$, except for the HH1 with $\Delta E_v = +0.060$ eV which agrees for $N \geq 10$ (figure 4.2).

There are subbands lower down in the valence band, within the energy range which has been studied, for N$\geq$ 6. For $\Delta E_V = +0.060$ eV the HH3 is close to the Kronig-Penney energies, but the HH2 is higher (figure 4.2). For this energy range the heavy-hole states are below the ZnTe heavy-hole edge, so the HH2 wavefunction will be similar to that of a HH1, but confined mainly in the ZnTe. Thus it interacts with the LH2, and is pushed up in energy. Conversely, the HH3 has a wavefunction similar to a confined HH2, in the ZnTe sublayers, and does not interact strongly with the LH2. The LH2 energy is above the Kronig-Penney calculated energy, due to the nonparabolicity of the ZnTe bulk light-hole band. With $\Delta E_V = +0.140$ eV, there is much less interaction between the LH2 and HH2, and both the HH2 and HH3 energies agree closely with the Kronig-Penney calculations for $3 \leq N \leq 15$ (figure 4.3).

### 4.2.1.4 : N = 16 − 30

Between $N = 16$ and $N = 25$ the LH2 crosses over the HH3, HH2 and HH1 subbands, according to the Kronig-Penney calculations (figures 4.2 and 4.3). The crossing of subband character also is found in the pseudopotential calculations. The question of whether the subbands cross or anticross will be considered in 4.2.2. Apart from near these crossings, over the range $N = 16$ to $N = 30$ there is close agreement between the energies calculated by the two methods near the bulk band edges, where light-hole bulk band nonparabolicity is not so important. With $\Delta E_V = +0.060$ eV, the LH2 for $N \geq 25$ is much closer in energy to the HH2 and HH3 than for $N \approx 12$, but there is little effect upon energy levels. For these values of $N$ the HH2 is in the heavy-hole well, so does not interact with the LH2. The HH3 is near the top of the well, so has a wavefunction similar to a mixture of HH3, localised in the CdTe sublayer, and HH2, localised in the ZnTe sublayer, so will have only a small interaction with the LH2, which is not enough to have a noticeable effect upon the energy level.

### 4.2.2 : Band Mixing and Wavefunctions.

In this section the bulk band composition of the superlattice zone-centre states near the HH1-LH1 crossing and HH1-LH2 anticrossing are examined, with two different valence-band offsets, $\Delta E_v = +0.060$ eV and +0.140 eV. The main aims are to compare the subband crossing and anticrossing, to test the calculation, and to examine the qualitative difference, if any, made by the change in valence-band offset.

With $\Delta E_v = +0.060$ eV, the heavy-hole wells are in the CdTe sublayers, the light-hole wells are in the ZnTe sublayers, whereas with $\Delta E_v = +0.140$ eV both heavy and light-hole wells are in the ZnTe. The bulk-band make-up of the H2 state (fig 4.5) is little affected by offset, except that the crossing is at a different N with each offset. The mixing, though small, is finite, even

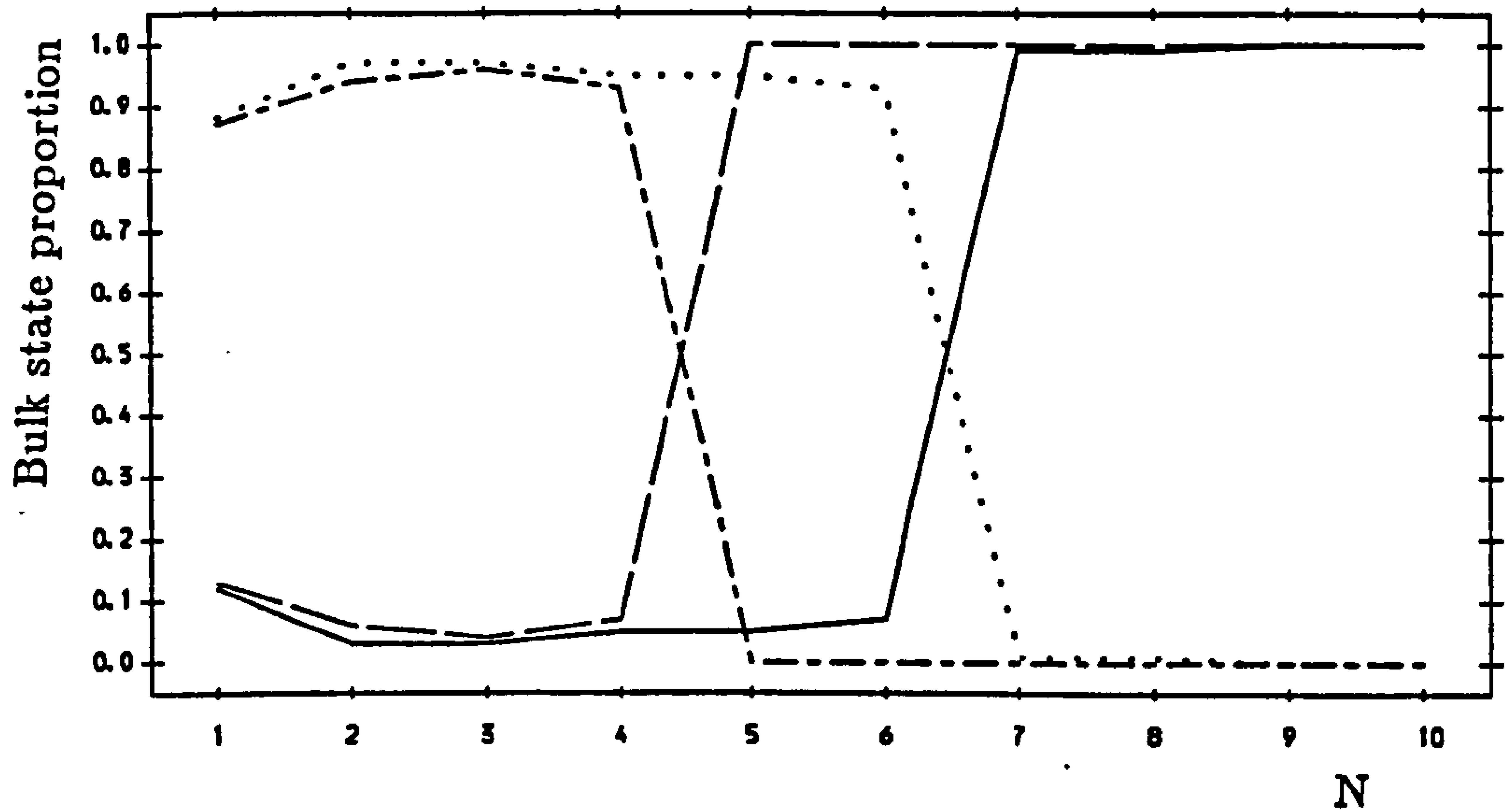


Figure 4.5. Coefficients squared of the bulk states which make up the second hole state of the $(CdTe)_N$-$(ZnTe)_N$ superlattice, matching at a plane through the centre of the Te interface layer; N varies from 1 to 10. Results are presented with two different valence band offsets, $\Delta E_V = +0.060$ eV and $+0.140$ eV. For the $+0.060$ eV offset, the bulk heavy hole state is shown by a full line, the bulk light hole state by a dotted line; for the $+0.140$ eV offset, the bulk heavy hole state is shown by a long-dashed line, the bulk light hole by a dot-dashed line.

though it is known from symmetry that the superlattice HH1 and LH1 states do not interact at $\overline{\Gamma}$. This does not in fact show a mixing of superlattice states - this is proved by calculations of interband matrix elements, which show no evidence of mixing (see 4.2.3) - but simply shows the coefficients squared of the bulk basis set used in this calculation. All these basis states are of the same symmetry, and so may mix in forming a superlattice state, but are of no special significance in themselves. Mixing appears in this calculation due to the nonparabolicity of the bulk bands – particularly of the ZnTe light-hole band, for which the states used in the calculations are more than 0.1 eV below the band edge – and as a result of the particular basis set used. A different basis set would show different combinations of different bands in the superlattice state, although the resultant superlattice state would be the same in any sufficiently detailed method, within the accuracy of the calculations. This shows the need for caution in the interpretation of graphs and tables of band mixing. A graph of composition is useful to show a trend, for example with layer width or as a function of an external perturbation, but for a quantitative study of a particular property it is necessary to perform further calculations.

The H3 state composition (fig 4.6) shows rapid change with N between N=15 and N=25. For N=15, the H3 state is the HH2, while for N=25 the H3 state is the HH1 state for both offsets. Interpretation of the graph of heavy and light-hole bulk coefficients squared again requires caution. The $\Delta E_v = +0.140$ eV data shows a sharp crossover between $N = 17$ and $N = 18$, very similar to that found for the LH1-HH1 crossover, reflecting the different symmetries of the HH2 and LH2. For N=19 to N=21, the LH2 and HH1 subbands anticross, and show strong mixing. The heavy-hole and light-hole are both in the same material, so there is a strong interaction between the wavefunctions. However, the crossing takes place over a narrower range of N than in unstrained superlattices, for example compared with the HH2-LH1 anticrossing in $(AlAs)_N$-$(GaAs)_N$ superlattices (Schulman and Chang, 1985), because the wells are of different depths and have different edges. For $N > 21$, the H3 state is the HH1. The data for

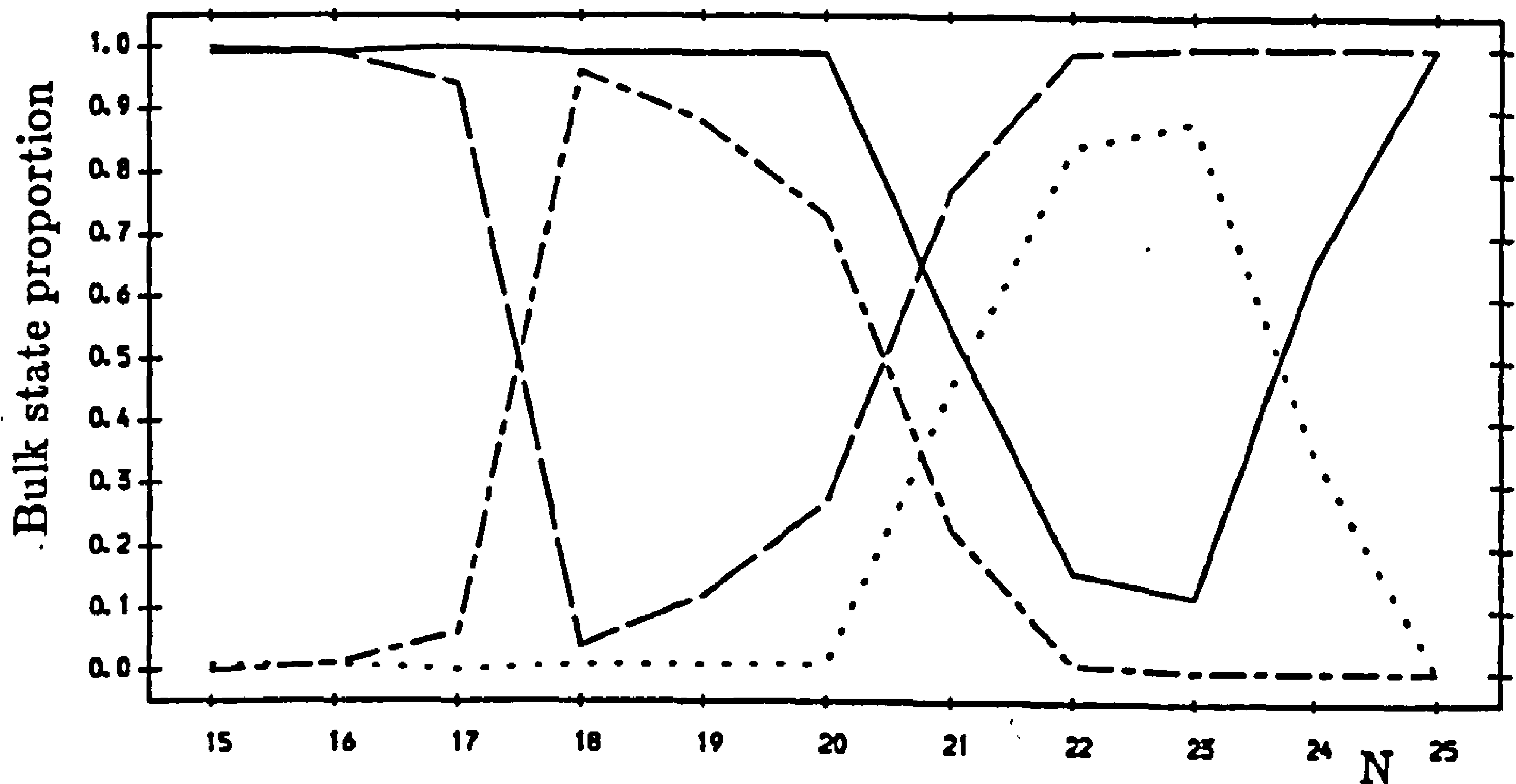


Figure 4.6. Coefficients squared of the bulk states which make up the third hole state of the $(CdTe)_N$-$(ZnTe)_N$ superlattice, matching at a plane through the centre of the Te interface layer; N varies from 15 to 25. Results are presented with two different valence band offsets, $\Delta E_V = +0.060$ eV and +0.140 eV. For the +0.060 eV offset, the bulk heavy hole state is shown by a full line, the bulk light hole state by a dotted line; for the +0.140 eV offset, the bulk heavy hole state is shown by a long-dashed line, the bulk light hole by a dot-dashed line.

$\Delta E_v = +0.060$ eV are less easily interpreted, since the H3 state is of mixed light and heavy-hole character between N=21 and N=24, reflecting two anticrossings, at N=21 and N=24; it is almost pure light-hole at N=22 and N=23. The charge density of the $(CdTe)_{21}$-$(ZnTe)_{21}$ H3 state, calculated with $\Delta E_v = +0.060$ eV, is plotted out in fig 4.7(a), along the superlattice axis and averaged over the plane of the layers. The $\Delta E_v = +0.060$ eV wavefunction (a) is LH2 mixed with (b) mainly HH3. Thus at N=21 the LH2 crosses the HH2, but due to the closeness in energy of the heavy-hole subbands is still close to the HH3, and there is a mixing. It is also mixed with the HH1 to a small extent, as shown by the lack of nodes in the heavy-hole plot (b). The reduction in heavy-hole character from N=21 to N=22, and from N=22 to N=23, shows the reduction in HH3 mixing, without much increase in HH1 mixing. For this offset the heavy-hole wells and light-hole wells are in different materials, so the LH2-HH1 interaction is weak. However, the HH3 is much less strongly bound in the CdTe sublayer than the HH1, so interacts with the LH2 quite strongly. For comparison of offsets, the H2 and H3 states are approximately equally separated in energy for the N=21 superlattice with $\Delta E_v = +0.140$ eV and the N=23 superlattice with $\Delta E_v = +0.060$ eV, but in the former case there is much greater mixing.

Figure (4.7) shows the extent to which wavefunctions of long period $(CdTe)_N$-$(ZnTe)_N$ superlattices are affected by the valence band offset, at certain layer widths. The probability density of the H3 wavefunction of the $(CdTe)_{21}$-$(ZnTe)_{21}$ superlattice with a valence band offset of $\Delta E_V = +0.14$ eV, averaged over the plane of the layer, is shown in figure 4.7 (c), and the heavy hole part of it is shown in figure 4.7 (d). The light hole part of the wavefunctions is very similar with both offsets, but the heavy hole part has changed dramatically. This is further evidence that the result of a calculation is particularly sensitive to the input parameters when the well depth is small. There is only a difference of 0.080 eV in valence band offset between the two calculations, approximately the uncertainty in this value, but the localisation and composition of the H3 state have changed greatly. These crossings and mixings—and the resultant optical

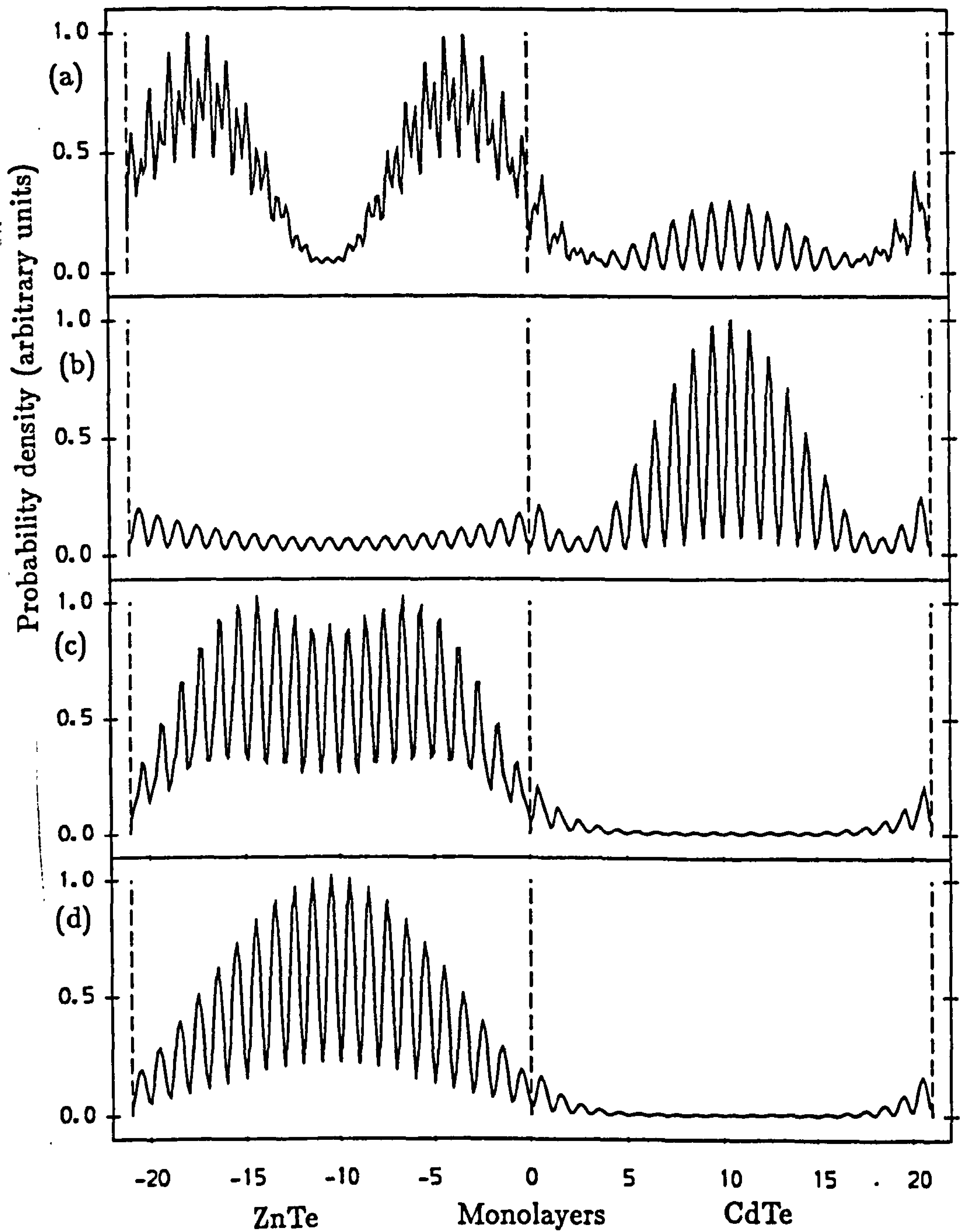


Figure 4.7. The probability density plot of the third hole wavefunction of the $(CdTe)_{21}$-$(ZnTe)_{21}$ near $\overline{\Gamma}$, averaged over the plane of the layer: (a) with $\Delta E_V = +0.060$ eV; (b) the heavy hole part of (a), showing the localisation in the CdTe sublayer; (c) with $\Delta E_V = +0.140$ eV; (d) the heavy hole part of (c), showing the localisation in the ZnTe sublayer.

properties—may be a sensitive test of the valence band offset.

A calculation has been performed of the HH1 wavefunctions of the $(CdTe)_{10}$-$(ZnTe)_{10}$ and $(CdTe)_{20}$-$(ZnTe)_{20}$ superlattices, with $\Delta E_v = +0.080$ eV (fig 4.8). With this offset the heavy-hole bulk edges are almost aligned in the two materials-there is a 4 meV well in the CdTe- so this allows a study of confinement in very small wells. The shorter period superlattice has strong interwell coupling, and the charge-density is distributed evenly across the CdTe layer. This is similar to the charge localisation found for short period InAs-GaSb superlattices (Gell *et al.*, 1986B), with a zero valence-band offset. The longer period superlattice has less interwell coupling, and so the probability density has a more confined appearance than that of the shorter. The results are quite different from the results of tight-binding calculations, in which interface states were found if the heavy-hole edges were aligned (Quiroga *et al.*, 1989).

### 4.2.3 : Matrix elements and comparison with experiment.

The interband momentum matrix elements squared for E1-H1 and E1-H2 for $\Delta E_v = +0.060$ eV, N=1-15, have been calculated (fig 4.9). The polarisation dependence shows that the H1 is HH1 for N=1-6, and LH1 for N=7-15, with no evidence of any mixing. The E1-LH1 matrix element decays with N, because it is spatially indirect, so the overlap is between tails of the wavefunctions, which decrease as a proportion of the total wavefunction as well width increases. Conversely the E1-HH1 matrix element is fairly constant with N because the transition is spatially direct. Note that the matrix elements at narrow widths are greater for sublayer widths of an even number of monolayers, or whole unit cells, than for odd monolayer widths. This is due to the different localisation of the valence and conduction bands in odd and even N superlattices.

Due to the poor quality of existing superlattices, it has not proved possible to measure the polarisation dependence of the optical spectra (Gil, 1990), and so all experiments in the literature have been made in (011)-polarisation. It is

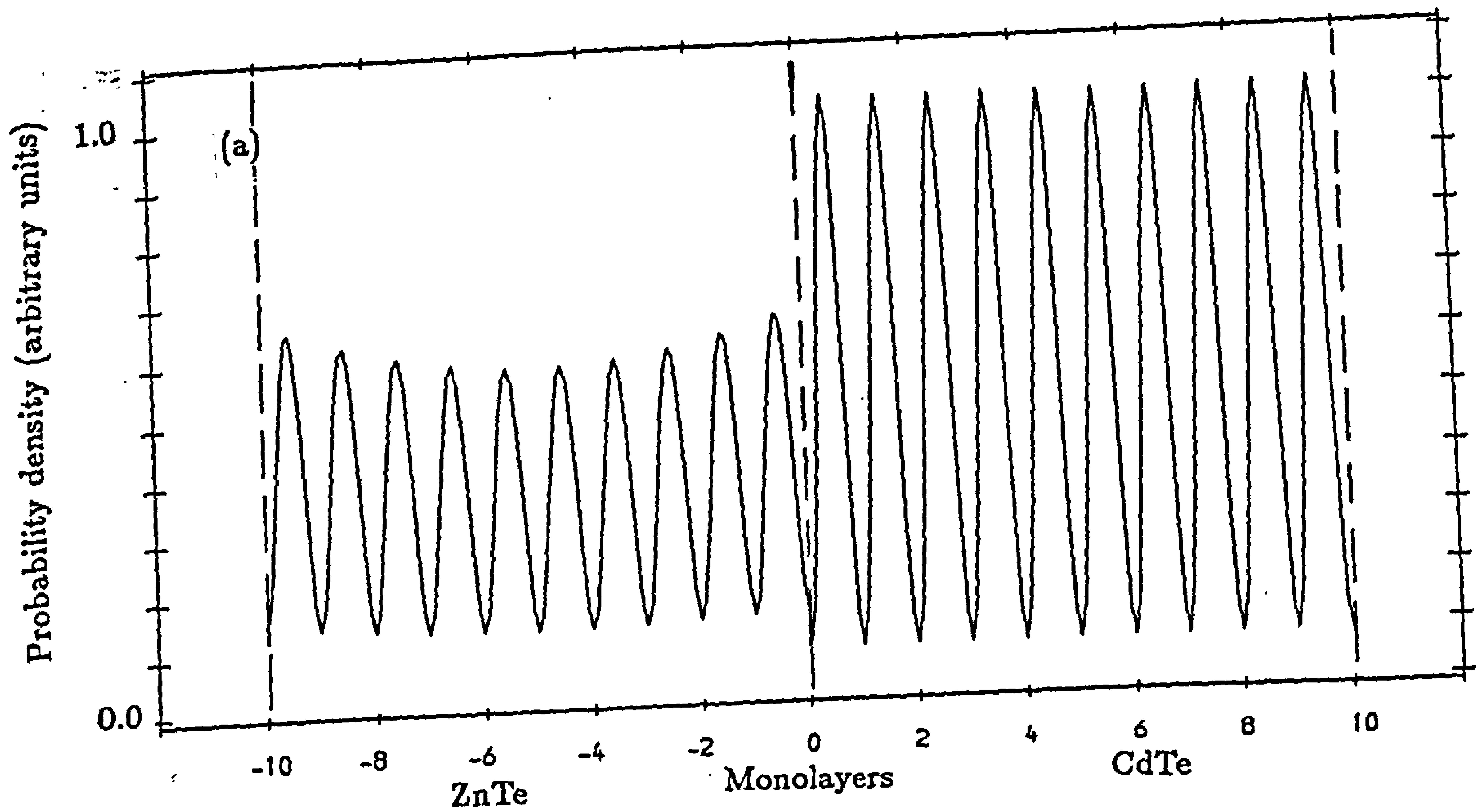


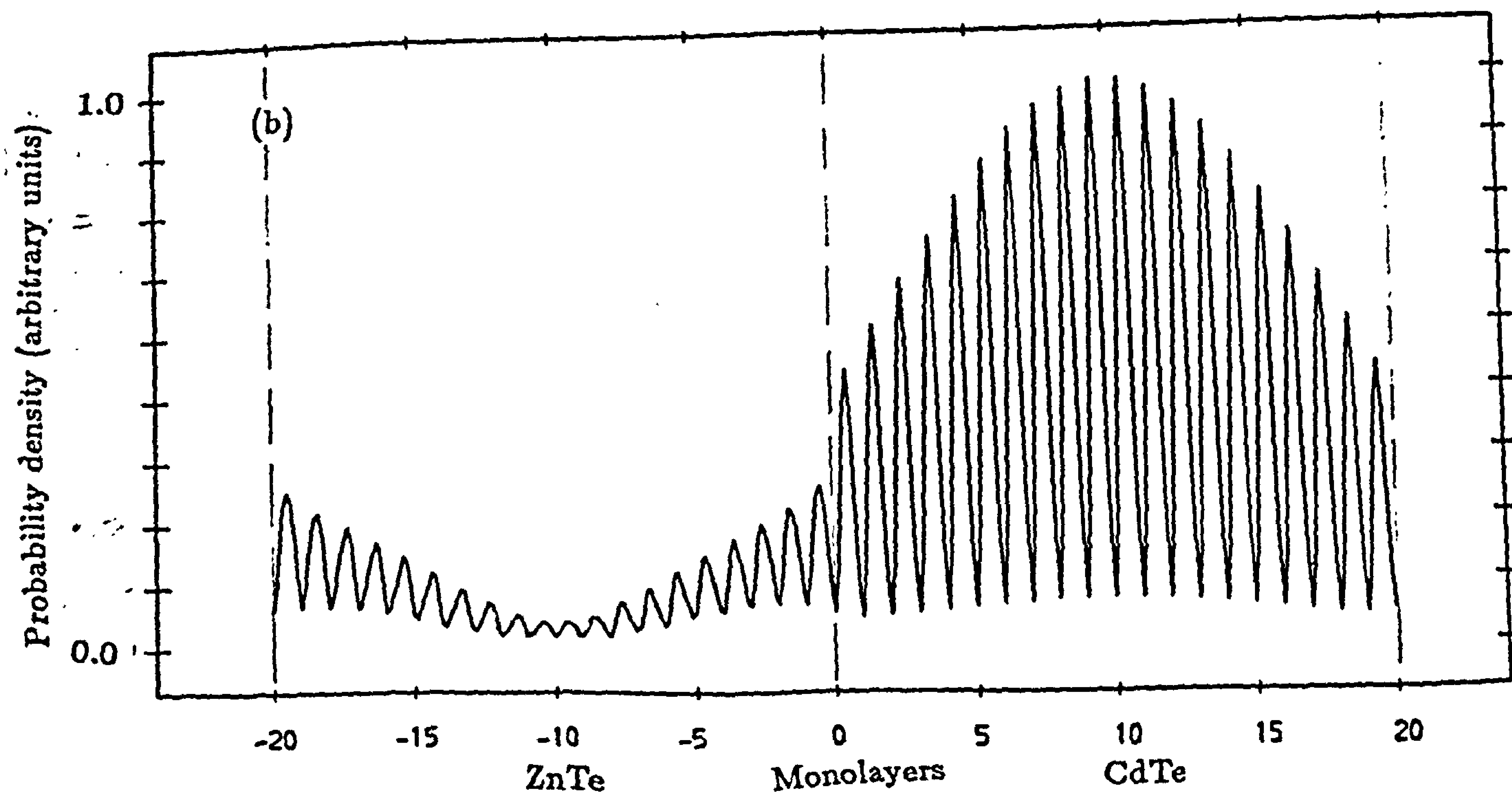


Figure 4.8. Probability density plots of the ground heavy hole (HH1) wavefunctions of the $(CdTe)_N$-$(ZnTe)_N$ superlattice, matching at a plane through the centre of the Te interface atomic plane, with $\Delta E_V = +0.080$ eV; (a) N=10, (b) N=20.

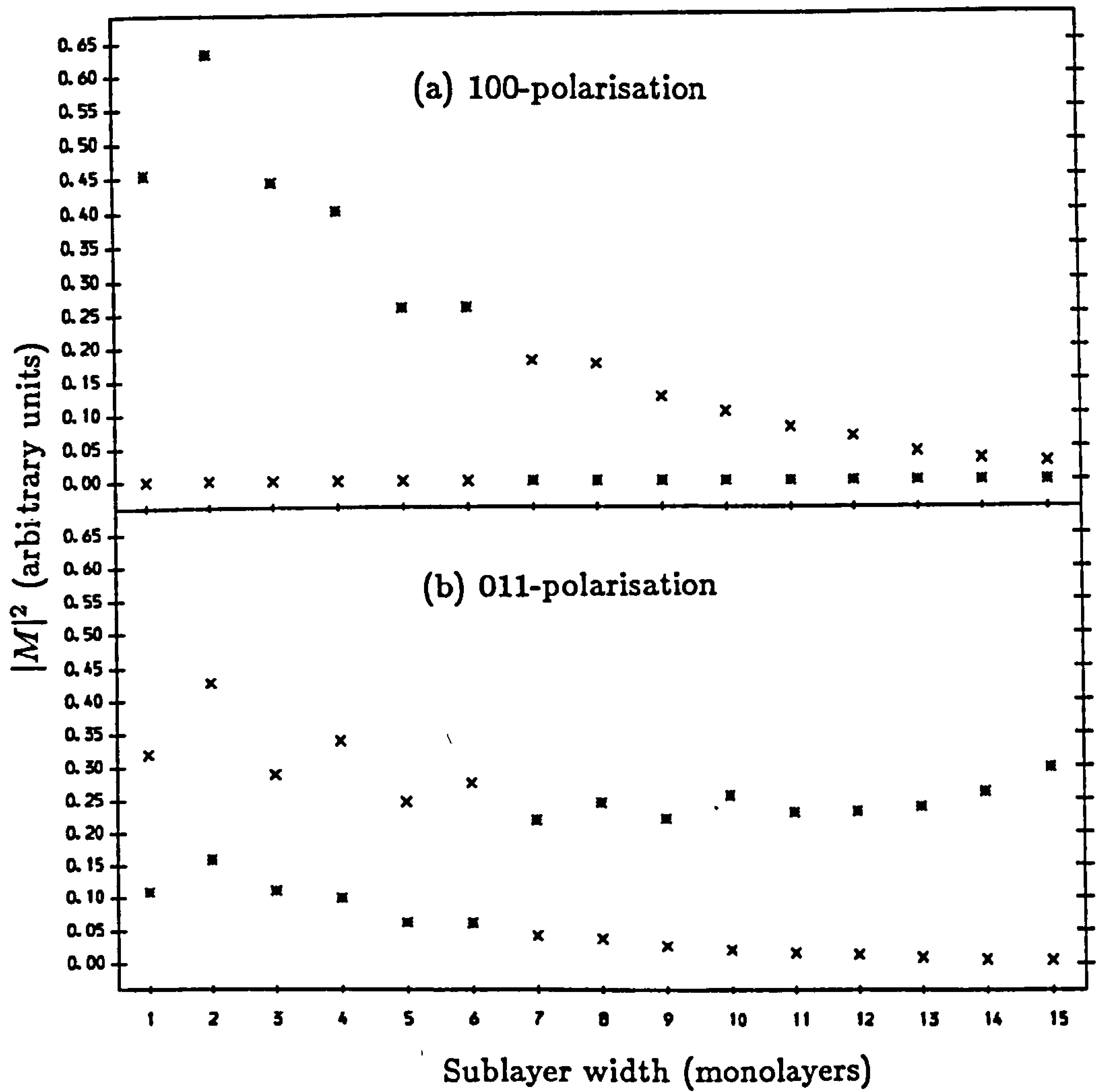


Figure 4.9. Interband matrix elements squared for the $(CdTe)_N$-$(ZnTe)_N$ superlattice matching at a plane through the centre of the Te interface atomic plane, with $\Delta E_v$ = +0.060 eV, N= 1 → 15; E1-H1 matrix elements marked by crosses, E1-H2 matrix elements by stars; in (a) 100-polarisation and (b) 011-polarisation.

known that the lowest energy transitions at 4K are E1-LH1 in $(CdTe)_7$-$(ZnTe)_6$ and $(CdTe)_8$-$(ZnTe)_{11}$ superlattices (Gil *et al.*, 1989). The absorption coefficient shows two closely spaced peaks for short period superlattices (Shtrikman and Finkman, 1989).

Comparison of experiment and theory is difficult, partly due to the variation in strain of the reported superlattices (which cannot be easily duplicated in the method used here), the uncertainty in layer widths, which are known to about 10 % accuracy (Shtrikman and Finkman, 1989), and that some experiments report photoluminescence bandgaps, while others report absorption bandgaps, but also because the pseudopotential bulk conduction band effective masses are too large, and so decrease the calculated bandgap. It has been found in attempts to compare experiment and theory for GaAlAs heterostructures that while absolute bandgaps may be difficult to match, the difference in energy of different transitions is a better guide, so this comparison will be made here.

The most straightforward comparison is for the N=6 superlattice, which has been measured in absorption (Shtrikman and Finkman, 1989). The calculated superlattice has the two transitions separated by 3 meV for $\Delta E_v = +0.060$ eV and by 14 meV for $\Delta E_v = +0.140$ eV, while the experimental superlattice had absorption peaks separated by $\approx$ 30 meV. The experimental HH1-LH1 splitting seems reasonably consistent with other experimental results, for example the $(CdTe)_7$-$(ZnTe)_6$ (Gil *et al.*, 1989), $(CdTe)_7$-$(ZnTe)_8$ (Mathieu *et al.*, 1988), and $(CdTe)_5$-$(ZnTe)_4$ (Shtrikman *et al.*, 1989; Shtrikman and Finkman, 1989) superlattices have HH1-LH1 splittings of $\approx 30 - 40$ meV. Attempts to compare experiment and theory using Kronig-Penney calculations (Mathieu *et al.*, 1990) have run into the same problem, that the HH1-LH1 splitting is consistently larger than calculated, by $\approx 10 - 40$ meV. The results seem to indicate that if a HH1-LH1 crossing does occur for a N-N superlattice, it must be at a narrower layer width than the N=4-7 found for the offsets used here. Calculations (Mathieu *et al.*, 1990) indicate that for a $(CdTe)_{N1}$-$(ZnTe)_{N2}$ superlattice, the HH1 and

LH1 will be degenerate for $N1 \times N2 \approx 30$. For $N1 \times N2$ greater than 30, the ground light hole is predicted to be higher than the ground heavy hole, while for $N1 \times N2$ less than 30 the ground heavy hole is predicted to be higher than the ground light hole. The point at which the crossover occurs differs depending upon the details of the calculation, but a crossover is predicted at some point in all calculations. There has been one reported superlattice of shorter period than this, with $N1 \times N2 = 20$ (Shtrikman *et al.*, 1989; Shtrikman and Finkman, 1989), but unfortunately there is no evidence as to the nature of the two peaks in the absorption.

There is still a discrepancy between experiment and theory for the CdTe-ZnTe superlattice, and further work is necessary to clear this up. The discrepancies cannot be explained simply by uncertainty in the valence band offset, and may be due to some combination of the poor quality of experimental superlattices and the uncertainty about the parameters used in calculations.

## 4.3 : Summary.

The electronic bandstructure, probability density plots of wavefunctions, and interband momentum matrix elements of $(CdTe)_N$-$(ZnTe)_N$ superlattices, with $N = 1$ to 30, have been calculated with a basis set of 130 plane waves for the bulk calculations, and using 20 bulk states in each region for the superlattice calculation, including spin. Two valence band offsets have been considered, $\Delta E_V = +0.06$ eV, for which the heavy-hole states are localised in the CdTe sublayers and the light-hole states in the ZnTe sublayers, and $\Delta E_V = +0.14$ eV, for which both the heavy- and light-hole states are localised in the ZnTe sublayers. The electron states are localised in the CdTe sublayers for both offsets. The valence band zone-centre energies show good agreement with calculations using the Kronig-Penney model, with effective masses and bulk band edges from the pseudopotential bulk bandstructure calculation, and there is little qualitative difference between the energy levels calculated using the two offsets. However, the localisation of the hole states is affected by the offset, and this would cause observable changes in the properties of the superlattices.

The E1-H1 and E1-H2 squared momentum matrix elements for $N = 1 - 15$ with $\Delta E_V = +0.06$ eV have been calculated. They show the expected polarisation dependence of the E1-HH1 and E1-LH1 matrix elements, and a crossover of hole character between $N = 6$ and 7, with no mixing. The E1-LH1 squared matrix element decays with well width because the transition is indirect in real space, so the overlap of electron and hole wavefunctions decreases with well width. Conversely, the E1-HH1 squared matrix element is fairly constant with well width because the electrons and heavy-holes are both confined in the CdTe sublayers.

A comparison with experimental absorption and photoluminescence results suggests that the smaller offset is qualitatively better than the larger, since it correctly predicts the localisation of the heavy- and light-holes, but that the predicted crossover of ground heavy- and light-holes as the layer width is altered

is not observed, although the nature of some of the peaks in the experimental absorption spectra has not been determined. The superlattice bandstructure is very sensitive to the strain parameters used in the calculations, because the large lattice mismatch causes a splitting at the top of the bulk valence bands of about the same size as the valence band offset, and it is expected that a better determination of the variation of some of the bulk levels with strain, together with a reassessment of the valence band offset, will bring experiment and theory into closer agreement. However, the main features of CdTe-ZnTe superlattices which are observed in experiment are explained by these calculations.

# CHAPTER FIVE

# INTERFACE MATCHING PLANES

## 5.1 : Introduction.

There is an ambiguity in the choice of interface plane for all matching methods, and particularly for those which include the atomic scale potential. The empirical pseudopotential complex bandstructure matching technique involves matching sums of the bulk states from adjacent sublayers over a plane. The position of this plane within the unit cell must be decided, and this is implemented mathematically as shown in chapter two.

In the first part of the chapter the physical basis behind the treatment of interfaces in different methods is considered, with the effect that this will have on the charge localisation and symmetry of superlattice wavefunctions. It is found that different systems are affected to varying extents by the choice of matching plane and treatment of interfaces, and the range of systems for which this choice will be important are considered. For the $Ga_{0.7}Al_{0.3}As$-GaAs-$Ga_{0.7}Al_{0.3}As$ quantum well (chapter two) varying the interface matching plane had little effect upon energy levels ($\leq 1$ meV), due to the deep wells in both the valence and conduction bands. The states near the bottom of the wells are little affected by changes at the interfaces because of the strong confinement,

but the charge density plots of the wavefunctions of the less well confined states higher up in the wells show some small asymmetry. The CdTe-ZnTe superlattice, considered in chapter four, has much shallower wells, particularly for the heavy-hole, and there is a greater difference between the atomic potentials in the different sublayers due to the high strain and ionicity, so atomic scale effects are expected to be more important. In order to look at the effect of the change of matching planes, a further set of calculations of the electronic states of $(CdTe)_N$-$(ZnTe)_N$ superlattices have been performed using interface matching planes at mid-bond positions. The results of these calculations are presented in section 5.4, and are compared with the results from chapter four, and with experiment.

## 5.2 : Interfaces and matching planes.

The potential affecting an electron in a heterostructure may be considered as the combination of an average electrostatic potential in each region with an atomic scale potential. Methods of electronic structure calculation differ over how much weight they give to each part. Most simple calculations emphasise the former, either by ignoring the atomic scale potential completely, or using a difference in effective mass in the matching conditions at the interfaces to account for the change in Bloch-functions between the sublayers. Simple methods which ignore the atomic scale potential have been very successful in calculating the properties of heterostructures with large valence and conduction band discontinuities, except when mixing between bands becomes important, for example $\Gamma - X$ mixing in the conduction band of GaAs-AlAs superlattices. However, when the well depth is very small or vanishes completely, any confinement is due to the atomic scale properties of the materials (Gell *et al.*, 1986B). Envelope function methods are still fairly successful at predicting energy levels in these cases, simply because the possible range of energy for confined states is small, but are less successful at calculating superlattice wavefunctions. The confinement of charge is strongly dependent upon the way in which the atomic scale potential is treated, and in particular how the interface between the two sublayers is treated. An additional complication is the charge transfer which occurs between the sublayers of a superlattice (Gilbert and Gurman, 1987), which affects a few monolayers on each side of the interface. However, the overall localisation of charge in wavefunctions in sublayers wider than a few monolayers, and the energy levels, intersubband matrix elements, and symmetry of states, can be predicted by non-self-consistent methods.

The effect on charge confinement near an interface between isovalent compound semiconductors may be modelled by considering the difference in polarity of bonds between the two constituent bulk materials. The possible interfaces between two materials of different ionicities, AB and CD, where A and C are the

cations and B and D the anions, are AD and BC. Using a simple definition of the polarity of a bond in an ionic semiconductor (Lambrecht and Segall, 1990), considering the probability that an electron in a polar bond is around one or the other atom, with $P_A+P_B=1$,

$$\alpha_{AB} = P_B - P_A.$$

$\alpha_{AB}$ is the polarity of bonds in the bulk of material AB, $P_B$ is the probability that the electron is around atom B, etc. For the bonds at the interfaces,

$$P_A + P_D = 1 - \frac{1}{2}(\alpha_{AB} - \alpha_{CD}), \text{ and}$$

$$P_C + P_B = 1 + \frac{1}{2}(\alpha_{AB} - \alpha_{CD}).$$

Unless the bonds in the two materials are of the same polarity, one of these will be greater than 1, the other will be less than 1. This indicates that, relative to the bulk of the layers, one with $\sum P > 1$ will be attractive and the other with $\sum P < 1$ will be repulsive to the valence band holes. The more attractive interface will be between the anion of the more ionic material and the cation of the less ionic material. The conduction band states are antibonding, so the opposite will be the case for electrons. Thus the wavefunction of hole states may show some asymmetry, although the exact extent of this will depend upon the system considered. In a real structure there will be a readjustment of charge at the interface, but some asymmetry may still result.

Relative to the bulk of a sublayer, any interface may be considered to be attractive or repulsive, and in an effective mass model this attraction or repulsion may be considered as a potential well or barrier. These interface potentials will be important if there is a lot of charge at the interface, or if the interface potential is large, so a combination of a deep well, thick sublayers and small interface potentials will make interface effects relatively unimportant, while for small well depths the interface potentials will be very important. In this case it

is possible that this model will predict bound states at isolated heterointerfaces. These are only found in the envelope function model when the effective mass inverts at an interface (see chapter six).

The extension to common ion heterostructures is straightforward. In the following discussion the bulk band edges are assumed to be aligned, i.e. there is a zero well depth. The interfaces may be either repulsive or attractive. If they are both repulsive they form a series of barriers, similar to those considered in the original Kronig-Penney model (Kronig and Penney, 1930), while if they are attractive there may be states bound at the interfaces, as found in tight-binding calculations of the electronic states of CdTe-ZnTe superlattices (Quiroga *et al.*, 1989). In a perfect heterostructure the interface ion cannot be ascribed to either of the two sublayers, and so the interfaces must be treated symmetrically, but in a real heterostructure systematic asymmetry can occur as a result of growth conditions. The model based upon bulk bond polarities can be extended by treating the common ion at the interface as an average of the bulk ions of that kind in the two sublayer materials. However, this does not apply to matching methods, which have a sharp interface at some point. The interface atoms may be treated as being both in one or the other layer, which would be expected to produce either wells or barriers at both interfaces, but this would change the thickness of the layers and introduce an arbitrary choice, so this approach has not been considered here. The matching planes may be taken either at the centre of the common ionic layer, in which case all bonds are bulk bonds and no asymmetry is expected, or at bond centre to model growth asymmetry. Thus, interface states at both interfaces are not expected to be found using methods in which the sublayers and interfaces are treated entirely in terms of bulk properties, but are possible if separate parameter sets are used for the interfaces.

In detailed non self-consistent electronic structure calculations, which take into account the atomic scale potential, the different ways in which the interfaces are treated may correspond to attractive or repulsive potentials. The problem

takes different forms depending upon the method which is used. Tight binding methods (Schulman and Chang, 1985; Quiroga *et al.*, 1989) need a set of atomic energy levels and interatomic matrix elements for each bulk material, plus additional sets for the interfaces, which introduces an extra choice into the calculation. Returning to the effective mass model set out above, some of these choices may correspond to attractive potentials at the interfaces, others to repulsive potentials, others to a zero potential. For example, in a tight-binding calculation of the electronic states of CdTe-ZnTe superlattices (Quiroga *et al.*, 1989) the energy levels of the Te atoms at the interfaces are taken to be the averages of those for the Te-ions in bulk CdTe and ZnTe, but the matrix elements between this ion and the Zn and Cd ions adjacent to it are taken to be the same as in the bulk materials. However, the bonds between the interface plane have changed from the bulk, so the matrix elements should also change somewhat.

The pseudopotential supercell method (Gell *et al.*, 1986A; Xia, 1989) does not involve the choice of an interface plane, and the common ion layer at the interface in a common ion superlattice can be treated as an average of the ion in the bulk material making up each sublayer, since a term is put into the calculation for each atomic layer. However, the way in which this is implemented may introduce an interface attractive or repulsive potential, as for the tight-binding method. Pseudopotential matching methods (Brand and Hughes, 1987) treat the superlattice as two blocks of bulk material joined at a plane parallel to the growth axis. The only degree of freedom is in the placing of the interface plane. If the atomic scale potential is included, as in the method of Brand and co-workers, the position of the matching plane relative to the interface atoms is important. If there is no common atom between the two sublayers, as in the GaSb-InAs superlattice, the matching plane may be either at or near bond centre (Flores *et al.*, 1978), producing one interface of a GaAs-type, one of a InSb-type. If there is a common atom between the layers, for example Zn in a ZnTe-ZnSe superlattice or As in a GaAs-AlAs superlattice, the choice is more difficult. Previous calculations have taken the interface to be at mid-bond

(Brand and Hughes, 1987; Hughes, 1989). Due to the difference in ionicity of the two materials this may produce some asymmetry in the wavefunctions. Alternatively, to treat the two interfaces symmetrically, both common interface ions may be taken to be part of the same layer. This changes the widths of the layers, so is not reasonable if there is an offset, though may be if there is not. Finally, the interface may be taken through the centre of the common ion plane. One problem with this approach is connected with the validity of matching pseudowavefunctions rather than real wavefunctions at the interfaces. Away from the atoms, these are approximately the same, but near the atoms they are not. However, the atomic cores only form a small part of the interface, so should not affect the states too strongly. In the special case of a common anion or cation superlattice, the core wavefunctions are the same on both sides of the interface, and so should match up without affecting other states.

5.3 : Symmetry of superlattice electronic states.

Consider a superlattice with a common ion between the sublayers, with a period of M monolayers of one semiconductor AB and N monolayers of another semiconductor AD, i.e. $(AB)_M$-$(AD)_N$. An A plane between a B and a D plane is an interface plane between an AB region and an AD region, i.e.

AB........ABADA......ADABA........BA,

and the interfaces are symmetrical about the centre of a layer. In a superlattice of this kind, the states at superlattice zone centre, $\overline{\Gamma}$, will be of either odd or even parity. A superlattice $(AB)_M$-$(CD)_N$ with no common ion between the layers has symmetry which depends upon the arrangement of ionic planes at the interfaces. If the two interfaces pair the same sets of ions, i.e.

AB......ABCD........DCBA.......BA

or AB......BADC......CDAB......BA,

then the superlattice Brillouin-zone centre states will have either odd or even parity, but if the two interfaces pair different sets of ions, i.e.

AB.........ABCD........CDAB........BA,

then the states at superlattice zone centre will not have a definite parity. In the envelope function approximation, the superlattice states are considered to be made up from products of bulk Brillouin zone centre light hole and heavy hole states, which are respectively of odd and even parity, with envelope functions of odd or even parity. Thus, if the superlattice Brillouin zone centre states have a definite parity, they will be made up from products of envelope function states with bulk Bloch functions, which all have the same parity. This determines which

states can mix, in the way described in chapter two, to make up superlattice Brillouin zone centre states. In particular, the ground heavy hole (HH1) is of even parity, while the ground light hole (LH1) is of odd parity, so the ground states cannot mix at the superlattice Brillouin-zone centre, but the first excited light-hole (LH2) is of even parity, so can mix with the ground heavy-hole, as is found for the CdTe-ZnTe superlattice (chapter four). If the superlattice zone centre states do not have a definite parity then this restriction upon which states may mix is removed, and for example the HH1 and LH1 may mix.

Returning to consider the superlattice calculation, the symmetry of states in superlattices with no common ion is clear, but that for superlattices with a common ion depends upon the way in which the interfaces are treated. If the matching plane is taken to be at the centre of the common ion interface plane, the full symmetry of the superlattice is preserved, but if the matching plane is taken to be at mid bond then the two interfaces are treated asymmetrically and some of the symmetry of the superlattice states is lost. The seriousness of this will depend upon the case, for example in GaAs-AlAs superlattices the main valence band mixing and anticrossing is between the HH2 and LH1 states (Chang and Schulman, 1985), which are both of the same parity and so may mix at the superlattice Brillouin zone centre, and so the treatment of the interfaces is not so important. Another case, the $(CdTe)_N$-$(ZnTe)_N$ superlattice, in which the HH1 and LH1 states are predicted by Kronig-Penney calculations to cross over as N is varied (Mathieu *et al.*, 1990), and for which the treatment of the interfaces is expected to be important, is considered in this chapter.

## 5.4 : Results with bond – centre matching.

### 5.4.1 : Introduction.

A second set of pseudopotential calculations have been performed of the electronic energy levels of the $(CdTe)_N$-$(ZnTe)_N$ superlattice, with N between 1 and 30. Apart from the change of interface matching plane, these calculations have been performed in the same way as those in chapter four. The interface matching plane has been taken to be at mid-bond, so that one interface is between a Zn ionic layer from the ZnTe and a Te ionic layer from the CdTe, the other is between a Cd ionic layer from the CdTe and a Te ionic layer from the ZnTe. The superlattice is considered in this calculation to have a lower symmetry than in the calculations presented in chapter four, and so all superlattice zone-centre states are of the same symmetry and may mix. This converts crossings into anticrossings, for example the LH1 and HH1 were found to have no interaction at zone-centre in the calculations presented in chapter four, but in this set of calculations can mix and so anticross as N is varied.

### 5.4.2 : Energy levels.

Calculations have been performed of valence band states with $\Delta E_V = 0$ (figure 5.1), $\Delta E_V = +0.06$ eV (figure 5.2) and $\Delta E_V = +0.14$ eV (figure 5.3), and of the lowest conduction band states with $\Delta E_V = +0.06$ eV (figure 5.4). The lowest conduction-subband energy level with $\Delta E_v = +0.060$ eV (figure 5.4) of the $(CdTe)_1$-$(ZnTe)_1$ superlattice at $\overline{\Gamma}$ is 60 meV below the average of the CdTe and ZnTe conduction-band edges, less than found in chapter four (figure 4.4). The HH1-LH1 splitting of the $(CdTe)_1$-$(ZnTe)_1$ at $\overline{\Gamma}$ is almost independent of valence band offset: 59 meV with $\Delta E_v = 0$ (fig. 5.1), 61 meV with $\Delta E_v = +0.06$ eV (fig. 5.2) and 57 meV with $\Delta E_v = +0.14$ eV (fig. 5.3), while the Kronig-Penney calculation predicts splittings of 23 meV, 21 meV, and 27

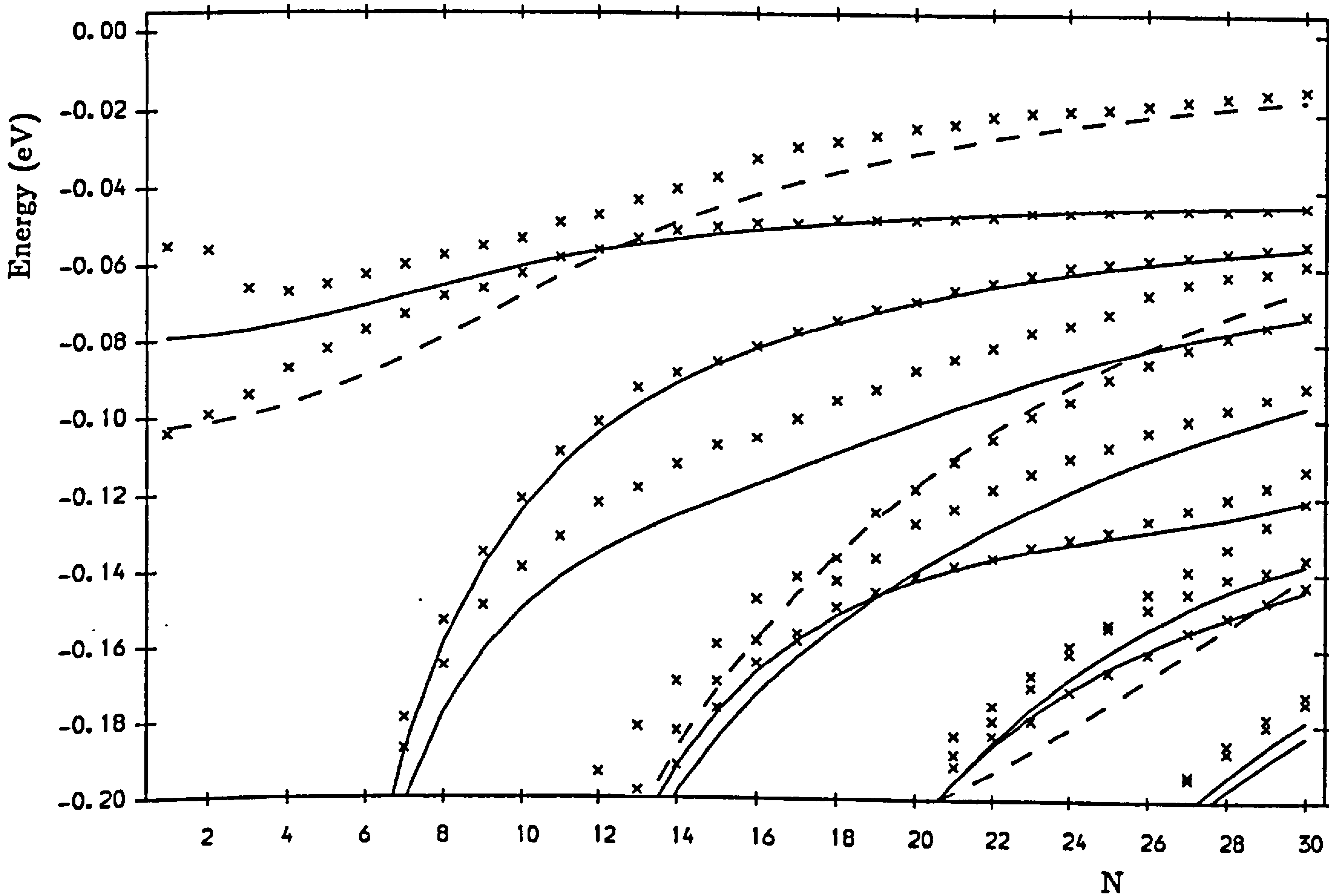


Figure 5.1. Valence band energy levels at $\overline{\Gamma}$ of the $(CdTe)_N$-$(ZnTe)_N$ superlattice with zero valence band offset, matching at a plane through the centre of a bond. N is between 1 and 30. Kronig-Penney results are marked by a full line for heavy-holes and a broken line for light-holes. Pseudopotential results are marked by crosses.

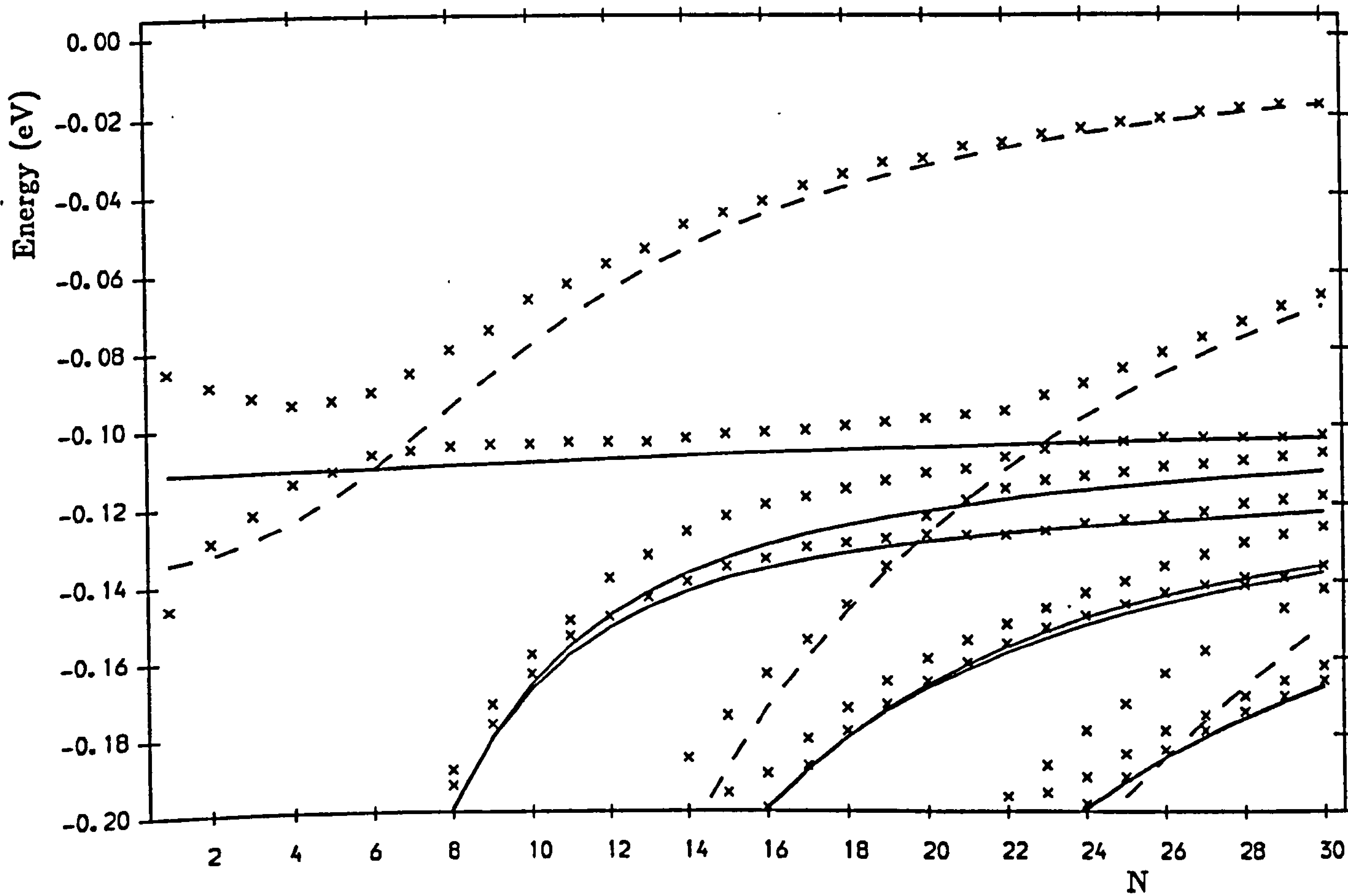


Figure 5.2. Valence band energy levels at $\overline{\Gamma}$ of the $(CdTe)_N$-$(ZnTe)_N$ superlattice with 0.06 eV valence band offset, matching at a plane through the centre of a bond. N is between 1 and 30. Kronig-Penney results are marked by a full line for heavy-holes and a broken line for light-holes. Pseudopotential results are marked by crosses.

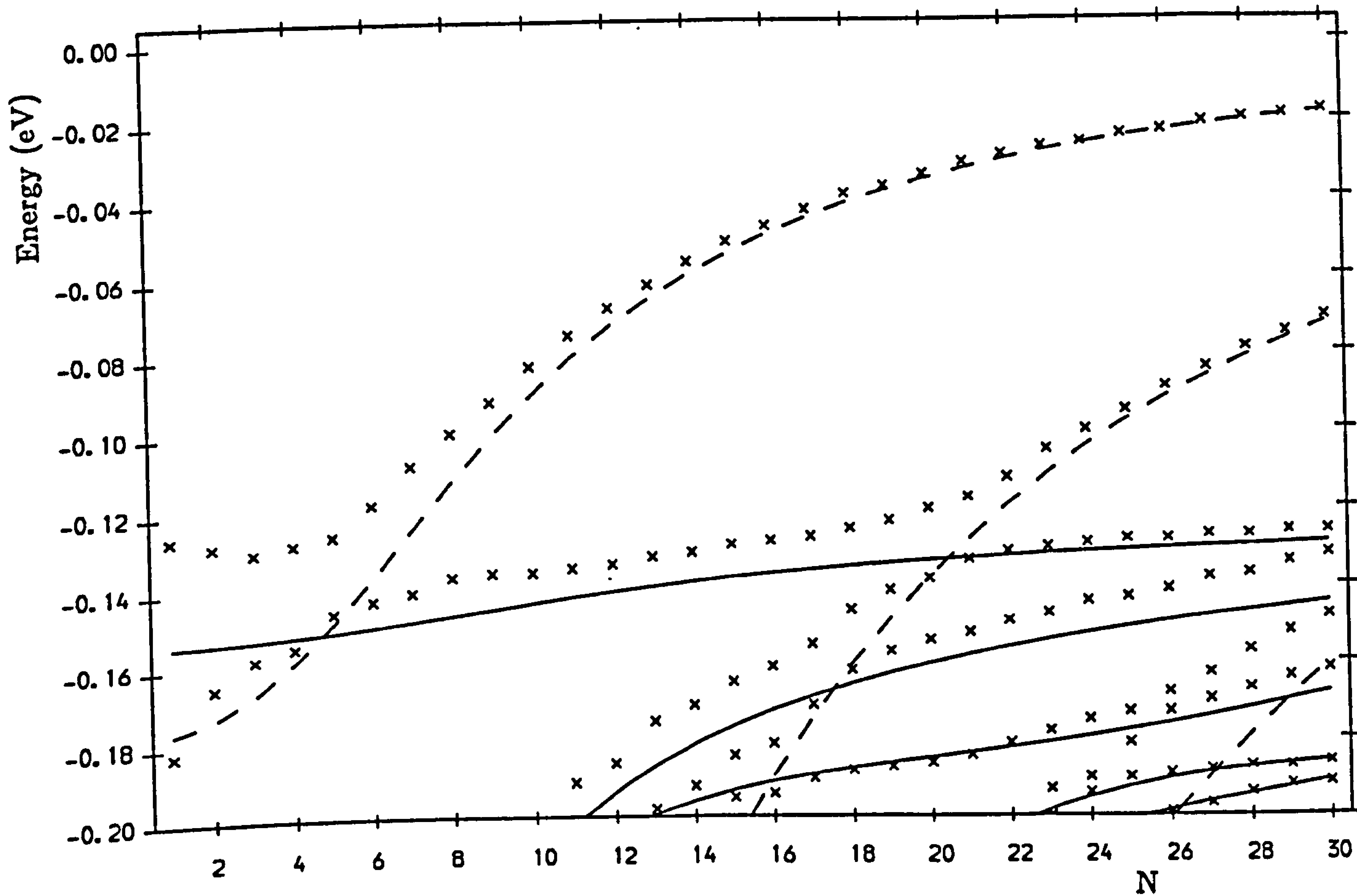


Figure 5.3. Valence band energy levels at $\overline{\Gamma}$ of the $(CdTe)_N$-$(ZnTe)_N$ superlattice with 0.14 eV valence band offset, matching at a plane through the centre of a bond. N is between 1 and 30. Kronig-Penney results are marked by a full line for heavy-holes and a broken line for light-holes. Pseudopotential results are marked by crosses.

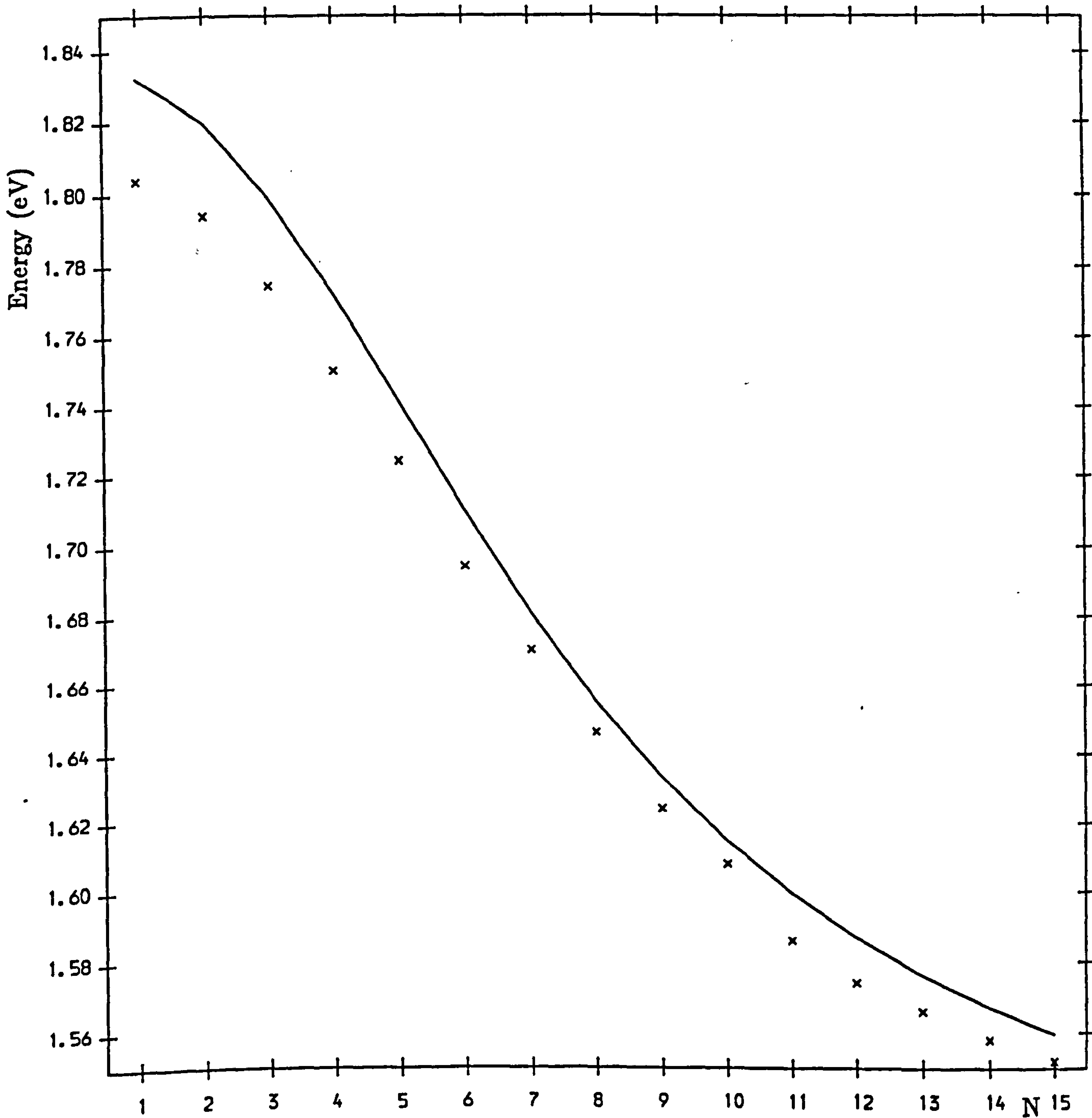


Figure 5.4 : Energy levels of the lowest conduction band subband at $\overline{\Gamma}$ of the $(CdTe)_N$-$(ZnTe)_N$ superlattice with $\Delta E_V = +0.060$ eV, matching at a plane through the centre of a bond; N varies between 1 and 15. Kronig-Penney results are marked by a full line; pseudopotential results are marked by crosses.

meV respectively. The HH1 state with $\Delta E_v = +0.060$ eV is above the CdTe bulk heavy-hole edge, and so is composed of evanescent states in both sublayers. Due to the lack of experimental results upon highly strained monolayer superlattices it is impossible to say whether the HH1 and LH1 edges are nearly degenerate, as found in chapter four, or split as found here. The lowest conduction-subband $\overline{\Gamma}$ energy with $\Delta E_v = +0.060$ eV (figure 5.4) shows a monotonic decrease for increasing N. A similar trend was found using a pseudopotential supercell method for $\overline{\Gamma}$ states related to bulk $\Gamma$-states in $(AlAs)_N$-$(GaAs)_N$ superlattices (Gell *et al.*, 1986A), and for strained II-VI superlattices using the tight-binding method (Wu *et al.*, 1990). However, this is different to the trend found in LDA calculations of $(AlAs)_N$-$(GaAs)_N$ short-period superlattices (Wei and Zunger, 1988), for which the $\overline{\Gamma}$ bandgap was found to increase between $N = 1$ and $N = 2$. At wider layer widths the E1 $\overline{\Gamma}$ energy decreases with N, and tends to the Kronig-Penney result. For $N \geq 6$ the pseudopotential and Kronig-Penney calculations agree (figure 5.4), to within the numerical error of the calculation (see appendix A).

For N=1-3, the HH1 and LH1 states at $\overline{\Gamma}$ are closer together at increasing N with all three offsets, but for $N > 3$ there are significant differences between the results with the different offsets. The calculation with $\Delta E_v = 0$ (figure 5.1) shows the least difference from the Kronig-Penney calculations. The heavy-hole is in an 84 meV deep well in the CdTe, and the light-hole in a 193 meV deep well in the ZnTe. The depth of the potential wells means that the asymmetry has a fairly small effect upon the energies of the states, which decreases the discrepancy from Kronig-Penney calculated energies of each state considered independently. The separate confinement of the heavy and light holes causes the overlap of the ground states to be small, which means that the interaction between them, and the consequent difference from the Kronig-Penney results, are small. The HH1 and LH1 are close together in energy over a wide range of N, and have a smallest splitting of 9 meV for $N \approx 11 - 12$. For N$\geq$ 20 the HH1 and LH1 energies agree very well with Kronig-Penney calculations. For

this offset the LH2 does not cross the HH1 for N$\leq$ 30, but there is a strong interaction between the HH3 and LH2, which forces the HH3 up in energy. This is much as found with symmetric interfaces. The HH2 is, however, very close to Kronig-Penney calculations for all N.

With $\Delta E_v = +0.060$ eV (figure 5.2), the heavy hole well is only 24 meV deep in the CdTe, so the HH1 and LH1 interact more strongly than with $\Delta E_v = 0$. The heavy hole well depth has reduced so the effect of the atomic asymmetry at the interfaces is increased, and the HH1 wavefunction is less strongly confined in the CdTe so the LH1 and HH1 wavefunctions have a larger overlap. At the anticrossing, N=6, the HH1 and LH1 are split by 16 meV, so the HH1-LH1 interaction has approximately doubled in strength compared with the calculation performed with zero valence band offset. At wider widths, $N \approx 6-18$, the HH1 is above the Kronig-Penney calculated energies by about 5 meV, partly due to interactions with the LH2. At $N = 20-24$, the HH1 and LH2 states anticross, then at $N \geq 25$, the HH1 state is very close to the calculated Kronig-Penney energy, indicating that the interface effects have little effect by themselves on energy levels, and that the changes from the results of chapter four are mainly due to band mixing (compare figures 4.2 and 5.2).

With $\Delta E_v = +0.140$ eV (figure 5.3), the difference between the Kronig-Penney and pseudopotential calculations is similar to that found with $\Delta E_v = +0.060$ eV (figure 5.2). The heavy hole well is deeper, 56 meV, but the light hole and heavy hole wells are both in the ZnTe, so the overlap between the LH1 and HH1 is large. The smallest HH1-LH1 splitting is 20 meV at $N = 5$. The HH1 energy for $N \approx 5-15$ is above the calculated Kronig-Penney energy by about 5 meV, as with $\Delta E_V = +0.06$ eV.

### 5.4.3 : Wavefunctions.

The H1 and H2 states anticross (figures 5.1-5.3), rather than cross, if the matching plane is taken to be at mid bond. In figure 5.5 are shown the charge

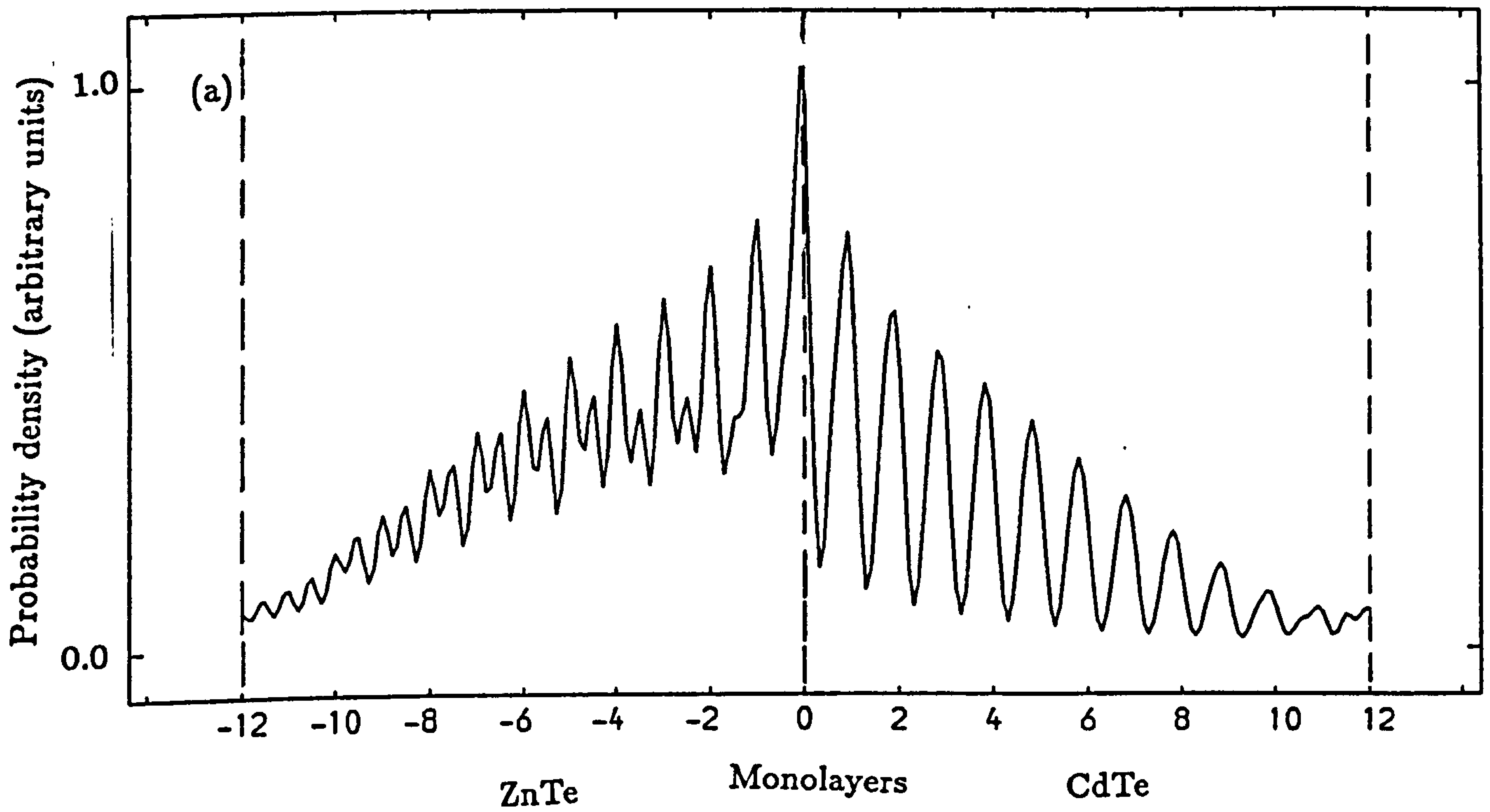


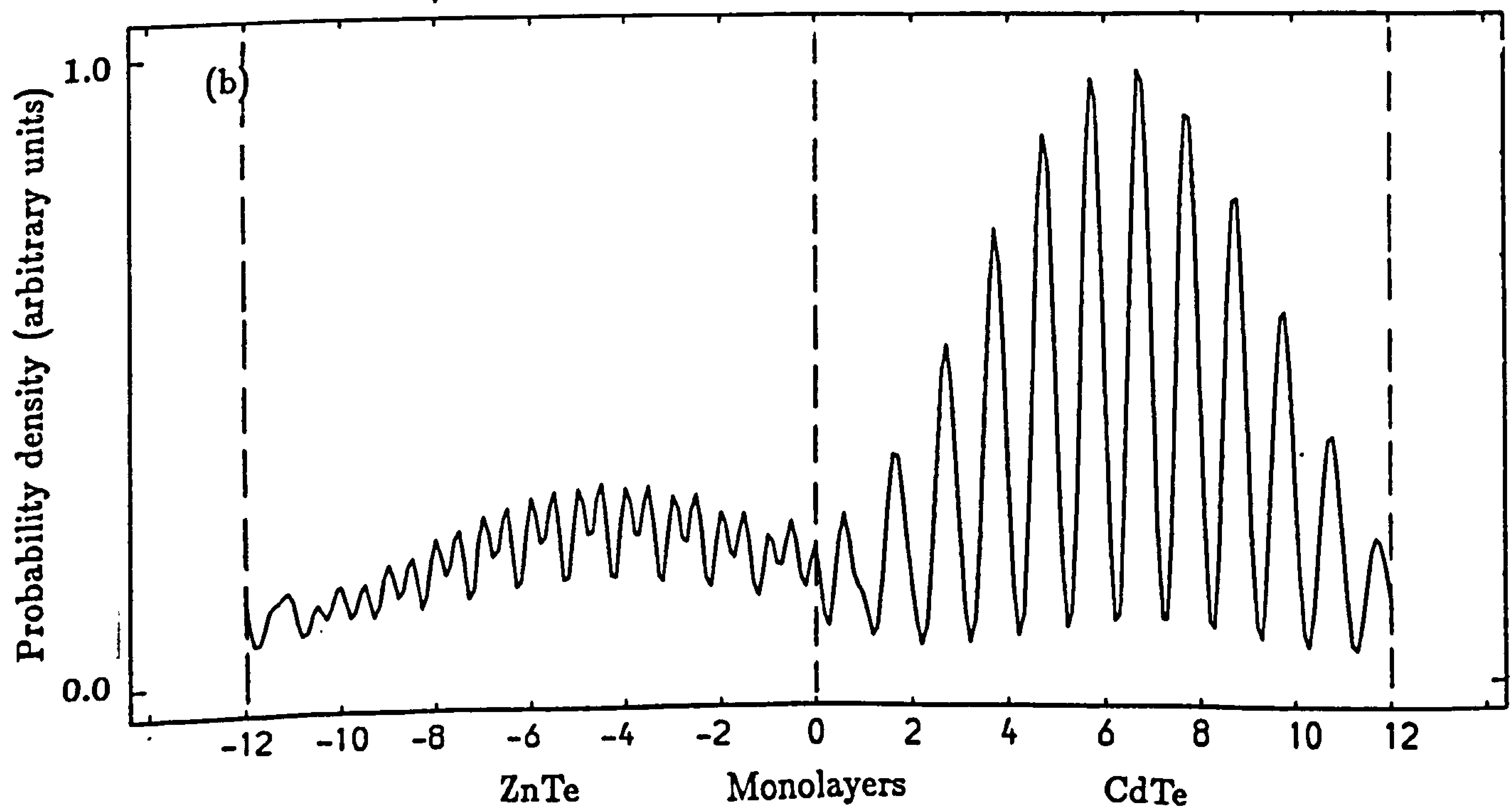


Figure 5.5. Probability density plots, averaged over the plane of the layer, of the wavefunctions of the $(CdTe)_{12}$-$(ZnTe)_{12}$ superlattice, with zero valence band offset, matching at bond centre; (a) H1 wavefunction, (b) H2 wavefunction.

density of the (a) H1 and (b) H2 states of the $(CdTe)_{12}$-$(ZnTe)_{12}$ superlattice with $\Delta E_v = 0$, plotted along the superlattice growth axis, averaged over the plane of the layers. The energies of these states are $-0.047$ eV and $-0.056$ eV, respectively. Both are of mixed heavy and light hole character, but the charge localisation is very different in the two cases. In figure 5.6 the bulk (a) heavy and (b) light hole contributions to the H1 state are shown. Both are asymmetrical towards the same interface, and the combination of two asymmetrical contributions leads to a total charge density which is strongly peaked at one interface. The peak is at the interface between a Zn ionic plane from the ZnTe and a Te ionic plane from the CdTe. This would be expected from the analysis given in section 5.2, since CdTe is more ionic than ZnTe. The heavy and light hole parts of the H2 state are shown in figure 5.6 (c) and (d) respectively. The light-holes 5.6(b) and (d) are very similar to each other, but the heavy-holes 5.6 (a) and (c) differ considerably. The difference in charge localisation between the H1 and H2 states is thus due to changes in the heavy-hole wavefunction with energy. This change is due to the relative asymmetry of the heavy-hole well at different depths. A state near the ZnTe heavy-hole edge is under a less asymmetric potential than one with an energy near the CdTe edge. Other wavefunctions with different values of N and $\Delta E_v$ show similar behaviour, with some having strong asymmetry, particularly HH1 wavefunctions near the band edge. However, most wavefunctions have a probability density plot close to that found with the matching plane at the plane through the Te-ion centre.

### 5.4.4 : Matrix Element calculations.

The E1-H1 and E1-H2 interband squared momentum matrix elements have been calculated for $N = 1-15$, with $\Delta E_v = +0.060$ eV (figure 5.7). The matrix elements show an anticrossing between $N = 5$ and $N = 7$, which is clearest for (100)-polarisation (figure 5.7 (a)) since the E1-HH1 matrix element is zero in

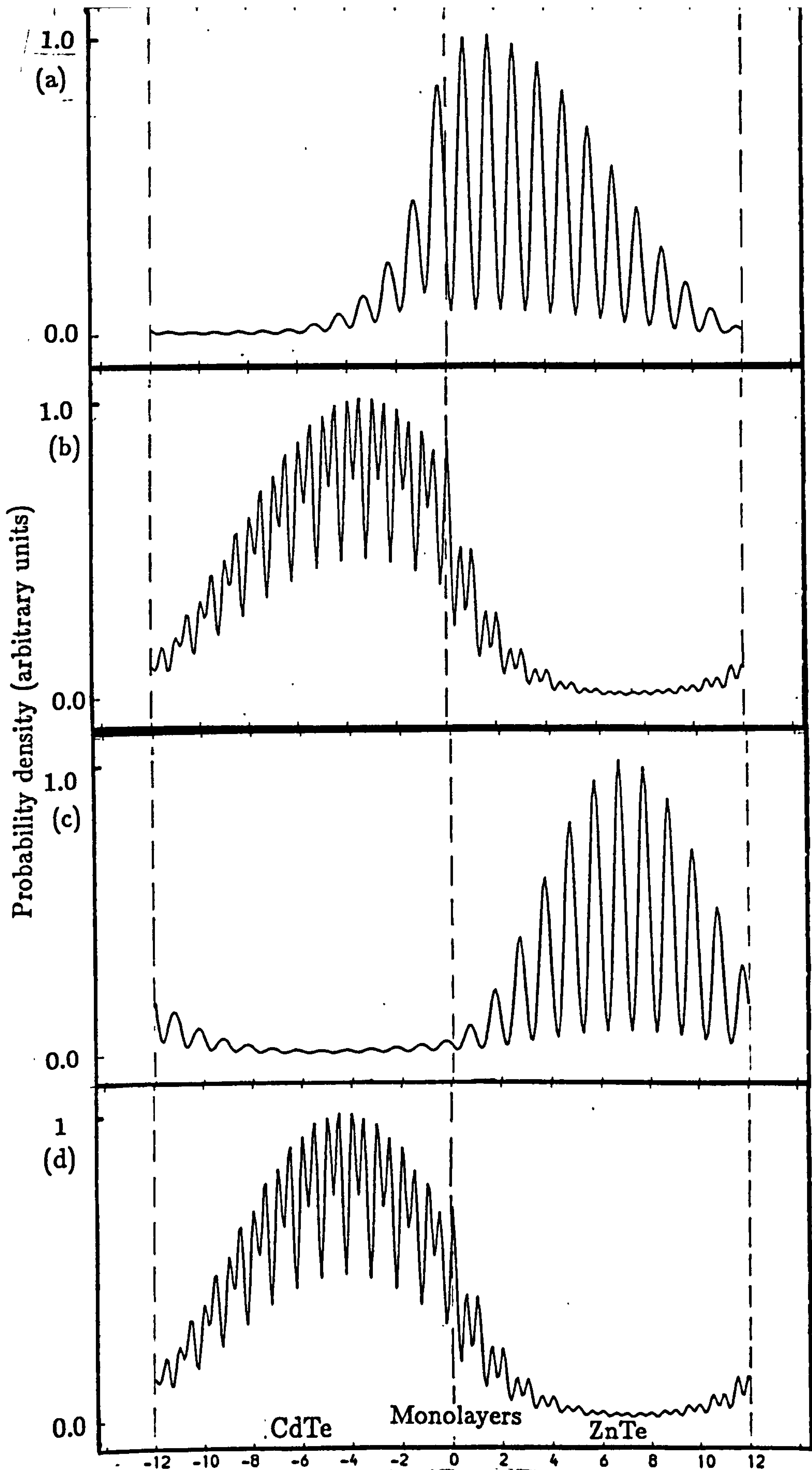


Figure 5.6. The bulk heavy and light hole contributions to the H1 and H2 wavefunctions of the $(CdTe)_{12}$-$(ZnTe)_{12}$ superlattice, with zero valence band offset, matching at bond centre. The graphs show the probability density squared averaged over the plane of the layers of the wavefunctions, with the coefficients for all the bulk states apart from the ones considered set to zero: (a) heavy hole contribution to the H1; (b) light hole contribution to the H1; (c) heavy hole contribution to the H2; (d) light-hole contribution to the H2.

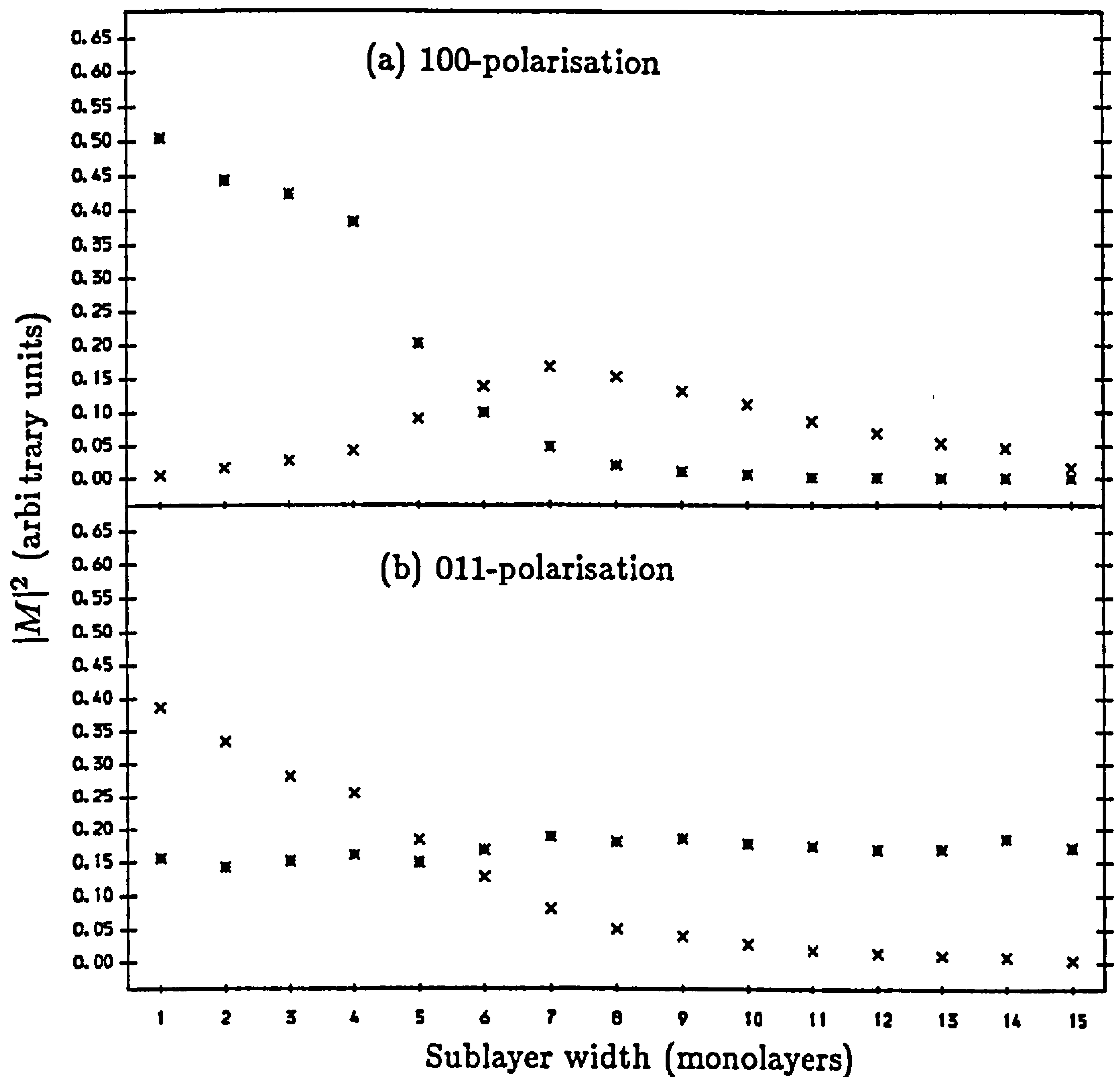


Figure 5.7 : Interband matrix elements squared for the $(CdTe)_N$-$(ZnTe)_N$ superlattice matching at an interface plane through a bond centre, with $\Delta E_v = +0.060$ eV, N= $1 \rightarrow 15$; E1-H1 matrix elements marked by crosses, E1-H2 matrix elements by stars; in (a) 100-polarisation and (b) 011-polarisation.

this polarisation. This mixing would show up clearly in polarisation dependent optical measurements, but unfortunately all experiments so far performed on CdTe-ZnTe heterostructures have been for light travelling perpendicular to the layers in (011)-polarisation. Comparison with calculations performed with the matching plane at the centre of the common Te-plane (figure 4.9) show two differences, the evidence of mixing in the matrix elements, and that the alternation of magnitude of $|M|^2$ for N odd or even is not observed in figure 5.7. The two calculations give very similar results for $N > 10$.

Comparison with experiment, by comparing the difference in energy of the $E1 - H1$ and $E1 - H2$ gaps for the $N = 6$ superlattice, gives slightly closer agreement than was found in chapter four. The experimental splitting is $\approx 30$ meV (Shtrikman and Finkman, 1989) while the calculated splittings are 17 meV, 16 meV and 26 meV for offsets 0.0, +0.06 and +0.14 eV respectively.

## 5.5 : Discussion.

The calculation of electronic states by the complex bandstructure matching method requires that the position of the interface between the sublayers be specified. In this chapter the effect of the change of interface matching plane upon the calculations is discussed, and a simple model for understanding the results based upon bulk bond polarities is presented. The symmetry of the resulting superlattice states is affected by the choice of matching plane, and some choices may allow interactions between states which with other matching planes would not interact. It is found that this change of symmetry is the main effect of the use of different matching planes. Calculations have been performed on the $(CdTe)_N$-$(ZnTe)_N$ superlattice with the interface matching plane at mid-bond, and are compared with the results of chapter four with the interface matching plane through the centre of the common Te ionic plane. Some differences are found, particularly at the crossing between the ground heavy- and light-hole states. When the matching planes were taken at the centre of the Te planes (chapter four) no mixing is found, and the bands cross as the sublayer width is varied, but when the matching planes are taken at mid-bond the two states mix and anticross as the sublayer width is varied. Differences are also found for very short period superlattices, particularly monolayer superlattices. In other regions both calculations produce results which are very similar for energy levels and interband momentum matrix elements.

The choice of interface matching plane in the complex bandstructure matching technique is important, although for many cases there is little difference between the results of calculations performed using different matching planes. For common ion superlattices, calculations performed with a matching plane through the centre of the common ion plane, as used in chapter four for calculations on $(CdTe)_N$-$(ZnTe)_N$ superlattices and in chapter six for calculations on $(HgTe)_{3N}$-$(ZnTe)_N$ superlattices, produce superlattice states of the correct symmetry, and so this is the best choice for future calculations using this method.

# CHAPTER SIX

# THE HGTE-ZNTE SUPERLATTICE

## 6.1 : Introduction and background.

### 6.1.1 : Introduction.

Semiconductor materials with a bandgap in the infrared, particularly materials which absorb in the atmospheric infrared windows at 3-5 $\mu$m (0.40 – 0.25 eV) and 8-14 $\mu$m (0.16 – 0.09 eV) are important for many technological applications. The second atmospheric window is of interest for communications, and covers the maximum of room temperature thermal radiation, so is a useful wavelength for measuring temperature gradients in the environment or in medical applications. A number of semiconductor materials have been considered for use at these wavelengths, but the most important technologically are those based upon alloys of HgTe with CdTe, which were first investigated in 1959 for the development of 10 $\mu m$ infrared detectors, and by the early 1970s were in use in commercial photodetectors (Dornhaus and Nimtz, 1983). It was suggested in 1979 that rather than alloying HgTe and CdTe, they could be formed into a superlattice (Schulman and McGill, 1979; 1980), and it was shown that these superlattices could be expected to span the two atmospheric infrared windows.

Both $Hg_{1-x}Cd_xTe$ alloys and HgTe-CdTe superlattices suffer from fundamental structural problems due to the weakness of the Hg-Te bond, which causes clustering of Hg atoms in the alloy, and interdiffusion between the layers in superlattices (Simon *et al.*, 1990). As a possible alternative material to $Hg_{1-x}Cd_xTe$, $Hg_{1-y}Zn_yTe$ alloys have been suggested and grown over the full composition range (Kashyap *et al.*, 1990; Marbeuf *et al.*, 1989). However, HgTe and ZnTe tend to segregate, which has caused difficulties with growth. A way around this problem is to form the HgTe and ZnTe into a superlattice (Faurie *et al.*, 1986). It has been shown that the interdiffusion coefficient between HgTe and ZnTe is one order of magnitude lower than that between HgTe and CdTe (Mullins *et al*, 1990). The HgTe-ZnTe superlattice is expected to have the same potential as an infrared detector as HgTe-CdTe superlattices, with the added potential of using the 6 % lattice mismatch to tailor properties of the superlattice. The first growth, by MBE, and study of properties of HgTe-ZnTe superlattices was in 1985 (Faurie *et al.*, 1986), and they have also been grown by MOVPE (Mullins *et al.*, 1990).

6.1.2 : Strain effects.

The sublayers of the superlattice are strained due to the lattice mismatch between bulk HgTe and ZnTe. In this chapter calculations have been performed of the properties of freestanding $(HgTe)_{3N}$-$(ZnTe)_N$ superlattices, in which the HgTe layers are under 2 % biaxial compressive strain and the ZnTe layers under 3.8 % biaxial tensile strain. This ratio of layer widths was chosen so as to study superlattices which have wide enough HgTe layers that there is a crossover between the highest hole subband and the lowest conduction subband, with at the same time narrow enough ZnTe barrier layers that there is significant dispersion of the conduction subband. For this strain the critical thicknesses are predicted to be about 300 Å HgTe and 100 Å ZnTe, using CdTe parameters (Miles *et al*, 1987), with the Matthews and Blakeslee model (Matthews and

Blakeslee, 1974). The critical thicknesses using ZnTe are within 7% of those for CdTe, while HgTe strain parameters are within experimental error (±10%) of those for CdTe, (Dornhaus and Nimtz, 1983, p122). The same curves may be used for all three materials, considering the accuracy of such calculations. These superlattices should be within the critical thickness for $N \leq 20$. Recent measurements of CdTe and ZnTe critical thicknesses (Cibert *et al.*, 1991) give critical thicknesses of about 25 monolayers for 2 % strain, as for the HgTe sublayers, and 10 monolayers for 3.8 % strain, as for the ZnTe sublayers. In the superlattice geometry these critical thicknesses may increase by a factor of about two (Houghton, 1990; Miles and McGill, 1989), suggesting that the superlattices would be within the critical thickness for $N \leq 16$.

The effect of biaxial strain on the bandstructure of zincblende semiconductors can be split into two parts, a hydrostatic strain and a uniaxial strain (O'Reilly, 1989). The hydrostatic strain alters the splitting between various levels, most importantly between the $\Gamma_6$ and $\Gamma_8$ levels, but does not change the symmetry of the crystal. The uniaxial strain reduces the symmetry of the semiconductor, the most important effect of which (for present purposes) is to remove the double degeneracy of the $\Gamma_8$ levels, splitting them into a $\Gamma_6$ and a $\Gamma_7$ level. For biaxial compression the $\Gamma_6$ level moves up, the $\Gamma_7$ level moves down, and vice-versa for biaxial tension. In a type-I or II superlattice the valence band subbands come from the bulk $\Gamma_8$-levels (or the $\Gamma_6^V$ and $\Gamma_7^V$ levels in a strained-layer superlattice), the conduction subbands from the $\Gamma_6^C$-level (where the superscripts V and C are used to distinguish between valence and conduction band bulk states of the same symmetry). The hydrostatic part of the strain only alters the bandgap, while the uniaxial part both alters the gap, and changes the ordering of the valence-band subbands. However, in a type-III superlattice both the conduction and valence subbands are related to the $\Gamma_8$ levels, so the hydrostatic part of the strain will have little effect upon the superlattice bandgap, while the uniaxial part changes the bandgap significantly,

and shifts the interface states associated with type-III superlattices either up or down relative to the heavy-hole states. Thus the strain alters the properties of a type-III superlattice by a different mechanism to that which is important in a type-I or type-II superlattice. The change in HgTe bulk $\Gamma_6 - \Gamma_8$ gap will change the bulk conduction band effective mass, which changes the superlattice bandgap.

### 6.1.3 : Valence band offset.

The valence band offset between the two materials comprising a superlattice is a very important factor in determining the properties of the superlattice. The HgTe/ZnTe offset has not yet been precisely determined. In all that follows $\Delta E_v(\text{HgTe/ZnTe}) = E_{\Gamma_8}(\text{HgTe}) - E_{\Gamma_8}(\text{ZnTe})$, unstrained. There are three sets of data in the literature to consider. First, the offset has been determined by experiment to be 0.250 $\pm 0.050$ eV in the (111)-direction (Duc *et al.*, 1987), 0.356 $\pm 0.050$ eV in the (100)-direction (Hsu and Faurie, 1988), and 0.170 eV (Marbeuf *et al.*, 1989), orientation independent. Second, calculations give values of 0.260 eV (Wei and Zunger, 1987), 0.337 eV (Van de Walle *et al.*, 1988), and $0.539 \pm 0.020$ eV (Bertho *et al.*, 1990). Third, there has been more work done on the HgTe/CdTe and ZnTe/CdTe offsets than on the HgTe/ZnTe offset; the last of these may be inferred from knowledge of the first two. The HgTe/CdTe offset has been shown to be large, $\geq 0.300$ eV (Johnson *et al.*, 1988), rather than the earlier value obtained from magneto-optical experiments of 0.040 eV (Berroir *et al.*, 1986), contradicting the common anion rule that the offset should be small (McCaldin *et al.*, 1976). The current consensus value is 0.350 eV (Meyer *et al.*, 1990). The ZnTe/CdTe valence band offset is thought to be about $0.075 - 0.100$ eV (see chapter 4). Assuming transitivity to hold, i.e. $\Delta E_v(A/C) = \Delta E_v(A/B) + \Delta E_v(B/C)$, then $\Delta E_v(\text{HgTe/ZnTe})$ may be inferred to lie between about 0.200 eV and 0.300 eV.

Considering all three sets of information, direct experiment, theory and in-

ference from better studied systems, the offset $\Delta E_v$(HgTe/ZnTe) is expected to be between +0.150 and +0.550 eV. There are a number of factors causing this large uncertainty. XPS measurements (Duc *et al.*, 1987; Hsu and Faurie, 1988) measure the difference in energy between core levels in a substrate and in a thin overlayer. The valence band offset is calculated on the assumption that the splitting between core levels and valence levels is unaffected by strain. This assumption is not reliable (Grant *et al.*, 1990), so these measurements can only be seen as an order of magnitude estimate of the offset. Other measurements (Marbeuf *et al.*, 1989) measure the change in relative energy of valence and core levels in HgZnTe alloys, but assume that the relative position of core levels is unaffected by alloying and strain, so again there is a large uncertainty in the value they propose. It has been shown (Wei and Zunger, 1987) that the influence of d-states upon the valence band offset between II-VI semiconductors is considerable, but other calculations do not take these into account (Van de Walle *et al.*, 1988; Bertho *et al.*, 1990). However, Wei and Zunger have themselves been criticised (Bertho *et al.*, 1990) for ignoring the effects of strain. The ZnTe/CdTe and HgTe/CdTe offsets have at least been shown through comparison between experiment and theory to be within certain regions (Gil *et al.*, 1989; Johnson *et al.*, 1988), so are probably more reliable. The most consistent sets of predictions for all three offsets are those of Duc *et al.* (1987), who find values of 0.35, 0.07 and 0.25 eV for the HgTe/CdTe, ZnTe/CdTe and HgTe/ZnTe valence band offsets, and of Wei and Zunger (1987) who calculate, for the same three offsets, 0.39, 0.13 and 0.26 eV. The calculations presented in this chapter have been performed using $\Delta E_v$(HgTe/ZnTe) = 0.250 eV. Taking a different value of offset, within the range discussed, would not change the nature of the states, e.g. by changing the localisation of superlattice states, but would make quantitative changes to calculated bandgaps and interband matrix elements.

As discussed in chapter four, for the ZnTe/CdTe valence-band offset, it is necessary to know the proportion of the change in the direct bandgap ($\Gamma_6 - \Gamma_8$)

of a semiconductor due to hydrostatic pressure which affects the valence and conduction bands. For ZnTe, the proportion $dE_V/dP = 0.33dE_g/dP$ is used, as in chapter four. For HgTe the value used is $dE_V/dP = 0.67dE_g/dP$, using the ratio of the deformation potentials $a_V = 3.8$ eV (Takita and Landwehr, 1981) and $a_C = -1.9$ eV (Wu and McGill, 1985). The effect of any inaccuracy in this ratio would be to shift the bandstructures relative to one another by up to about 50 meV, which is much less than the uncertainty in the offset itself. The energy levels are shown schematically in figure 6.1, to show the relative movement of the different energy levels due to the offset, and the hydrostatic and uniaxial parts of the strain.

The resulting critical point energies, taking account of strain and valence band offset, are given in table 6.1. The bulk bandstructures of both materials are shown in figure 6.2, along [100], with the offset used in the calculations.

| Critical Point | HgTe | ZnTe |
|---|---|---|
| $\Gamma_6$ | -0.045 | 2.283 |
| $\Gamma_{HH}$ | 0.269 | -0.036 |
| $\Gamma_7$ | 0.153 | 0.147 |

Table 6.1. Bulk critical points of bandstructure used in calculations. $\Gamma_6$ refers to the conduction band in ZnTe and the light-hole band in HgTe, while $\Gamma_7$ refers to the light-hole band in ZnTe and the conduction band in HgTe. $\Gamma_{HH}$ is the heavy-hole band-edge, of $\Gamma_6$ symmetry, in both materials.

Energy (eV)

0.3
0.2
0.1
0.0
-0.1

(a) (b) (c)

$\Gamma_8$ 0.0
$\Gamma_8$ 0.25
$\Gamma_6$ -0.06
$\Gamma_8$ 0.06
$\Gamma_8$ 0.21
$\Gamma_6$ -0.05
$\Gamma_7$ 0.147
HH -0.04
HH 0.27
$\Gamma_7$ 0.153
$\Gamma_6$ -0.05

ZnTe HgTe ZnTe HgTe ZnTe HgTe

Figure 6.1. Critical point energy levels of unstrained and strained HgTe and ZnTe. (a) The energy levels in unstrained HgTe and ZnTe, with the valence band top of ZnTe as the zero of energy, and with a valence band offset of $\Delta E_V$ (HgTe/ZnTe) = +0.250 eV. (b) The shifted energy levels due to the hydrostatic part of the strain in the $(HgTe)_{3N}$-$(ZnTe)_N$ superlattice. (c) The bulk energy levels, with biaxial strain.

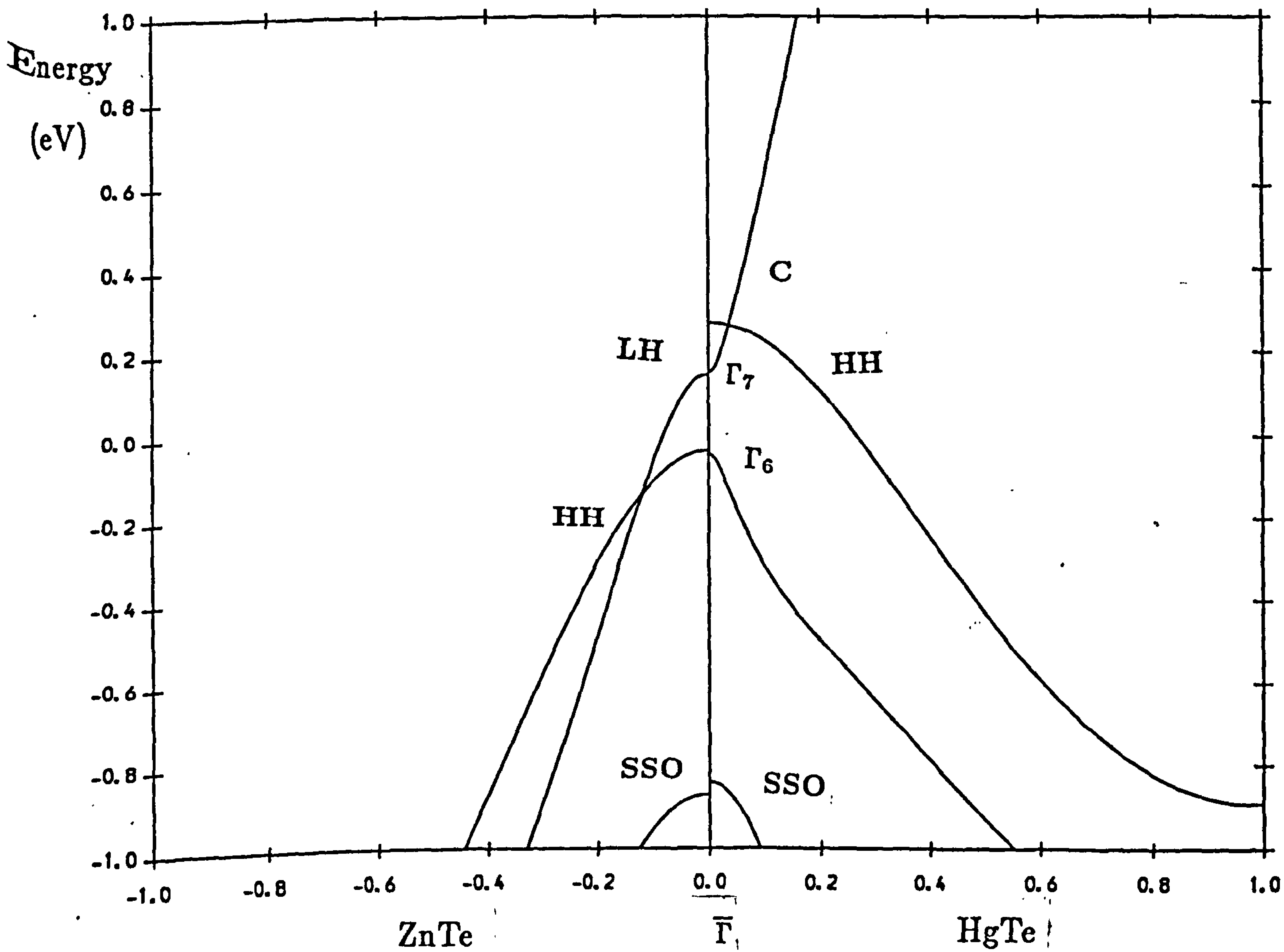


Figure 6.2. Bulk strained bandstructures of HgTe and ZnTe along [100] between $E =$ -1.0 eV and 1.0 eV, with $\Delta E_V$ (HgTe/ZnTe) = 0.25.

## 6.2 : Superlattice Electronic Structure.

Calculations have been carried out with a basis set of 130 plane waves for the bulk calculation, and using 20 bulk states in each region, with spin. The interface matching plane is through the centre of the common Te-ionic plane.

### 6.2.1 : Energy levels.

The $\overline{\Gamma}$ and $\overline{X}$ critical point energy levels of the $(HgTe)_{3N}$-$(ZnTe)_N$ superlattices, with N=1-10, which will be used to calculate bandgaps later, are shown in fig 6.3. There are three important sets of states to consider.

(1) In the valence band, below $E = 0.269$ eV, there is a series of heavy-hole subbands.

(2) The opposite curvature of the $\Gamma_7$ states, the ZnTe light-hole and the HgTe conduction band, produces a pair of interface states. These are discussed in the following section.

(3) Above the HgTe $\Gamma_7$ edge, there is a series of conduction subbands related to the bulk $\Gamma_7$ edges.

The three types of state are denoted respectively by HH1-HH(N), S1 and S2 (the upper and lower interface states, respectively) and E1-E(M) on fig 6.3 and in the following discussion. The notation used is from the literature (Gerchikov and Subashiev, 1990).

### 6.2.2 : Interface states.

It has been reported that there are states bound at the interfaces between sublayers if one material is zero-gap, e.g. HgTe, and the other is direct gap, e.g. CdTe or ZnTe. These were first reported for HgTe-CdTe superlattices, and are a consequence of the matching of bulk states of the same symmetry and effective masses of opposite signs, on the two sides of the interface (Chang *et al.*, 1985;

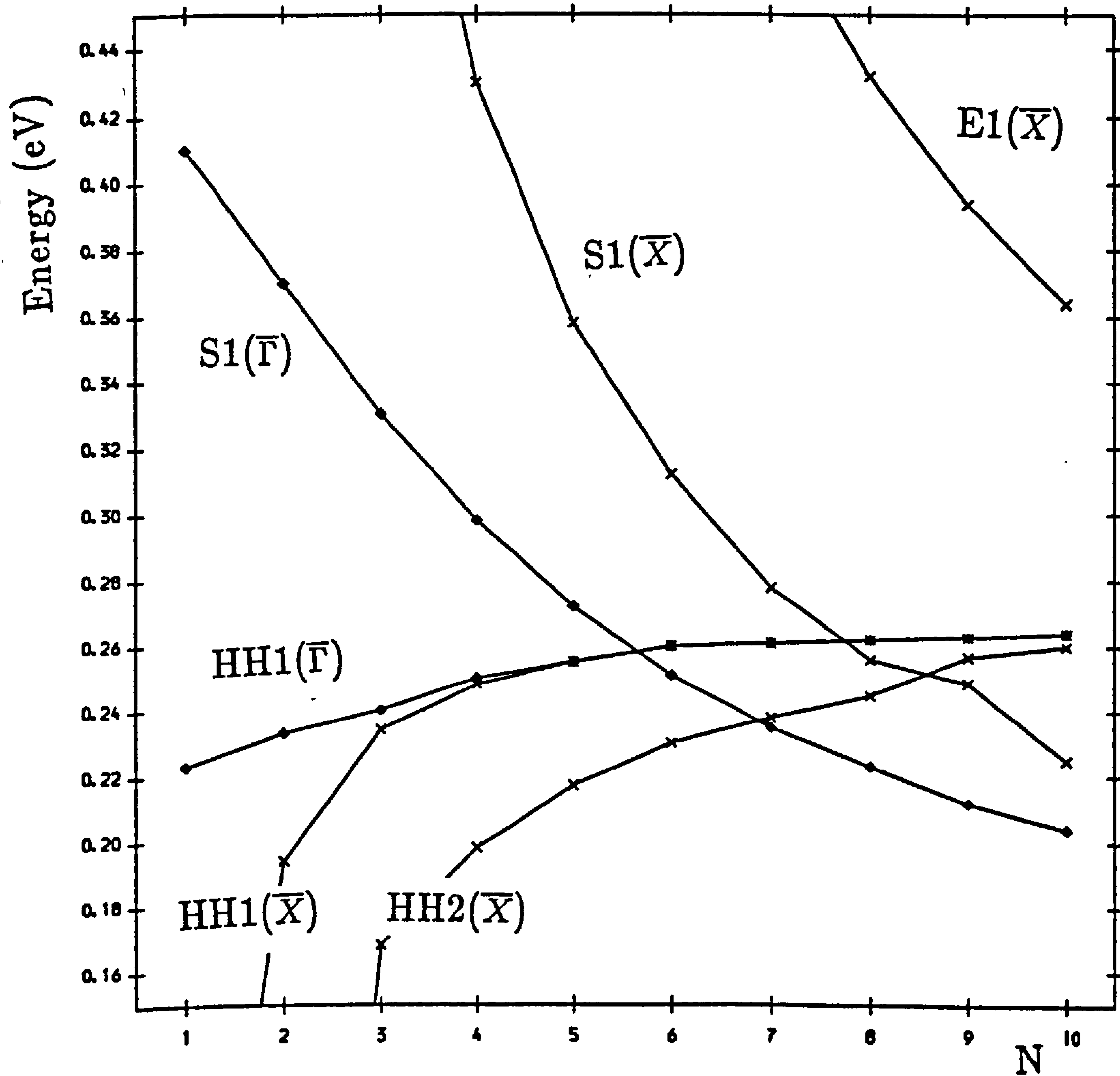


Figure 6.3. Energy levels at $\overline{\Gamma}$ and $\overline{X}$ of the $(HgTe)_{3N}$-$(ZnTe)_N$ superlattice. Only those levels are indicated which are used later to calculate bandgaps (figure 6.9).

Lin-Liu and Sham, 1985; Cade, 1985; Gerchikov and Subashiev, 1990). The lowest conduction band in HgTe is of the same symmetry as the light-hole band in ZnTe or CdTe. The existence of such states may be shown from a one-band envelope-function method calculation. We will first consider the nearly lattice matched HgTe-CdTe system for simplicity. Considering wavefunction $\psi$ and derivative of wavefunction divided by effective mass $\frac{1}{m^*} d\psi/dx$ to be continuous at the interfaces, it is found that at an isolated interface between HgTe and CdTe that there is a solution with energy (Chang *et al*, 1985)

$$E = -\frac{m_A}{m_A + |m_B|} V_P$$

where $m_A$ and $m_B$ are the HgTe conduction band and CdTe valence band effective masses, and the energy zero is chosen to be at the HgTe conduction band minimum. The offset is $V_P$. The energy of the state E is within the gap ($-V_P$ to 0) so the solution represents an interface state.

There are also real heavy-hole states in the HgTe in the region of the gap between $-V_P$ and 0, which the interface state may be able to couple to, particularly away from superlattice Brillouin-zone centre, so it will not be fully localised at the interfaces and should more accurately be called a quasi-interface state (Chang *et al.*, 1985).

In a quantum well or superlattice the states at adjacent interfaces will interact. At wide layer widths these will form symmetric and antisymmetric combinations of the original interface states, which for sufficiently wide layers will be degenerate. However, for narrower sublayers an energy splitting will open up between the symmetric and antisymmetric interface states. From an envelope function calculation it is found that, for a $(HgTe)_N$-$(CdTe)_M$ superlattice, if $N/M \geq |m_A/m_B| \approx 4$, the symmetric interface state lies higher in energy, while if $N/M \leq |m_B/m_A|$ the situation is reversed (Chang *et al.*, 1985). The energy of a heterostructure state is determined by the sum of the kinetic energies in the HgTe and CdTe layers, and the contributions from each sublayer are of opposite

sign due to the reversal of the effective masses. Thus, for some combinations of well and barrier widths the two interface states will cross (Meyer *et al.*, 1988A).

The state at an isolated interface is a combination of CdTe valence band states and HgTe conduction band states. When these broaden out into two bands, one will be occupied and the other empty (Chang *et al*, 1985; Gerchikov and Subashiev, 1990). In the short period HgTe-CdTe superlattice the higher interface band is a conduction subband and the lower interface subband is a valence subband. For longer period superlattices the properties of the superlattice depend strongly upon whether the higher interface subband lies above the highest heavy-hole subband for all $\underline{q}_{SL}$, or there is any overlap, or the highest heavy-hole subband is higher. This will be discussed in the following sections.

The HgTe-ZnTe superlattice will have interface states similar to those described above for the HgTe-CdTe superlattice. The lattice mismatch strain shifts the various energy bands in the two materials relative to one another, but does not change the type of states found. In fact, for the combination of well and barrier widths and valence band offset used in the calculations, the bulk ZnTe $\Gamma_7^{lh}$ and HgTe $\Gamma_7^c$ bands are nearly aligned, so the interface states are similar to those found for the HgTe-CdTe superlattices with zero valence band offset (Schulman and McGill, 1979; Meyer *et al.*, 1988A). The states are not simply symmetric and antisymmetric combinations of isolated interface states, since for the layer widths considered there is a strong interaction between the interfaces, and there are real states at all energies in the HgTe. For the superlattices considered, the upper state is electron-like, and the lower state is light hole-like, as discussed in the literature (Meyer *et al.*, 1988 A), i.e. the upper state rises and the lower state falls in energy as the well width is narrowed. At wide layer widths, the upper state would be an antisymmetric combination and the lower state a symmetric combination of the isolated interface states, if they did not couple with the heavy holes.

## 6.2.3 : Bandstructure.

In this section the bandstructure of $(HgTe)_{3N}$-$(ZnTe)_N$ superlattices with N=1-10 is studied. There is a crossover between the upper interface state S1 and the heavy-hole states (figure 6.3). In particular, the S1 and HH1 states cross at $\overline{\Gamma}$ between N=5 and N=6, and at $\overline{X}$ between N=7 and N=8. Thus the study can be neatly divided into three parts: if $N \leq 5$, S1 lies above HH1 and is the lowest conduction subband, while HH1 is the highest valence subband, and there is a direct energy gap at $\overline{\Gamma}$; if N=6 or N=7, S1 lies below HH1 at $\overline{\Gamma}$, but above at $\overline{X}$; if $N \geq 8$, S1 lies below HH1 at both $\overline{\Gamma}$ and $\overline{X}$. In figures 6.4 to 6.7 the bandstructure of the superlattices along $k_{SL}$ is shown, between $E = -0.050$ eV and $E = +0.600$ eV, with (6.4) N=3, (6.5) N=6, (6.6) N=8, and (6.7) N=9. The energy zero is the unstrained ZnTe valence band top.

Fig 6.4 shows the bandstructure of the $(HgTe)_9$-$(ZnTe)_3$ superlattice between $E = -0.050$ eV and $E = 0.500$ eV. There is a $\overline{\Gamma}$ HH1-S1 gap of 0.09 eV, corresponding to a wavelength of 14 $\mu$m, and a $\overline{X}$ HH1-S1 gap of 0.33 eV, or 4 $\mu$m. The lower valence bands are strongly hybridised: the interface state S2 has a much greater dispersion than the heavy-hole states, and so interacts with a number of states. There is a large interaction at the S2-HH2 anticrossing, near $E = 0.140$ eV, but a smaller interaction at the S2-HH3 anticrossing near $E = 0$. Along the $k_{SL}$ axis, all states have $\Gamma_5$ symmetry and interact and anticross rather than cross. Symmetry arguments only show that there is an interaction, but not how large that interaction is. In this case, states which would mix at $\overline{\Gamma}$ or $\overline{X}$, the S2 and HH2, interact strongly, whereas those which would not mix at $\overline{\Gamma}$ or $\overline{X}$, the S2 and HH3, interact weakly.

The band-edge optical properties are studied in 6.3 for N between 1 and 10. However, to study fully the potential of these superlattices as materials for optical devices, the optical matrix elements for all possible interband transitions need to be determined. This has been done for the $N = 5$ superlattice; these results will be presented in 6.4, where a full comparison with available

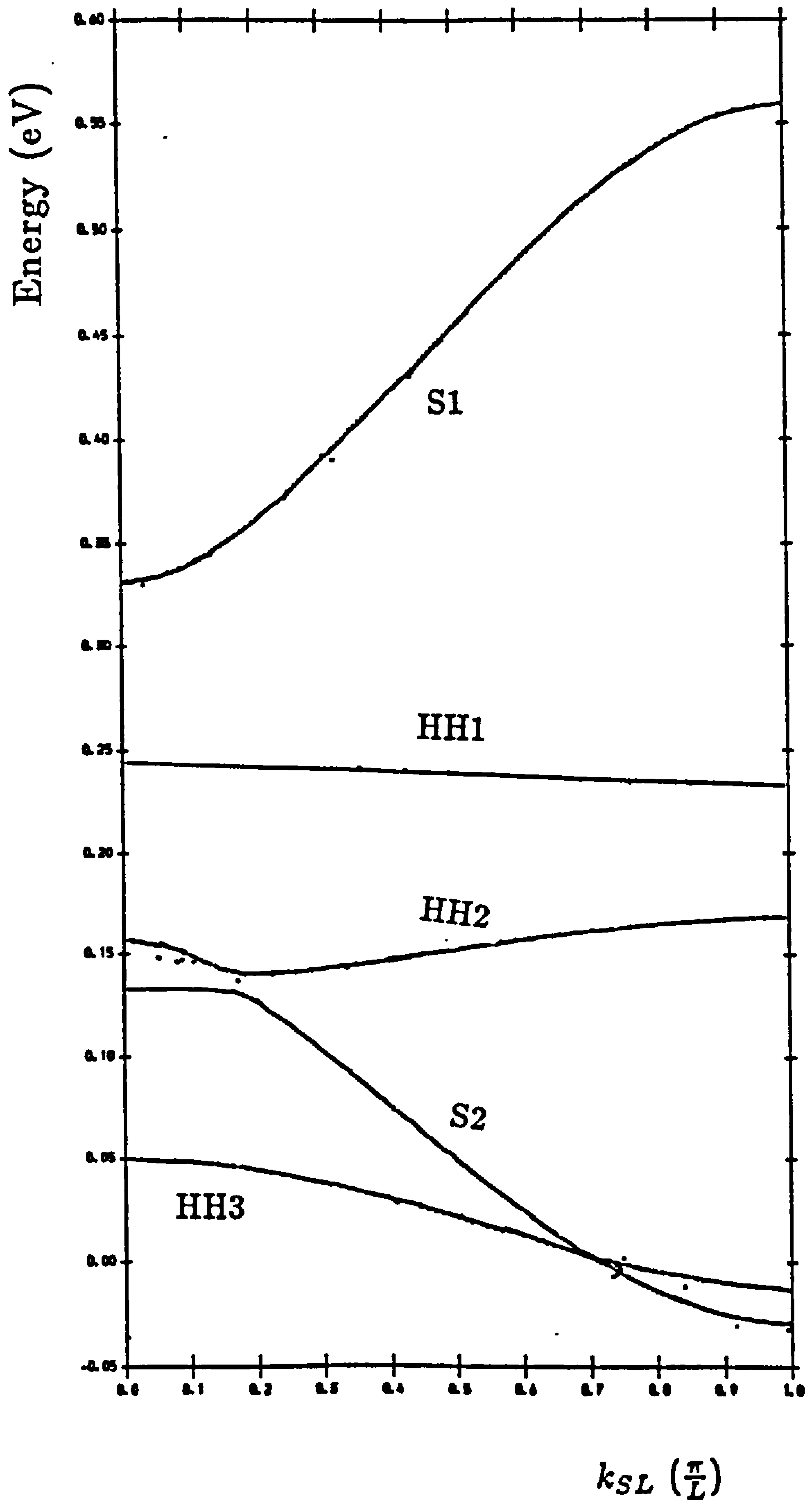


Figure 6.4. Bandstructure of $(HgTe)_9$-$(ZnTe)_3$ superlattice along $k_{SL}$ between $E = -0.05$ eV and 0.60 eV.

experimental and theoretical results will be made.

All of the superlattices with $N \leq 5$ have a positive bandgap at $\overline{\Gamma}$ between the HH1 subband and the S1 subband. For $N \geq 6$ this bandgap becomes negative.

Figure 6.5 shows the bandstructure along $k_{SL}$ of the $(HgTe)_{18}$-$(ZnTe)_6$ superlattice between $E = -0.050$ eV and $E = +0.600$ eV. The S1 has a lower energy than the HH1 at $\overline{\Gamma}$, but a higher energy at $\overline{X}$. Thus the upper valence subband is S1-like at $\overline{\Gamma}$, HH1-like at $\overline{X}$, the lowest conduction subband is S1-like at $\overline{X}$, HH1-like at $\overline{\Gamma}$, with a bandgap of $\leq 1$ meV at $q \approx 0.25(\pi/L)$. Semimetallic HgTe-CdTe and $Hg_{1-x}Zn_xTe$ -CdTe superlattices have shown very high hole mobilities, $\geq 10^5$ $cm^2V^{-1}$ $s^{-1}$ (Meyer *et al.*, 1988 B), the highest found in II-VI semiconductors. The mobility increases with decreasing temperature - this is probably related to the decrease in the region of the Brillouin-zone which is occupied as temperature decreases, i.e. only the regions nearest to the bandgap of lowest effective mass are occupied at very low temperatures.

HgTe-CdTe and $Hg_{1-x}Zn_xTe$-CdTe superlattices are found to have a range of hole mobilities, due to the wide variation in bandgap and hence of effective mass with $k_{SL}$ (see 6.4) (Hoffman *et al.*, 1990B). The highest mobility holes have an effective mass close to that of the electrons at low temperatures, where only regions close to the anticrossing are occupied, but that falls off with increasing temperature above 30K. This has been interpreted as being due to the large anisotropy in the HH1 in-plane dispersion (Meyer *et al.*, 1988 A; 1989). At higher temperatures, higher energy states which have a larger effective mass will be populated, and hence the mobility will decrease. A tight-binding calculation performed on a $(HgTe)_{19}$-$(Hg_{0.15}Cd_{0.85}Te)_9$ superlattice with $\Delta E_v = 0.350$ eV (Meyer *et al.*, 1989, 1990) found the S2 only 50 meV lower in energy than the HH1 at $\overline{\Gamma}$, and above the HH2, whereas in the $(HgTe)_{18}$-$(ZnTe)_6$ superlattice (fig 6.5), the S2 is $\approx 110$ meV below the HH1, and also below the HH2 and HH3. This increased separation will improve the HH1 in-plane mass isotropy. It is possible that the higher hole mobility in HgTe-ZnTe semimetallic superlattices may not fall off so quickly with temperature as for HgTe-CdTe superlattices,

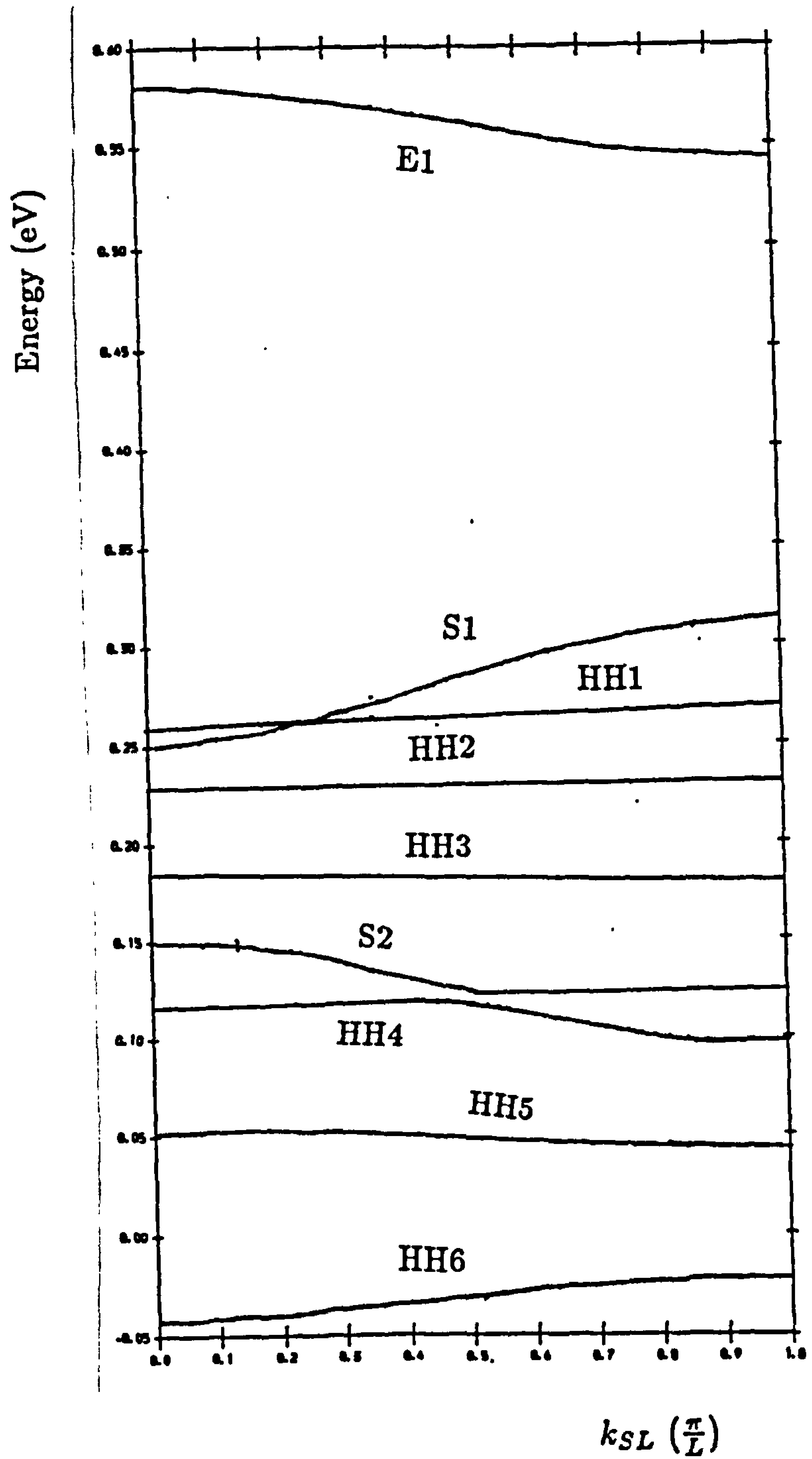


Figure 6.5. Bandstructure of $(HgTe)_{18}$-$(ZnTe)_6$ superlattice along $k_{SL}$ between $E = -0.05$ eV and 0.60 eV.

which would be important for device applications, but this has not been measured in experiment. The interface state S2 is shifted down by the strain in the HgTe-ZnTe superlattice, so the S2-HH1 splitting is highly controllable and could be increased by increasing the strain, although careful control over layer widths is important because the strain also moves the S1 states down relative to the HH1.

The bandstructure of the $(HgTe)_{21}$-$(ZnTe)_7$ superlattice is very similar to figure 6.5. For larger well widths, however, the S1 subband moves completely below the HH1 subband.

The $(HgTe)_{24}$-$(ZnTe)_8$ superlattice (fig 6.6) has an upper valence band which is HH2-like at $\overline{\Gamma}$ and S1-like at $\overline{X}$, with a crossover of band character near $k_{SL} = 0.6(\pi/L)$. The HH1 is the lowest conduction subband. The superlattice is a semiconductor with an $\overline{X}$ bandgap of $\approx$ 5 meV. Semimetallic behaviour observed in HgTe-based superlattices has been explained as being due to the overlap of the S1 and HH1 bands (Meyer *et al.*, 1990), but there will always be a bandgap since the bands anticross rather than cross, and S1-HH1 anticrossing behaviour is expected to exist for only a narrow range of layer widths. This range is mainly dependent upon the barrier width. For a CdTe-HgTe-CdTe quantum well, according to a calculation using a three-band Kane model, the S1 and HH1 states cross for a well width of 70Å, the S1 and HH2 states cross at a well width of 85 Å, with $E_g$(85 Å) $\approx$ 20 meV (Gerchikov and Subashiev, 1990). This corresponds to about 21 and 26 monolayers, respectively, or $N \approx 7$ and $N \approx 9$ for the superlattice calculated here. The semimetallic region thus occurs at narrower well widths for the HgTe-ZnTe superlattice than for HgTe-CdTe quantum wells, mainly due to the effect of the intrinsic strain in the superlattice, in spite of the smaller valence-band offset and the larger bandgap of ZnTe than CdTe. This contrasts with the results of an empirical pseudopotential supercell calculation (Beavis *et al.*, 1990A), which found a wider bandgap for HgTe-$Zn_{0.32}Cd_{0.68}Te$ superlattices than for HgTe-CdTe superlattices. HgTe-CdTe superlattices with HgTe well widths of between $\approx$ 75 Å and $\approx$ 110 Å have been observed to be

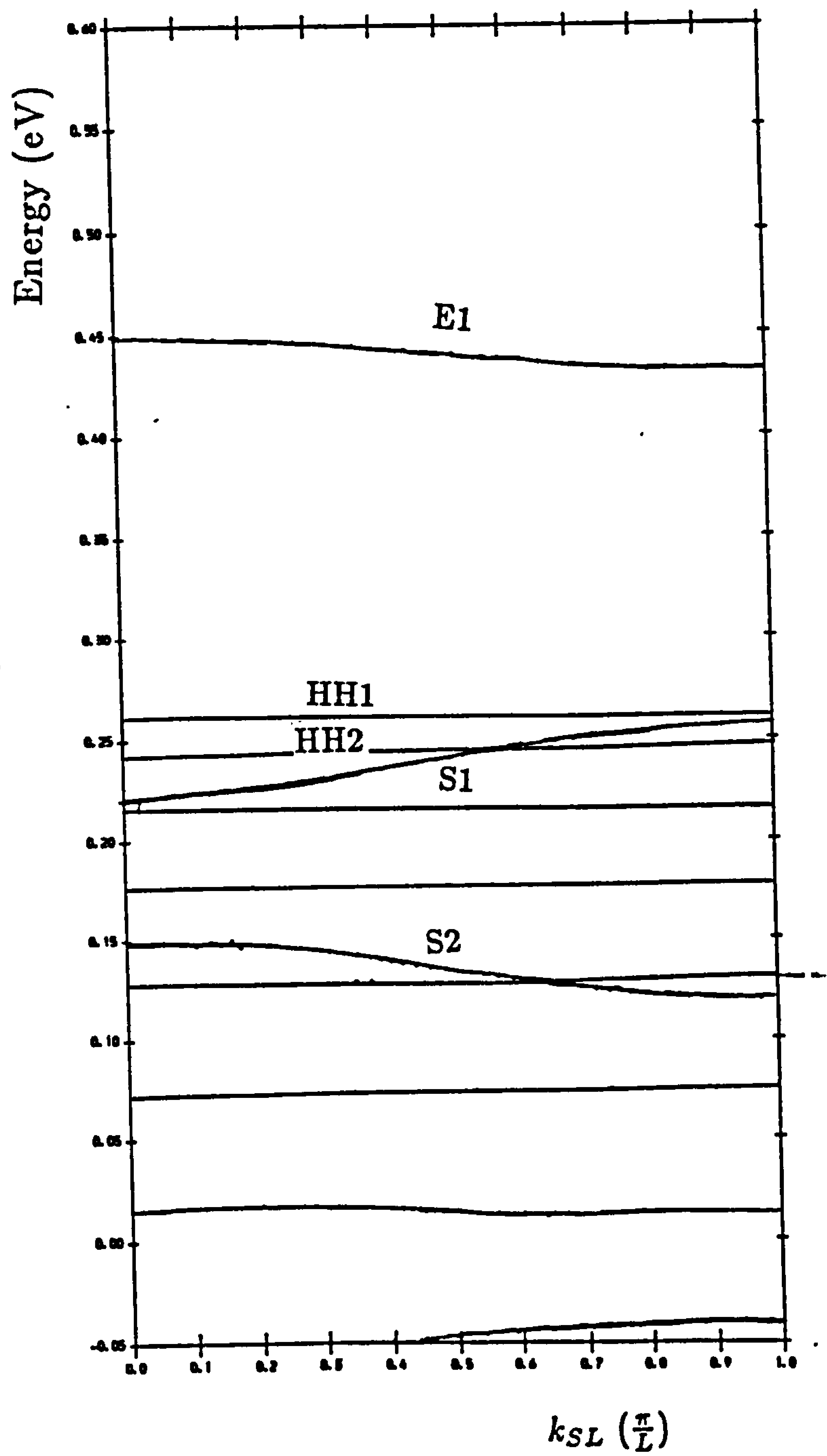


Figure 6.6. Bandstructure of $(HgTe)_{24}$-$(ZnTe)_8$ superlattice along $k_{SL}$ between $E = -0.05$ eV and 0.60 eV.

semimetallic, while a superlattice with a well width of 128 Å and a barrier width of 89 Å was found to have a bandgap of $\approx$ 16 meV (Hoffman *et al.*, 1990 A). This confirms the prediction of a semiconductor-semimetal-semiconductor transition, although the semimetallic region extends over a larger range of layer widths than predicted.

For longer period superlattices, $N > 9$, the S1 band lies entirely below the HH2 band, as shown for the $(HgTe)_{27}$-$(ZnTe)_9$ superlattice in figure 6.7. Thus the HH2 is the top of the valence band, the HH1 is the bottom of the conduction band. The in-plane bandstructure of this superlattice will be complicated, with both the S1 and HH2 possibly having electron-like in-plane bandstructure, which would affect the bandgap. The in-plane bandstructure of the CdTe-HgTe-CdTe quantum well in this regime (i.e. S1 below HH2) has been studied (Gerchikov and Subashiev, 1990), and it is found that the bandgap is still near $\overline{\Gamma}$, due to the light electron-like in-plane bandstructure of the HH1 band, so some idea of the optical properties can be gained from a study of the interband matrix elements at $\overline{\Gamma}$. A study of the zone-centre matrix elements and optical properties of $(HgTe)_{3N}$-$(ZnTe)_N$ superlattices will be presented in the following section.

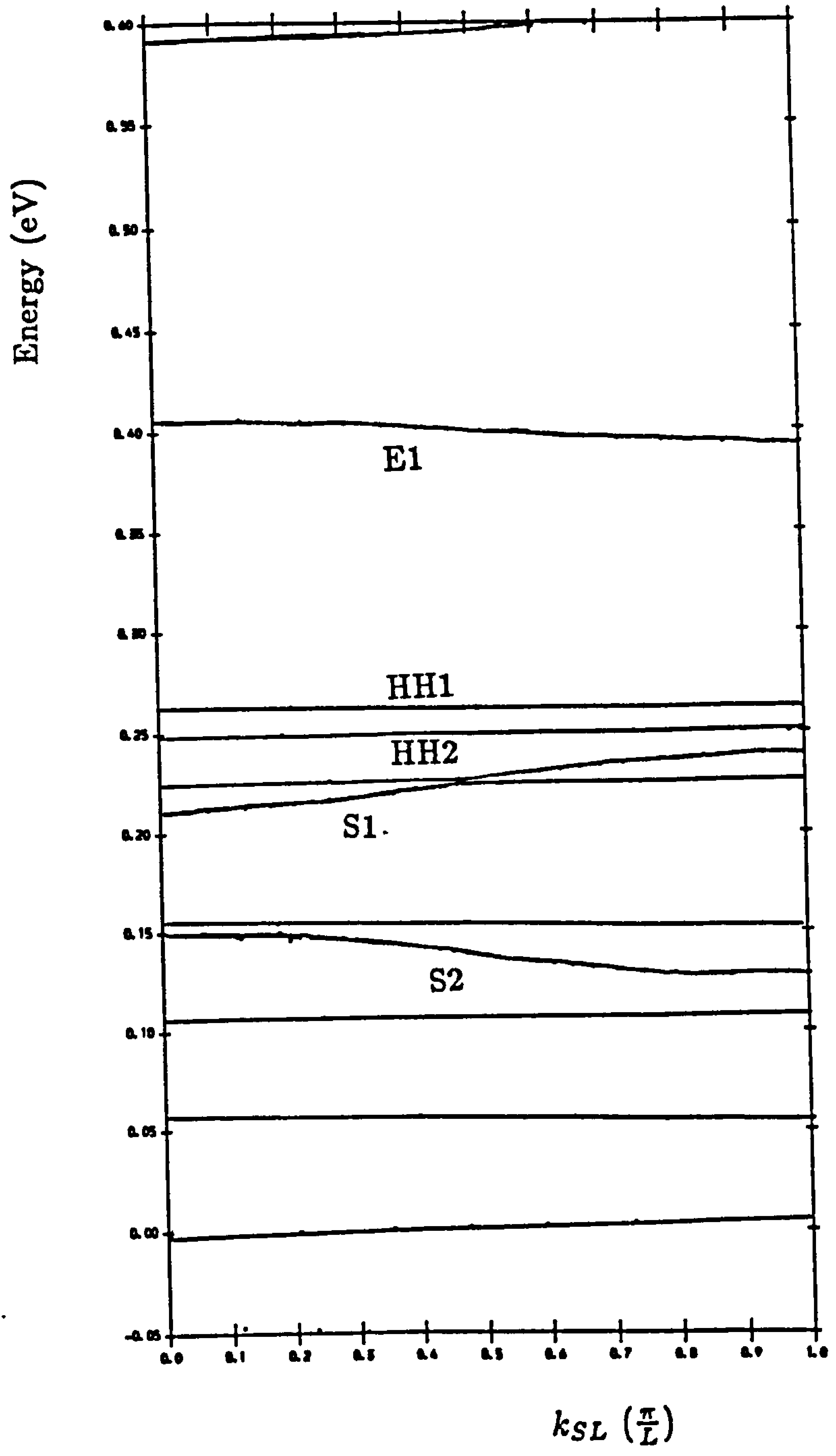


Figure 6.7. Bandstructure of $(HgTe)_{27}$-$(ZnTe)_9$ superlattice along $k_{SL}$ between $E = -0.05$ eV and 0.60 eV.

## 6.3 : Optical Properties.

### 6.3.1 : Introduction.

In part 6.2 it was noted that as well width is varied, for a fixed well/barrier width ratio of three, there are three regions to consider, depending upon whether the upper interface state S1 is a conduction or valence state, or is degenerate with the HH1 level, forming a semimetal. In that section, most attention was paid to the crossover region where the bandgap is close to zero, with reference to various experimental studies of the electronic properties, to see what may be inferred about the bandstructure near this crossover. In the following pages, the superlattice optical properties will be studied, considering the two semiconducting regions separately.

### 6.3.2 : Region 1, $N \leq 5$.

For short period superlattices, the interface state S1 lies above the HH1 state, and so forms the lowest conduction subband. Fig 6.8 shows (a) the S1-HH1 bandgap and (b) the squared matrix element for $N = 1$ to 5. The superlattices will all absorb across the first atmospheric window, $3-5$ $\mu$m, and those with N between 3 and 5 will also absorb across the second, $8-14$ $\mu$m. To absorb at a wavelength of 8 $\mu$m or longer a $Hg_{1-x}Cd_xTe$ alloy would need $0.16 \leq x \leq 0.21$ (Dornhaus and Nimtz, 1983). The comparison of bandgaps with experiment is difficult due to the paucity of experimental information available. A HgTe-ZnTe superlattice with layer widths 40Å HgTe and 23Å ZnTe was found to have a bandgap of $6-8$ $\mu$m, or $0.2-0.15$ eV at 300K (Faurie *et al.*, 1986). A HgTe-CdTe superlattice with layer widths 40Å HgTe and 20Å CdTe had a bandgap measured by IR photoluminescence of 0.157 eV at 300K (Faurie, 1986) which reduced to $\approx$ 0.08 eV at low temperatures; this change of bandgap with temperature is typical of those found in other Hg-based

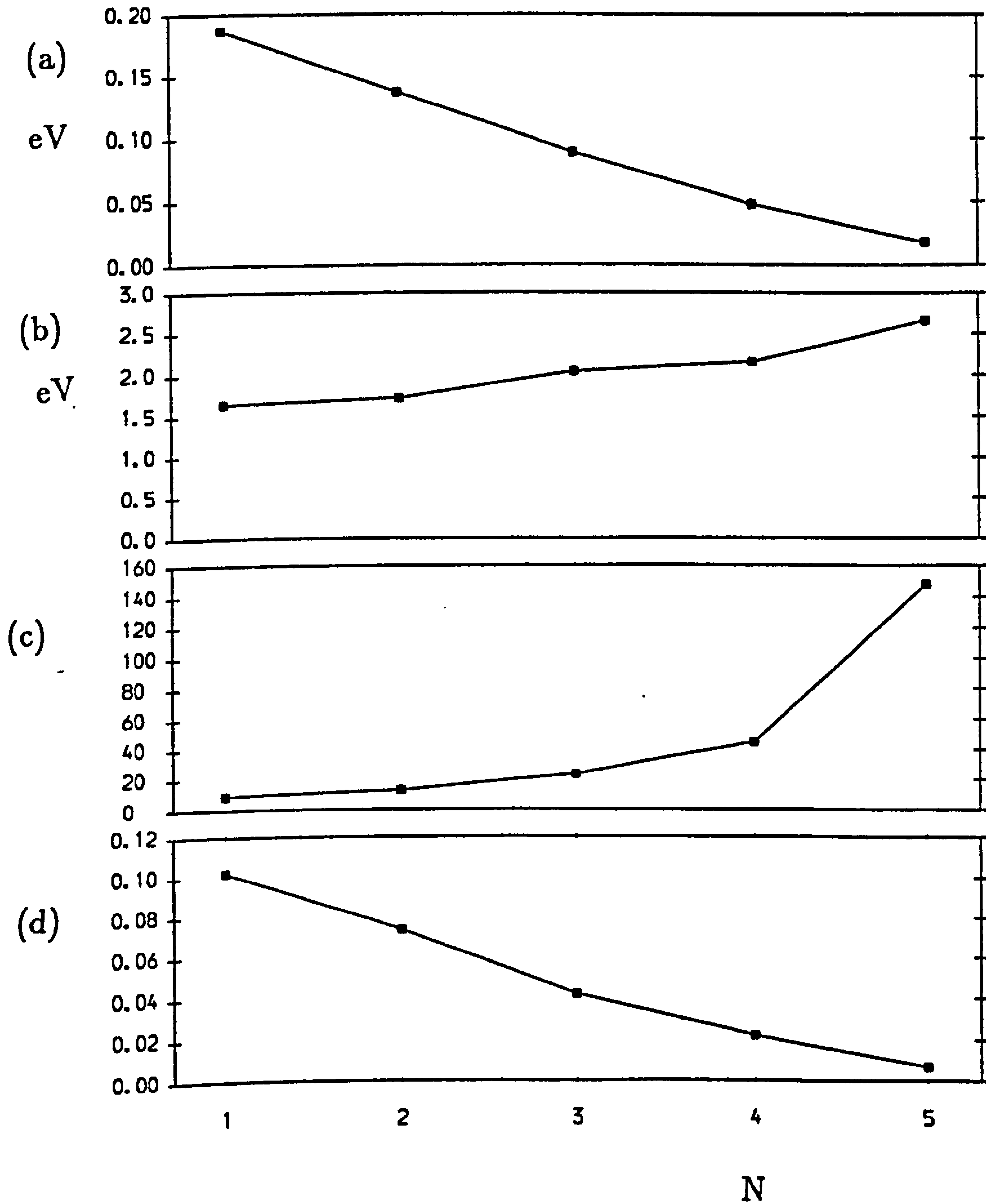


Figure 6.8. Properties of the $(HgTe)_{3N}$-$(ZnTe)_N$ superlattice with N between 1 and 5.

(a) Lowest bandgap, (b) $\frac{2}{m}|M^{\overline{\Gamma}}_{HH1-S1}|^2$, in (011)-polarisation, (c) $\overline{\Gamma}$-oscillator strength, (d) HH1 in-plane effective mass at $\overline{\Gamma}$.

II-VI superlattices (Yang *et al.*, 1990). If the HgTe-ZnTe superlattice bandgap showed a similar change with temperature, then the low temperature bandgap would be close to the 0.05 eV bandgap calculated for the $(HgTe)_{12}$-$(ZnTe)_4$ superlattice, i.e. 40 Å HgTe and 12 Å ZnTe, making allowance for the effects of strain and interdiffusion at interfaces (Simon *et al.*, 1990). The lowest energy interband matrix element has a magnitude $\approx$ 2 eV, close to the values calculated in pseudopotential calculations on HgTe-CdTe superlattices, which find matrix elements between the lowest conduction subband and highest HH subband, with in-plane polarisation, to be $\approx$ 1.8 eV (Beavis *et al.*, 1990A) and 1.77 eV (Xia, 1989). The trend in matrix elements, increasing with well width, appears to be in conflict with the results of Beavis, who found a decrease in matrix element with well width for short period HgTe-$Hg_{0.2}Cd_{0.8}Te$ superlattices. However in that calculation the barrier width was fixed at 38.8 Å, enough to confine the electron and hole states, so the main effect is a change in the S1 state as it moves towards the HgTe $\Gamma_7$ band-edge, and so becomes increasingly confined at the interfaces as the well width increases. In the results presented here, the HgTe $\Gamma_7$ band-edge is lower down, so the nature of the state will not change much with well width, and the main effect is due to the varying barrier width, which changes the confinement of the two states at different rates, and so changes the overlap of the wavefunctions.

In figure 6.8 (c) the $\overline{\Gamma}$ oscillator strength and (d) the HH1 $\overline{\Gamma}$ effective masses in the (011) direction, are shown. The trends with well width are in agreement with the results of other calculations (Beavis *et al.*, 1990A). It will be shown later (section 6.4) that the S1-HH1 oscillator strength largely determines the HH1 $\overline{\Gamma}$ effective mass, particularly for narrow gap superlattices. The oscillator strength is determined from (Bassani and Pastori Parravicini, 1975),

$$f_{ab}^{(j)} = \frac{2|M_{ab}^{(j)}|^2}{m(E_a - E_b)} \qquad 6.1$$

where $\frac{2}{m}|M_{ab}^{(j)}|^2$ is the matrix element for the $j$th component of linear

momentum ($j = x, y, z$).

Then the effective mass can be determined using $\underline{k}.\underline{p}$ theory:

$$(\frac{m_0}{m_b^*})^{(j)} = 1 + \sum_a f_{ab}^{(j)} \qquad 6.2$$

6.3.3 : Region 3, N $\geq$ 8.

For the longer period superlattices with $N \geq 8$, the top valence subband edge is the HH2 at $\overline{X}$ (with the exception of $N = 8$, where the top is S1 at $\overline{X}$), while the bottom conduction subband edge is the HH1 at $\overline{X}$, giving a very narrow bandgap of about 10 meV, which decreases with HgTe well width (figure 6.9). However, a consideration of the interband optical matrix elements (table 6.2) for the $(HgTe)_{27}$-$(ZnTe)_9$ superlattice shows that the HH2-HH1 transition is forbidden in 011-polarisation, and very weak in 100-polarisation.

| States | 100-polarisation | 011-polarisation |
|---|---|---|
| HH2-HH1 | 0.005 | 0.000 |
| HH2-E1 | 0.000 | 1.0 |
| S1-HH1 | 0.000 | 0.24 |
| S1-E1 | 1.4 | 0.07 |

Table 6.2. Interband momentum matrix elements squared, $\frac{2}{m}|M|^2$, in eV, at $\overline{X}$, of the $(HgTe)_{27}$-$(ZnTe)_9$ superlattice.

The main interband optical transitions are the S1-HH1 and HH2-E1 transitions. The absorption edge in HgTe-based type-III superlattices is very broad (Mullins *et al.*, 1990; Faurie, 1986), much broader than for HgCdTe alloys (Dornhaus and Nimtz, 1983). This may be explained for long period superlattices by the combination of the two main zone-centre absorption edges with HH2-HH1

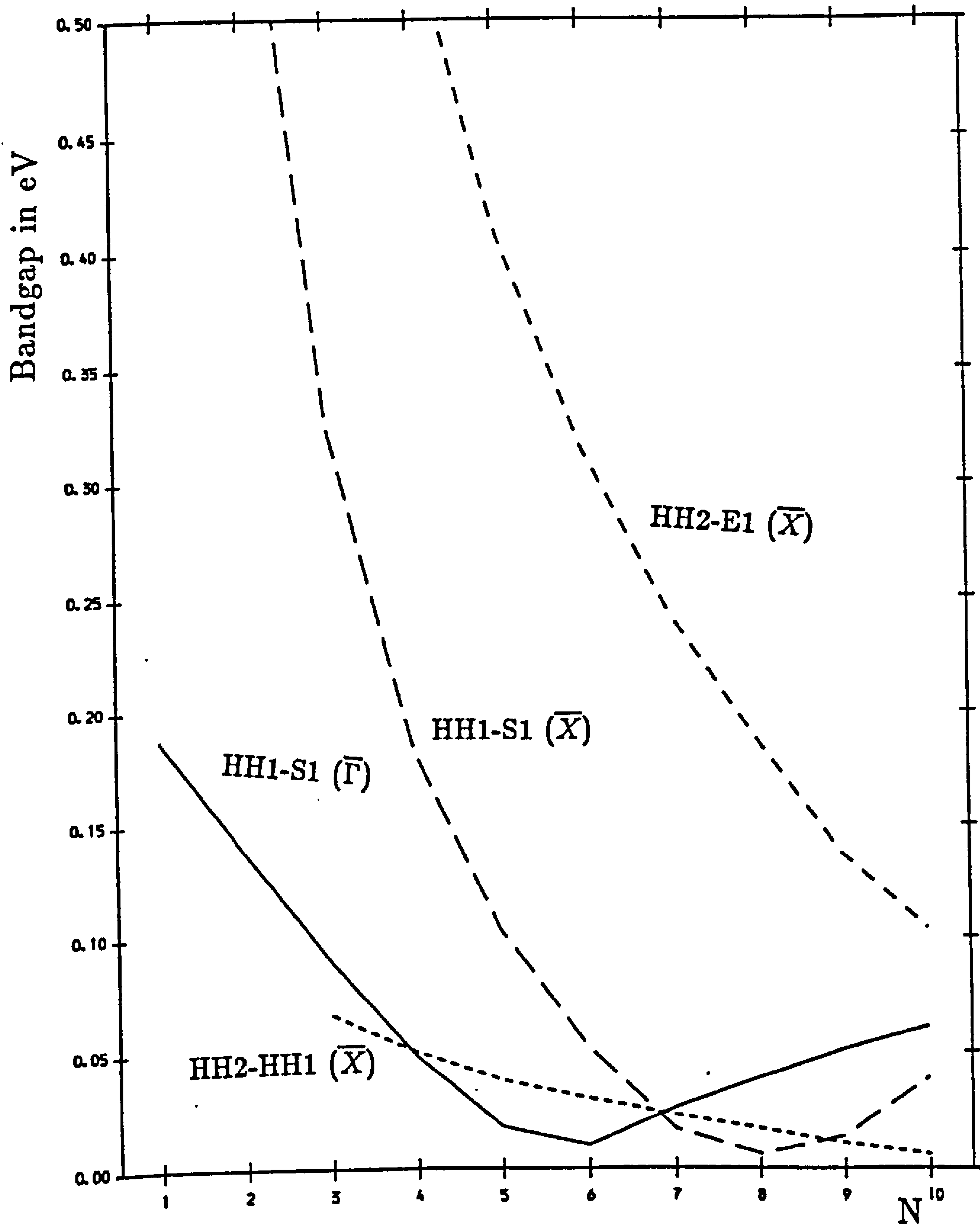


Figure 6.9. $(HgTe)_{3N}$-$(ZnTe)_N$ superlattice bandgaps vs. $N$, with $N$ between 1 and 10. HH2-HH1 at $\overline{X}$ (- - - - - -). HH1-S1 at $\overline{\Gamma}$ (——), and at $\overline{X}$ (— — —). HH2-E1 at $\overline{X}$, (- - - -).

absorption away from zone-centre, where mixing may cause this transition to become allowed. Superlattices in this region should have two main absorption edges, one which decreases in energy with well width, and a lower one which increases in energy with well width. Experiments which measure the bandgap by some other means than optical absorption or luminescence may detect a third bandgap at a much lower energy than either of the other two (fig 6.9). There is some experimental confirmation that the lowest band-edge in long period HgTe-CdTe superlattices is optically forbidden, and that the optical absorption edge is at a higher energy. The $(HgTe)_{30}$-$(ZnTe)_{10}$ superlattice, with a period of 100 Å HgTe and 30 Å ZnTe, has a calculated S1-HH1 edge at 39 meV, a HH2-E1 edge at 110 meV, and a forbidden HH2-HH1 gap at 12 meV. For comparison, a HgTe-CdTe superlattice with HgTe layers 100 Å thick and CdTe layers 36 Å thick showed IR absorption at 111 meV (Faurie, 1986) at temperatures from 30K to 300K, while magneto-optical experiments at low temperature found a gap of $\approx$ 20 meV, with a selection rule for transitions between Landau levels appropriate for both states being composed of bulk p-states (Berroir *et al.*, 1986). The agreement between the E1-HH2 gap in the calculation and the experimental absorption edge is clearly fortuitous, but the occurence of two separate edges, the lower optically forbidden, the upper showing a strong absorption, gives qualitative support to these calculations. Only one absorption edge was reported (Faurie, 1986), but whether this is the combination of two close in energy is uncertain. The magneto-optical lower absorption edge in this particular superlattice has been used as one of the main measures of the HgTe/CdTe valence band offset (Johnson *et al.*, 1988), but a comparison of momentum matrix element calculations with the experimental results shows that the lower bandgap cannot be the S1-HH1 gap, as assumed in the literature. A naive reanalysis of the work of Johnson *et al.* (1988) suggests a valence-band offset of $\approx$ 700 meV between HgTe and CdTe, and thus of $\approx$ 600 meV between HgTe and ZnTe. A large valence-band offset between HgTe and CdTe, of about 600 meV, might also explain the results of low temperature magneto-optical experiments performed

on a 90 Å HgTe/ 40 Å CdTe multiple quantum well (Choi *et al.*, 1990), which were compared to a transfer matrix EFA method, and fitted with an offset of 40 meV. A study of magnetoabsorption in three HgTe/$Hg_{0.15}Cd_{0.85}Te$ superlattices at room temperature was fitted using a transfer matrix method by an offset between 500 and 850 meV, depending upon the choice of input parameters (Yoo *et al.*, 1990). It is possible that these results support a temperature dependence of the valence band offset (Van Vechten and Malloy, 1990), with an increase in offset of around 300 meV between 4 K and 300 K, although no such dependence was found in a recent study of temperature dependent infrared absorption from Hg-based II-VI superlattices (Yang *et al.*, 1990). Tersoff (1989) has also criticised the 350 meV offset, suggesting an increase to $\approx$ 500 meV, by comparing various model calculations. However, a recent theoretical calculation found a valence band offset of 300 meV (Qteish and Needs, 1991). The available theoretical and experimental evidence supports a valence band offset between HgTe and CdTe which is large, $>$ 300 meV, rather than small, $\approx$ 40 meV, but there is still quite a lot of uncertainty about the absolute magnitude of the offset. An increase in the HgTe/CdTe offset would also suggest an increase in the HgTe/ZnTe offset, so would be of importance for the work reported here.

It is also possible that interdiffusion between the layers may affect the bandgap of HgTe-CdTe superlattices very strongly, and calculations (Simon *et al.*, 1990; Beavis *et al.*, 1990 A,B; Beavis and Jaros, 1990) show that the energy of interface states will be most strongly affected. If this is true, the interface state may play no part in the properties of this superlattice, save for those of very good quality, and the main bandgap will therefore be the HH2-E1 gap. This gap has a smooth decrease with increasing well width, as found in early experimental results (Faurie, 1986). Thus the quality of the interfaces of this superlattice is very important. A full reanalysis of the available experimental information on HgTe-CdTe superlattices is beyond the scope of this chapter, but is necessary to determine the valence band offset at this heterojunction. The

interdiffusion between HgTe and ZnTe is reported to be an order of magnitude smaller than between HgTe and CdTe (Mullins *et al.*, 1990), which could also give the HgTe/ZnTe superlattice an advantage.

## 6.4 : The $(HgTe)_{15} - (ZnTe)_5$ superlattice.

### 6.4.1 : Introduction.

In this section a detailed analysis of the electronic structure and optical properties of the $(HgTe)_{15}$-$(ZnTe)_5$ superlattice will be presented. This superlattice has the smallest bandgap of the short period ($N \leq 5$) superlattices considered in 6.3.2. The S1 subband is the lowest conduction subband and the HH1 is the highest valence subband. At higher energies than the S1 subband are a series of subbands of unusual character, emanating from the HgTe $\Gamma_7$ conduction-band edge. It is of interest to determine the selection rules for interband transitions, so the interband momentum matrix elements at $\overline{\Gamma}$ and $\overline{X}$ have been calculated between six valence-bands and five conduction bands (four at $\overline{X}$). The effective mass of the HH1 subband has also been determined, to see whether the variation with $k_{SL}$, found for HgTe-CdTe superlattices (Meyer *et al.*, 1990), is also found here.

### 6.4.2 : Bandstructure and wavefunctions.

The bandstructure of the superlattice along $k_{SL}$ is shown in figure 6.10 between $-0.050$ eV and 1.820 eV. In fig 6.11 the highest valence subband HH1 and lowest conduction subband S1 are shown in greater detail. There are five conduction subbands, approximately evenly spaced in energy, and six valence subbands, five heavy-hole with little dispersion and one light-hole with a much greater dispersion, in the energy range considered. There is an anticrossing between S2 and HH4 near $q = 0.8(\pi/L)$. The superlattice $\overline{\Gamma}$ and $\overline{X}$ energies are listed in table 6.3. The bandgap between S1 and HH1 is 0.017 eV at $\overline{\Gamma}$ and 0.103 eV at $\overline{X}$. The higher conduction bands, E1-E3, all have roughly equal dispersion, $\approx$ 60 meV, lower than that of S1, $\approx$ 90 meV. This is another difference from

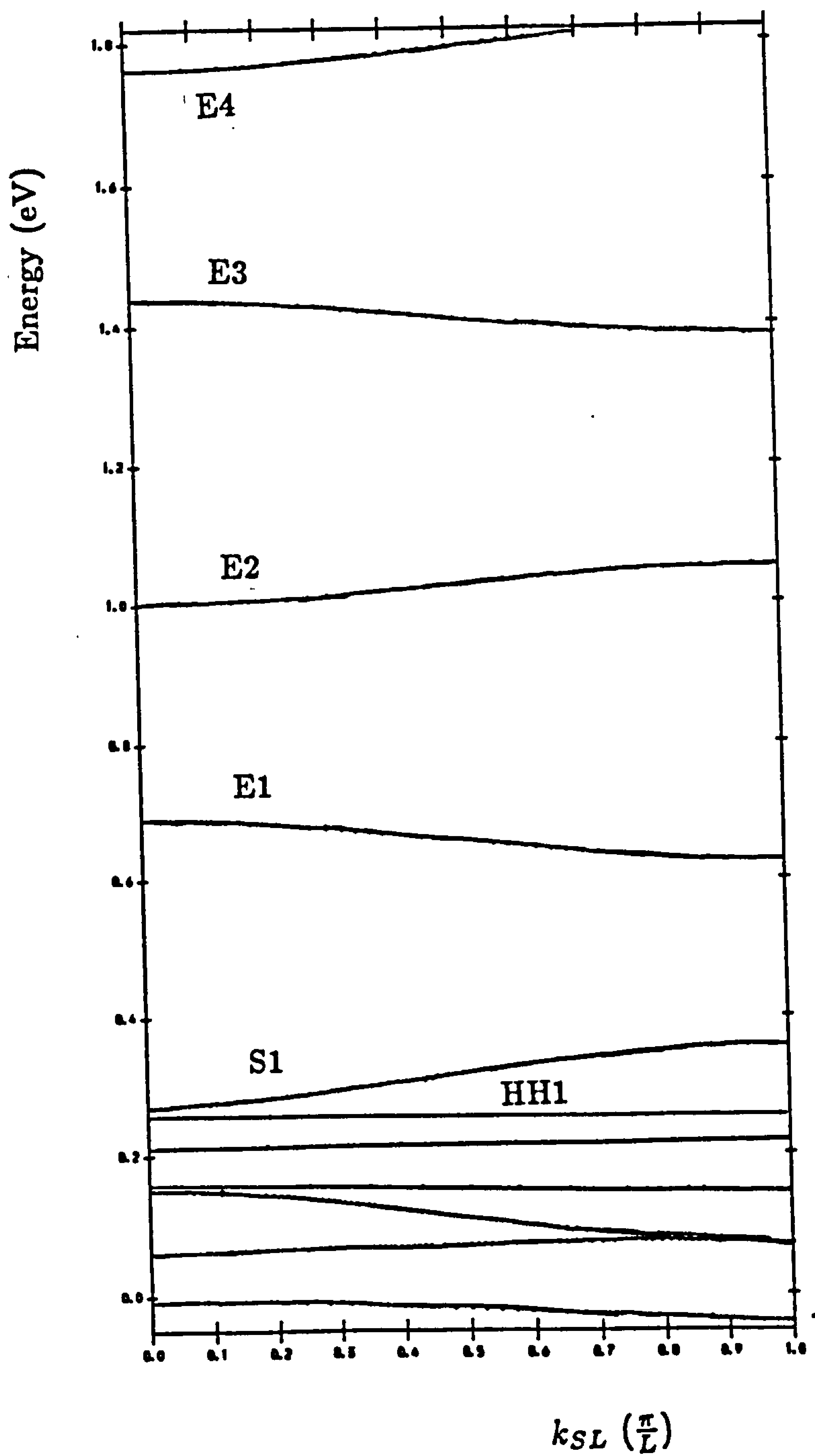


Figure 6.10. Bandstructure of the $(HgTe)_{15}$-$(ZnTe)_5$ superlattice between $E = -0.05$ eV and 1.82 eV.

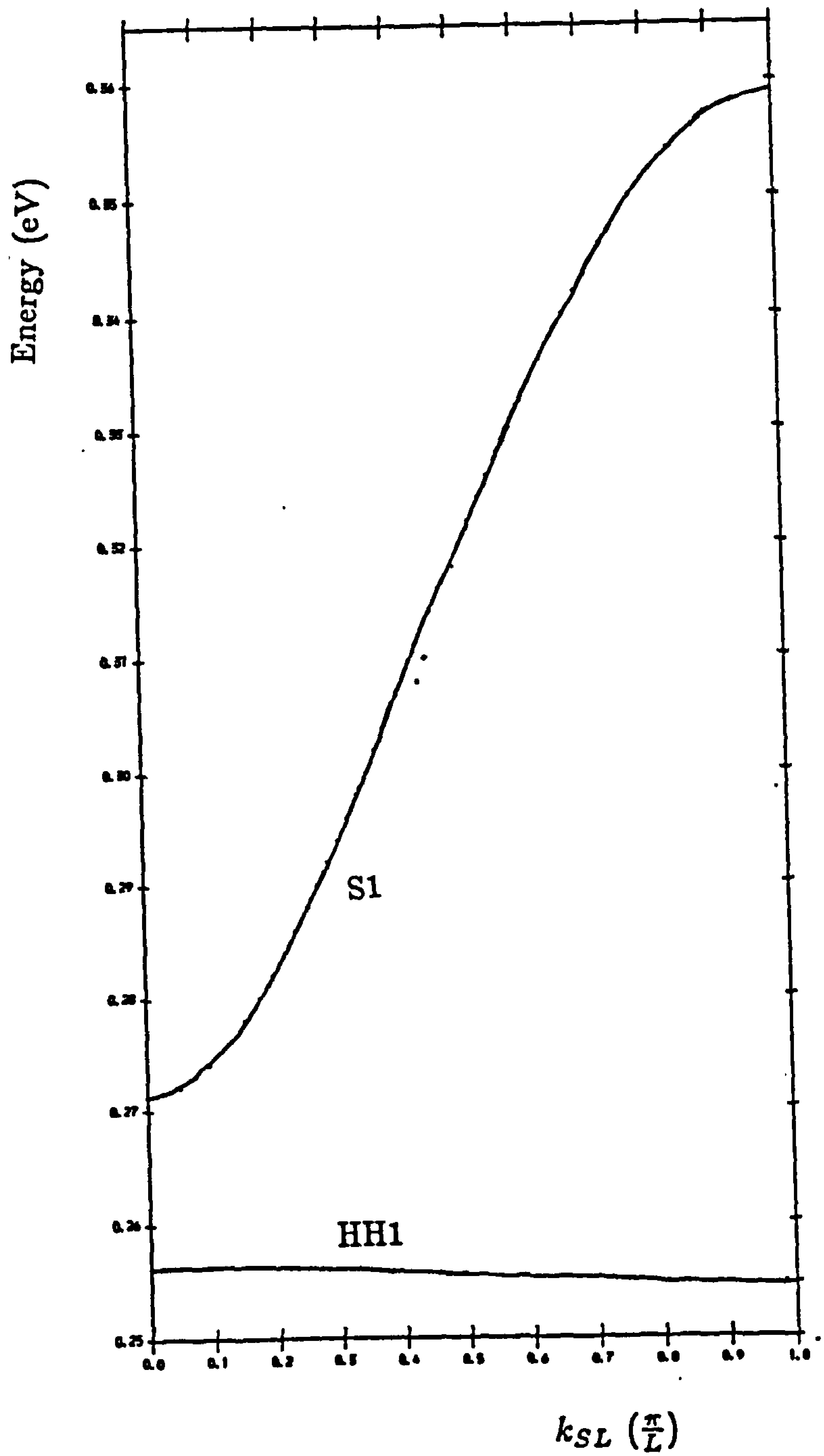


Figure 6.11. Bandstructure of the $(HgTe)_{15}$-$(ZnTe)_5$ superlattice between $E = 0.25$ eV and 0.40 eV.

| State | Point | Energy |
|---|---|---|
| E4 | $\overline{X}$ | — |
| | $\overline{\Gamma}$ | 1.764 |
| E3 | $\overline{\Gamma}$ | 1.438 |
| | $\overline{X}$ | 1.384 |
| E2 | $\overline{X}$ | 1.054 |
| | $\overline{\Gamma}$ | 1.002 |
| E1 | $\overline{\Gamma}$ | 0.688 |
| | $\overline{X}$ | 0.628 |
| S1 | $\overline{X}$ | 0.358 |
| | $\overline{\Gamma}$ | 0.272 |
| HH1 | $\overline{\Gamma}$ | 0.255 |
| | $\overline{X}$ | 0.255 |
| HH2 | $\overline{X}$ | 0.217 |
| | $\overline{\Gamma}$ | 0.214 |
| HH3 | $\overline{\Gamma}$ | 0.156 |
| | $\overline{X}$ | 0.149 |
| S2 | $\overline{\Gamma}$ | 0.148 |
| | $\overline{X}$ | 0.083 |
| HH4 | $\overline{X}$ | 0.073 |
| | $\overline{\Gamma}$ | 0.065 |
| HH5 | $\overline{\Gamma}$ | -0.007 |
| | $\overline{X}$ | -0.032 |

Table 6.3 $(HgTe)_{15}$-$(ZnTe)_5$ superlattice critical point energies (eV).

type-I or II superlattices, for which the higher conduction bands are less well confined and so have larger dispersion than the lower bands.

The charge density of the $\overline{\Gamma}$ wavefunctions, averaged over the plane of the layers, along the x-axis, the superlattice growth axis, is plotted in figure 6.12 (valence band), and 6.13 (conduction band). The heavy-hole states are much as found in type-I superlattices. The lower interface state S2 is only slightly more concentrated in the HgTe than in the ZnTe. It appears quite different to the interface states which have been reported in HgTe-CdTe superlattices with calculations performed using a large valence band offset (Beavis *et al.*, 1990A; Jaros *et al.*, 1987; Bastard, 1988A, pp 79-83) because it is close to the band edges of both materials and so the evanescent states which make it up have very long decay lengths, and there is a strong interaction between the interfaces. However, it is similar to calculations performed with a small or zero offset (Schulman and McGill, 1979).

The conduction band states (figure 6.13) at $\overline{\Gamma}$ are unlike the conduction subband states in type I or II superlattices. The lowest conduction subband, S1, is an interface state typical of those reported for HgTe-CdTe superlattices and quantum wells (Xia, 1989; Bastard, 1988A, pp79-83; Beavis *et al.*, 1990 B; Jaros *et al.*, 1987). The higher conduction subband states, E1-E4, have not been previously described in such detail for type-III superlattices. The energy of the state E1 has been calculated in an analytical investigation of the CdTe-HgTe-CdTe subband structure using the three band Kane model (Gershikov and Subashiev, 1990). A charge density plot of the state E1 (called E2 in the paper) has been shown for a HgTe-CdTe superlattice with a period of 26 Å of HgTe and 32 Å of CdTe (Jaros *et al.*, 1987), although in that paper the charge density of the state is found to decrease towards the interfaces, similarly to a type-I superlattice $n = 1$ state. The charge density of the state E1 (called E2 in that paper) has been shown in an envelope form from a pseudopotential supercell calculation (Xia, 1989), and is found to be similar to the E1 state shown in figure 6.13, except that a greater proportion of the charge is near the interfaces

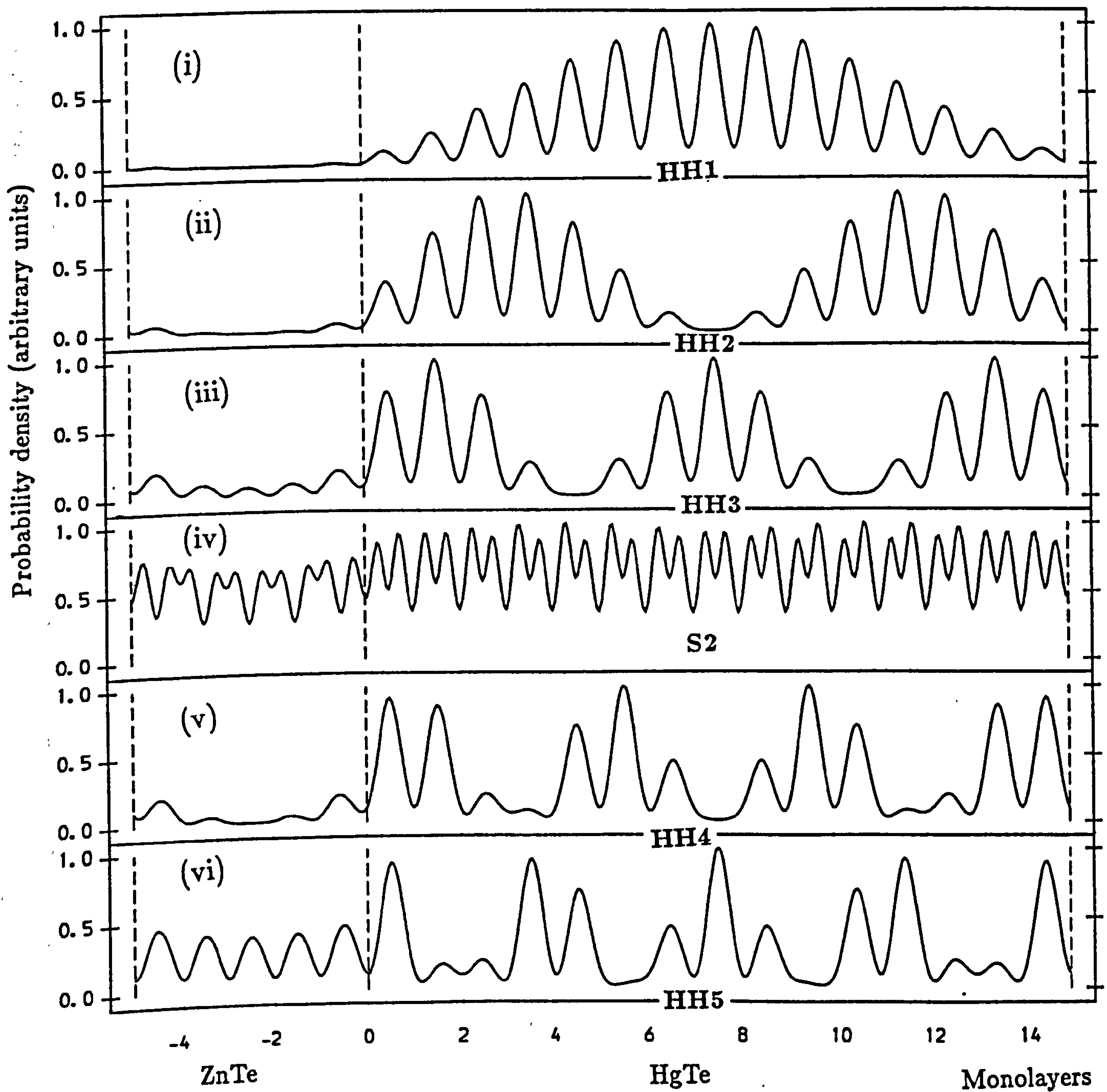


Figure 6.12. Probability density plots of the $\overline{\Gamma}$ valence band wavefunctions of the $(HgTe)_{15}$-$(ZnTe)_5$ superlattice, averaged over the plane of the layers. (i) HH1, (ii) HH2, (iii) HH3, (iv) S2, (v) HH4, (vi) HH5.

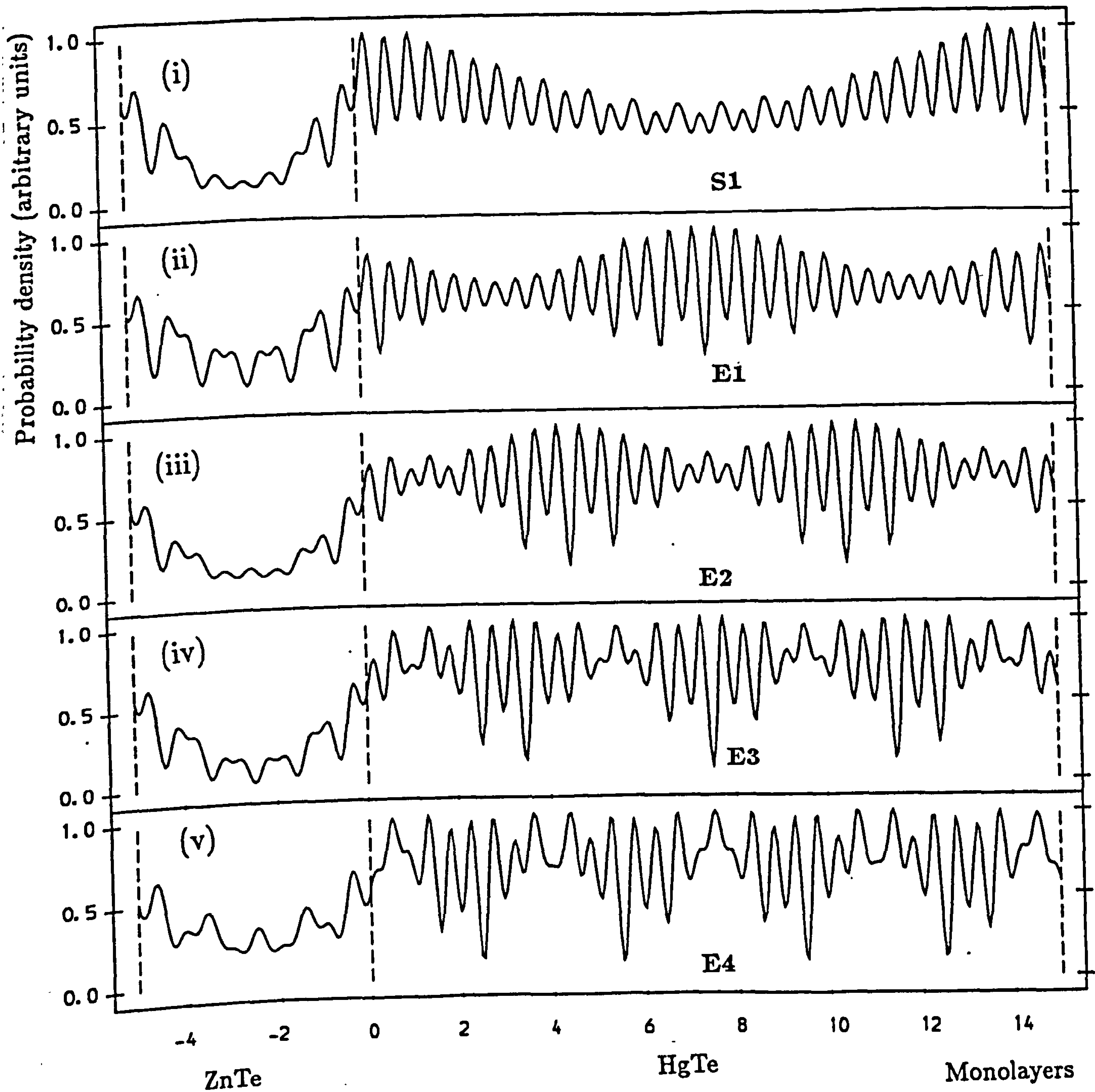


Figure 6.13. Probability density plots of the $\overline{\Gamma}$ conduction band wavefunctions of the $(HgTe)_{15}$-$(ZnTe)_5$ superlattice, averaged over the plane of the layers. (i) S1, (ii) E1, (iii) E2, (iv) E3, (v) E4.

in the supercell calculation. The higher conduction states, E2-E4, have not been previously described.

There are two distinctive features of the states E1-E4. They have no distinct envelope structure, and do not have a definite parity. The states are evenly spaced in energy, and all have about the same dispersion, due to the non-parabolicity of the lowest bulk conduction band, which has an $E - k_x$ relationship which is close to linear over the region of interest (see figures 6.2 and 3.8). The atomic scale variation of the states is similar to that found for light-hole states in type-I superlattices (see figure 2.7 for comparison). There is a periodic variation, with one to four peaks respectively for E1 to E4, imposed upon a constant background.

6.4.3 : Momentum Matrix Elements.

The interband momentum matrix elements are listed in table (6.4) (a) $\overline{\Gamma}$ in 011-polarisation, (b) $\overline{\Gamma}$ in 100-polarisation, (c) $\overline{X}$ in 011-polarisation, (d) $\overline{X}$ in 100-polarisation. At $\overline{\Gamma}$, selection rules are not clear, except that the largest matrix elements are HH1-S1 and S2-S1, and HH(n)-E(n-1), where n=2-5. There is no parity selection rule for any of the interband matrix elements, due to the lack of definite parity of the conduction band states. The $\overline{\Gamma}$ polarisation dependence of S2-S1 and S2-E(m), m=1-4, matrix elements is much as for the LH1 matrix elements in type I or II superlattices, e.g. $|M^{100}_{S2-S1}|^2/|M^{011}_{S2-S1}|^2 = 3.2$, and $|M^{100}_{S2-E4}|^2/|M^{011}_{S2-E4}|^2 = 5.4$, where tight-binding theory would predict a ratio of 4.0 (chapter two, table 2.2).

Most of the $\overline{X}$ matrix elements are very close to the $\overline{\Gamma}$ matrix elements, save for those which involve the S1 or S2 states, which are considerably different. The change in the matrix elements involving the S2 subband is because at $\overline{X}$ the S2 subband is below the ZnTe light-hole edge, and so is mainly in the ZnTe layer, which causes a reduction in magnitude and change in polarisation dependence. It is also heavily mixed with the HH4 subband at $\overline{X}$, but this simply causes a splitting of the matrix element. The change in matrix elements involving the S1 subband is more unusual. The S1-HH1 matrix element decreases by a factor of about seven from $\overline{\Gamma}$, while the S1-HH3 and S1-HH5 matrix elements vanish completely at $\overline{X}$. For the S1-HH1 matrix element, further calculations have been performed at $q = 0.35(\pi/L)$ and $q = 0.67(\pi/L)$. These show that the matrix element falls off sharply away from $\overline{\Gamma}$, by a factor of three between $q = 0.05(\pi/L)$ and $q = 0.35(\pi/L)$ (fig. 6.14 (a)). The bulk band composition of the superlattice states was determined, and it was found that near $\overline{\Gamma}$ there is a strong spin-orbit band mixing in the interface state S1, but that away from $\overline{\Gamma}$ the mixing falls away. The matrix element is closely correlated with the percentage spin-split-off band mixing (fig 6.14(b)).

| | S1 | E1 | E2 | E3 | E4 |
|---|---|---|---|---|---|
| HH1 | 2.6602 | 0.0005 | 0.0008 | 0.0001 | 0.0002 |
| HH2 | 0.0054 | 0.5679 | 0.0021 | 0.0011 | 0.0005 |
| HH3 | 0.1008 | 0.0032 | 0.6397 | 0.0027 | 0.0082 |
| S2 | 2.3093 | 0.0012 | 0.0749 | 0.0057 | 0.0299 |
| HH4 | 0.0035 | 0.0003 | 0.0081 | 1.1065 | 0.0145 |
| HH5 | 0.0716 | 0.0023 | 0.0056 | 0.0189 | 0.5414 |

(a) $\overline{\Gamma}$ 011-polarisation.

| | S1 | E1 | E2 | E3 | E4 |
|---|---|---|---|---|---|
| HH1 | 0.0000 | 0.0000 | 0.0000 | 0.0000 | 0.0000 |
| HH2 | 0.0036 | 0.0000 | 0.0003 | 0.0000 | 0.0001 |
| HH3 | 0.0005 | 0.0004 | 0.0000 | 0.0000 | 0.0000 |
| S2 | 7.4202 | 0.0017 | 0.3054 | 0.0031 | 0.1600 |
| HH4 | 0.0065 | 0.0000 | 0.0015 | 0.0000 | 0.0000 |
| HH5 | 0.0000 | 0.0001 | 0.0000 | 0.0004 | 0.0000 |

(b) $\overline{\Gamma}$ 100-polarisation.

| | S1 | E1 | E2 | E3 |
|---|---|---|---|---|
| HH1 | 0.3969 | 0.0006 | 0.0000 | 0.0002 |
| HH2 | 0.0008 | 0.8280 | 0.0001 | 0.0026 |
| HH3 | 0.0000 | 0.0044 | 0.7437 | 0.0057 |
| S2 | 0.0875 | 0.0059 | 0.0024 | 0.2903 |
| HH4 | 0.1371 | 0.0034 | 0.0065 | 0.1204 |
| HH5 | 0.0006 | 0.0019 | 0.0018 | 0.0019 |

(c) $\overline{X}$ 011-polarisation.

|  | S1 | E1 | E2 | E3 |
|---|---|---|---|---|
| HH1 | 0.0000 | 0.0000 | 0.0000 | 0.0000 |
| HH2 | 0.0000 | 0.0000 | 0.0000 | 0.0000 |
| HH3 | 0.0000 | 0.0009 | 0.0000 | 0.0000 |
| S2 | 0.0338 | 0.0003 | 0.0173 | 0.0000 |
| HH4 | 0.0507 | 0.0001 | 0.0376 | 0.0000 |
| HH5 | 0.0005 | 0.0016 | 0.0005 | 0.0013 |

(d) $\overline{X}$ 100-polarisation.

Table 6.4 $(HgTe)_{15}$-$(ZnTe)_5$ interband matrix elements $\frac{2}{m}|M|^2$ in eV.

|  | HH1 $\overline{\Gamma}$ | HH1 $\overline{X}$ |
|---|---|---|
| HH2 | 0.0001 | 0.0000 |
| HH3 | 0.0003 | 0.0005 |
| S2 | 0.0485 | 0.0064 |
| HH4 | 0.0000 | 0.0011 |
| HH5 | 0.0003 | 0.0011 |

(a) 011-polarisation.

|  | HH1 $\overline{\Gamma}$ | HH1 $\overline{X}$ |
|---|---|---|
| HH2 | 0.0139 | 0.0120 |
| HH3 | 0.0000 | 0.0000 |
| S2 | 0.0004 | 0.0004 |
| HH4 | 0.0030 | 0.0009 |
| HH5 | 0.0001 | 0.0000 |

(b) 100-polarisation.

Table 6.5 $(HgTe)_{15}$-$(ZnTe)_5$ intersubband $\frac{2}{m}|M|^2$ in eV.

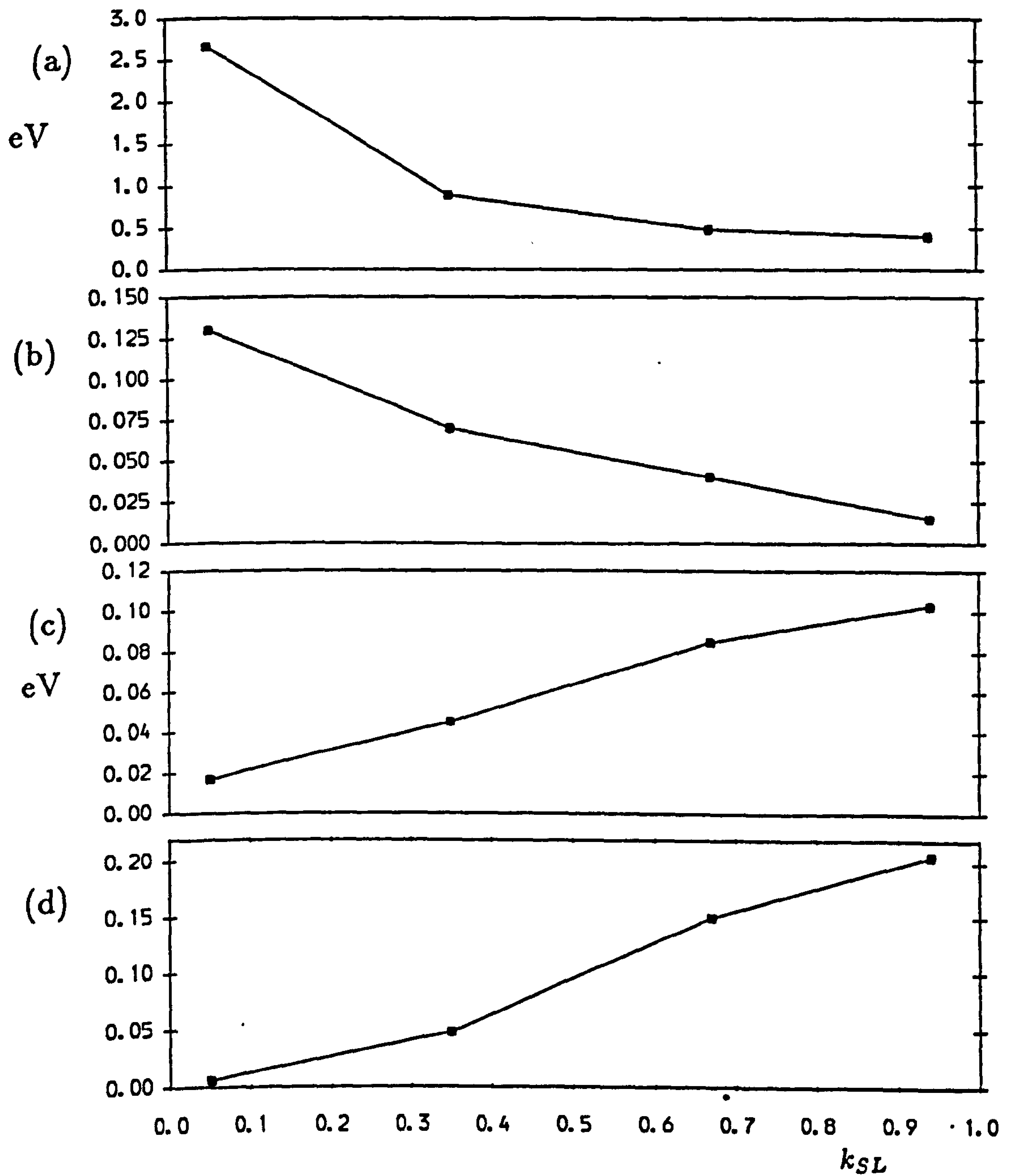


Figure 6.14. $k_{SL}$ dependence of properties of the $(HgTe)_{15}$-$(ZnTe)_5$ superlattice. (a) HH1-S1 $\frac{2}{m}|M|^2$ in (011)-polarisation, (b) spin-split-off bulk band admixture to S1 subband, (c) $E_g$, (d) in-plane (011) effective mass of the HH1 subband.

### 6.4.4 : Effective mass.

The effective mass of the HgTe-CdTe superlattice HH1 state has been found to vary along $k_{SL}$ for narrow gap superlattices (Meyer *et al.*, 1988 B). The major reason for this variation is the change in S1-HH1 bandgap with $k_{SL}$, and it is found that $m^*_{HH1}(k_{SL}) \propto E_g(k_{SL})$, i.e. that only the interaction with the S1 subband contributes significantly to the HH1 effective mass, and that the interband matrix element doesn't vary with $k_{SL}$ in the tight-binding calculations which have found this effect. From the calculations of interband matrix elements, presented in tables (6.4)(a-d) and of intraband matrix elements, table (6.5), it is found that the HH1 (011) effective mass is determined overwhelmingly by the S1-HH1 interaction in the HgTe-ZnTe superlattice also. This was used earlier in calculations of effective masses for N=1-5 (figure 6.8). However, the HgTe-ZnTe HH1-S1 matrix element also varies with $k_{SL}$. Using the formulas presented earlier to calculate the oscillator strength $f_{S1-HH1}(k_{SL})$ and the effective mass $m^*$, it is found that the HH1 effective mass in the layer plane is 0.0067 $m_0$ at $\overline{\Gamma}$ and 0.1709 $m_0$ at $\overline{X}$, i.e. it increases by a factor of 27 between $\overline{\Gamma}$ and $\overline{X}$. The increase of $E_g$ between $\overline{\Gamma}$ and $\overline{X}$ is only by a factor of six (fig 6.14(c)). The variation of effective mass with $k_{SL}$ is shown in fig 6.14(d). The effective mass ratio can be increased by optimising the well/barrier ratio and layer thicknesses. The effective mass ratio of 27 found in tight-binding calculations (Meyer *et al.*, 1989) was for a superlattice with a bandgap ratio $E_g^{\overline{X}}/E_g^{\overline{\Gamma}} \approx 27$. Thus the HgTe-ZnTe superlattice has the potential of a much greater effective mass ratio than the HgTe-CdTe superlattice. The empirical pseudopotential supercell calculations which have been performed for HgTe-CdTe superlattices have only considered zone-centre matrix elements and effective masses (Beavis *et al.*, 1990A,B; Beavis and Jaros, 1990; Xia, 1989), so it is unclear whether a change in matrix element with $k_{SL}$ might also be found in these calculations.

## 6.5 : Summary.

The HgTe-ZnTe superlattice has been studied in this chapter, and has been shown to have the potential of optical and electronic properties comparable with those of the HgTe-CdTe superlattice. The splitting between the top hole subband and the interface state in the valence band can be varied by changing the strain, which offers the possibility that HgTe-ZnTe semimetallic superlattices may have high mobilities up to higher temperatures than HgTe-CdTe superlattices, due to the increased parabolicity of the heavy-hole in-plane bandstructure. The interband and intraband (intersubband) momentum matrix elements of the superlattice have been considered in some detail, in order to study the selection rules in type-III superlattices, and it has been shown that some of the optical properties measured in experiment for HgTe-based superlattices may need to be reinterpreted. The mass dispersion of the highest heavy-hole subband, measured in experiment, and predicted theoretically for narrow gap type-III superlattices has been shown to occur in HgTe-ZnTe superlattices, and in addition is enhanced by a variation of interband matrix element for superlattice k-vectors parallel to the growth axis. There is a need for more experimental and theoretical work before the properties of this fascinating system will be fully understood.

# CHAPTER SEVEN

# SUMMARY AND CONCLUSION

## 7.1 : Summary.

The work presented in this thesis is a study of the electronic bandstructure and intersubband momentum matrix elements of the highly strained II-VI telluride superlattices CdTe-ZnTe and HgTe-ZnTe. There are three main elements to this work, the development of the theory needed to calculate the properties, the comparison of the approach taken here and results obtained with those of other workers, and an analysis of the current level of understanding of the systems studied and their potential as new materials.

The history and motivation of the study of semiconductor heterostructures, and the position of the systems studied within this, are reviewed in chapter one. The various theoretical approaches used are considered, with an emphasis on the underlying physical assumptions. The method used here is identified as one which produces results with an accuracy approaching that of *ab-initio* methods, but is more computationally efficient. Most importantly, the computer time needed does not depend upon the period of the superlattice.

In chapter two the method used for the calculation of the bandstructure of superlattices and quantum wells is described. The most computationally

intensive part of the calculation, the initial generation of the bulk bandstructure, is performed prior to the superlattice or quantum well calculation, so the bandstructure, wavefunctions, and any other properties of the heterostructures can be determined quickly. This imparts a great degree of flexibility to the method. The calculational approach is presented in a fairly abstract mathematical form, then it is shown how this can be used to calculate the properties of heterostructures on a computer. The extraction of wavefunctions, and the use of these to calculate the probability density distribution of the wavefunctions, and the intersubband momentum matrix elements, is described. The problem of the choice of matching plane is introduced, though a full discussion is left to chapter five. Calculations are presented of $Ga_{0.7}Al_{0.3}As$-GaAs-$Ga_{0.7}Al_{0.3}As$ quantum well and $Ga_{0.7}Al_{0.3}As$-GaAs superlattice energy levels, wavefunctions and intersubband momentum matrix elements. The bulk band nonparabolicity is included implicitly, as is the anisotropic polarisation dependence of the momentum matrix elements.

In chapter three the extension of the theoretical approach to calculate the properties of strained layer heterostructures is described. The deformation of the strained layers is calculated using macroscopic elasticity theory, and the expressions required for these calculations are derived, to calculate the lattice constants of the sublayers in a freestanding strained layer superlattice with a period consisting of a certain number of monolayers of each of two materials.

The change of the bulk bandstructures of the sublayers is calculated using the empirical pseudopotential method. Curves are used which approximate to the behaviour of the local pseudopotential in q-space under strain, and these curves are adjusted to give a reasonable fit to experiment. The use of this approach to model the variation of the lowest direct bandgap with hydrostatic pressure is illustrated by calculations on the II-VI tellurides. Finally the bulk semiconductor bandstructures under the biaxial strain in the strained layers are shown. Once the bulk strained bandstructure is available, the calculation of the states of semiconductor heterostructures proceeds as for unstrained heterostruc-

tures, as outlined in chapter two.

Chapter four consists of calculations of the electronic bandstructure and intersubband momentum matrix elements of the II-VI strained layer telluride superlattice CdTe-ZnTe. This superlattice has not been fully studied in the literature, and many questions remain, including uncertainty over the value of the valence band offset. There have been a number of calculations of the properties of the CdTe-ZnTe superlattices by the Kronig-Penney method and using the envelope function approximation, and one by the empirical tight-binding method. Calculations are performed of the valence- and conduction-subbands of $(CdTe)_N$-$(ZnTe)_N$ superlattices, with $N = 1$ to 30. The calculations give reasonable agreement with experiment, better than found in tight-binding calculations (Quiroga *et al.*, 1989), and the differences between experiment and theory may be due to inaccuracies in the constants used to account for the effects of pressure and strain upon the bulk bandstructures, or to the poor quality of the experimental superlattices. The results for superlattice Brillouin-zone centre states of short period superlattices, $N = 1 \rightarrow 2$, are compared with calculations in the literature. The main qualitative features of other calculations are found.

In chapter five, the choice of interface matching plane in boundary condition methods is considered. The source of the problem is that the method used is not self-consistent, and the calculations rely upon the transfer of charge between the sublayers being small enough to not affect the heterostructure properties significantly. Since the ionicity of the materials making up a heterostructure is reflected in the pseudopotential method, the position of the matching plane relative to to the positions of the ionic planes at the interfaces may be important in the calculations. The position of the matching plane was found to be not very important for $Ga_{0.7}Al_{0.3}As$-GaAs-$Ga_{0.7}Al_{0.3}As$ quantum wells, but to be of more importance in the $(CdTe)_N$-$(ZnTe)_N$ superlattice calculation, so another set of calculations is performed for $(CdTe)_N$-$(ZnTe)_N$ superlattices, but this time with a different interface matching plane. The calculations presented in chapter

four used a matching plane at the centre of the common Te-anion layers, while those presented in chapter five use a matching plane near bond centre. The calculations which use a matching plane at the centre of the common Te-anion layers are shown to find states close to those expected from calculations using the envelope-function approximation (chapter four), while the calculations with a matching plane at mid-bond find some asymmetry in the states. The main effect of the asymmetry is to allow some states to mix which did not mix in the calculations of chapter four, but there are also changes for short period superlattices. It is concluded that it is better to use a matching plane through the centre of a common ion plane when performing calculations on superlattices with a common ion.

In chapter six the $(HgTe)_{3N}$-$(ZnTe)_N$ superlattice is considered. The aim of the chapter was to consider the unusual properties which have been reported for HgTe-CdTe superlattices, to see whether the same properties may be observed for this superlattice, and to compare the two systems. The variation of energy levels with $N$ is considered, showing the crossover of the lowest conduction subband and the highest valence subband. As found for the HgTe-CdTe superlattice, this leads to a semiconductor-semimetal-semiconductor transition as HgTe sublayer width is increased, and it is suggested that the electronic properties of HgTe-ZnTe superlattices may be superior to those of HgTe-CdTe superlattices due to the strain, which increases the splitting between the top heavy-hole subband and the lower interface state, and so may improve the heavy-hole in-plane subband isotropy. The band-edge optical properties of the short period superlattices— those of shorter period than the semimetallic region— are described, and are found to be in qualitative agreement with calculations and experiment for short period HgTe-CdTe superlattices. The optical properties of the long period superlattices are described—these have not been calculated for long-period HgTe-CdTe superlattices. It is shown that the interpretation of long-period HgTe-CdTe superlattice optical properties in the literature may be misleading, and that this could lead to a change in the estimated valence band

offset. However, the incomplete character of the experimental information, and the uncertainty as to the effect of interface quality upon the superlattice properties, makes it impossible to be certain.

The bandstructure of one superlattice, the $(HgTe)_{15}$-$(ZnTe)_5$, and its wavefunctions and momentum matrix elements, is examined in detail. The upper conduction band subbandstructure and wavefunctions are properly described for the first time for any HgTe-based superlattice. The polarisation dependent momentum matrix elements between all the states at superlattice zone centre are described, and compared with calculations in the literature for HgTe-based superlattices. The matrix elements at superlattice growth-direction Brillouin-zone-edge ($\overline{X}$) are described for the first time, and show a significant change from the superlattice zone-centre ($\overline{\Gamma}$) matrix elements. In particular, the lowest electron to highest hole intersubband squared momentum matrix element decreases by a factor of about seven from $\overline{\Gamma}$ to $\overline{X}$. The ground heavy-hole in-plane effective mass has been reported to be proportional to the bandgap along $k_{SL}$ in HgTe-CdTe superlattices, this is known as effective mass dispersion (Meyer *et al.*, 1988 B). The change in matrix element found in the $(HgTe)_{15}$-$(ZnTe)_5$ superlattice would increase this mass dispersion by a factor of seven, compared to that expected if the effective mass were proportional to the bandgap. This suggests that the HgTe-ZnTe superlattice has the potential of higher effective mass dispersion than the HgTe-CdTe superlattice. All previous calculations which have found an effective mass dispersion have been performed by the tight-binding method, which does not describe the conduction band very well. The change in matrix element was due to the change in lowest conduction subband composition with $k_{SL}$, which the tight-binding method calculation might not detect.

## 7.2 : Suggestions for further work.

The calculations described within this thesis could be extended to calculate the bandstructure of superlattices with different combinations of layer widths, or to calculate the bandstructure and wavefunctions in detail for any of the systems already considered. This work would be very profitable for the HgTe-based heterostructures. Superlattices made of different pairs of constituents could also be considered. These calculations would require no changes to the programs used here. Superlattices with a period made of three or more materials could be studied (Osbourn, 1983), although there has been little experimental work in this direction to compare with. These calculations would require the extension of the computer programs, although this could be done easily using the theory presented in chapter two. Calculations could be performed of the electronic states of heterostructures under an external perturbation, for example hydrostatic or uniaxial strain, or an electric field. The application of an externally applied strain is dealt with using an extension of the theory described in chapter three. The calculation of states under an electric field is straightforward for a field applied in the growth direction, since the heterostructure can be described as a series of monolayers with an energy shift between each successive pair, and using the theory of chapter two (Monaghan and Brand, 1987). However a transverse electric field would require a different method since the matching of complex bandstructure at an interface assumes that the layers are periodic in the layer plane. The bandstructure and wavefunctions calculated using the method of chapters two and three could be used to calculate other properties of the superlattice, for example the optical absorption spectrum.

## 7.3 : Conclusion.

The pseudopotential method provides a good description of both the conduction and valence bands, and so is suitable for the calculation of interband matrix elements. Other empirical pseudopotential calculations of superlattice states have been by supercell methods, e.g. the approach of Jaros and co-workers (Jaros, 1990). Supercell calculations can take account of self-consistency, and do not have any problems with the choice of an interface matching plane. However, for most calculations of the electronic states of ideal semiconductor superlattices, the matching method produces results as good as those from a supercell approach, but is far more computationally efficient. This allows for studies of the variation of energy levels, band-mixing and intersubband matrix elements with sublayer widths, and of the variation of matrix elements over the superlattice Brillouin zone, to be carried out in a reasonable amount of time. The majority of properties of superlattices can be described by a model which treats the superlattice as an infinite, defect-free ordered structure, and those which cannot may be due to the inadequacy of the method, or of the bulk constants which are used. For example, the interface states of HgTe-based superlattices have been predicted to be strongly affected by interdiffusion (Simon *et al.*, 1990; Beavis *et al.*, 1990 A), but these effects have not been definitely identified in experimental results. For both the II-VI strained-layer superlattices considered here, there are discrepancies between experiment and theory, but it is not clear whether these deviations are mainly due to inadequate knowledge of bulk deformation potentials and valence band offsets, or are due to deviations from ideality. Advances in experimental measurements (Mathieu *et al*, 1991) and thorough theoretical calculations (Qteish and Needs, 1991) should help to clear up these problems. The method described in this thesis can be used to define where discrepancies exist, and to resolve them.

## Limits

The matrix coefficients $P^n$ and $Q^n$ which appear in chapter two, contain terms of the form $exp(ik_j^n x_n)$. For real bulk states these simply take account of the positions of the interface matching planes by a phase factor. However, for evanescent bulk states these terms represent a change in the magnitude of the state depending upon the position in the crystal. The normalisation of the bulk evanescent states in the calculation is arbitrary, so the magnitude of the exponentials is fixed at the interfaces. Changing the magnitudes of the coefficients of any particular bulk state will just change the coefficients of that state in the superlattice or quantum well state. The change of the evanescent state across the heterostructure sublayer is taken account of through the matrices $\underline{\mathbf{D}}_n$, introduced in equation 2.22.

The matrices $\underline{\mathbf{D}}_n$ contain terms of the form $exp(ik_j(x_n - x_{n-1}))$. For those terms for which $k_j$ is imaginary or complex, these represent terms which decay or grow across the layer. If $k_j(x_n - x_{n-1})) >> 1$, this term may need to be limited. The use of this limit has been discussed in the literature (Brand and Hughes, 1987; Mailhiot and Smith, 1986).

At an isolated interface, the wavefunction may be built up from bulk functions which decay away from it. If another parallel interface is nearby, as in a superlattice layer, the decaying tails of these functions will form part of the sum at this second interface. In the superlattice calculation, these decaying states are included as part of the sum. In general, the wavefunction is only affected by them very close to the interface. For a fairly wide layer, the tail may have decayed so far that its inclusion causes numerical problems. Thus, when the matching terms are calculated, a lower limit is imposed upon the wavefunction, of $exp(-XLIM)$, where $XLIM$ is a real number, and is generally 10 or greater.

In the calculations presented in this thesis, the magnitude of each exponential was fixed at the interface at which it is large, and was considered to decay from there. In most cases the use of this limit will have no effect upon the energy levels or momentum matrix elements. However, in a few cases the numerical instability of the calculations with wide sublayers meant that a limit of about $exp(-6)$ or $exp(-4)$ had to be imposed, which affected the energy levels by a few meV, for example in the conduction band of the $(CdTe)_N$-$(ZnTe)_N$ superlattice with the matching plane at bond centre, for $N > 10$, shown in figure 5.4, where the energy levels found by pseudopotential calculations are $5 - 10$ meV below those found by the Kronig-Penney method.

# APPENDIX B

## Formfactors for GaAs, AlAs, and $Ga_{0.7}Al_{0.3}As$

In this appendix the formfactors which have been used in chapter two to calculate the electronic states of GaAs-$Ga_{0.7}Al_{0.3}As$ quantum wells and superlattices are presented, with the resultant critical point energies with the valence band offset used in the calculation. The formfactors for the binary semiconductors are from the literature (Gell *et al.*, 1986A): they are fitted to give the correct critical point energy levels for a calculation using 65 plane waves. However, the fit was made without spin, while the calculation is performed with 130 plane waves, including spin, so for the calculations the input bulk conduction and valence bands are shifted to give the correct energy gaps (Madelung *et al.*, 1982A) with spin. It has been shown in an empirical pseudopotential calculation (Gell *et al.*, 1987) that the optical properties of AlGaAs superlattices are almost unaffected if the interaction between valence and conduction bands is ignored, so this shift should not be a problem for the optical matrix element calculations of chapter two. The GaAs-AlAs valence band offset used is 0.55 eV (Batey and Wright, 1986). In calculating the alloy bandstructure the virtual crystal approximation (Dornhaus and Nimtz, 1983) has been used; recent measurements of the alloy bandgap (Bosio *et al.*, 1988) support this approximation for this alloy, and give the alloy bandgap as

$$E^{\Gamma}_{\mathrm{gap}}(x) = 1.5194 + 1.36x + 0.22x^2 \text{ eV},$$

where $x$ is the proportion of Al in the alloy; this gives a bandgap of 1.947 eV for the 30 % Al alloy. The formfactors and resulting critical point energies used in the calculations are listed in table B.1.

| Material | AlAs | GaAs | $Ga_{0.7}Al_{0.3}As$ |
|---|---|---|---|
| $V_S^3$ | -0.2307 | -0.2396 | -0.2369 |
| $V_S^8$ | 0.0254 | 0.0126 | 0.0164 |
| $V_S^{11}$ | 0.0700 | 0.0600 | 0.0630 |
| $V_A^3$ | 0.0725 | 0.0700 | 0.0708 |
| $V_A^4$ | 0.0625 | 0.0500 | 0.0538 |
| $V_A^{11}$ | -0.0075 | 0.0100 | 0.0048 |
| $s_\mu$ | 0.001382 | 0.001479 | 0.001450 |
| $s_\alpha$ | 1.38 | 1.38 | 1.38 |
| $\Gamma_{8V}$ | -0.550 | 0.000 | -0.162 |
| $\Gamma_{6C}$ | 2.103 | 1.519 | 1.785 |
| $X_C$ | 1.678 | 2.007 | 1.908 |

Table B.1. Formfactors (Ry) and critical point energies (eV) used in the calculations in chapter two.

The constants $S_\mu$ and $S_\alpha$ are used to calculate the spin-orbit splitting. The contribution to the Hamiltonian from the spin-orbit coupling is given by

$$SOC_{s,s'} = -i\lambda S(\underline{G} - \underline{G}')\underline{\sigma}.\underline{K} \times \underline{K}'$$

$$= [-i\lambda^S cos((\underline{G} - \underline{G}').\underline{\tau}) + \lambda^A sin((\underline{G} - \underline{G}').\underline{\tau})].[\underline{\sigma}.\underline{K} \times \underline{K}']$$

(Chelikowsky and Cohen, 1976),

where

$$\lambda^S = \frac{S_\mu(S_\alpha + 1)}{2}$$

and

$$\lambda^A = \frac{S_\mu(S_\alpha - 1)}{2}$$

(Hughes, 1989).

The values of $S_\mu$ and $S_\alpha$ used for the bandstructure calculations of the materials used in this thesis are given in appendices B and C.

## Formfactors for CdTe, ZnTe, and HgTe

In this appendix the formfactors for the II-VI telluride semiconductors which have been used in the calculations of strained bandstructure in chapter three, and for the superlattice calculations of chapters four and five, are presented, together with the bulk parameters which were used to find the fits. The symmetric pseudopotential formfactor is $-\frac{2}{3}E_F$ at $q = 0$ (Cohen and Heine, 1970, p87). This is found using

$$k_F = (\frac{3\pi^2 Z}{\Omega_0})^{1/3}$$

and

$$E_F = k_F^2,$$

with all formfactors in Rydbergs. Since $Z = 4$ for all II-VI compounds, $k_F$ is only dependent upon the lattice parameter, $A$, through $\Omega = A^3/8$. The values of $A$, $\Omega_0$, and $-\frac{2}{3}E_F$ for the three compounds under consideration are given in table C.1.

| Compound | Lattice parameter (a.u) | $\Omega_0$ | $-\frac{2}{3}E_F$ (Ry) |
|---|---|---|---|
| ZnTe | 11.53 | 191.7 | -0.4836 |
| CdTe | 12.24 | 229.2 | -0.4293 |
| HgTe | 12.21 | 227.5 | -0.4314 |

Table C.1.

The pseudopotential calculation can calculate changes in bandstructure due to changes in lattice parameters, but to compare this with experiment it is necessary to know the extent of the deformation of the crystal produced by an

applied hydrostatic pressure, through the Murnaghan equation of state (equation 3.17), and the perpendicular strain found in a strained layer (equation 3.3); for these it is necessary to know Poisson's ratio, $\nu$, Young's modulus $E_{100}$, the Bulk modulus $B_0$, and the pressure derivative of the Bulk modulus, $B'_0$. These are related, and may be expressed in terms of the compliances $S_{11}$ and $S_{12}$ as

$$\nu = -S_{12}/S_{11}$$

$$E_{100} = 1/S_{11}$$

$$B_0 = \frac{1}{3(S_{11} + 2S_{12})}$$

using the relationships given in the literature (e.g. Madelung *et al.*, 1982A, p25). In practice the strain parameters for the II-VI semiconductors are not known to any great accuracy, so the best value of each is used, rather than deriving them all from some common set of constants. They are all checked for consistency. The values of strain parameters used in the calculations of chapters three, four, five and six, are given in table C.2. $\nu$ is calculated from the values of the compliances $S_{11}$ and $S_{12}$ shown. Values of $B'_0$ could not be found for CdTe and HgTe, so the value for ZnTe was used for all three semiconductors.

| Material | $S_{11}(10^{-1}$ MPa) | $S_{12}(10^{-1}$ MPa) | $\nu$ | $B_0$(GPa) | $B'_0$ |
|---|---|---|---|---|---|
| CdTe | 3.581(I) | -1.394(I) | 0.389 | 42.4(I) | 4.7 |
| ZnTe | 2.380(I) | -0.857(I) | 0.360 | 48.0(II) | 4.7(III) |
| HgTe | 3.980(III) | -1.638(III) | 0.412 | 47.6(III) | 4.7 |

Table C.2. Lattice parameters of the II-VI telluride semiconductors.

(I) Gil *et al.*, 1989. (II) Strössner *et al.*, 1987. (III) Madelung *et al.*, 1982B, p241, 2-4K values.

The bandstructure of the semiconductors was calculated to fit a set of physical parameters, which include the bandgaps $E_0^\Gamma = E_C^\Gamma - E_V^\Gamma$, $E^L = E_C^L - E_V^L$, and $E^X = E_C^X - E_V^X$, the first and second pressure derivatives of $E_g$, and the uniaxial splitting deformation potential $b$, which is defined by

$$E_{HH}^\Gamma - E_{LH}^\Gamma = 2b\frac{S_{11} - S_{12}}{S_{11} + S_{12}}\epsilon$$

where $E_{HH}^\Gamma - E_{LH}^\Gamma$ is the splitting produced between the heavy and light-hole bands at $\Gamma$ by a biaxial strain $\epsilon$. The effective masses are more difficult to fit, and tend to be larger than found in experiment, if the bandgaps are fitted reasonably well. The experimental parameters are shown in table C.3. A comparison with experimental variation of direct bandgap under hydrostatic pressure has been shown in chapter three. Fitted values of $b$ are shown in table C.4. The formfactors and spin parameters, and resultant bulk unstrained critical point energies are given in table C.4.

| Material | CdTe(expt) | ZnTe(expt) | HgTe(expt) |
|---|---|---|---|
| $E_0^\Gamma$(eV) | 1.6063(I) | 2.3945(I) | -0.303(II) |
| $dE_0/dP$(meV/GPa) | 65(III) | 109(IV) | 120(II) |
| $\frac{1}{2}d^2E_0/dP^2$ (meV/GPa$^2$) | 0(III) | -3.9(IV) | 0(II) |
| $E^L$ (eV) | 3.44(II) | 3.41(II) | 2.12(II) |
| $E^X$ (eV) | 5.49(II) | 5.41(II) | 5.0(II) |
| $\Delta_0$ (eV) | 0.97(II) | 0.91(II) | 1.08(II) |
| $b$ (eV) | -0.95(IV) | -1.2(IV) | -1.5(II) |

Table C.3. Physical parameters for the II-VI tellurides.

I: Neumann *et al.*, 1988.

II: Madelung *et al.*, 1982B.

III: Dunstan *et al.*, 1988.

IV: Gil *et al.*, 1989.

| Material | CdTe | ZnTe | HgTe |
|---|---|---|---|
| $V_S^3$ | -0.23 | -0.23 | -0.24798 |
| $V_S^8$ | 0.02 | 0.04 | -0.01867 |
| $V_S^{11}$ | 0.042 | 0.06 | 0.03600 |
| $V_A^3$ | 0.1216 | 0.09553 | 0.07407 |
| $V_A^4$ | 0.05619 | 0.04692 | 0.06193 |
| $V_A^{11}$ | 0.02864 | 0.03045 | 0.01553 |
| $S_\mu$ | 0.00420 | 0.00454 | 0.00407 |
| $S_\alpha$ | 1.00 | 1.00 | 1.50 |
| $E_0^\Gamma$ (eV) | 1.6075 | 2.3947 | -0.31433 |
| $\Delta_0$ (eV) | 0.9816 | 0.8929 | 1.047 |
| $E^L$ (eV) | 3.11 | 3.22 | 2.11 |
| $E^X$ (eV) | 4.63 | 4.38 | 4.25 |
| $b$ (eV) | -0.93 | -1.22 | -1.22 |

Table C.4. Formfactors (Ry) used in calculations of chapters four and five, with resulting critical point energy gaps (eV).

The variation of formfactors with $q$ are given in terms of seven constants, A-G, in equations 3.13 to 3.16. These are listed in table C.5.

| Constant | CdTe | ZnTe | HgTe |
|---|---|---|---|
| A | -0.00954 | -0.01741 | -0.00871 |
| B | 0.08296 | 0.11468 | 0.07623 |
| C | -0.42930 | -0.48360 | -0.43140 |
| D | 0.49736 | 0.43382 | 0.45443 |
| E | 0.14443 | 4.0147 | 0.08040 |
| F | 0.23995 | 1.3740 | 0.03219 |
| G | 0.02969 | 0.03045 | 0.01389 |

Table C.5.

## REFERENCES


Abram R.A. and Jaros M., 1989, NATO ASI Ser.B: Physics Vol.189, Band structure engineering in semiconductor microstructures.

Anastassakis E., 1990, paper at European Physical Society Condensed Matter Division conference, Lisbon.

Averous M., 1979, Phys.Stat.Sol.(b) **95**, 9.

Bassani F. and Brust D., 1963, Phys.Rev. **131**, 1524.

Bassani F. and Parravicini P.G., 1975, Electronic States and Optical Transitions in Solids (Oxford:Pergamon).

Bastard G., 1981, Phys.Rev.B, **24**, 5693.

Bastard G., 1988 A, Wave mechanics applied to semiconductor heterostructures, les editions de physique.

Bastard G., 1988 B, Phys.Rev.Lett. **60**, 2561.

Batey J. and Wright S.L., 1986, J.Appl.Phys. **59**, 200.

Beavis A.W., Jaros M., Zoryk A. and Morrison I., 1990A, Semicond.Sci.Technol. **5**, 1051.

Beavis A.W., Jaros M. and Morrison I., 1990B, 5th int. conf. on superlattices and microstructures, Berlin, 1990 — to be published in Superlattices and Microstructures.

Beavis A.W. and Jaros M., 1990, Phys.Rev.B**41**, 7903.

Berroir J.M., Guldner Y. and Voos M., 1986, IEEE J.Quantum Electron. QE-**22**, 1793.

Bertho D., Simon A., Boiron D., Jouanin C. and Priester C., 1990, J.Crystal Growth, **101**, 372.

Bosio C., Staehli J.L., Guzzi M., Burri G. and Logan R.A., 1988, Phys.Rev.B**38**, 3263.

Brand S., Monaghan S. and Szydlik J.P., 1987, Semicond.Sci.Technol., **2**, 123.

Brand S. and Hughes D.T., 1987, Semicond.Sci.Technol., **2**, 607.

Brey L. and Tejedor C., 1987, Phys.Rev.B, **35**, 9112.

Cade N.A., 1985, J.Phys.C: Solid State Phys. **18**, 5135.

Camphausen D.L., Connell G.A.N. and Paul W., 1971, Phys.Rev.Lett. **26**, 184.

Cardona M., 1972, Proc.Int.School Phys. "Enrico Fermi", LII, 514, Academic Press.

Chang Y.C., 1982, Phys.Rev.B, **25**, 605.

Chang Y.C. and Schulman J.N., 1982, Phys.Rev.B, **25**, 3975.

Chang Y.C. and Schulman J.N., 1985, Phys.Rev.B, **31**, 2069.

Chang Y.C., Schulman J.N., Bastard G., Guldner Y. and Voos M., 1985, Phys.Rev.B**31**, 2557.

Chelikowsky J.R. and Cohen M.L., 1976, Phys.Rev.B**14**, 556.

Cho H.-S. and Prucnal P.R., 1987, Phys.Rev.B**36**, 3237.

Choi J.B., Ghenim L., Mani R., Drew H.D., Yoo K.H., and Cheung J.T., 1990, Phys.Rev.B**41**, 10872.

Christen J., Krahl M. and Bimberg D., 1990, Superlattices and Microstructures, **7**, 1.

Chu X., Sivananthan S. and Faurie J.P., 1988, Superlattices and Microstructures **4**, 173.

Cibert J., Gobil Y., Dang Le Si, Tatarenko S.,Feuillet G., Jouneau P.H. and Saminadayar K., 1990, Applied Physics Letters **56**, 292.

Cibert J., Andre R., Deshayes C., Feuillet G., Jouneau P.H., Dang Le Si, Mallond R., Nahmani A., Saminadayar K. and Tatarenko S., 1991, Superlatt. and Microstr. **9**, 271.

Claessen L.M., 1989, p.7 in Abram and Jaros, 1989.

Cohen M.L. and Bergstresser, 1966, Phys.Rev. **141**, 789.

Cohen M.L. and Chelikowsky, 1982, Handbook on Semiconductors **1**, chapter 4B, p.219.

Cohen M.L. and Heine V., 1970, Solid State Phys., **24**, 37, (New York: Academic).

Collet J.H., Kalt H., Dang Le Si, Cibert J., Samaninadayar K., and Tatarenko S., 1991, Phys.Rev.B**43**, 6843.

Dingle R., Wiegmann W. and Henry C.H., 1974, Phys.Rev.Lett. **33**, 827.

Dornhaus R. and Nimtz G., 1983, Narrow-Gap Semiconductors, Springer-Verlag, p119.

Duc Tran Minh, Hsu C., Faurie J.P., 1987, Phys.Rev.Lett. **58**, 1127.

Dunstan D.J., Gil B. and Homewood K.P., 1988, Phys.Rev.B**38**, 7862.

Dunstan D.J., Gil B., Preister C. and Homewood K.P., 1989, Semicond.Sci.Technol. **4**, 241.

Dunstan D.J. and Adams A.R., 1990, Semicond.Sci.Technol., **5**, 1202.

Esaki L., 1986, J.Quantum Electron. QE-**22**, 1611.

Fang Z.M., Persson A. and Cohen R.M., 1988, Phys.Rev.B, **37**, 4071.

Faurie J.P., Million A. and Piaguet J., 1982, Appl.Phys.Lett. **41**, 713.

Faurie J.P., 1986, IEEE J.Quantum Electron. QE-**22**, 1656.

Faurie J.P., Sivananthan S., Chu X. and Wijewarnasuriya P.A., 1986, Applied Physics Letters **48**, 785.

Faurie J.P., 1989, p.21 in Abram and Jaros, 1989.

Feldman R.D., 1990, J.Vac.Sci.Technol.A **8**, 1888.

Flores F., Tejedor C. and Martin-Rodero A., 1978, Phys.Stat.Sol. (b) **88**, 591.

Flores F. and Tejedor C., 1987, J.Phys.C:Solid State Phys. **20**, 145.

Frank F.C. and Van der Merwe J.H., 1949 A, Proc. Roy. Soc. of London, Ser. A, **198**, 205.

Frank F.C. and Van der Merwe J.H., 1949 B, Proc. Roy. Soc. of London, Ser. A, **198**, 216.

Fujiwara K., Tsukada N., Nakayama T. and Nishino T., 1987, Appl.Phys.Lett. **51**, 1717.

Fujiwara K., Tsukada N., Nakayama T. and Nishino T., 1989, Solid State Commun. **69**, 63.

Fujiyasu H. and Mochizuki K., 1985, J.Appl.Phys. **57**, 2960.

Gell M.A., Ninno D., Jaros M. and Herbert D.C., 1986A, Phys.Rev.B **34**, 2416.

Gell M.A., Wong K.B., Ninno D. and Jaros M., 1986B, J.Phys.C:Solid State Phys. **19**, 3821.

Gell M.A., Ninno D., Jaros M., Wolford D.J., Keuch T.F. and Bradley J.A., 1987, Phys.Rev.B**35**, 1196.

Gerard J.-M. and Marzin J.-Y., 1990, Surf.Sci. **229**, 433.

Gerchikov L.G. and Subashiev A.V., 1990, Phys.Stat.Solidi (b) **160**, 443.

Giannozzi P., Grosso G. and Pastori Parravicini G., 1990, Rivista del Nuovo Cimento, Vol. **13**, No.3, 1.

Gil B., Dunstan D.J., Calatayud J., Mathieu H. and Faurie J.P., 1989, Phys.Rev.B**40**, 5522.

Gil B., 1990, Private Communication.

Gilbert T.G. and Gurman *S.J., 1987,* Superlatt. and Microstr. **3**, 17.

Gilbert T.G. and Gurman S.J., 1989, Semicond.Sci.Technol. **4**, 765.

Glass A.M., 1987, Science **235**, 1003.

Grant R.W., Waldrop J.R., Kraut E.A. and Harrison W.A., 1990, J.Vac.Sci.Technol.B, **8**, 736.

Greenaway D.L. and Harbeke G., 1968, Optical properties and band structure of semiconductors, Pergamon Press.

Harrison W.A., 1980, Electronic structure and the properties of solids, W.H. Freeman and Company.

Hefetz Y., Lee D., Nurmikko A.V., Sivananthan S., Chu X. and Faurie J.P., 1986, Phys.Rev.B**34**, 4423.

Heine V., 1963, Proc.Phys.Soc.London, **81**, 300.

Hoffman C.A., Meyer J.R., Bartoli F.J., Lansari Y., Cook J.W. Jnr., and Schetzina J.F., 1990A, Surf.Sci. **228**, 45.

Hoffman C.A., Meyer J.R. and Bartoli F.J., 1990B, Mat.Res.Soc.Symp.Proc. Vol.**161**, 403.

Houghton D.C., Peroviuc D.D., Baribeau J.-M., and Weatherly G.C., 1990, J.Appl.Phys. **67**, 1850.

Hsu C. and Faurie J.P., 1988, J.Vac.Sci.Technol.B **6**, 773.

Hughes D.T., 1989, PhD thesis, the University of Durham.

Ishibashi A., Mori Y., Itabashi M. and Watanabe N., 1985, J.Appl.Phys. **58**, 2691.

Jaros M., Zoryk A. and Ninno D., 1987, Phys.Rev.B**35**, 8277.

Jaros M., 1988, Phys.Rev.Lett. **60**, 2560.

Jaros M., 1989, Physics and applications of semiconductor microstructures, Clarendon Press : Oxford.

Jaros M., 1990, pp175-258 in Pearsall T.P., 1990 A.

Johnson N.F., Hui P.M. and Ehrenreich H., 1988, Physics Review Letters **61**, 1993.

Kashyap P., Jain M. and Sehgal H.K., 1990, Infrared Phys. **30**, 285.

Katnani A.D. and Margaritondo G., 1983, J.Appl.Phys. **54**, 2522.

Kinch M.A. and Goodwin M.W., 1985, Journal of Applied Physics **58**, 4455.

Ko D.Y.K., Edwards G. and Inkson J.C., 1990, Semicond.Sci.Technol. **5**, 200.

Kobayashi H., Iwamura H., Saku T. and Otsuka K., 1983, Electronics Letters, **19**, 166.

Kohn W., 1957, Solid State Physics **5**, 257, Academic Press Inc.: New York.

Kronig R. de L. and Penney W.G., 1930, Proc.Roy.Soc.London Ser. A, **130**, 499.

Lambrecht W.R.L. and Segall B., 1990, Phys.Rev.B **41**, 2832.

Lin-Liu Y.R. and Sham L.J., 1985, Phys.Rev.B**32**, 5561.

Madelung O., Schulz M., and Weiss H., 1982A, Landolt and Bornstein Vol **17a**.

Madelung O., Schulz M., and Weiss H., 1982B, Landolt and Bornstein Vol **17b**.

Mailhiot C. and Smith D.L., 1986, Phys.Rev.B**33**, 8360.

Marbeuf A., Ballutaud D., Triboulet R., Dexpert H., Lagarde P. and Marfaing Y., 1989, Phys.Chem.Solids **50**, 975.

Marsh A.C. and Inkson J.C., 1984, J.Phys.C: Solid State Phys. **17**, 6561.

Mathieu H., Allegre J., Chatt A., Lefebvre P. and Faurie J.P., 1988, Phys.Rev.B**38**, 7740.

Mathieu H., Chatt A., Allegre J. and Faurie J.P., 1990, Phys.Rev.B**41**, 6082.

Mathieu H., Allegre J., and Gil B., 1991, Phys.Rev.B**43**, 2218.

Matthews J.W. and Blakeslee A.E., 1974, J.Crystal Growth **27**, 118.

Matthews J.W. and Blakeslee A.E., 1975, J.Crystal Growth **29**, 273.

Melz P.J., 1971, J.Phys.Chem.Sol. **32**, 209.

Menendez J., Pinczuk A., Valladores J.P., Feldman R.D. and Austin R.F., 1987, Applied Physics Letters **50**, 1101.

Meyer J.R., Bartoli F.J., Hoffmann C.A. and Schulman J.N., 1988 A, Phys.Rev.B**38**, 12457.

Meyer J.R., Hoffman C.A., Bartoli F.J., Han J.W., Cook J.W. Jr, Schetzina J.F., Chu X., Faurie J.P., and Sculman J.N., 1988 B, Phys.Rev.B**38**, 2204.

Meyer J.R., Hoffman C.A., Bartoli F.J., and Schulman J.N., 1989, J.Vac.Sci.Technol. A **7**, 404.

Meyer J.R., Hoffman C.A. and Bartoli F.J., 1990, Semicond.Sci.Technol. **5**, S90.

Miles R.H., Wu G.Y., Johnson M.B., McGill T.C., Faurie J.P. and Sivananthan S., 1986, Applied Physics Letters **48**, 1383

Miles R.H., McGill T.C., Sivananthan S., Chu X. and Faurie J.P., 1987, J.Vac.Sci.Technol.B **5**, 1263.

Miles R.H. and McGill T.C., 1989, J.Vac.Sci.Technol.B **7**, 753.

Monaghan S. and Brand S., 1987, Superlattices and Microstructures, **3**, 697.

Monfroy G., Sivananthan S., Chu X., Faurie J.P., Knox R.D. and Staudenmann J.L., 1986, Applied Physics Letters **49**, 152.

Mullins J.T., Clifton P.A., Brown P.D., Hall D.O. and Brinkman A.W., 1990, Mat.Res.Soc.Symp.Proc. Vol.**161**, 357.

Murnaghan F.D., 1944, Proc. Nat.Acad. Sci. **30**, 244.

McCaldin J.D., McGill T.C. and Mead C.A., 1976, Phys.Rev.Lett., **36**, 56.

McCaldin J.D., 1989, p36 in McGill *et al.*, 1989A.

McGill T.C., Sotomayor-Torres C.M. and Gebhart W., 1989A, Growth and Optical Properties of Wide-Gap II-VI Low-Dimensional Semiconductors, NATO ASI:Series B,. Plenum.

McGill T.C., Miles R.H., Rajakarumanayake Y. and McCaldin J.D., 1989B, p53 in McGill *et al.*, 1989A.

Neumann Ch., Nöthe A. and Lipari N.O., 1988, Phys.Rev.B**37**, 922.

Ohno H., Mendez E.E., Brum J.A., Hong J.M., Agullo-Rueda F., Chang L.L., and Esaki L., 1990, Phys.Rev.Lett., **64**, 2555.

Osbourn G.C., 1983, J.Vac.Sci.Technol. B, 379.

O'Reilly E.P., 1989, Semicond.Sci.Technol. **4**, 121.

Parker G.H. and Mead C.A., 1968, Phys.Rev.Lett., **21**, 605.

Pearsall T.P., 1990 A, Semiconductors and semimetals vol.32, Strained layer superlattices: Physics, Academic Press inc.

Pearsall T.P., 1990 B, p.1 of Pearsall T.P., 1990 A.

Qteish A. and Needs R.J., 1991, J.Phys.Condens.Matter **3**, 617.

Quiroga L., Camacho A., Brey L. and Tejedor C., 1989, Phys.Rev.B**40**, 3955.

Quiroga L., Rodríguez F.J., Camacho A. and Tejedor C., 1990, Phys.Rev.B**42**, 11198.

Rajakarunanayake Y., Miles R.H., Wu G.Y. and McGill T.C., 1988, Phys.Rev.B**37**, 10212.

Schulman J.N. and McGill T.C., 1979, Applied Physics Letters **34**, 663.

Schulman J.N. and McGill T.C., 1980, Solid State Communications **34**, 29.

Schulman J.N. and Chang Y.C., 1985, Phys.Rev.B, **31**, 2056.

Shtrikman H., Riezman A., Tenne R., Mahalu D. and Finkman E., 1989, Applied Physics Letters **55**, 553.

Shtrikman H. and Finkman E., 1989, Superlattices and Microstructures **6**, 55.

Simon A., Bertho D., Boiron D. and Jouanin C., 1990, Phys.Rev.B**42**, 5221.

Smith D.L. and Mailhiot C., 1990, Rev.Mod.Phys. **62**, 173.

Sooryakumar R., 1988, Comments Cond.Mat.Phys. **14**, 43.

Strössner K., Ves S., Kim Chul Koo, Cardona M., 1987, Solid State Commun. **61**, 275.

Takita K. and Landwehr G., 1981, Phys.Status Solidi B **106**, 259.

Tamm I., 1932, Phys.Z.Sowjetunion **1**, 733.

Tersoff J., 1989, Phys.Rev.B**40**, 10615.

Todd J.D., 1981, Structural theory and analysis (second edition), MacMillan publishers Ltd.

Triboulet R., 1990, Semicond.Sci.Technol. **5**, 1073.

Van de Walle C.G., Shahzad K. and Olego D.J., 1988, J.Vac.Sci.Technol.B, **6**, 1350.

Van de Walle C.G., 1989, Phys.Rev.B **39**, 1871.

Van Vechten J.A. and Malloy K.J., 1990, J.Phys.:Condens.Matter **2**, 281.

Ves S., Strössner K., Christensen N.E., Kim C.K., and Cardona M., 1985, Solid State Commun. **56**, 479.

Wei S.-H. and Zunger A., 1987, Phys.Rev.Lett., **59**, 144.

Wei S.-H. and Zunger A., 1988, J.Appl.Phys. **63**, 5794.

Weiner J.S., Chemla D.S., Miller D.A.B., Haus H.A., Gossard A.C., Wiegmann W. and Burrus C.A., 1985, Appl.Phys.Lett., **47**, 664.

Wu G.Y. and McGill T.C., 1985, Applied Physics Letters **47**, 634.

Wu Y.-H., Fujita Shizuo and Fujita Shigeo, 1990, Journal of Applied Physics **67**, 908.

Xia J.-B., 1989, Phys.Rev.B**39**, 3310.

Yamanishi M. and Suemune I., 1984, Jap.J.Appl.Phys., **23**, L35.

Yang Z., Lansari Y., Han J.W., Yu Z. and Schetzina J.F., 1990, Mat.Res.Soc.Symp.Proc. Vol. **161**, 257.

Yoo K.H., Aggarwal R.W., Ram-Mohan L.R. and Wu O.K., 1990, J.Vac.Sci.Technol.A **8**, 1194.

Zoryk A. and Jaros M., 1987, Applied Physics Letters **50**, 1191.